UNIVERSITY OF CALIFORNIA

Santa Barbara

Asymmetric Miktoarm Star Polymers: Design, Synthesis, Self-Assembly, and Mechanical Properties

A dissertation submitted in partial satisfaction of the

requirements for the degree Doctor of Philosophy

in Chemistry

by

Adam Edward Levi

Committee in charge:

Professor Craig Hawker, Co-Chair

Professor Christopher Bates, Co-Chair

Professor Glenn Fredrickson

Professor Michael Chabinyc

Professor Javier Read de Alaniz

June 2021

The dissertation of Adam Edward Levi is approved.

Javier Read de Alaniz

Glenn Fredrickson

Michael Chabinyc

Christopher Bates, Committee Co-Chair

Craig Hawker, Committee Co-Chair

June 2021

Asymmetric Miktoarm Star Polymers: Design, Synthesis, Self-Assembly, and Mechanical Properties

ACKNOWLEDGEMENTS

The work presented in this thesis was only possible because of the collaborations I had with so many other researchers and professors. Jing Ren, a postdoc at the time in the Hawker group, was the first person to take me under his wing and taught me the skills I needed to tackle the synthetic challenges I was facing early on and generally an excellent ethos on how to conduct research. Then Prof. Josh Lequieu started as a postdoc in Glenn's group and together we made a fantastic team. Much of the success of our studies presented in Chapter 2 as well as Chapter 3 I owe to Josh. I think what we had was the epitome of experiment-theory collaboration, elevating the quality of both sides. I look back very fondly on the hours I spent in his office learning about the capabilities of simulation techniques, teaching Josh about what is possible with synthesis, and of course sharing our love of surfing. I have also learned a lot from Morgan Bates, who I have been working with almost since the beginning. Her knowledge of synthesis and self-assembly was invaluable. I am also thankful for Sanjoy Mukherjee, the first postdoc in the Bates group. His contributions to my projects and our group in general were essential, both scientific and otherwise. Similar to how Josh helped elevated my synthetic work with his simulations, Renxuan Xie did the same with his expertise in rheology. The success of the super-soft bottlebrushes would not have been possible without Sanjoy and Ren and I was lucky to be a part of the team and learn so much from the both of them. Jeffrey Self, who started at the same time as me, was always someone I could talk to and felt like we would be on the same page. Being the first two students in a new lab and no established projects put a lot of pressure on our shoulders and I am really proud of what our lab has accomplished. Not to sound too cliché, but I always felt like "if we build it, they will come". Jacob Horne, an extremely talented undergraduate researcher that I had the pleasure of working with for three

years, was vital to building many of the synthetic and experimental techniques now widely used in our research group. This entire thesis would not be the same without him. What I didn't realize about "if we build, it they will come" is that when they arrived, they would build it even better. Jacob Blankenship came and took what I was doing to an entirely different level. His hard work and synthetic expertise were essential to the success of the studies presented in Chapter 3 and Chapter 4. Continuing this trend, Patrick Getty has taken these star polymers in new direction outside the scope of this thesis, and I am excited to see what the future holds for him and this project.

Of course, I am tremendously thankful for my advisors Prof. Chris Bates and Prof. Craig Hawker. From our first conversation Chris was clear he wanted me to work "with" him, not "for" him. After almost five years that is still the case. Having the honor of being one of Chris' first graduate students we learned a lot together. I am extremely thankful for all the time Chris took not just to discuss our research but also to educate me on how to present data both written and orally. Chris motivated me to elevate my skills and get outside of my comfort zone. This is not to say it was easy but pushing yourself past what you think you are capable of rarely is. Craig too was an excellent advisor, always offering sage advice and perspective and never holding back on criticism necessary for me to grow. I really enjoyed our discussions and banter at our group meetings together.

I must also thank those that heavily influenced me before coming to UCSB. In particular Prof. Matthew Tirrell, who I had the pleasure of working for almost my entire undergraduate education. I learned so much about how to be a good scientist and person from Matt. He also played an important role in my decision to go to UCSB, which ultimately turned out to be one of the best decisions I have ever made. I learned so much from Matt and the

people in his group, in particular David Goldfeld and Prof. Samanvaya Srivastava. It feels like things have come full circle with David now a postdoc in Craig's group and with Sam now a professor at UCLA, just down the street. I also want to thank Dr. Yi Liu who was an excellent mentor for the summer I spent with him at LBNL and helped rekindle my fervor for science after a challenging year in undergrad.

My expression of gratitude would not be complete without recognizing all those outside academia who supported me. I am so fortunate to have parents who from an early age instilled a love of science and encouraged my curiosity of the world around me. To this day they have always been there to help me through tough situations. I want to thank all of my friends who made graduate school so much fun.

In particular Nnamdi Akporji, Raymond Borg, and Dakota Rawlings, brilliant scientists in their own right and a ton of fun to be around. Living with Nnamdi for almost four years was awesome, he was my rock, and I will look back on these years with him with great fondness. With Ray and Dakota, I learned and fell in love with kiteboarding, surfing, and hydrofoiling, passions that I will keep for the rest of my life. I know these will be life-long friends.

CURRICULUM VITAE OF ADAM EDWARD LEVI
June 2021

Education

2016 – 2021, University of California, Santa Barbara, Department of Chemistry and Biochemistry

2012 – 2016, The University of Chicago, Bachelor of Science Chemistry

Professional Employment

2016 – Present, Graduate Student, UC Santa Barbara
Materials Research Lab
Advisors: *Prof. Christopher Bates and Prof. Craig Hawker*
Polymer synthesis, polymer architecture, star polymers, bottlebrush polymers, polymer physics, block copolymers, self-assembly, mechanical properties of elastomeric polymers

2013 – 2016, Undergraduate Research Assistant, The University of Chicago
Institute for Molecular Engineering
Advisor: *Prof. Matthew Tirrell*
Block polyelectrolyte complexation; hydrogels; peptide amphiphile micelles

2014, Undergraduate Research Intern, Lawrence Berkeley National Laboratory
Molecular Foundry
Advisor: *Dr. Yi Liu*
Synthesis and characterization of organic semiconducting polymers

Publications

1. Renxuan Xie, Sanjoy Mukherjee, **Adam E. Levi**, Veronica G. Reynolds, Hengbin Wang, Michael L. Chabinyc, Christopher M. Bates, "Room temperature 3D printing of super-soft and solvent free elastomers" *Sci*. *Adv*. 2020, 6, eabc6900
2. Samanvaya Srivastava, **Adam E. Levi**, David J. Goldfeld, Matthew V. Tirrell, "Structure, Morphology, and Rheology of Polyelectrolyte Complex Hydrogels Formed by Self-Assembly of Oppositely Charged Triblock Polyelectrolytes," *Macromolecules* 2020, 53, 5763-5774
3. Cheng Zhang, Morgan W. Bates, Zhishuai Geng, **Adam E. Levi**, Daniel Vigil, Stephanie M. Barbon, Tessa Loman, Kris T. Delaney, Glenn H. Fredrickson, Christopher M. Bates, Andrew K. Whittaker, Craig J. Hawker, "Rapid Generation of Block Copolymer Libraries Using Automated Chromatographic Separation," *Journal of the American Chemical Society*, 2020, 142, 9843–9849
4. Jeffrey L. Self, Caitlin S. Sample, **Adam E. Levi**, Kexin Li, Renxuan Xie, Javier Read de Alaniz, Christopher M. Bates, "Dynamic Bottlebrush Polymer Networks: Self-Healing in Super-Soft Materials," *Journal of the American Chemical Society*, 2020, 142, 7567-7573
5. Morgan W. Bates, Stephanie M. Barbon, **Adam E. Levi**, Ronald M. Lewis III, Haley K. Beech, Kasper M. Vonk, Cheng Zhang, Glenn H. Fredrickson, Craig J. Hawker,

Christopher M. Bates, "Synthesis and Self-Assembly of AB_n Miktoarm Star Polymers," *ACS Macro Letters* 2020, 9, 396–403

6. Sanjoy Mukherjee, Renxuan Xie, Veronica G. Reynolds, Takumi Uchiyama, **Adam E. Levi**, Eric Valois, Hengbin Wang, Michael L. Chabinyc, and Christopher M. Bates, "Universal Approach to Photo-Crosslink Bottlebrush Polymers," *Macromolecules* 2020, 53, 1090–1097
7. **Adam E. Levi**, Liangbing Fu, Joshua Lequieu, Jacob D. Horne, Jacob Blankenship, Sanjoy Mukherjee, Tianqi Zhang, Glenn H. Fredrickson, Will R. Gutekunst, Christopher M. Bates, "Efficient Synthesis of Asymmetric Miktoarm Star Polymers," *Macromolecules* 2020, 53, 702–710
8. Veronica G. Reynolds, Sanjoy Mukherjee, Renxuan Xie, **Adam E. Levi**, Amalie Atassi, Takumi Uchiyama, Hengbin Wang, Michael L. Chabinyc, Christopher M. Bates, "Super-soft solvent-free bottlebrush elastomers for touch sensing," *Materials Horizon*, 2020, 7, 181–187
9. **Adam E. Levi**, Joshua Lequieu, Jacob D. Horne, Morgan W. Bates, Jing M. Ren, Kris T. Delaney, Glenn H. Fredrickson, Christopher M. Bates, "Miktoarm Stars via Grafting-Through Copolymerization: Self-Assembly and the Star-to-Bottlebrush Transition," *Macromolecules* 2019, 52, 1704–1802
10. Anand Rahalkar, Guangmin Wei, Ryan Nieuwendaa, Vivek M. Prabhu, Samanvaya Srivastava, **Adam E. Levi**, Juan J. de Pablo, and Matthew V. Tirrell, "Effect of temperature on the structure and dynamics of triblock polyelectrolyte gels," *Journal of Chemical Physics* 2018, 149, 163310
11. Jing M. Ren, Jimmy Lawrence, Abigail S. Knight, Allison Abdilla, Raghida Bou Zerdan, **Adam E. Levi**, Bernd Oschmann, Will R. Gutekunst, Sang-Ho Lee, Youli Li, Alaina J. McGrath, Christopher M. Bates, Greg G. Qiao, Craig J. Hawker, "Controlled Formation and Binding Selectivity of Discrete Oligo(methyl methacrylate) Stereocomplexes," *Journal of the American Chemical Society*, 2018, 140, 1945–1951
12. Samanvaya Srivastava, Marat Andreev, **Adam E. Levi**, David J. Goldfeld, Jun Mao, William T. Heller, Vivek M. Prabhu, Juan J. de Pablo, Matthew V. Tirrell, "Gel phase formation in dilute triblock copolyelectrolyte complexes," *Nature Communications* 2017, 8, 14131

Awards

2020, Yzurdiaga Graduate Student Fellowship, *UC Santa Barbara*

2019, Robert H. DeWolfe Distinguished Teaching Fellowship, *UC Santa Barbara*

2019, American Chemical Society Travel Honorarium, *American Chemical Society*

2017/2018, Mellichamp Sustainability Fellowship, *UC Santa Barbara*

2017, Phi Lambda Upsilon Award for Academic Excellence, *UC Santa Barbara*

Patents

1. Xie, Renxuan; Mukherjee, Sanjoy; Reynolds, Veronica; **Levi, Adam**; Chabinyc, Michael; Bates, Christopher M. "Room-temperature 3D printing of a Super-soft and Solvent-free Elastomer" (UC Case No. 2020-702)
2. Reynolds, Veronica; Mukherjee, Sanjoy; Xie, Renxuan; **Levi, Adam**; Chabinyc, Michael; Bates, Christopher M. "Capacitive pressure sensor with bottlebrush elastomer dielectric layer for ultra-low pressure sensing" U.S. Patent Application 15/931,254, May 13, 2020

Field of Study

Major Field: Materials Chemistry
Studies in Synthetic Control of Architecture and Properties with Professor Christopher M. Bates and Professor Craig J. Hawker

ABSTRACT

Asymmetric Miktoarm Star Polymers: Design, Synthesis, Self-Assembly, and Mechanical Properties

by

Adam Edward Levi

Asymmetric miktoarm star polymers, comprising a single A arm coupled to a multitude of B or AB′ arms, produce unique material properties. In particular, morphologies at significantly elevated volume fraction of the A material can be obtained. For instance, the performance of thermoplastic elastomers (TPEs) stands to significantly improve from increasing the volume fraction of A while maintaining an elastic matrix. However, existing synthetic strategies are beleaguered by complicated reaction schemes restricted in both the monomer scope and yield. Bottlebrushes copolymers, on the other hand, are easily synthetically accessible using Grubbs third-generation catalyst via the ring-opening metathesis co-polymerization (ROMP) of macromonomers. The well controlled synthesis of bottlebrush copolymers at low backbone degrees of polymerization (*n*) was demonstrated. Self-assembly in the bulk was studied as a function of molecular composition, arm stoichiometry, and *n*. Insights generated from scattering experiments and self-consistent field theory simulations indicate these materials behave as disperse miktoarm stars at low *n* with a transition to brush-like conformations as *n* increases. The star-to-bottlebrush transition is quantifiable for both statistical and diblock sequences by unique signatures in the experimental scaling of domain spacing and simulated distribution of backbone/side-chain density within lamellar unit cells. These findings represent a conceptual framework that simplifies the synthesis of miktoarm star polymers.

These conclusions were used to develop a second-generation synthetic approach, coined "μSTAR", miktoarm synthesis by termination after ring-opening metathesis polymerization, wherein asymmetry is introduced by first homopolymerizing a macromonomer followed by in situ enyne-mediated termination to install a single mikto-arm with exceptional efficiency. This modular μSTAR platform cleanly generates AB_n and $A(BA')_n$ miktoarm star polymers with unprecedented versatility in the selection of A and B chemistries as demonstrated using many common polymer building blocks. The average number of B or BA′ arms (n) is easily controlled by the equivalents of Grubbs catalyst. While these materials are characterized by dispersity in n that arises from the statistics of polymerization, they self-assemble into mesophases at elevated volume fractions of the A material that are identical to those predicted for precise miktoarm stars. In particular phases at significantly elevated volume fraction of the A material were obtained. The μSTAR technique provides a significant boost in design flexibility and synthetic simplicity while retaining the salient phase behavior of precise miktoarm star materials.

The usefulness of μSTAR for generating high performing materials was demonstrated by synthesizing sustainable and high molecular weight asymmetry miktoarm star polymers and examining their performance as TPEs. Stiff, tough, and elastic TPEs at greater than 50% volume fraction were tested. The versatility and efficiency of μSTAR at generating a library of stars facilitated the elucidation of structure-property relationships in this unique class of materials. Comparisons to literature examples of thermoplastic elastomers show that these sustainable stars offer advantages over other sustainable linear as well as petroleum derived TPEs.

TABLE OF CONTENTS

LIST OF FIGURES

LIST OF TABLES

Chapter 1. Polymers with Complex Architecture

1.1 Origins of Elastomeric Polymers

The study of branching in polymers is almost as old as the field itself. Not long after founding the fielding of synthetic polymer chemistry, Herman Staudinger polymerized styrene with divinylbenzene.[1] He observed a significant difference in material properties between the fully soluble linear poly(styrene) and the gel-like branched styrene–divinylbenzene copolymer. Staudinger recognized that this material was structurally similar to the types of rubbers Goodyear had discovered decades prior with his experimentation on vulcanized natural rubbers.[2]

Advancements in polymer synthesis progressed quickly, and by the 1950s polymer chemists produced the first block polymers.[3] The power of anionic synthesis was on full display as it allowed unprecedented control, leading to low dispersity polymers of increasing complexity. These block polymers captured the attention of polymer physicists because they self-assembled into a variety of phases depending on the volume fraction of each block (f_A, f_B, …), the degree of polymerization (N), and an enthalpic interaction parameter (χ).

The first commercially successful block copolymers produced with this technique emerged in the form of thermoplastic elastomers. These ABA triblock copolymers comprise a rubbery, low glass transition temperature (T_g) B block flanked by two hard, high-T_g A blocks. The first examples employed polystyrene as the hard A block and a polydiene (such as polyisoprene or polybutadiene) as the soft B block. These proved to be effective synthetic rubbers useful in a variety of applications from automotive to footwear and medical devices.[4,5]

At up to 30 percent polystyrene by volume, these block polymers self-assemble into spherical or cylindrical morphologies with discrete domains of polystyrene in a continuous matrix of the polydiene. While vulcanized rubbers employ permanent covalent crosslinks to solidify the otherwise viscous polydiene, the hard domains of the high T_g block act as physical crosslinks. In turn, the viscous behavior of the polydiene allows the material to reversibly deform under stresses that would otherwise lead to irreversible plastic deformation with pure polystyrene (**Figure 1.1**). These hard domains also serve as reinforcing filler, just as vulcanized rubbers include hard particles to enhance mechanical properties. For both thermoplastic elastomers and vulcanized rubbers, increasing the filler loading improves mechanical properties up to a maximum beyond which further loading weakens the material.[6] In the case of thermoplastic elastomers, greater than 30 percent volume fraction polystyrene will cause the individual domains of polystyrene to merge and produce a continuous domain. This hard, continuous matrix prohibits reversible elastomeric behavior.[4]

One of the biggest selling points of these materials is, unlike vulcanized rubbers, they are thermally and solution processable. Heating the material above the glass transition temperature of the hard block allows the material to be molded and, if heated further past the order–disorder transition temperature (T_{ODT}), the material will flow. This feature enhances process flexibility as the material develops its elastomeric character immediately upon cooling. Similarly, adding the appropriate solvent will fully dissolve the material, and upon subsequent drying it will regain its properties. This feature further broadens the scope of processing techniques. Vulcanized rubbers, on the other hand, require a slower and irreversible crosslinking step that necessitates curing the material in its final shape.

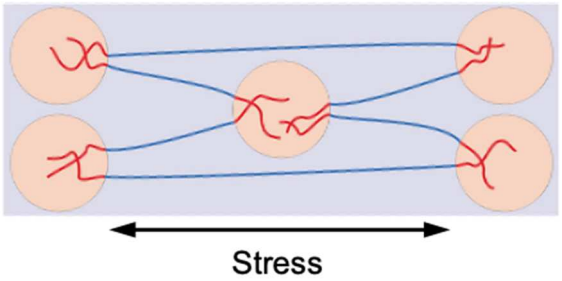

Figure 1.1. ABA triblock thermoplastic elastomer under stress. The soft B block depicted in blue absorbs the stress by reversibly deforming while the hard A blocks, depicted in red, hold the material together.

1.2 Branched Thermoplastic Elastomers

In the 1970s, the study of branched polymers and block polymers merged when the first star block polymers of polystyrene and polyisoprene were made.[7] Fetters showed that these star-shaped thermoplastic elastomers with up to 29 arms (*n*) were stronger in tension and less viscous in the melt than their linear counterparts.[8] The increased strength resulted from the increased domain connectivity due to multiple arms emanating from one branching point. This central branching point also serves as a crosslinking point, which strengthens the material.

To further strengthen the material would require finding a way to surpass the traditional 30 percent volume fraction limit of the hard phase. Finding a way to increase the volume fraction past this limit while still maintaining a cylindrical morphology would enhance the mechanical properties of thermoplastic elastomers. Specially, increasing the amount of reinforcing filler while maintaining this morphology would make the material stiffer, meaning a higher modulus, and also tougher, meaning it could absorb more energy without breaking while maintaining elasticity.[9] The best solution to deflecting phase boundaries to higher volume fraction thus far comes in the form of a type of star polymer with some additional complexities. Asymmetric miktoarm stars block polymers are able to impart this exact property while still maintaining the advantages that Fetters observed with his star polymers. Miktoarm

stars, coming from the Greek word *mikto* meaning mixed, comprise a star polymer wherein at least two different types of arms are connected to the one central core. The asymmetry refers to having just one unlike arm and a multitude of similar arms (**Figure 1.2**, right).

Prior self-consistent field theory (SCFT) simulations and experimental studies showed that asymmetric AB_n miktoarm stars deflect phase boundaries such that traditional morphologies could occur at a higher volume fraction of A (f_A) than they could in linear diblocks.[10–12] These architectures open up a new morphological landscape, enabling the self-assembly of much more complex structures.[13,14] These observations are a result of architectural asymmetry. The combination of steric congestion and incompatibility of A and B blocks at the star polymer core causes the domain interface to curve towards the single A arm, allowing the multitude of B arms to entropically relax on the convex side. This phenomenon results in an enhanced stability of morphologies with curved interfaces (i.e. spherical and cylindrical phases) at higher f_A (**Figure 1.2**).

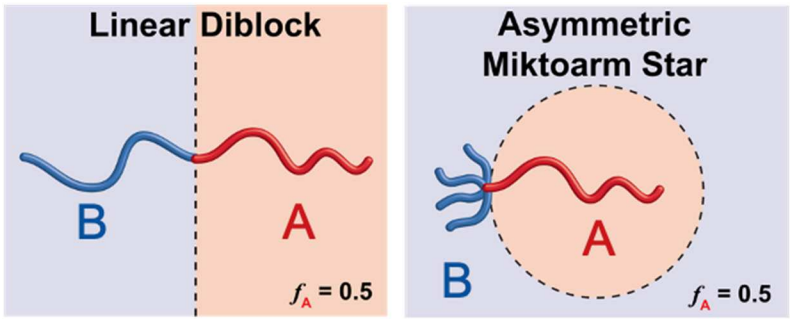

Figure 1.2. The asymmetric AB_n miktoarm star architecture (right) favors curved interfaces that deflect phase boundaries, stabilizing spheres and cylinders of the A block at larger f_A than is possible with linear AB diblocks (left).

While AB_n miktoarm star polymers have been experimentally shown to self-assemble into cylindrical domains at higher f_A than what is traditionally possible, the lack of triblock motif prohibits B block domain bridging.[11] As a result, these materials are not thermoplastic elastomers as the material will have no mechanical integrity. One solution is to add another A

block at the end of each B block (**Figure 1.3**).[15] This A block has the same chemical makeup, but can have a different molecular weight than the single homopolymer A arm and so it is denoted A′.

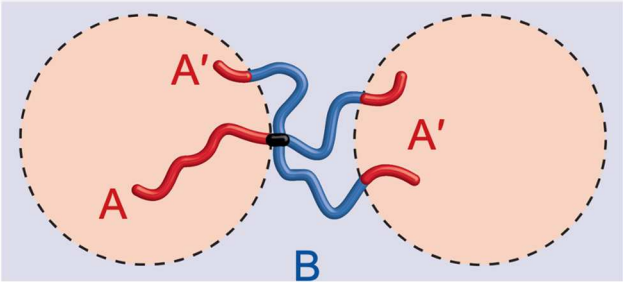

Figure 1.3. A(BA′)$_n$ miktoarm star architecture with each block labeled, showcasing the domain connectivity enabled by the A′ blocks.

The A(BA′)$_n$ miktoarm star architecture not only provides the domain bridging that is essential to mechanical performance, but also further enhances phase boundary deflection as a result of the block bidispersity effect.[16] The block bidispersity is defined as $\tau \equiv \frac{N_A}{N_A+N_{A'}}$ where N_A is the degree of polymerization of the A block and $N_{A'}$ is the degree of polymerization of the A′ block. SCFT simulations by Lynd and coworkers found $\tau = 0.9$ achieved the highest degree of phase boundary deflection.[17] Simulated phase diagrams of an A(BA′)$_3$ miktoarm star show the impressive phase boundary deflection this architecture is capable of compared to a linear AB diblock (**Figure 1.4**). Lequieu and coworkers explored the phase behavior in greater depth and found that an optimal value of $\tau = 0.925$ could produce discrete cylindrical domains of the A block at almost 80 percent f_A.[18] While the ability of SCFT to predict block polymer phase behavior is undeniable, it cannot predict dynamic material properties such as mechanical behavior; empirical measurements must be used to determine how the large number of parameters that define A(BA′)$_n$ stars (f_A, τ, N, n) affect these properties.

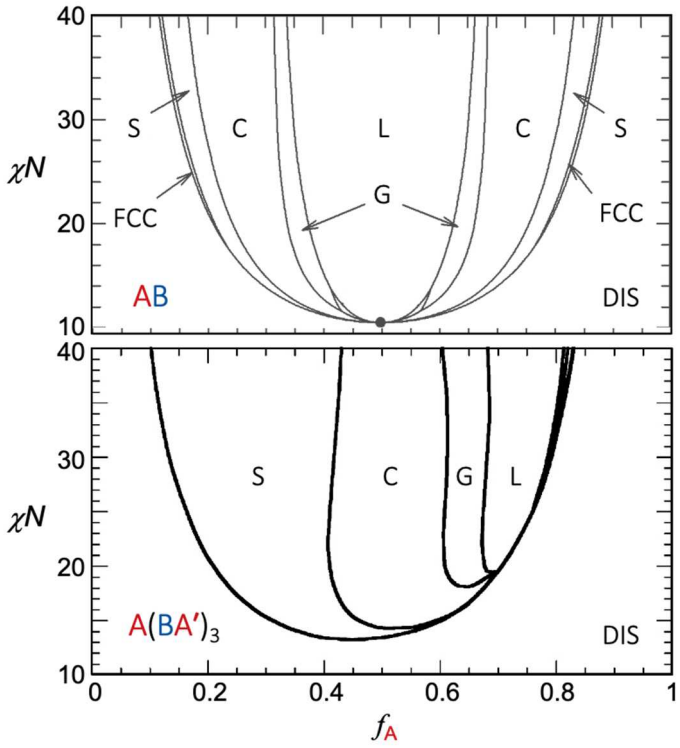

Figure 1.4. SCFT-generated phase diagrams for AB linear diblock (top) and A(BA′)$_3$ miktoarm star polymer at $\tau = 0.9$ (bottom) in χN vs. f_A phase space. S, C, G, and L correspond to spherical, cylindrical, gyroid, and lamellar phases, respectively. Adapted with permission from *Macromolecules*. Copyright 2010 American Chemical Society.[17,19]

1.3 Synthesis of Branched Thermoplastic Elastomers

Despite decades of progress in the field of synthetic polymer chemistry, anionic synthesis is still the gold standard for the synthesis of complex architectures. Unfortunately, anionic synthesis also has many drawbacks, especially in the case of miktoarm star polymers. Rigorous purification requirements, limited monomer scope, and sequence constraints are inherent to any anionic polymerization. In the case of stars, the coupling chemistry required to join star polymer arms together at molecular weights relevant to mechanical performance often suffers from extremely slow kinetics, which can take months.[20] Incomplete conversion of the polymer coupling is guaranteed, and thus time-consuming fractionation is required to purify the stars.[21–23] In addition, the extensive use of break seals and constricted heat seals over the

course of these reactions necessitate custom complex glassware to be hand blown for each reaction (**Figure 1.5**).[24] Running these reactions requires the chemist be not only proficient and patient, but also a highly skilled scientific glass blower, an exceedingly rare combination.

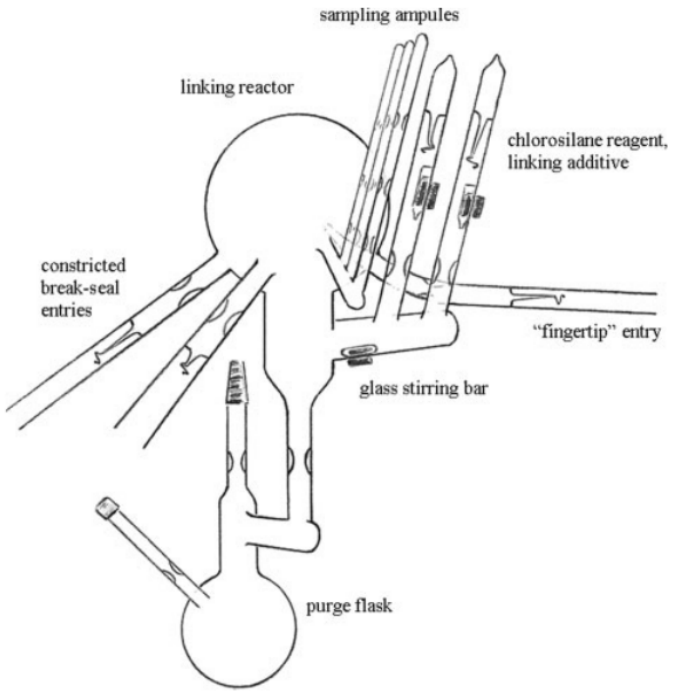

Figure 1.5. Complex glassware used in the anionic synthesis of A(BA′)$_n$ miktoarm star polymers. Reprinted with permission from *Journal of Polymer Science Part A: Polymer Chemistry*. Copyright 2005 John Wiley and Sons.[25]

Despite the many unique properties of miktoarm star block polymers, synthetic challenges are a major roadblock to their widespread adoption. While there are other synthetic routes available, none have the precision or throughput required to make high molecular weight A(BA′)$_n$ stars efficiently. The standard approach to generating precise connectivity at a common junction uses "core-first" and "grafting-to" reaction schemes or some combination thereof (**Figure 1.6**).[26] Common to all these methods are tedious synthetic routes that often include multiple coupling, polymerization, (de)protection, and purification steps such as fractional precipitation and high performance liquid chromatography.[22,27,28] Moreover,

changing the number of arms is non-trivial since a new core starting material must be selected each time. These drawbacks make the traditional approaches too cumbersome for exploring the vast multiparameter space of miktoarm stars. A synthetic route towards miktoarm stars that yields well-defined materials with sufficient versatility to vary architectural parameters would enable the exploration of miktoarm phase space. More advanced synthetic techniques are necessary to investigate this complex system.

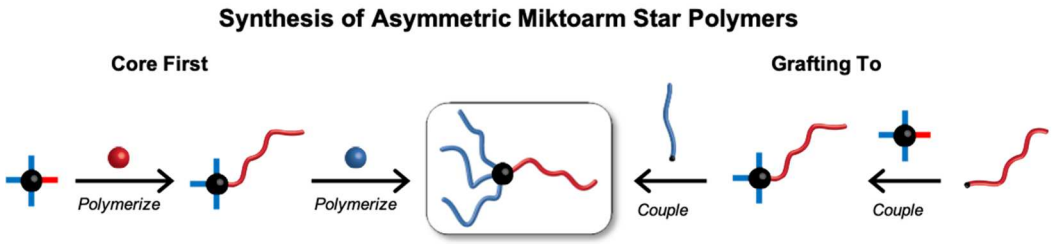

Figure 1.6. Overview of synthetic methods to create asymmetric miktoarm star polymers: "core-first" and "grafting-to", which generate precise arm connectivity.

1.4 An Architectural Spectrum

Despite the difficulties associated with synthesizing certain architectures, the breadth of architectures that are now synthetically accessible is only limited by our ability to imagine them. Stars, rings, dendritic structures, H polymers, linear multiblocks, grafted polymers and combinations thereof have all been synthesized.[29] While each architecture is defined by unique features, there is an architectural spectrum that relates many of them.[29]

Recently, the architectural motif of bottlebrush polymers has captured the attention of polymer chemists and material scientists for their novel material properties. Comprising a polymeric backbone with densely grafted polymeric side chains, bottlebrush polymers differ from comb and other grafted polymers in that the grafting density, the number of side chains per backbone repeat unit, is sufficiently high to cause a large degree of steric crowding around the backbone.[30] As a result of this crowding, the sidechains and backbone adopt an extended

conformation, leading to a low degree of entanglement,[31,32] a stretched conformation,[33,34] and large domain spacing in block bottlebrush polymers.[35–37] Bottlebrushes have interesting physical and mechanical properties that make them attractive materials for a diversity of applications: photonics,[38,39] drug delivery,[40,41] battery membranes,[42] lithography,[43,44] 3D printing,[45] touch sensing,[46] and dielectric elastomers.[47] Part of the widespread interest can be attributed to the ease of synthesis: advancements in ring-opening metathesis polymerization (ROMP) have enabled the facile preparation of bottlebrushes, even at ultra-high molecular weights.[48,49]

There have been several studies that investigate the effect of various parameters on bottlebrush behavior. Recently, Grubbs and coworkers investigated the effect of grafting density (z) on bottlebrush block copolymer self-assembly by randomly copolymerizing a small molecule and macromonomer.[30] In particular they examined the effect of grafting density on the scaling of the lamellar domain spacing (d^*) with the backbone degree of polymerization (N_{BB}). They found that the grafting density affects the scaling exponent γ where $d^* \sim N_{BB}^{\gamma}$. In particular when $z = 0.2$ there was a critical transition in the scaling of γ with z, corresponding to the onset of bottlebrush behavior (**Figure 1.7**). For values of z greater than 0.2, there is a relatively weak dependence of γ on z. For values of z less than 0.2 there is a much stronger dependence of γ on z. Reducing the grafting density past this critical point results in self-assembly behavior that rapidly resembles a linear diblock polymer. In fact, at $z = 0$ the value of $\gamma = 0.69$ is close to the theoretical value of 2/3 for a strongly segregated diblock polymer.[50] This study elegantly shows how grafting density defines the relationship between linear and bottlebrush polymers.

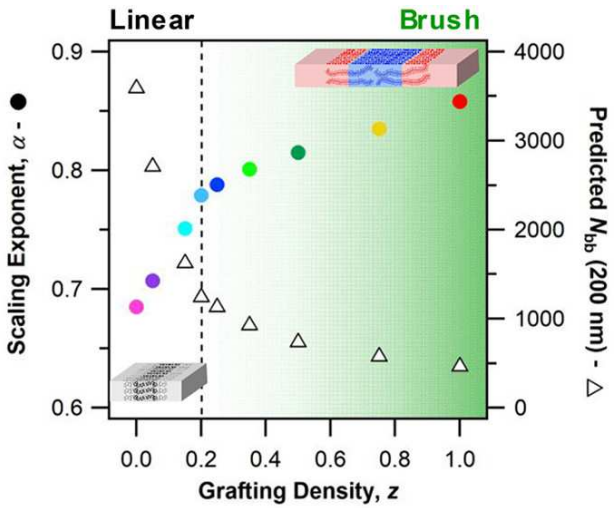

Figure 1.7. Plot of scaling exponent (circles) and predicted backbone degree of polymerization (N_{bb}) for d^* = 200 nm (triangles) as a function of grafting density. The bottlebrush and linear regimes are delineated at 20 percent grafting density. Reprinted with permission from *ACS Nano*. Copyright 2017 American Chemical Society.[30]

The vast majority of work on bottlebrush polymers has focused on systems with relatively short side chain degree of polymerization (N_{SC}) and large N_{BB}. In their study of grafting density, Grubbs and coworkers studied symmetric diblock bottlebrushes with N_{BB} = 44–533 and N_{SC} = 32–42. More recently, Hillmyer and Matsen studied the lamellar self-assembly of nine block bottlebrush polymers with N_{BB} = 10–281 and N_{SC} = 34–45.[51] They observed that domain spacing scaled with $\gamma \approx 0.3$ for $N_{BB} < 20$, and increased to $\gamma \approx 0.9$ for larger backbone degrees of polymerization. Notably, they used SCFT to demonstrate that block bottlebrush polymers pack into an end-to-end bilayer arrangement rather than an interdigitated arrangement and had much more flexible backbones than previously thought.

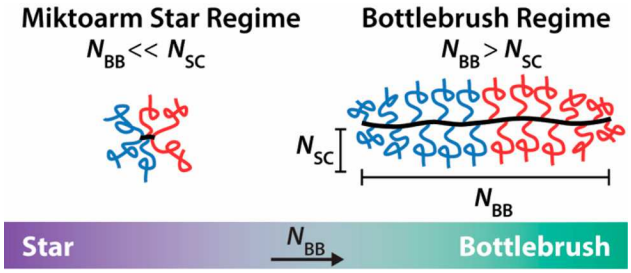

Figure 1.8. Illustration of the proposed star-to-bottlebrush transition for bottlebrushes with small backbone degrees of polymerization (N_{BB}). Adapted with permission from *Macromolecules*. Copyright 2019 American Chemical Society.[52]

Though these studies of scaling behavior have been highly instructive for the understanding the properties of large bottlebrush polymers, the behavior of short bottlebrush polymers with $N_{BB} \ll N_{SC}$, have received considerably less attention. The regime corresponding to $N_{BB} \ll N_{SC}$ is particularly interesting because these bottlebrushes exhibit behavior typically restricted to star polymers (**Figure 1.8**). Previous work on bottlebrush homopolymers indicates bottlebrushes can undergo a bottlebrush-to-star transition at low N_{BB}, whereby the cylinder-like configuration characteristic of long bottlebrushes transitions to configurations that are increasingly sphere-like.[32,53–59] This transition is especially apparent in both the zero-sheer viscosity of bottlebrush homopolymers[32] and in solution scattering experiments.[55,56] These prior findings are intriguing because unlike miktoarm star polymers, bottlebrushes are much easier to synthesize in a high throughput manner. However, no prior studies have definitively determined when the onset of the star-to-bottlebrush transition occurs and what factors govern this onset. Determining this crossover would open an entirely new approach to the synthesis of miktoarm star polymers. This could enable the application of these stars in a variety of applications outside of thermoplastic elastomers. The subject of this dissertation is the synthesis, self-assembly, and material properties of graft block polymers with low N_{BB} and high N_{SC}.

1.5 Outline of Dissertation

In **Chapter 2** we demonstrate that Grubbs-type grafting through copolymerization of two distinct macromonomers in the limit of $N_{BB} \ll N_{SC}$, produces well-defined materials with

excellent control over ensemble-averaged properties, including molar mass, dispersity, composition, and number of branch points. The dependence of self-assembly on these molecular design parameters was systematically probed using small angle X-ray scattering and self-consistent field theory simulations. Our analysis supports the notion that two-component bottlebrush copolymers with small N_{BB} behave like miktoarm star polymers. The star-to-bottlebrush transition is quantifiable for both statistical and diblock sequences by unique signatures in the experimental scaling of domain spacing and simulated distribution of backbone/side-chain density within lamellar unit cells. These findings represent a conceptual framework that simplifies the synthesis of miktoarm star polymers when dispersity in the number of arms and composition can be tolerated.

Chapter 3 builds on the findings of Chapter 2 to produce asymmetric miktoarm star polymers that can deflect phase boundaries. We introduce a new synthetic approach coined "μSTAR" — Miktoarm Synthesis by Termination After Ring-opening metathesis polymerization — that circumvents traditional synthetic limitations by constructing the block–block junction in a scalable, one-pot process involving (1) grafting-through polymerization of a macromonomer followed by (2) *in-situ* enyne-mediated termination to install a single mikto-arm with exceptional efficiency. This modular μSTAR platform cleanly generates AB_n and $A(BA')_n$ miktoarm star polymers with unprecedented versatility in the selection of A and B chemistries as demonstrated using many common polymer building blocks. The average number of B or BA′ arms (n) is easily controlled by the equivalents of Grubbs catalyst. While these materials are characterized by dispersity in n that arises from the statistics of polymerization, they self-assemble into mesophases that are identical to those predicted for precise miktoarm stars. The μSTAR technique provides a significant boost in design flexibility

and synthetic simplicity while retaining the salient phase behavior of precise miktoarm star materials.

In **Chapter 4** we use μSTAR to synthesize high molecular weight $A(BA')_n$ stars and demonstrate their usefulness as thermoplastic elastomers. By exploiting the modularity and ease of varying *n* inherent to μSTAR, the many parameters that define $A(BA')_n$ stars are explored and their effects on the mechanical properties are elucidated.

1.6 References

(1) Staudinger, H.; Heuer, W. Über Hochpolymere Verbindungen, 94. Mitteil.: Über Ein Unlösliches Poly□styrol. *Ber. Dtsch. Chem. Ges. B* **1934**, *67*, 1164–1172.

(2) Goodyear, C. Improvement in India-Rubber Fabrics. U.S. Patent 3,633, 1844.

(3) Szwarc, M.; Levy, M.; Milkovich, R. POLYMERIZATION INITIATED BY ELECTRON TRANSFER TO MONOMER. A NEW METHOD OF FORMATION OF BLOCK POLYMERS. *J. Am. Chem. Soc.* **1956**, *78*, 2656.

(4) Holden, G. Thermoplastic Elastomers. In *Rubber Technology*; Morton, M., Ed.; Springer US, 1987; pp 465–481.

(5) Geoffrey, H.; Milkovich, R. Block Polymers of Monovinyl Aromatic Hydrocarbons and Conjugated Dienes. Belgian Patent 627,652, 1963.

(6) Morton, M. *Rubber Technology*, 3rd Ed.; Springer US, 1999.

(7) Price, C.; Watson, A. G.; Chow, M. T. An Investigation of the Effect of Chain Geometry on the Two-Phase Morphology of Polystyrene/Polyisoprene Block Copolymers. *Polymer (Guildf).* **1972**, *13* (7), 333–336.

(8) Bi, L. K.; Fetters, L. J. Synthesis and Properties of Block Copolymers. 3. Polystyrene-

Polydiene Star Block Copolymers. *Macromolecules* **1976**, *9* (5), 732–742.

(9) Holden, C.; Bishop, E. T.; Legge, N. R. Thermoplastic Elastomers. **1969**, *57* (26), 37–57.

(10) Grason, G. M.; Kamien, R. D. Interfaces in Diblocks: A Study of Miktoarm Star Copolymers. *Macromolecules* **2004**, *37* (19), 7371–7380.

(11) Yang, L.; Hong, S.; Gido, S. P.; Velis, G.; Hadjichristidis, N. I5S Miktoarm Star Block Copolymers: Packing Constraints on Morphology and Discontinuous Chevron Tilt Grain Boundaries. *Macromolecules* **2001**, *34* (26), 9069–9073.

(12) Beyer, F. L.; Gido, S. P.; Velis, G.; Hadjichristidis, N.; Tan, N. B. Morphological Behavior of A5B Miktoarm Star Block Copolymers. *Macromolecules* **1999**, *32* (20), 6604–6607.

(13) Xie, N.; Li, W.; Qiu, F.; Shi, A. C. σ Phase Formed in Conformationally Asymmetric AB-Type Block Copolymers. *ACS Macro Lett.* **2014**, *3* (9), 909–910.

(14) Bates, M. W.; Barbon, S. M.; Levi, A. E.; Lewis, R. M.; Beech, H. K.; Vonk, K. M.; Zhang, C.; Fredrickson, G. H.; Hawker, C. J.; Bates, C. M. Synthesis and Self-Assembly of ABn Miktoarm Star Polymers. *ACS Macro Lett.* **2020**, *9* (3), 396–403.

(15) Shi, W.; Lynd, N. A.; Montarnal, D.; Luo, Y.; Fredrickson, G. H.; Kramer, E. J.; Ntaras, C.; Avgeropoulos, A.; Hexemer, A. Toward Strong Thermoplastic Elastomers with Asymmetric Miktoarm Block Copolymer Architectures. *Macromolecules* **2014**, *47* (6), 2037–2043.

(16) Matsen, M. W. Equilibrium Behavior of Asymmetric ABA Triblock Copolymer Melts. *J. Chem. Phys.* **2000**, *113* (13), 5539–5544.

(17) Lynd, N. A.; Oyerokun, F. T.; O'Donoghue, D. L.; Handlin, D. L.; Fredrickson, G. H.

Design of Soft and Strong Thermoplastic Elastomers Based on Nonlinear Block Copolymer Architectures Using Self-Consistent-Field Theory. *Macromolecules* **2010**, *43* (7), 3479–3486.

(18) Lequieu, J.; Koeper, T.; Delaney, K. T.; Fredrickson, G. H. Extreme Deflection of Phase Boundaries and Chain Bridging in A(BA′)n Miktoarm Star Polymers. *Macromolecules* **2020**, *53* (2), 513–522.

(19) Milner, S. T. Chain Architecture and Asymmetry in Copolymer Microphases. *Macromolecules* **1994**, *27* (8), 2333–2335.

(20) Zhu, Y.; Gido, S. P.; Moshakou, M.; Iatrou, H.; Hadjichristidis, N.; Park, S.; Chang, T. Effect of Junction Point Functionality on the Lamellar Spacing of Symmetric (PS)n(PI)n Miktoarm Star Block Copolymers. *Macromolecules* **2003**, *36* (15), 5719–5724.

(21) Tselikas, Y.; Iatrou, H.; Hadjichristidis, N.; Liang, K. S.; Mohanty, K.; Lohse, D. J. Morphology of Miktoarm Star Block Copolymers of Styrene and Isoprene. *J. Chem. Phys.* **1996**, *105* (6), 2456–2462.

(22) Avgeropoulos, A.; Hadjichristidis, N.; Copolymer, S. B. Synthesis of Model Nonlinear Block Copolymers of A(BA)2, A(BA)3, and (AB)3A(BA)3 Type. *J. Polym. Sci. Part A Polym. Chem.* **1997**, *35*, 813–816.

(23) Velis, G.; Hadjichristidis, N. Synthesis of Model PS(PI)5 and (PI)5PS(PI)5 Nonlinear Block Copolymers of Styrene (S) and Isoprene (I). *Macromolecules* **1999**, *32* (2), 534–536.

(24) Hadjichristidis, N.; Hirao, A. *Anionic Polymerization: Principles, Practice, Strength, Consequences and Applications*; 2015.

(25) Uhrig, D.; Mays, J. W. Experimental Techniques in High-Vacuum Anionic

Polymerization. *J. Polym. Sci. Part A Polym. Chem.* **2005**, *43* (24), 6179–6222.

(26) Ren, J. M.; McKenzie, T. G.; Fu, Q.; Wong, E. H. H.; Xu, J.; An, Z.; Shanmugam, S.; Davis, T. P.; Boyer, C.; Qiao, G. G. Star Polymers. *Chem. Rev.* **2016**, *116* (12), 6743–6836.

(27) Liu, H.; Pan, W.; Tong, M.; Zhao, Y. Synthesis and Properties of Couplable ABCDE Star Copolymers by Orthogonal CuAAC and Diels-Alder Click Reactions. *Polym. Chem.* **2016**, *7* (8), 1603–1611.

(28) Lee, D.; Jung, H. Y.; Park, M. J. Solid-State Polymer Electrolytes Based on AB3-Type Miktoarm Star Copolymers. *ACS Macro Lett.* **2018**, *7*, 1046–1050.

(29) Polymeropoulos, G.; Zapsas, G.; Ntetsikas, K.; Bilalis, P.; Gnanou, Y.; Hadjichristidis, N. 50th Anniversary Perspective: Polymers with Complex Architectures. *Macromolecules* **2017**, *50* (4), 1253–1290.

(30) Lin, T.-P.; Chang, A. B.; Luo, S.-X.; Chen, H.-Y.; Lee, B.; Grubbs, R. H. Effects of Grafting Density on Block Polymer Self-Assembly: From Linear to Bottlebrush. *ACS Nano* **2017**, *11* (11), 11632–11641.

(31) Namba, S.; Tsukahara, Y.; Kaeriyama, K.; Okamoto, K.; Takahashi, M. Bulk Properties of Multibranched Polystyrenes from Polystyrene Macromonomers: Rheological Behavior I. *Polymer (Guildf).* **2000**, *41*, 5165–5171.

(32) Dalsin, S. J.; Hillmyer, M. A.; Bates, F. S. Molecular Weight Dependence of Zero-Shear Viscosity in Atactic Polypropylene Bottlebrush Polymers. *ACS Macro Lett.* **2014**, *3* (5), 423–427.

(33) Wintermantel, M.; Schmidt, M.; Tsukahara, Y.; Kajiwara, K.; Kohjiya, S. Rodlike Combs. *Macromol. Rapid Commun.* **1994**, *15* (3), 279–284.

(34) Wintermantel, M.; Gerle, M.; Fischer, K.; Schmidt, M.; Wataoka, I.; Urakawa, H.; Kajiwara, K.; Tsukahara, Y. Molecular Bottlebrushes. *Macromolecules* **1996**, *29* (3), 978–983.

(35) Runge, M. B.; Bowden, N. B. Synthesis of High Molecular Weight Comb Block Copolymers and Their Assembly into Ordered Morphologies in the Solid State. *J. Am. Chem. Soc.* **2007**, *129* (34), 10551–10560.

(36) Brett Runge, M.; Lipscomb, C. E.; Ditzler, L. R.; Mahanthappa, M. K.; Tivanski, A. V.; Bowden, N. B. Investigation of the Assembly of Comb Block Copolymers in the Solid State. *Macromolecules* **2008**, *41* (20), 7687–7694.

(37) Rzayev, J. Synthesis of Polystyrene−Polylactide Bottlebrush Block Copolymers and Their Melt Self-Assembly into Large Domain Nanostructures. *Macromolecules* **2009**, *42* (6), 2135–2141.

(38) Sveinbjornsson, B. R.; Weitekamp, R. A.; Miyake, G. M.; Xia, Y.; Atwater, H. A.; Grubbs, R. H. Rapid Self-Assembly of Brush Block Copolymers to Photonic Crystals. *Proc. Natl. Acad. Sci.* **2012**, *109* (36), 14332–14336.

(39) Vatankhah-Varnosfaderani, M.; Keith, A. N.; Cong, Y.; Liang, H.; Rosenthal, M.; Sztucki, M.; Clair, C.; Magonov, S.; Ivanov, D. A.; Dobrynin, A. V.; Sheiko, S. S. Chameleon-like Elastomers with Molecularly Encoded Strain-Adaptive Stiffening and Coloration. *Science* **2018**, *359* (6383), 1509–1513.

(40) Johnson, J. A.; Lu, Y. Y.; Burts, A. O.; Xia, Y.; Durrell, A. C.; Tirrell, D. A.; Grubbs, R. H. Drug-Loaded, Bivalent-Bottle-Brush Polymers by Graft-through ROMP. *Macromolecules* **2010**, *43* (24), 10326–10335.

(41) Lu, X.; Tran, T. H.; Jia, F.; Tan, X.; Davis, S.; Krishnan, S.; Amiji, M. M.; Zhang, K.

Providing Oligonucleotides with Steric Selectivity by Brush-Polymer-Assisted Compaction. *J. Am. Chem. Soc.* **2015**, *137* (39), 12466–12469.

(42) Bates, C. M.; Chang, A. B.; Momčilović, N.; Jones, S. C.; Grubbs, R. H. ABA Triblock Brush Polymers: Synthesis, Self-Assembly, Conductivity, and Rheological Properties. *Macromolecules* **2015**, *48* (14), 4967–4973.

(43) Sun, G.; Cho, S.; Clark, C.; Verkhoturov, S. V.; Eller, M. J.; Li, A.; Pavía-Jiménez, A.; Schweikert, E. A.; Thackeray, J. W.; Trefonas, P.; Wooley, K. L. Nanoscopic Cylindrical Dual Concentric and Lengthwise Block Brush Terpolymers as Covalent Preassembled High-Resolution and High-Sensitivity Negative-Tone Photoresist Materials. *J. Am. Chem. Soc.* **2013**, *135* (11), 4203–4206.

(44) Cheng, L.; Gadelrab, K. R.; Kawamoto, K.; Yager, K. G.; Johnson, J. A.; Alexander-Katz, A.; Ross, C. A. Templated Self-Assembly of a PS-Branch-PDMS Bottlebrush Copolymer. *Nano Lett.* **2018**, *18* (7), 4360–4369.

(45) Xie, R.; Mukherjee, S.; Levi, A. E.; Reynolds, V. G.; Wang, H.; Chabinyc, M. L.; Bates, C. M. Room Temperature 3D Printing of Super-Soft and Solvent-Free Elastomers. *Sci. Adv.* **2020**, *6* (46), 1–11.

(46) Reynolds, V. G.; Mukherjee, S.; Xie, R.; Levi, A. E.; Atassi, A.; Uchiyama, T.; Wang, H.; Chabinyc, M. L.; Bates, C. M. Super-Soft Solvent-Free Bottlebrush Elastomers for Touch Sensing. *Mater. Horizons* **2020**, *7* (1), 181–187.

(47) Vatankhah-Varnoosfaderani, M.; Daniel, W. F. M.; Zhushma, A. P.; Li, Q.; Morgan, B. J.; Matyjaszewski, K.; Armstrong, D. P.; Spontak, R. J.; Dobrynin, A. V.; Sheiko, S. S. Bottlebrush Elastomers: A New Platform for Freestanding Electroactuation. *Adv. Mater.* **2017**, *29*, 1604209.

(48) Xia, Y.; Olsen, B. D.; Kornfield, J. A.; Grubbs, R. H. Efficient Synthesis of Narrowly Dispersed Brush Copolymers and Study of Their Assemblies: The Importance of Side Chain Arrangement. *J. Am. Chem. Soc.* **2009**, *131* (51), 18525–18532.

(49) Verduzco, R.; Li, X.; Pesek, S. L.; Stein, G. E. Structure, Function, Self-Assembly, and Applications of Bottlebrush Copolymers. *Chem. Soc. Rev.* **2015**, *44* (8), 2405–2420.

(50) Matsen, M. W.; Bates, F. S. Unifying Weak- and Strong-Segregation Block Copolymer Theories. *Macromolecules* **1996**, *29* (4), 1091–1098.

(51) Dalsin, S. J.; Rions-Maehren, T. G.; Beam, M. D.; Bates, F. S.; Hillmyer, M. A.; Matsen, M. W. Bottlebrush Block Polymers: Quantitative Theory and Experiments. *ACS Nano* **2015**, *9* (12), 12233–12245.

(52) Levi, A. E.; Lequieu, J.; Horne, J. D.; Bates, M. W.; Ren, J. M.; Delaney, K. T.; Fredrickson, G. H.; Bates, C. M. Miktoarm Stars via Grafting-Through Copolymerization: Self-Assembly and the Star-to-Bottlebrush Transition. *Macromolecules* **2019**, *52* (4), 1794–1802.

(53) Tsukahara, Y.; Namba, S.; Iwasa, J.; Nakano, Y.; Kaeriyama, K.; Takahashi, M. Bulk Properties of Poly (Macromonomer) s of Increased Backbone and Branch Lengths. **2001**, 2624–2629.

(54) Dalsin, S. J.; Hillmyer, M. A.; Bates, F. S. Linear Rheology of Polyolefin-Based Bottlebrush Polymers. *Macromolecules* **2015**, *48* (13), 4680–4691.

(55) Pesek, S. L.; Li, X.; Hammouda, B.; Hong, K.; Verduzco, R. Small-Angle Neutron Scattering Analysis of Bottlebrush Polymers Prepared via Grafting-through Polymerization. *Macromolecules* **2013**, *46* (17), 6998–7005.

(56) Wataoka, I.; Urakawa, H.; Kajiwara, K.; Schmidt, M.; Wintermantel, M. Structural

Characterization of Polymacromonomer in Solution by Small-Angle X-Ray Scattering. **1997**, *44*.

(57) Ahn, S.; Carrillo, J.-M. Y.; Han, Y.; Kim, T.-H.; Uhrig, D.; Pickel, D. L.; Hong, K.; Kilbey, S. M.; Sumpter, B. G.; Smith, G. S.; Do, C. Structural Evolution of Polylactide Molecular Bottlebrushes: Kinetics Study by Size Exclusion Chromatography, Small Angle Neutron Scattering, and Simulations. *ACS Macro Lett.* **2014**, *3* (9), 862–866.

(58) Paturej, J.; Sheiko, S. S.; Panyukov, S.; Rubinstein, M. Molecular Structure of Bottlebrush Polymers in Melts. *Sci. Adv.* **2016**, *2* (11).

(59) Denesyuk, N. A. Bottle-Brush Polymers as an Intermediate between Star and Cylindrical Polymers. *Phys. Rev. E - Stat. Physics, Plasmas, Fluids, Relat. Interdiscip. Top.* **2003**, *68* (3), 11.

Chapter 2. Miktoarm Stars via Grafting-Through Copolymerization: Self-Assembly and the Star-to-Bottlebrush Transition[1]

2.1 Background

Block polymers are important in fundamental[1–3] and applied[4–6] research due to their synthetic tractability, facile processing, and unique self-assembly. A wealth of experimental and theoretical methods are now available to create materials with prescribed control over desired properties spanning molecular to macroscopic length scales. One design parameter with powerful potential is the careful placement of branching. For example, bottlebrush polymers (**Figure 2.1a**) are characterized by a long polymeric backbone with additional polymeric side-chains protruding off of many or all repeat units.[7] The steric congestion encoded by this connectivity tends to elongate backbone conformations, providing value for applications including photonics,[8,9] electrochemical devices,[10] dielectric elastomers,[11] lithography,[12,13] giant surfactants,[14] and drug delivery.[15,16] Miktoarm star polymers (**Figure 2.1b**) are another type of branched macromolecule characterized by chemically-distinct chains connected at a common junction.[17] Asymmetry in arm type (e.g., A_mB_n, $m \neq n$) significantly perturbs the traditional two-component block copolymer phase diagram, with consequences for contemporary topics like complex phase behavior[18] and thermoplastic elastomers.[19] The opportunities afforded by branched block polymers are only beginning to emerge.

---

[1]This chapter was originally published in *Macromolecules*. Reproduced with permission from *Macromolecules* 2019, 52, 1794-1802. Copyright 2019, American Chemical Society.

Despite the many advantageous properties of branched block polymers, traditional synthetic strategies can be laborious. Discrete miktoarm stars typically require a complicated series of convergent or divergent chemical manipulations to build.[20] While possible using various (de)protection and controlled polymerization methodologies, any extensive exploration of the vast design space that underpins exquisite material performance is often infeasible. In contrast, bottlebrushes with 100% grafting density (one side-chain per backbone repeat unit) are actually relatively easy to access via grafting-through polymerization of end-reactive monotelechelic macromonomer precursors.

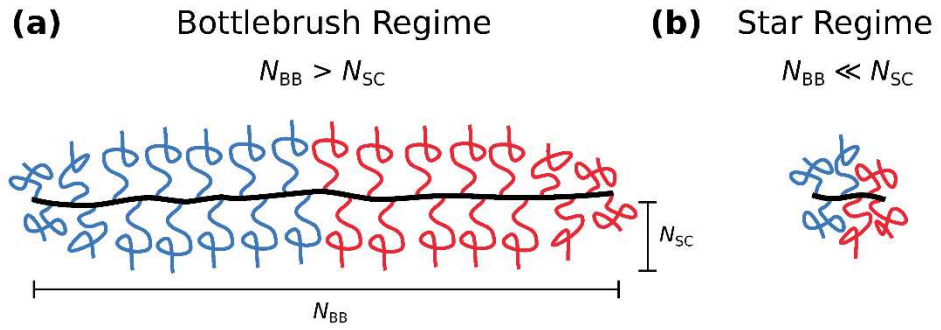

Figure 2.1. A densely grafted copolymer in two limits of backbone and side-chain length. **(a)** Bottlebrush ($N_{BB} >> N_{SC}$), and **(b)** miktoarm star ($N_{BB} << N_{SC}$).

Motivated by the challenge to construct well-defined miktoarm star polymers in a simple and versatile fashion, here we exploit the benefits of grafting-through copolymerization and demonstrate that it generates hetero-arm stars in the limit of short total backbone degrees of polymerization (N_{BB}) with sufficiently long side-chain degrees of polymerization (N_{SC}). Small angle X-ray scattering and self-consistent field theoretic (SCFT) simulations reveal three distinguishable regimes of self-assembly that we relate to chain conformations straddling: (I) compositional dispersity-dominated behavior at low N_{BB}, (II) a star-to-bottlebrush transition regime, and (III) bottlebrush. The specific details of this star-to-bottlebrush crossover are a function of N_{BB}, N_{SC}, and macromonomer sequence (diblock vs. statistical). As described

below, these insights into the self-assembly of miktoarm star polymers containing molar mass and compositional dispersity (arising from macromonomer copolymerization) strengthen our fundamental understanding of this exciting material platform.

2.2 Synthesis of Macromonomers and Bottlebrush Copolymers

Norbornene-terminated macromonomers (MM) of poly(lactide) (PLA) and poly(4-methyl-ε-caprolactone) (P4MCL) were prepared via ring-opening transesterification polymerization as described in the experimental section (**Schemes 2.1–2.2**). Two molar masses were synthesized for each: PLA-MM-3.3 = 3.3 kg mol^{-1}, PLA-MM-12 = 12 kg mol^{-1}, P4MCL-MM-3.7 = 3.7 kg mol^{-1}, and P4MCL-MM-11 = 11 kg mol^{-1}, all of which exhibit unimodal molar mass distributions (**Figure 2.2**) and low dispersities ($Đ \leq 1.11$, **Table 2.1**) characterized by size-exclusion chromatography (SEC) multi-angle light scattering (MALS).

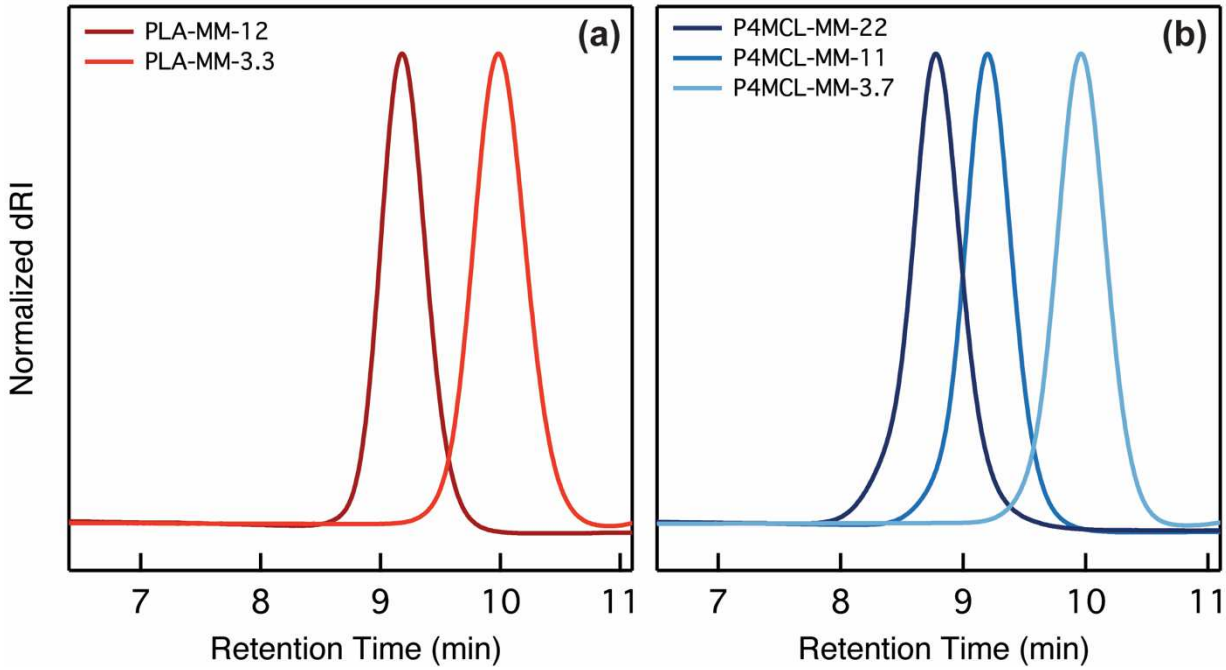

Figure 2.2. Normalized differential refractive index (dRI) signal SECs of **(a)** PLA and **(b)** P4MCL macromonomers.

Table 2.1. Characterization of PLA and P4MCL macromonomers.

Macromonomer	$M_{n,NMR}$[a]	$M_{n,SEC\text{-}MALS}$[a,b]	$M_{n,SEC\text{-}dRI}$[a,c]	$Đ$[c]	N_{SC}[d]	$N_{SC,vol}$[e]
PLA-MM-3.3	3.3	3.3	4.4	1.11	43	35
PLA-MM-12	13	12	19	1.06	160	130
P4MCL-MM-3.7	3.6	3.7	4.7	1.09	27	48
P4MCL-MM-11	11	11	19	1.09	86	150
P4MCL-MM-22	22	22	33	1.11	170	300

[a]In units of kg mol^{-1}. [b]Absolute values measured using size-exclusion chromatography with light scattering and differential refractive index detectors. [c]Relative to polystyrene standards. [d]Chemical degree of polymerization calculated from $M_{n,SEC\text{-}MALS}$ using a repeat molar mass of 72 g mol^{-1} (PLA) and 128 g mol^{-1} (P4MCL). [e]Volumetric degree of polymerization calculated from $M_{n,SEC\text{-}MALS}$ using a reference volume of 118 □^{3} and density of 1.03 g cm^{-3} for P4MCL and 1.25 g cm^{-3} for PLA.

These macromonomers were then subjected to ring-opening metathesis copolymerization (ROMP) using a Grubbs third generation bis-pyridine derivative[21] (G3) in two ways: (1) with sequential addition ("block", **Scheme 2.3**), and (2) from a preformed mixture that results in statistical incorporation ("statistical", **Scheme 2.4**). Statistical and diblock copolymers prepared from PLA-MM-12 and P4MCL-MM-11 are hereafter denoted as the S12 and B12 series, respectively (**Figure 2.4**). Likewise, PLA-MM-3.3 and P4MCL-MM-3.7 were copolymerized to generate two series called S3 and B3. We will collectively refer to these materials as "bottlebrush polymers," although as substantiated later, shorter variants are more appropriately termed miktoarm stars. **Figure 2.5** reports selected size-exclusion chromatograms for B12 (**Figure 2.5a**) and S12 (**Figure 2.5b**) copolymers at only the lowest backbone degrees of polymerization (as measured with multi-angle light scattering size-exclusion chromatography). The synthesis using the Grubbs third generation catalyst is well controlled even when targeting backbone degrees of polymerization as low as 3.

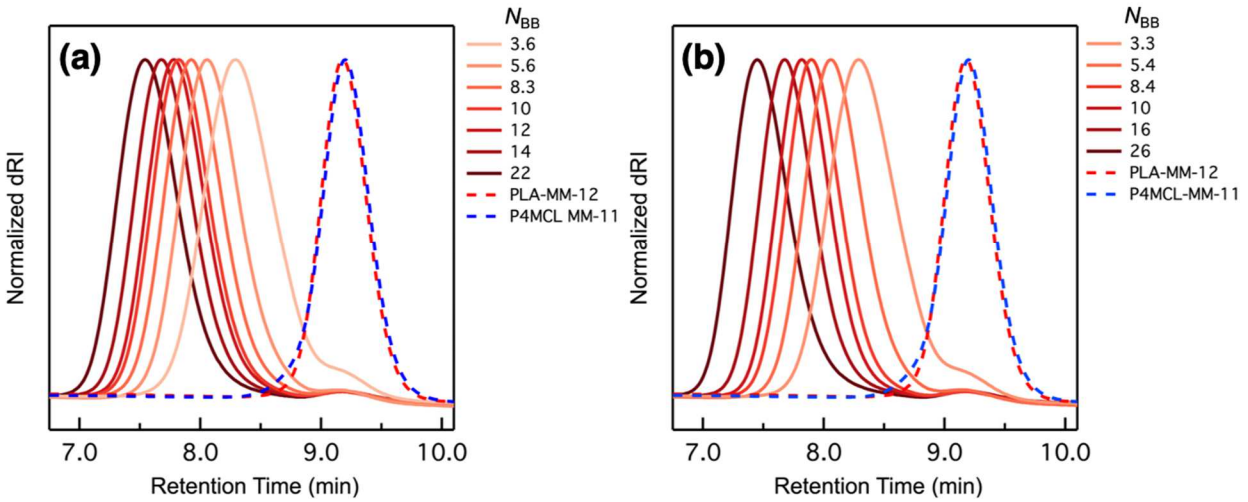

Figure 2.3 Normalized differential refractive index (dRI) signal SECs of low-N_{BB} bottlebrush copolymers with 12 kg mol^{-1} PLA (PLA-MM-12) and 11 kg mol^{-1} P4MCL (P4MCL-MM-11) side-chains. PLA and P4MCL macromonomers are shown in red and blue dashed lines, respectively. Sequence: (a) block, (b) statistical.

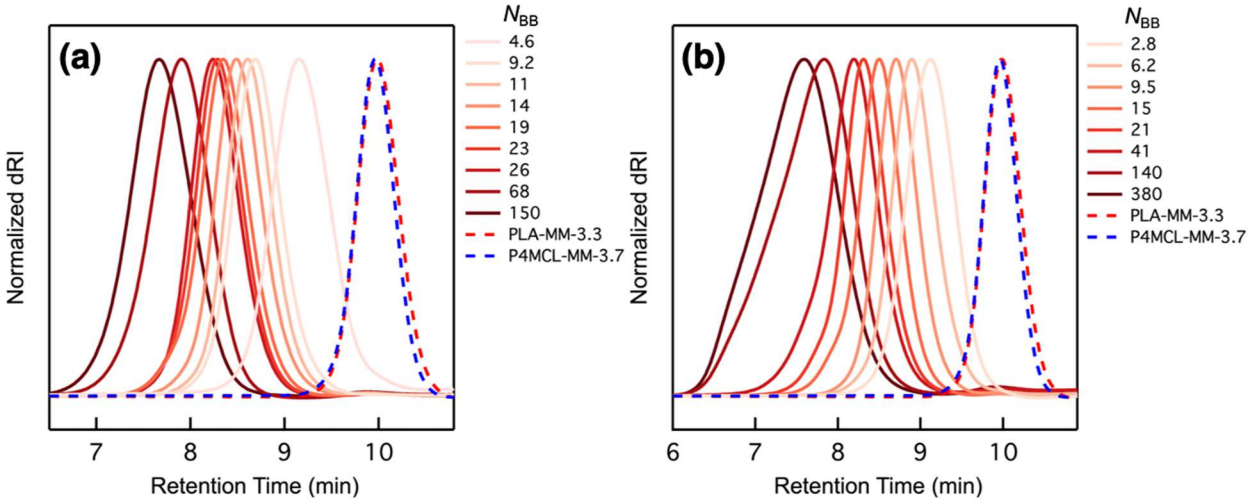

Figure 2.4 Normalized differential refractive index (dRI) signal SECs of low-N_{BB} bottlebrush copolymers with 3.3 kg mol^{-1} PLA (PLA-MM-12) and 3.7 kg mol^{-1} P4MCL (P4MCL-MM-11) side-chains. PLA and P4MCL macromonomers are shown in red and blue dashed lines, respectively. Sequence: (a) block, (b) statistical.

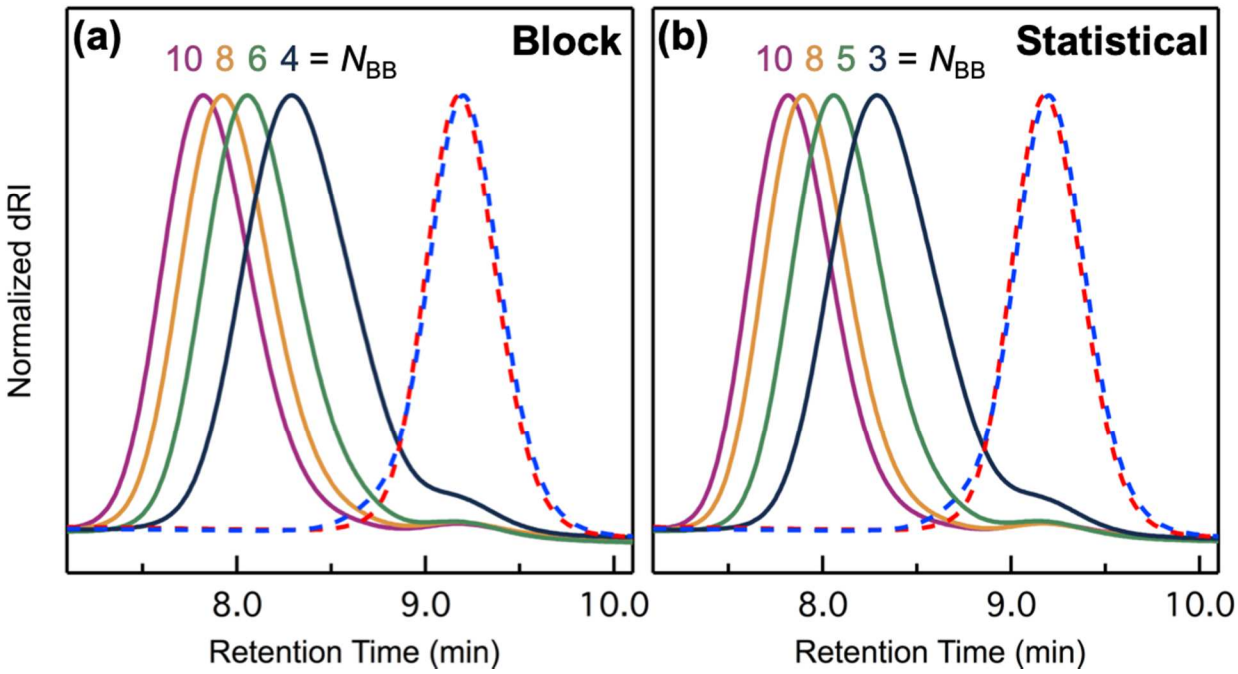

Figure 2.5. Normalized differential refractive index (dRI) signal SECs of low-N_{BB} bottlebrush copolymers with 12 kg mol^{-1} PLA (PLA-MM-12) and 11 kg mol^{-1} P4MCL (P4MCL-MM-11) side-chains. PLA and P4MCL macromonomers are shown in red and blue dashed lines, respectively. Sequence: (a) block, (b) statistical. The small bump near 9.2 min is residual macromonomer (< 3% by area in all samples).

2.3 Self-assembly of Bottlebrush Copolymers

To interrogate the bulk self-assembly, the bottlebrush polymers were studied using synchrotron small angle X-ray scattering (SAXS) (**Figures 2.6–2.7**). Both the B12 and S12 series form well-ordered nanostructures that exhibit Bragg reflections (q/q^* = 1, 2, 3, 4, 5, …) consistent with lamellar periodicity.[22]

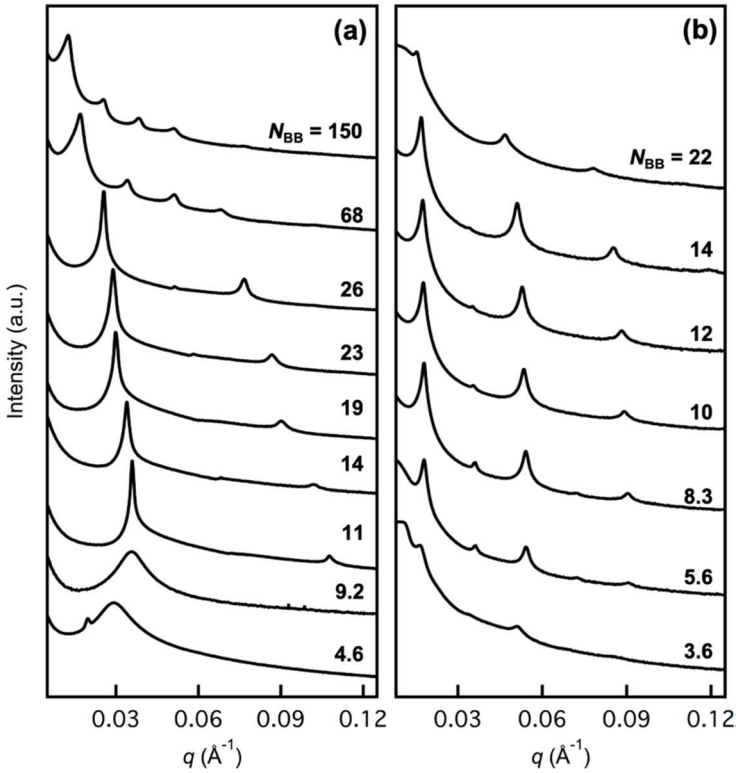

Figure 2.6. SAXS patterns (log intensity vs. q) of (a) B3 and (b) B12 copolymers.

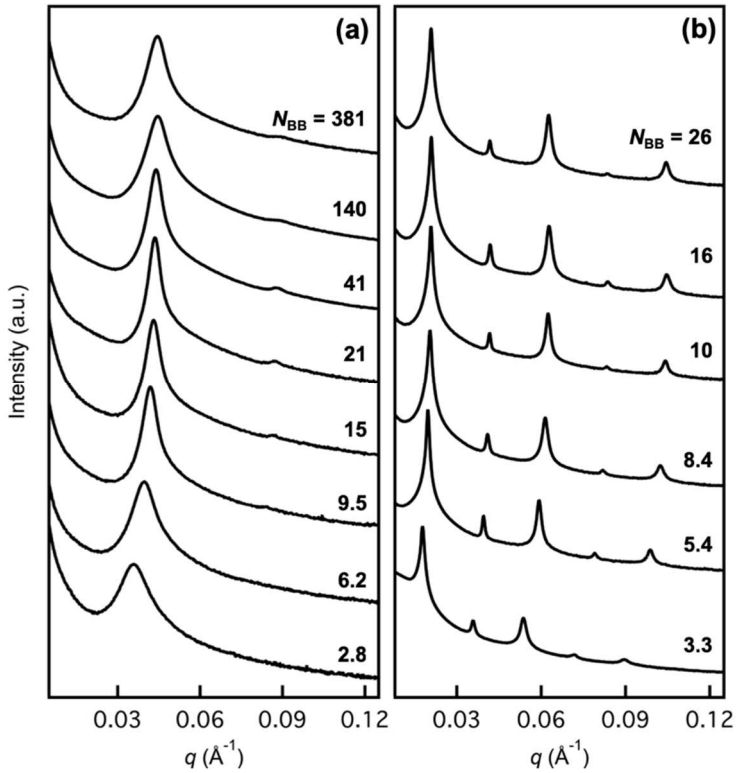

Figure 2.7. SAXS patterns (log intensity vs. q) of **(a)** S3 and **(b)** S12 copolymers.

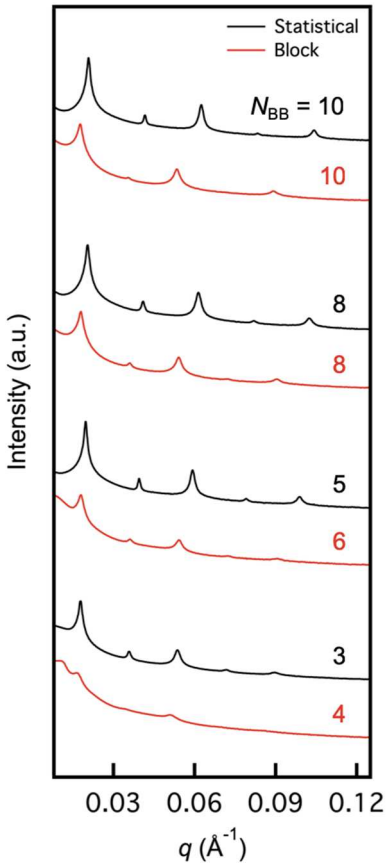

Figure 2.8. SAXS patterns (log intensity vs. q) of samples S12 (red, N_{BB} = 3, 5, 8, 10) and B12 (black, N_{BB} = 4, 6, 8, 10). All Bragg reflections (q/q^* = 1, 2, 3, 4, 5, …) are consistent with lamellar periodicity.[22]

Remarkably, even samples at the lowest N_{BB} down to N_{BB} = 3 display higher order peaks (**Figure 2.8**). In contrast, lower molar mass samples ($N_{BB} \lesssim 9$) from B3 and S3 with shorter side-chains do not order at small N_{BB} as a result of the moderate Flory–Huggins interaction parameter between PLA and P4MCL — χ = 0.10 at 298 K with a 118 □^{3} reference volume (correlation–hole scattering is evident).[23] Sharper primary peaks and the emergence of secondary peaks when $N_{BB} \gtrsim 10$ suggest a transformation to ordered nanostructures although definitive morphological assignment remains inconclusive in the absence of a sufficient number of reflections. We suspect that these samples are still lamellar based on their volume fractions and proximity in phase space to those described in **Figure 2.6b** and **2.7b**. **Tables**

2.2–2.5 summarize the pertinent bottlebrush polymer synthesis and self-assembly data.

Table 2.2. Characterization of B3-XX block copolymers synthesized from PLA-MM-3.3 and P4MCL-MM-3.7, where XX is the backbone degree of polymerization.

Sample ID	M_n[a,b]	M_n[a,c]	$Đ$[c]	f_{PLA}[d]	N_{BB}[e]	d^* (nm)[f]
B3-5	16	14	1.22	0.51	4.6	21.6
B3-9	32	29	1.19	0.67	9.2	17.8
B3-11	37	33	1.20	0.49	11	17.5
B3-14	49	40.	1.18	0.48	14	18.5
B3-19	66	50.	1.21	0.48	19	21.0
B3-23	79	54	1.19	0.49	23	21.8
B3-26	92	57	1.18	0.49	26	24.6
B3-68	230	100	1.25	0.50	68	36.9
B3-150	510	130	1.25	0.50	150	49.8

[a]In units of kg mol^{-1}. [b]Absolute values measured using size-exclusion chromatography with light scattering and differential refractive index detectors. [c]Relative to polystyrene standards. [d]Measured with ^{1}H NMR using a density of 1.03 g/cm^3 for P4MCL and 1.25 g/cm^3 for PLA.[23] [e]Absolute backbone chemical degree of polymerization (measured with light scattering) as calculated using a repeat molar mass of 72 g mol^{-1} (PLA) and 128 g mol^{-1} (P4MCL). [f]Calculated from the primary SAXS peak position (q^*) using $d^* = 2\pi/q^*$.

Table 2.3. Characterization of B12-XX block copolymers synthesized from PLA-MM-12 and P4MCL-MM-11, where XX is the backbone degree of polymerization.

Sample ID	M_n[a,b]	M_n[a,c]	$Đ$[c]	f_{PLA}[d]	N_{BB}[e]	d^* (nm)[f]
B12-4	41	57	1.25	0.48	3.6	38.4
B12-6	66	86	1.16	0.48	5.6	35.2
B12-8	96	100	1.15	0.47	8.3	35.2
B12-10	120	120	1.15	0.47	10	35.5
B12-12	140	130	1.15	0.47	12	36.1
B12-14	160	150	1.16	0.48	14	37.2
B12-22	260	170	1.18	0.47	22	41.2

[a]In units of kg mol^{-1}. [b]Absolute values measured using size-exclusion chromatography with light scattering and differential refractive index detectors. [c]Relative to polystyrene standards. [d]Measured with ^{1}H NMR using a density of 1.03 g/cm^3 for P4MCL and 1.25 g/cm^3 for PLA.[23] [e]Absolute backbone chemical degree of polymerization (measured with light scattering) as calculated using a repeat molar mass of 72 g mol^{-1} (PLA) and 128 g mol^{-1} (P4MCL). [f]Calculated from the primary SAXS peak position (q^*) using $d^* = 2\pi/q^*$.

Table 2.4. Characterization of S3-XX statistical copolymers synthesized from PLA-MM-3.3 and P4MCL-MM-3.7, where XX is the backbone degree of polymerization.

Sample ID	M_n[a,b]	M_n[a,c]	$Đ$[c]	f_{PLA}[d]	N_{BB}[e]	d^* (nm)[f]
S3-3	9.8	16	1.22	0.48	2.8	17.8
S3-6	22	21	1.22	0.49	6.2	15.9
S3-10	33	28	1.19	0.48	9.5	15.0
S3-15	50.	41	1.21	0.48	15	14.6
S3-21	73	53	1.23	0.48	21	14.4
S3-41	140	65	1.32	0.47	41	14.3
S3-140	490	120	1.40	0.48	140	14.1
S3-380	1300	140	1.37	0.48	380	14.1

[a]In units of kg mol^{-1}. [b]Absolute values measured using size-exclusion chromatography with light scattering and differential refractive index detectors. [c]Relative to polystyrene standards. [d]Measured with ^{1}H NMR using a density of 1.03 g/cm^3 for P4MCL and 1.25 g/cm^3 for PLA.[23] [e]Absolute backbone chemical degree of polymerization (measured with light scattering) as calculated using a repeat molar mass of 72 g mol^{-1} (PLA) and 128 g mol^{-1} (P4MCL). [f]Calculated from the primary SAXS peak position (q^*) using $d^* = 2\pi/q^*$.

Table 2.5. Characterization of S12-XX statistical copolymers synthesized from PLA-MM-12 and P4MCL-MM-11, where XX is the backbone degree of polymerization.

Sample ID	M_n[a,b]	M_n[a,c]	$Đ$[c]	f_{PLA}[d]	N_{BB}[e]	d^* (nm)[f]
S12-3	38	55	1.25	0.49	3.3	35.3
S12-5	63	86	1.14	0.49	5.4	32.0
S12-8	97	110	1.13	0.48	8.4	30.8
S12-10	120	120	1.13	0.48	10	30.3
S12-16	180	150	1.14	0.48	16	30.2
S12-26	300	190	1.18	0.47	26	30.2

[a]In units of kg mol^{-1}. [b]Absolute values measured using size-exclusion chromatography with light scattering and differential refractive index detectors. [c]Relative to polystyrene standards. [d]Measured with ^{1}H NMR using a density of 1.03 g/cm^3 for P4MCL and 1.25 g/cm^3 for PLA.[23] [e]Absolute backbone chemical degree of polymerization (measured with light scattering) as calculated using a repeat molar mass of 72 g mol^{-1} (PLA) and 128 g mol^{-1} (P4MCL). [f]Calculated from the primary SAXS peak position (q^*) using $d^* = 2\pi/q^*$.

2.4 Self-Consistent Field Theory Model

The bottlebrush model employed here represents both the side-chains and backbone by continuous Gaussian chains. Previous work has represented the backbone by the more sophisticated worm-like chain model, which was necessary to capture the backbone stiffening that occurs in the large N_{BB} limit.[24] Whereas the worm-like chain model is a defensible assumption when N_{BB} is large, it is less certain that the worm-like chain model is necessary or appropriate when N_{BB} is small because the side-chains will have less stiffening effect on the backbone. Since the behavior of bottlebrushes in the low N_{BB} limit is the emphasis of this paper, the choice was made of continuous Gaussian chains to represent the backbone.

The model was idealized to represent PLA and P4MCL side-chains as Gaussian chains with equivalent degrees of polymerization $N_{SC} \equiv N_{PLA} = N_{P4MCL}$, and the statistical segment lengths of the side-chains and backbone were set to be identical: $b \equiv b_{PLA} = b_{P4MCL} = b_{BB}$. Interactions between PLA and P4MCL side-chains were set to $\chi N_{SC}^{3\,kDa} = 10$, whereas the backbone was considered to be athermal and did not interact enthalpically with either type of side-chain. These simplifications were made so that our computational analysis of the star-to-bottlebrush transition would be as general as possible and could extend beyond the details of the specific chemistries employed. However, in order to compare the domain spacing between simulations and experiments, we use b_{PLA} = 8 □ (calculated at 30 °C from a polyolefin reference volume of 118 Å^3) as measured by Anderson and Hillmyer.[25]

2.4.1 Self-Consistent Field Theory Bottlebrush Polymer Model

This model consists of three species, A and B which correspond to PLA or P4MCL side-chains, and species C which represents the backbone (**Figure 2.9a**). In our model, the A

and B side-chains are parameterized to have the same degree of polymerization, $N_{SC} \equiv N_A = N_B$, and all chains are parameterized to have the same statistical segment length, $b_A = b_B = b_C$. The number of A and B side-chains are given by n_A and n_B, and the total number of side-chains by $n = n_A + n_B$. The density of side-chain grafts along the backbone is set by *d*, which is the contour distance along the backbone between adjacent side-chain grafting sites. In our model, *d* is defined relative to N_{SC} of the 3 kDa side-chains such that $\frac{d}{N_{SC}^{3kDa}} = 0.05$. This ratio approximates the experimental ratio of distance between grafting sites and the length of the 3 kDa side-chains (see **Figure 2.9a**). The larger 6 kDa and 12 kDa side-chains were modeled by increasing N_{SC} such that $N_{SC}^{12kDa} = 2N_{SC}^{6kDa} = 4N_{SC}^{3kDa}$. The backbone degree of polymerization in the model is then $N'_{BB} = d(n-1)$. Note that because the backbone is represented by a continuous Gaussian chain and was assumed to have the same statistical segment as the side-chains, the model N'_{BB} is related to the experimental N_{BB} through the relationship $N_{BB} = n = N'_{BB}/d + 1$.

The partition function is given by the strictly incompressible Multi-species Exchange model, which is a generalization of the two-component exchange model to an arbitrary number of species,[26] where the single chain partition function, Q, is now that of a bottlebrush copolymer. Interactions between A and B side-chains are given by χ_{AB}. The backbone is considered to be athermal and does not interact with the A or B side-chains (i.e. $\chi_{AC} = \chi_{BC} = 0$).

Dispersity is incorporated into the model by explicitly simulating an ensemble of bottlebrush chains, with the volume fraction of each chain chosen from a specified probability distribution. Here we assume that the side-chain length N_{SC} is fixed, and only incorporate

dispersity in the number of A and B side-chains included in the bottlebrush, n_A and n_B, respectively. Since ROMP is a living polymerization, the distribution resulting of molecular weights should ideally follow a Poisson distribution. In the Poisson distribution, the variance is equal to the mean and so the dispersity is fixed at $Đ = 1 + 1/M_n$. In practice, non-idealities in the polymerization lead to dispersities exceeding this ideal value. To incorporate these non-idealities into the simulated distribution, we use instead use a Gaussian distribution which closely approximates the Poisson distribution, but permits the mean and variance to be treated as independent parameters. Specifically, we assume that the probability distribution is a discrete Gaussian distribution

$$\phi(n_A, n_B) = \frac{1}{4\pi\sigma^2} e^{-\left[(n_A - n_A^*)^2 + (n_B - n_B^*)^2\right]/4\sigma^2} \qquad \textbf{Eq. 2.1}$$

where $n_A^* = n_B^* = n/2$ is the experimentally targeted number of A and B side-chains, and σ is obtained from the experimental dispersity, $Đ$, through the relationship $\sigma = n(Đ - 1)^{1/2}$. Since σ increases with n, explicitly representing the entire $\phi(n_A, n_B)$ distribution can be challenging when n is large. Instead, we Monte-Carlo sample a fixed number chains from $\phi(n_A, n_B)$ and then simulate the subset of chains explicitly. The number of samples is chosen to be 25 for the block bottlebrushes and 81 for the statistical bottlebrushes, which was found to result in low sampling errors for all n examined. For block bottlebrushes, all A and B side-chains were placed contiguously along the backbone, regardless of the specific values of n_A and n_B. For statistical bottlebrushes with polydispersity, n_A and n_B side-chains were ordered randomly along the backbone. The necessity of sampling this ensemble of different random bottlebrushes is why additional chains were needed to reduce sampling error. In the absence of dispersity, statistical brushes were approximated as alternating brushes, with A and B side-

chains alternating along the polymer backbone. Error bars in Figure 4b indicate the errors due to this statistical sampling of different dispersities.

The quantities that characterize the bottlebrush backbone, $P_{interface}$ and λ_{BB} are obtained by first defining a conditional probability $P(r|r_0)$, the probability that the backbone end is at position r, given that the center of the backbone is at position r_0. The location of r_0 is chosen to be at the center of the A–B lamellar interface. $P(r|r_0)$ is obtained by modifying the backbone propagator, $q_C(r,s)$ to have a non-uniform initial condition such that $q_C(r, N_{BB}/2) = \delta(r - r_0)$. This type of analysis has been employed previously to compute bridging fractions in multi-block linear chains[27,28] and backbone statistics of bottlebrushes.[29] Additional details of this calculation as well as plots of $P(r|r_0)$ are given later.

Once $P(r|r_0)$ is obtained the probability of finding the backbone end at the interface, $P_{interface}$ is then

$$P_{interface} = \int_{r\in\mathcal{I}} \mathrm{d}r P(r|r_0) \qquad \textbf{Eq. 2.2}$$

where $\mathcal{I}$ is the interfacial region centered at r_0 with width $w = (\frac{\mathrm{d}\phi_A}{\mathrm{d}r}\Big|_{r=r_0})^{-1}$. Similarly, the backbone dimension, λ_{BB}, is defined as the root-mean difference of $P(r|r_0)$,

$$\lambda_{BB} = 2\left[\int \mathrm{d}r\, P(r|r_0)\,(r-r_0)^2\right]^{1/2} \qquad \textbf{Eq. 2.3}$$

where the pre-factor accounts for the fact that $P(r|r_0)$ only includes the extension of half the backbone. The side-chain dimension, λ_{SC}, is defined as twice the unperturbed radius of gyration of the side-chains,

$$\lambda_{SC} = 2\left(\frac{b^2 N_{SC}}{6}\right)^{1/2}. \qquad \textbf{Eq. 2.4}$$

Similarly, the units length in our SCFT calculations are normalized relative to the unperturbed radius of gyration of a 3 kDa side-chain, $(b^2 N_{SC}/6)^{1/2}$. To convert lengths from simulation units to nanometers, we use statistical segment length of $b_{PLA} = 8$ □, as measured by Anderson and Hillmyer,[25] and $N_{PLA} = 42$, which gives a side-chain radius of gyration of 2.6 nm.

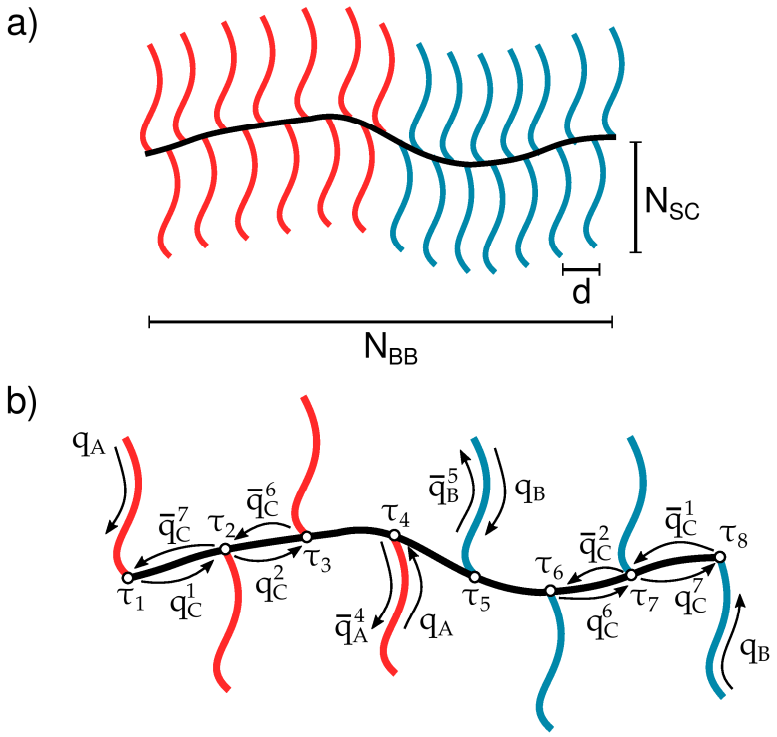

Figure 2.9. (a) Parameterization of the bottlebrush model. N_{BB} and N_{SC} denote the degree of polymerization of backbone and side-chains, respectively. The spacing between side-chain grafts along the backbone is given by d. (b) Illustration of single chain propagator notation for bottlebrush side-chains and backbone. Mathematical definitions of each variable are given in the text.

2.4.2 Numerical Bottlebrush Implementation

The large molecular weight associated with bottlebrush polymers can result in much more expensive simulations than those with linear polymer chains. In a typical SCFT implementation, the computational expense scales linearly with the total contour length of the polymer chain. In bottlebrush polymers with many side-chains, the large number of side-chains

results in a very long contour length and consequently, very expensive simulations. Here we outline an efficient numerical bottlebrush implementation that avoids this undesirable linear scaling and introduce an algorithm that scales almost independently of the number of side-chains.

The bottlebrush model is defined according to **Figure 2.9** with A and B side-chains grafted to a C backbone. The number of A and B side-chains are given by n_A and n_B with $n = n_A + n_B$. The j^{th} side-chain is specified to intersect the backbone at contour position $s = \tau_j$, where

$$\tau_j = d(j-1) \qquad 1 \leq j \leq n \qquad \textbf{Eq. 2.5}$$

The forward propagators of the side-chains satisfy the modified diffusion equation

$$\frac{\partial}{\partial s} q_K(r,s) = \frac{b_K^2}{6} \nabla^2 q_K(r,s) - w_K q_K(r,s) \qquad \textbf{Eq. 2.6}$$

with initial condition $q_K(r,0) = 1$, K = A or B, and s ranges from 0 to N_{SC}. Note that this equation does not contain an arm index dependence and so Equation 6 is only solved once per arm species. The forward propagator of the backbone is obtained by dividing the backbone into $n-1$ segments, with contour variable $\tau_j \leq s < \tau_{j+1}$. Each of segment satisfies the modified diffusion equation

$$\frac{\partial}{\partial s} q_C^j(r,s) = \frac{b_C^2}{6} \nabla^2 q_C^j(r,s) - w_C q_C^j(r,s) \qquad \textbf{Eq. 2.7}$$

with the initial condition of each segment

$$\mathrm{q}_C^j(r,\tau_j) = \begin{cases} q_K(r, N_{SC}) & j = 1 \\ q_C^{j-1}(r,\tau_j) q_K(r, N_{SC}) & \text{else} \end{cases} \qquad \textbf{Eq. 2.8}$$

where K = A or B depending on the type of side-chain grafted at τ_j.

The backwards propagator of the backbone is obtained by again dividing the backbone into $n-1$segments, where $\bar{q}_C^j$ is the backwards propagator for the segment from $s = N'_{BB} - \tau_{n-j}$ to $s = N'_{BB} - \tau_{n-j-1}$. Each segment satisfies the diffusion **Equation 2.7** with the following initial conditions

$$\bar{q}_C^j(r, N'_{BB} - \tau_j) = \begin{cases} q_K(r, N_{SC}) & j = 1 \\ \bar{q}_C^{j-1}(r, N'_{BB} - \tau_{n-j-1}) q_K(r, N_{SC}) & \text{else} \end{cases} \quad \textbf{Eq. 2.9}$$

where *K* = A or B depending on the type of side-chain grafted at $N'_{BB} - \tau_j$. The backwards propagator of the j^{th} side-chain satisfies **Equation 2.6** with the initial condition

$$\bar{q}_K^j(r, 0) = q_C(r, \tau_j) \bar{q}_C(r, N'_{BB} - \tau_j). \quad \textbf{Eq. 2.10}$$

The density of the K-type side-chains is given by

$$\phi_K(r) = \frac{1}{Q} \int_0^{N_{SC}} \mathrm{d}s \, q_K(r, s) \sum_{i \in K}^{n} \bar{q}_K^i(r, N_{SC} - s) \quad \textbf{Eq. 2.11}$$

where *K* = A or B and the sum runs over all backbone positions grafted to an A or B side-chain. Similarly, the backbone density is given by

$$\phi_C(r) = \frac{1}{Q} \int_0^{N_{BB}} \mathrm{d}s \, q_C(r, s) \bar{q}_C(r, N_{BB} - s). \quad \textbf{Eq. 2.12}$$

A schematic diagram of these propagators is shown in **Figure 2.9b**. Note that the sum in Equation 11 runs over all side-chains, and so solving for each $\bar{q}_K^i(r, N_{SC} - s)$ independently would result in an undesirable computational expense that increases linearly with the number of side-chains. However, since the entire sum satisfies the modified diffusion equation, we can instead sum over the initial conditions $\bar{q}_K^i(r, 0)$ for each side-chain and then solve the modified diffusion equation *once* for each side-chain type. This feature allows the computational time

of our algorithm to scale almost independently of the total number of side-arms, and permits the efficient simulation of bottlebrush polymers with SCFT.

2.4.3 Bottlebrush Backbone Characterization from SCFT

In order to describe the conditional probability $P(r|r_0)$ invoked in the main text, we first identify the interface position r_0 by finding the maximum of $\mathrm{d}\phi_A/\mathrm{d}r$. In the lamellar phases examined here this maximum is degenerate and is a plane parallel to the lamellar domains. For simplicity, we choose r_0 as the midpoint of the simulation cell in these degenerate dimensions. A modified propagator is then defined as

$$\tilde{q}_C^{(n/2)}(r, N'_{BB}/2) = \begin{cases} q_C^{(n/2)}(r, N'_{BB}/2) & r = r_0 \\ 0 & \text{otherwise} \end{cases} \qquad \textbf{Eq. 2.13}$$

which has the effect of constraining the midpoint of the backbone to position r_0. This modified propagator is used to solve **Equation 2.7**, to obtain $\tilde{q}_C^n(r, N'_{BB})$ which is used to obtain the conditional density

$$\tilde{\rho}(r) = \frac{1}{Q}\tilde{q}_C^n(r, N_{BB})\bar{q}_C^0(r, 0) \qquad \textbf{Eq. 2.14}$$

which gives the density of the bottlebrush end, given that the midpoint is constrained to the interface. Finally, normalizing $\tilde{\rho}(r)$ gives $P(r|r_0) = \dfrac{\tilde{\rho}(r)}{\int \mathrm{d}r\, \tilde{\rho}(r)}$.

2.5 Bottlebrush Copolymer Scaling Trends

Characteristic domain spacings $d^* = 2\pi/q^*$ were extracted from principal scattering peaks (q^*) and plotted against N_{BB} (**Figure 2.10a**). Three qualitatively distinct scaling regimes are evident in each experimental dataset: (I) a shallow but significant decrease in d^* (approximately 3 to 4 nm) as N_{BB} increases at small N_{BB} (circa ≤ 6), (II) an intermediate

transition with a weak dependence ($6 < N_{BB} \leq 15$), and (III) a region of constant slope (either increasing or flat) at large N_{BB} (roughly > 15). The last limit (regime III, $N_{BB} \rightarrow \infty$) is consistent with previous experiments[24,30,31] that rationalize the dissimilar dependence of $d^* \sim N_{BB}^{\alpha}$ for statistical ($\alpha \approx 0$) and block ($0 << \alpha < 1$) sequences by different orientations of the bottlebrush backbone — approximately parallel or perpendicular to the lamellar interface, respectively. The remainder of this chapter focuses on the behavior at smaller N_{BB} that is less well-understood.

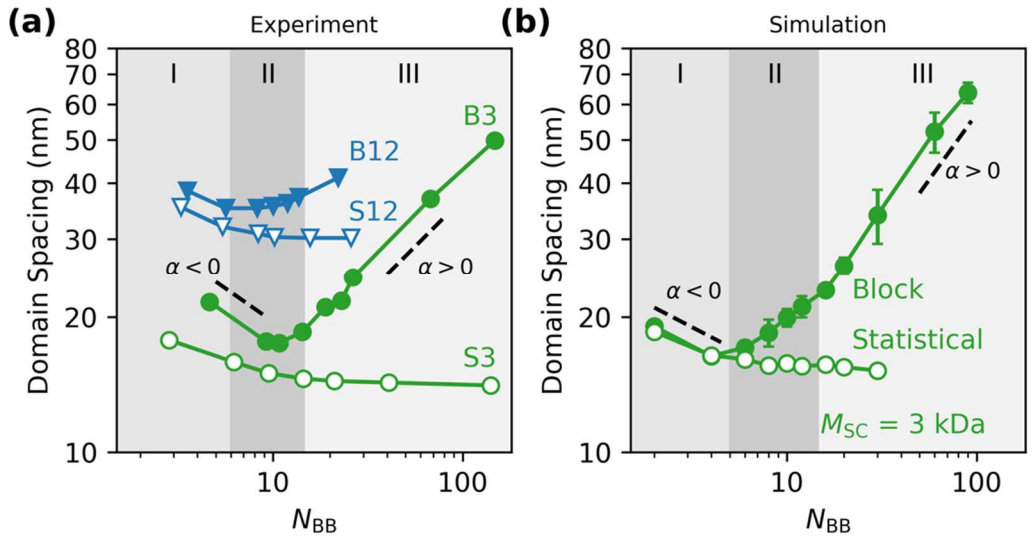

Figure 2.10. Log–log plot of lamellar domain spacing versus N_{BB} for bottlebrush copolymers comprising statistical (open symbols) and blocky (closed symbols) sequences. (a) Experimental SAXS data for B3/S3 (green) and B12/S12 (blue). (b) SCFT-predicted domain spacing with composition and arm number dispersity for M_{SC} = 3 kg mol^{-1}. The scaling exponent α in region III is 0.4 and 0.6 for the experimental and SCFT data, respectively.

For the shortest backbone lengths (regime I), we attribute the decrease in d^* with increasing N_{BB} ($\alpha < 0$) to dispersity effects that arise from the unavoidable distribution in composition and number of arms inherent to the ROMP copolymerization of two homopolymer macromonomers. SCFT calculations (**Equations 2.1–2.14**) of block bottlebrushes in the absence of dispersity fail to capture the experimental trend and instead

predict a monotonic increase in d^* with N_{BB} (**Figure 2.11**). In contrast, simulations conducted with a variety of different chains varying in their number of arms and composition reveals qualitatively similar curves (**Figure 2.10b**) as experiments (**Figure 2.10a**) at all N_{BB} for ≈ 3 kg mol^{-1} side-chains with statistical and blocky sequences. While the best agreement between simulation and experiment is obtained by including both types of dispersity, compositional dispersity is the most significant (**Figure 2.11**).

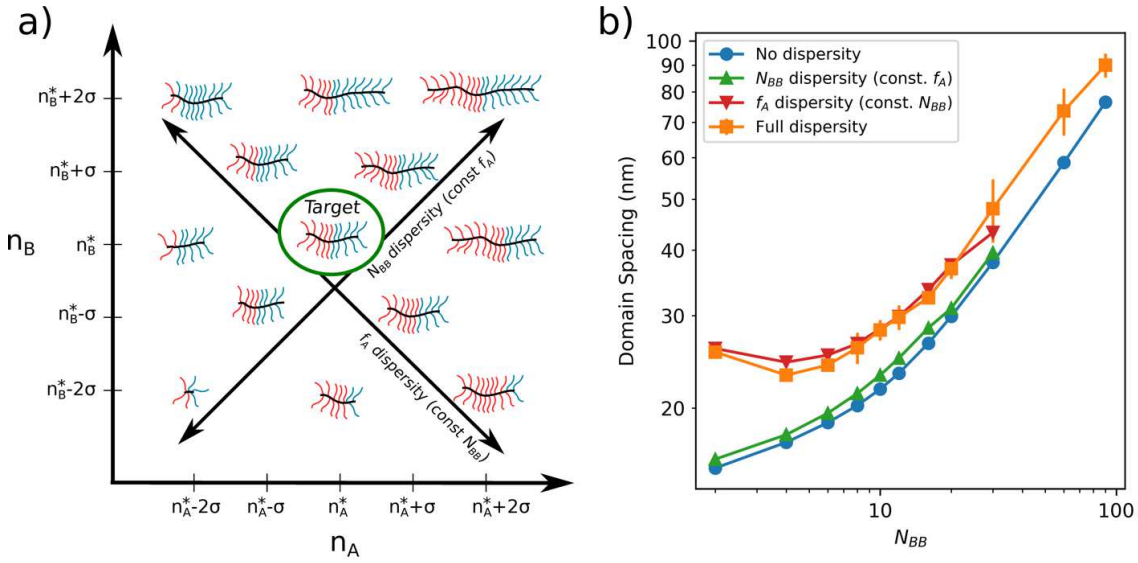

Figure 2.11. (a) Illustration of compositional (f_A) and N_{BB} dispersity, where n_A* and n_B* are the average degree of polymerization of macromonomers A and B and σ is the standard deviation in n based off of $Đ$. (b) Effects of the different types of dispersity on domain spacing.

The signature of each experimental scaling regime is recovered, in particular the negative slope for small N_{BB}. This effect appears to originate from an appreciable concentration of homopolymer bottlebrushes that form due to compositional dispersity, which swell the lamellae and dilate domain periodicity. Since probability biases more homopolymer at short average backbone degrees of polymerization, as N_{BB} reaches 20 repeat units, the aforementioned scaling (regime III) is essentially unaffected by such dispersity and α asymptotes. Together, these results indicate that dispersity, and especially compositional

dispersity, play an important role in the self-assembly of short bottlebrush polymers synthesized via grafting-through copolymerization.

One might anticipate that regime II, the region of intermediate scaling, is indicative of a transition from star-like to bottlebrush-like conformations as N_{BB} grows. The approximate plateau in d^* (which is readily apparent in the B12 block sequence) would then be consistent with two competing effects: (1) fewer homopolymers and less swelling, which together decrease domain spacing with increasing N_{BB}, and (2) the star-to-bottlebrush transition that results from an amplification of steric congestion surrounding the elongating backbone, extending chain configurations and raising d^*.

Figure 2.12 illustrates the key characteristics of regimes I, II, and III. We are particularly interested in understanding the transition region (II) in more detail since it distinguishes well-established bottlebrush behavior from the miktoarm star materials of interest. Because this is difficult with experiments, we instead develop a more detailed SCFT analysis to clarify the location of the miktoarm star-to-bottlebrush crossover.

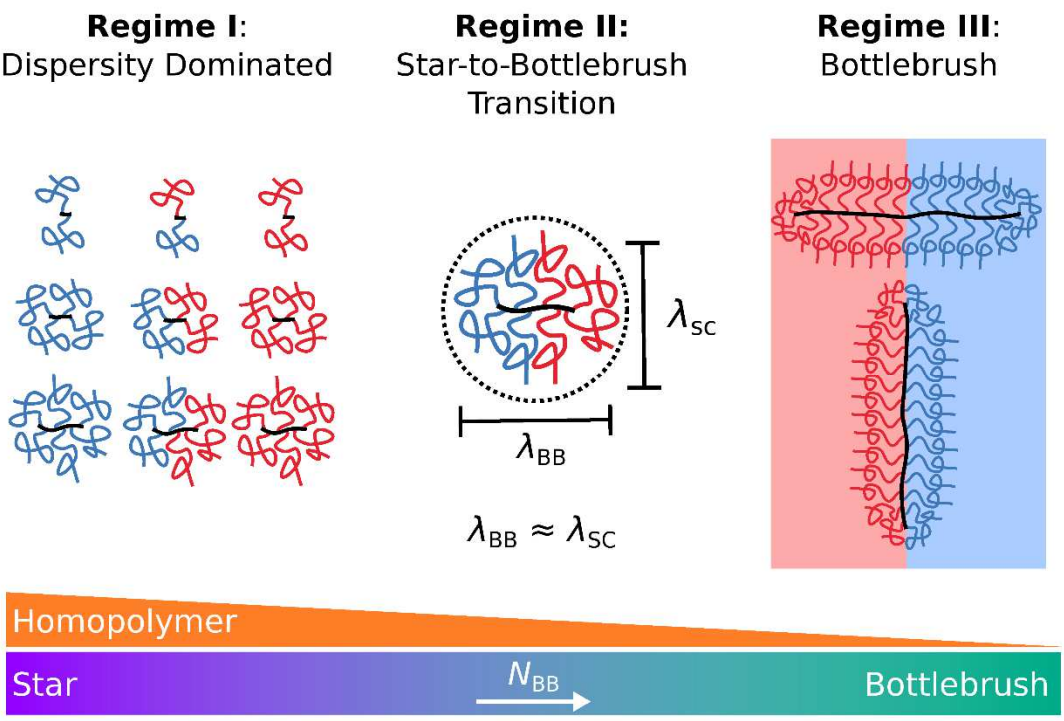

Figure 2.12 Illustrations describing the factors that control scaling ($d^* \sim N_{BB}^{\alpha}$) in the three regimes observed with two-component bottlebrush copolymers. (a) Small N_{BB}: dispersity in the number of arms and composition results in $\alpha < 0$. (b) Moderate N_{BB}: chain conformations transition from miktoarm star to bottlebrush when backbone (λ_{BB}) and side-chain extensions (λ_{SC}) become comparable as the concentration of homopolymers tapers off; $\alpha \gtrsim 0$. (c) Large N_{BB}: backbone orientation depends on sequence (consistent with prior experiments[30] and the SCFT simulations reported herein.)

2.6 Miktoarm Star-to-Bottlebrush Transition

To elucidate the details of the miktoarm star-to-bottlebrush transition using SCFT, we begin by examining the effect of backbone length on the domain spacing of block bottlebrush copolymers in the absence of dispersity, which allows us to decouple the competing effects of homopolymer-induced swelling and backbone elongation that characterize the intermediate scaling regime II. When dispersity is removed from our SCFT calculations (**Figure 2.13**), only two regimes are observed: one at large N_{BB} corresponding to rapidly increasing domain spacing (III′) and another at low N_{BB} corresponding to slower domain spacing growth (II′). As noted

previously by Dalsin et al.,[24] this decrease in α is attributed to the onset of miktoarm-star-like behavior. We denote the crossover between regimes II′ and III′ by N_{BB}*, e.g., N_{BB}* ≈ 12 for 3 kg mol^{-1} side-chains. This value corresponds well with the experimentally observed transition from the large N_{BB} regime III to the intermediate N_{BB} regime II that falls somewhere around N_{BB} = 12 (**Figure 2.10a**).

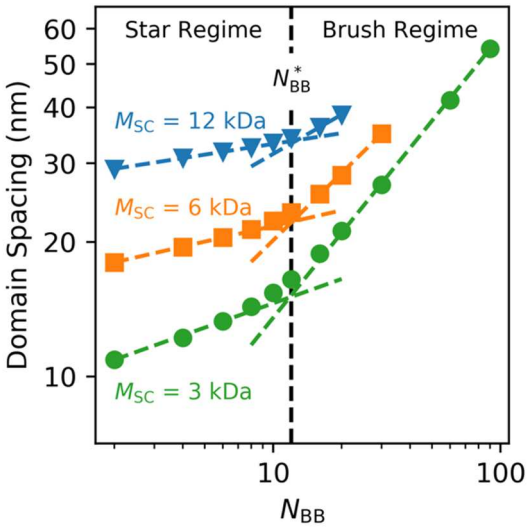

Figure 2.13. SCFT calculations of block bottlebrush copolymer domain spacing as a function of backbone length N_{BB}. Different colors denote side-chain lengths of M_{SC} = 3, 6, and 12 kg mol^{-1}. The change in slope occurs at N_{BB}*, which is nearly constant for all simulated side-chain lengths.

For larger 6 and 12 kg mol^{-1} side-chains, the bottlebrushes exhibit a weaker dependence of domain spacing on N_{BB} as indicated by lower values of α across the whole range (regimes II′ and III′). This is consistent with our experimental results comparing 3 and 12 kg mol^{-1} side-chains (**Figure 2.10a**) and suggests that larger side-chains lead to slightly more flexible backbones at the values of N_{BB} probed. Nevertheless, despite their lower values of α, the bottlebrushes with M_{SC} = 6 and 12 kg mol^{-1} also exhibit two scaling regimes at low and high N_{BB}, again with a crossover at N_{BB}*. Remarkably, the value of N_{BB}* is approximately constant

for all side-chain lengths commensurate with experiments, M_{SC} = 3, 6, and 12 kg mol^{-1} (**Figure 2.13**). Evidently, even for relatively short 3 kg mol^{-1} side-chains, the backbone stiffening due to steric repulsion is essentially saturated, thereby leading to a conserved star-to-bottlebrush transition at N_{BB}* = 12. Additional simulations indicate that N_{BB}* will decrease with shorter 1.5 kg mol^{-1} side-chains (**Figure 2.14a**), and it is also very slightly dependent on the segregation strength χN_{SC} (**Figure 2.14b**).

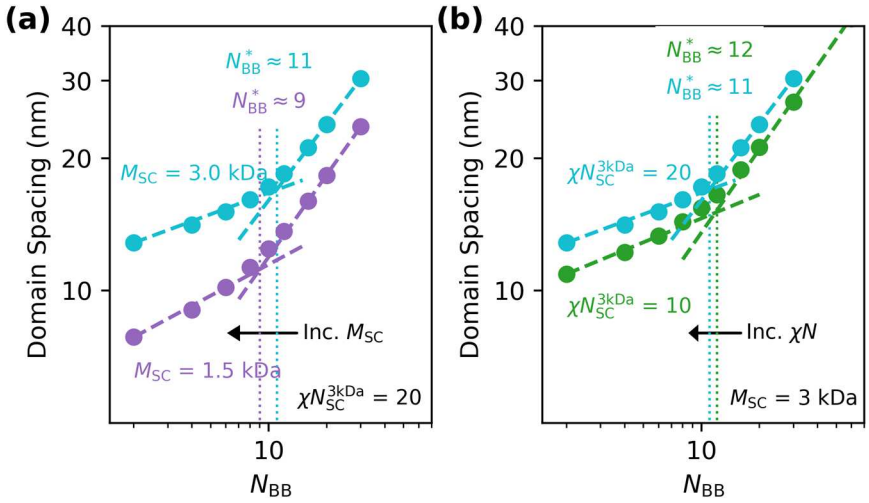

Figure 2.14. Location of N_{BB}* as a function of side-chain length and segregation strength (calculated using SCFT). (a) N_{BB}* decreases as side-chain length changes from M_{SC} = 3 to 1.5 kg mol^{-1}. Recall that N_{BB}* becomes invariant for $M_{SC} \geq$ 3 kg mol^{-1} (main text, Figure 6). Note that these simulations set χN_{SC}^{3kDa} = 20 instead of χN_{SC}^{3kDa} = 10 as used elsewhere in this work so that microphase separation could be achieved at N_{BB} = 2. (b) N_{BB}* is slightly affected by χN; increasing χN_{SC}^{3kDa} from 10 to 20 produces a small decrease in N_{BB}*.

The independence of N_{BB}* with most M_{SC} predicted by SCFT is consistent with our experimental data; although it is difficult to precisely pinpoint N_{BB}* in **Figure 2.10a** due to the effects of dispersity, N_{BB}* = 12 nonetheless appears to be the approximate location of the change in α scaling for both 3 and 12 kg/mol side-chains. As demonstrated, SCFT predictions of domain spacing are useful for identifying N_{BB}* with block bottlebrushes and comparing model predictions with experiments, but this analysis does little to explain the molecular origin

of the shift in α at $N_{BB} = N_{BB}$*. We next turn to different SCFT calculations to assess this aspect of the star-to-bottlebrush transition.

2.6.1 Molecular Explanation of the Miktoarm Star-to-Bottlebrush Transition

One molecular signature of the star-to-bottlebrush transition is a change in backbone conformation as a function of N_{BB} *with the block sequence*. **Figure 2.15a** shows simulated backbone density profiles for monodisperse samples with N_{BB} = 6, 12 and 30 and M_{SC} = 3 kg mol^{-1}. When N_{BB} is large (regime III, e.g., N_{BB} = 30), the backbone conformations of statistical and block bottlebrushes exhibit large differences. Statistical brushes orient their backbones parallel to the lamellar interface, which leads to a density profile that is strongly peaked at x/L_0 = 0.5, where x is the position within a unit cell and L_0 is the natural periodicity. In contrast, block bottlebrush backbones preferentially orient perpendicular to the interface, thereby smearing out the density profile across a lamellar unit cell. (These data are consistent with the illustrations in **Figure 2.12c** and prior experimental literature.[24,30,31]) However, such sequence effects become nearly indistinguishable as N_{BB} decreases. For a short bottlebrush with N_{BB} = 6, block and statistical backbone distributions are essentially identical, with both density profiles strongly peaked at the lamellar interface (**Figures 2.15–2.16**). The independence of backbone distribution on side-chain arrangement at low N_{BB} indicates that the backbone has no preferred orientation within the lamellar interface. Intermediate backbone lengths corresponding to $N_{BB} = N_{BB}$* = 12 exhibit a density profile that is mixed between these two extremes; the density is peaked at the interface, but there is still appreciable backbone density within the interior of lamellar domains. This finding suggests that the configuration of a *block* bottlebrush backbone can be used as a hallmark of the star-to-bottlebrush transition: when the

backbone of a *block* bottlebrush begins to localize near the domain interface, it starts to behave like a star.

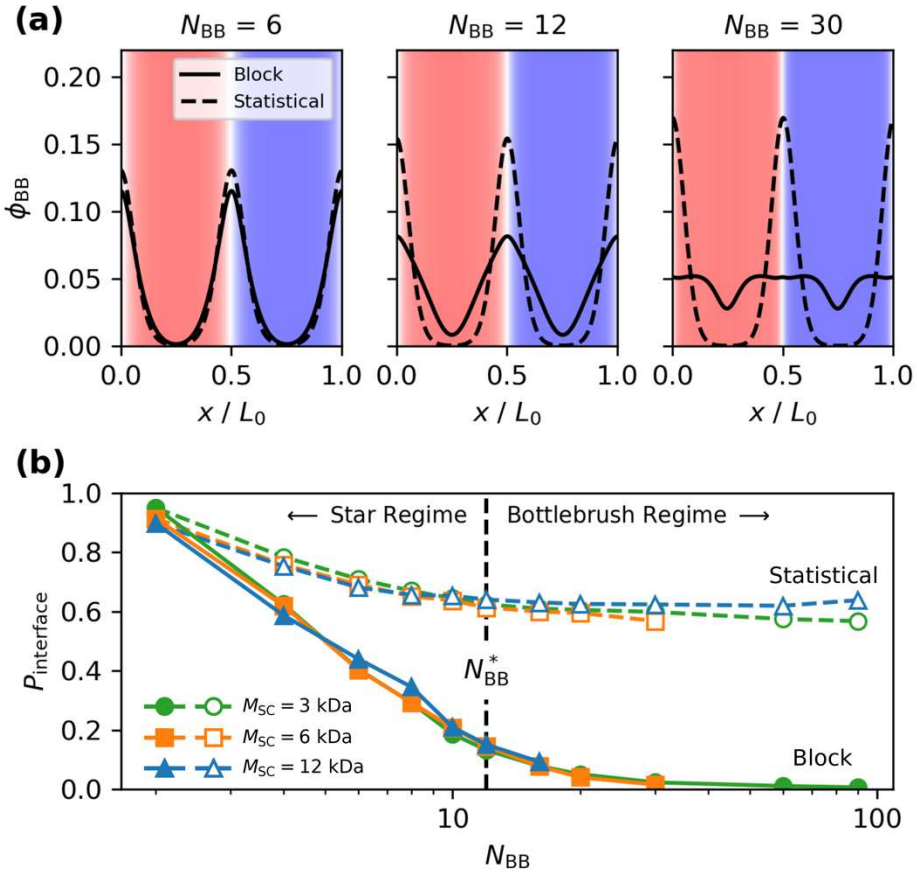

Figure 2.15. (a) SCFT calculations of backbone segment distribution, ϕ_{BB}, across a lamellar period with statistical and block macromonomer sequences (M_{SC} = 3 kDa) for N_{BB} = 6, N_{BB} = 12 (= N_{BB}*), and N_{BB} = 30. The red, blue, and white shading indicates PLA-rich domains, P4MCL-rich domains, and the interface, respectively. x denotes the position within a lamellar unit cell and L_0 is the domain periodicity. (b) Probability of backbone localization at the interface, $P_{interface}$, for different N_{BB} and M_{SC}.

To quantify this transition in greater detail, we examine the probability of finding a bottlebrush backbone at the domain interface, $P_{interface}$, as a function of N_{BB} (**Figures 2.15b**). For statistical bottlebrushes, this probability is approximately constant for $N_{BB} > N_{BB}$* before increasing at small backbone lengths. Note that this implies the statistical sequence does undergo a small change in backbone distribution as a function of N_{BB}, but the effect is rather

minimal. In contrast, the probability for block sequences is highly variable; it is approximately zero when $N_{BB} > 20$, before increasing for smaller N_{BB}. Notably, what we have previously defined as $N_{BB}^* = 12$ corresponds roughly to the onset of this dramatic backbone redistribution. Consistent with our observation in **Figure 2.13**, changing M_{SC} from 3 to 12 kg mol^{-1} has little effect on backbone localization to the interface as measured by $P_{interface}$.

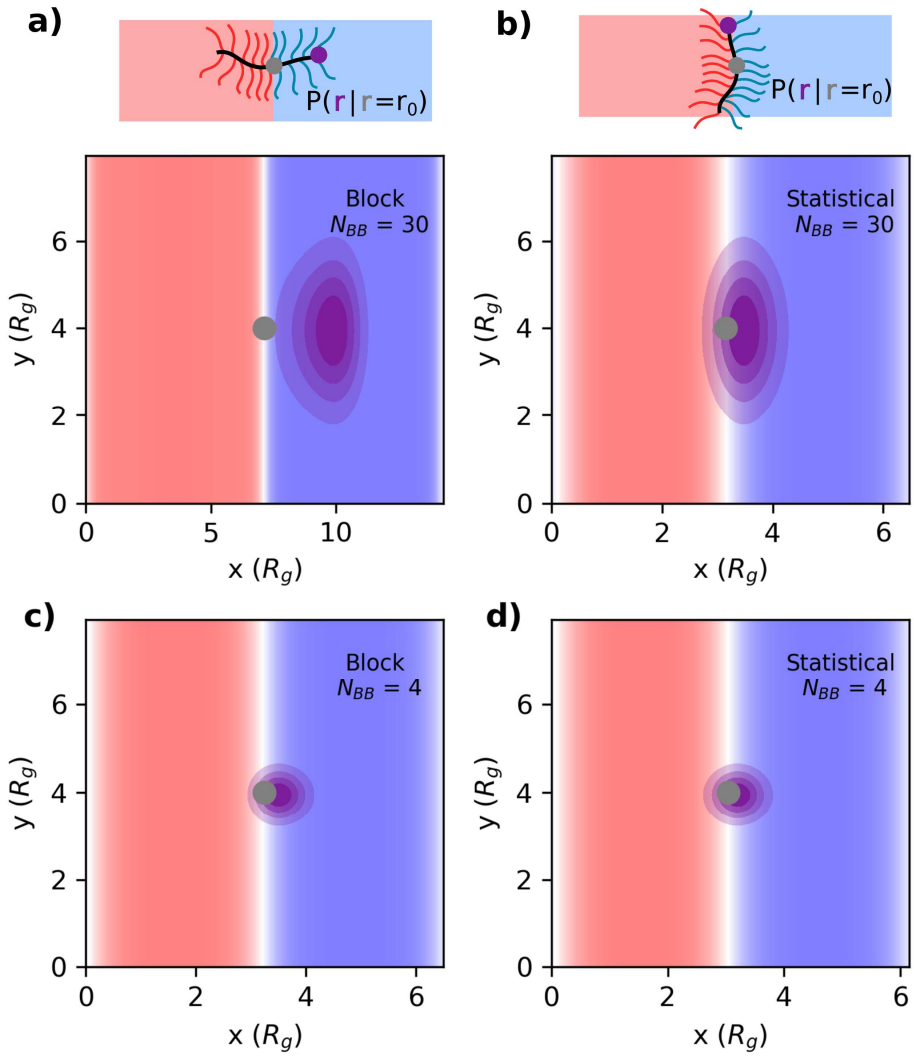

Figure 2.16. Values of P(r|r$_0$) for different bottlebrushes. (a) Block bottlebrush with $N_{BB} = 30$. (b) Statistical bottlebrush with $N_{BB} = 30$. (c) Block bottlebrush with $N_{BB} = 4$. (d) Statistical bottlebrush with $N_{BB} = 4$.

Taken together, these results offer a molecular explanation for the scaling regimes II

and III observed in **Figures 2.10** and **2.13**. For $N_{BB} > N_{BB}^*$, the backbone extension is large relative to the interface, and domain spacing scales strongly with N_{BB}. In contrast when $N_{BB} < N_{BB}^*$, the backbone extension is comparable to the interface width, leading to localization of the backbone at the interface and signaling increasingly miktoarm-star-like behavior. Experimental measurements of domain-spacing versus N_{BB} thus provide an excellent metric for identifying this molecular transition, specifically with *block* bottlebrush copolymers.

2.6.2 Miktoarm Star-to-Bottlebrush Transition in Statistical Copolymers

Since statistical bottlebrushes undergo a comparably modest backbone redistribution as a function of N_{BB}, the analysis described in **Figure 2.15** cannot similarly be used as a proxy to interrogate their star-to-bottlebrush crossover. Clear signatures of the star-to-bottlebrush transition with the statistical sequence are also absent from the experimental data in **Figure 2.10a**, so the analysis presented up to now cannot examine the role that macromonomer sequence (i.e., block vs. statistical) plays in the star-to-bottlebrush transition. In order to probe sequence effects in more detail, it was necessary to compute the relative extension of the bottlebrush backbone (λ_{BB}) and side-chains (λ_{SC}). Once these lengths were determined, we define a dimensionless quantity $\lambda_{BB}/\lambda_{SC}$ that describes the aspect ratio of a given bottlebrush polymer. For $\lambda_{BB}/\lambda_{SC} \gg 1$, a bottlebrush is highly elongated and the molecules are expected to adopt more cylindrical-like configurations. In contrast, for $\lambda_{BB}/\lambda_{SC} \ll 1$, the backbone is vanishingly small and bottlebrush polymers should instead mimic spherical or star-like objects. The star-to-bottlebrush transition is then expected to occur circa $\lambda_{BB}/\lambda_{SC} \approx 1$. If our prior analysis is robust, this crossover will correspond with N_{BB}^* as identified above.

We therefore used SCFT simulations to compute $\lambda_{BB}/\lambda_{SC}$ for both sequences

(statistical and block) with varying N_{BB} and identified the value at which $\lambda_{BB}/\lambda_{SC} = 1$ (**Figure 2.17**). In both cases, $\lambda_{BB}/\lambda_{SC} = 1$ at similar values of N_{BB} (8 for block, 14 for statistical). For block bottlebrushes, the previously identified value of N_{BB}* = 12 correlates quite well with $\lambda_{BB}/\lambda_{SC} \approx 1$, indicating that $\lambda_{BB}/\lambda_{SC}$ is a suitable metric for establishing the location of a star-to-bottlebrush transition. This result has two important consequences. First, the correspondence between N_{BB}* and $\lambda_{BB}/\lambda_{SC} = 1$ provides an additional physical explanation for the star-to-bottlebrush transition — it suggests that the change in slope at N_{BB}* can be correctly thought of as the point when a bottlebrush molecule transitions from a cylindrical-like to a spherical object. Second, the consistent picture that emerges from our different analyses of the block sequence, coupled with similar values of N_{BB} for $(\lambda_{BB}/\lambda_{SC})_{block} = 1$ and $(\lambda_{BB}/\lambda_{SC})_{statistical} = 1$, allows us to posit that the star-to-bottlebrush transition is largely independent of sequence. Both block and statistical copolymers seem to transition at almost equivalent backbone lengths. There may be a slightly earlier transition for the block sequence due to a small bias for stiffer backbones, but this effect is modest.

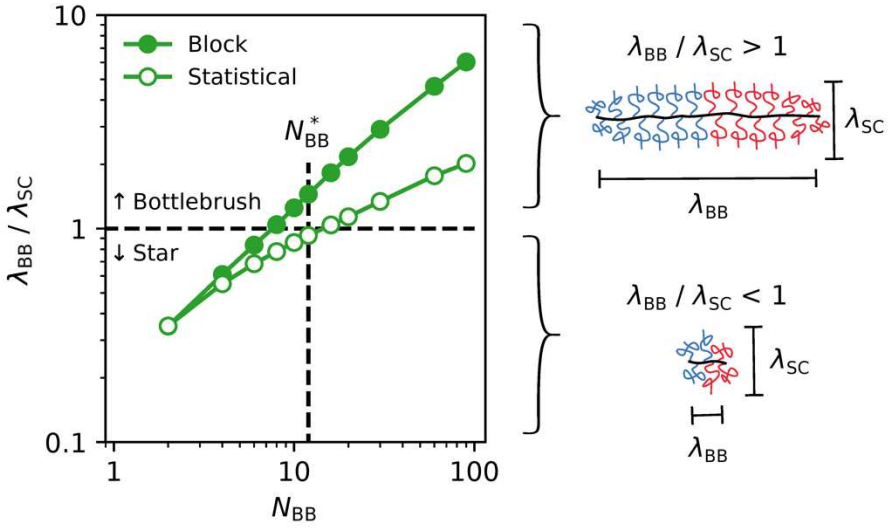

Figure 2.17. Calculated bottlebrush aspect ratio ($\lambda_{BB}/\lambda_{SC}$) for block and statistical macromonomer sequences with M_{SC} = 3 kg mol^{-1}. The value of N_{BB} where $\lambda_{BB}/\lambda_{SC} \approx 1$

2.7 Discussion

The virtues of ring-opening metathesis polymerization are now well-known and have ushered in an era of synthetic simplicity that has changed the accessibility of cutting-edge materials for numerous applications.[8–16] Major efforts by Bowden,[32,33] Wooley,[34,35] and Grubbs[36–38] have adapted ROMP to construct bottlebrush polymers (N_{BB} >> N_{SC}) with amazing control over molar mass and dispersity. Less attention has been devoted to exploiting this versatile chemistry in the opposite limit, $N_{BB} < N_{SC}$. In the context of *bulk* phase behavior, although a few reports[24,29] include samples with $N_{BB} < N_{SC}$, efforts have not focused heavily on this regime. Here, we have demonstrated that the sequential or statistical grafting-through copolymerization of two macromonomers with $N_{BB} < N_{SC}$ results in materials that self-assemble into well-ordered lamellar structures. While we have not yet attempted to do so, there are no fundamental limitations that prevent the extension of this approach to other, more complex, design targets — for example, ≥ 3 distinct chemistries and multiblock side-chains[34,35]

or sequences.[10] Synthesizing miktoarm star polymers with the present technique affords a number of advantages that revolve around versatility. The *average* number of arms and composition are easily manipulated by stoichiometry, but of course, the price paid is dispersity in both. (Since ring-opening transesterification polymerization and ROMP are controlled, the unavoidable dispersity in molar mass is similar to other miktoarm star polymerization strategies.) These distributions could be either a benefit[39] or burden[40] depending on perspective. Either way, we have systematically studied their effect in the context of self-assembly and chain conformations. Finally, as a tangential observation, the dispersity accompanying our approach seems to counteract the phase boundary deflection that is characteristic of asymmetric (in connectivity) miktoarm star polymers.[41] For example, Grason has previously predicted[42] and Tselikas observed[43] hexagonally-packed cylinder phases at roughly symmetric volume fractions $f_A \approx 0.5$ in an AB_3 miktoarm star polymer. Herein, samples synthesized near this composition with a 1:3 ratio of A:B side-chains are decidedly lamellar (**Figure 2.18**).

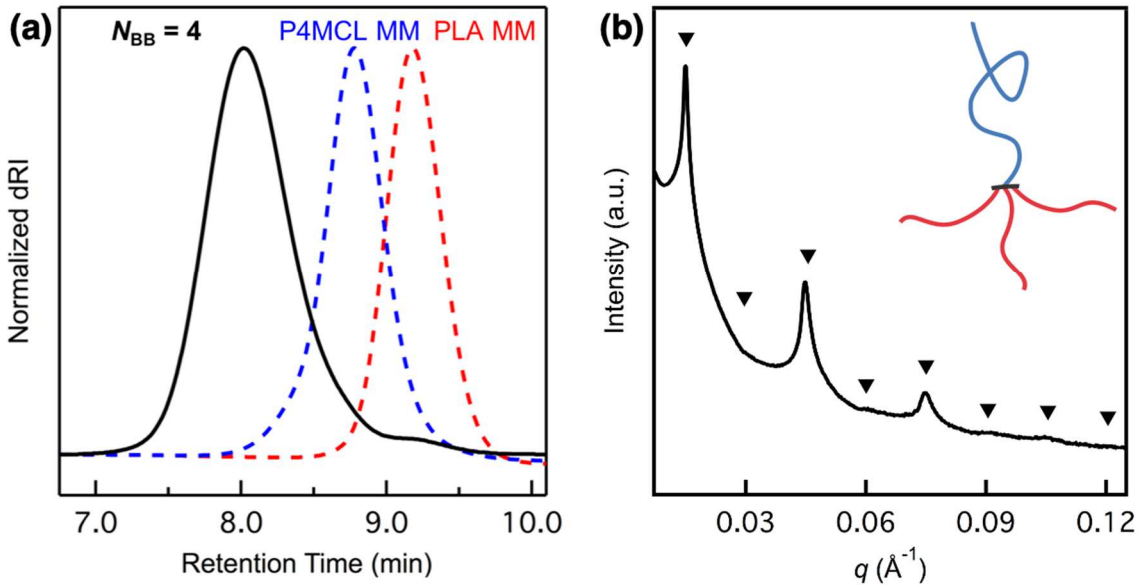

Figure 2.18. (a) SECs (normalized differential refractive index signal) of an AB_3 copolymer with asymmetric architecture (on average). A = P4MCL-MM-22 and B = PLA-MM-12 at roughly symmetric volume fraction (f_{PLA} = 0.48). SEC-MALS: M_n = 59 kg mol^{-1}, $Đ$ = 1.17. (b) SAXS of the AB_3 copolymer consistent with a lamellar morphology (q/q^* = 1, 2, 3, 4, 5, …) as indicated by the triangular markers. Inset: illustration of the asymmetric copolymer.

Johnson and coworkers have pioneered the use of ROMP to construct "core-crosslinked" molecules termed "mikto-brush-arm star polymers"[44–46] that bear some similarities to the materials described herein. Their synthetic method also leverages the benefits of ROMP to build arms via macromonomer copolymerization. The key distinction is a final step involving the addition of multi-functional norbornene crosslinker, which forms a compact core that polymerized macromonomers protrude from. Such core-crosslinking has undoubtedly proven useful in a variety of applications[46–53] but the molecular connectivity is fundamentally different compared to low-N_{BB} statistical and block bottlebrush polymers. No crosslinking step is involved in our approach and the core of each star polymer is precisely the well-defined poly(norbornene) backbone that is formed during ROMP in the absence multi-functional additives.

The star-to-bottlebrush transition has been investigated in other material systems, many

of which employed just one type of side-chain chemistry. A recent report analyzed atactic poly(propylene) bottlebrush polymer melts with varying degrees of polymerization and concluded, based on zero-shear viscosity data, that the star-to-bottlebrush change in chain conformation likely occurs over the range N_{BB} = 26–74.[54] Small angle neutron scattering measurements of polystyrene bottlebrush side-chains in a good solvent place the transition somewhere around N_{BB} = 120.[55] We speculate that these numbers are larger than those ascertained here due to differences in the free energy of two- and one-component polymers. As previously discussed, the transition from bottlebrush-to-star conformations for bottlebrush *co*polymers occurs when N_{BB} decreases towards 12. With the block sequence, this value marks the beginning of backbone unalignment so that it resides at the lamellar interface with no favored orientation. However, this transformation is presumably quite difficult if the backbone cannot occupy a tight region of space around the interface; otherwise, the system would be forced to create enthalpically-unfavorable contacts between the two different types of side-chains. From the present analysis, $\lesssim$12 repeat units is apparently sufficient to overcome this energetic dichotomy, but the thermodynamic landscape would undoubtedly change without such constraints (e.g., homopolymer bottlebrushes).

A transition reminiscent of the star-to-bottlebrush crossover has also been observed in polymers produced from branched macromonomers containing both poly(styrene) and poly(dimethylsiloxane) (PDMS) side-chains.[29] Note that the composition dispersity inherent to statistical ROMP *co*polymerization can be suppressed using this approach, but the homopolymerization of diblock macromonomers eliminates control over the average number of each arm type — the resulting star or bottlebrush materials are necessarily A_nB_n. Nevertheless, in this case, the monotonic increase in domain spacing observed for samples

with increasing N_{BB} ($\lesssim$ 10) is believed to originate from chain stretching effects that saturate at modest backbone lengths. These data support our conclusion that compositional dispersity dominates the d^* vs. N_{BB} scaling ($\alpha < 0$) observed in **Figure 2.10** (regime I). In analogy to recent work from Zhong,[56] the impact of compositional dispersity on additional physical properties would also be interesting to probe, for example the glass transition temperature, order−disorder temperature, and storage modulus.

Finally, we draw comparisons to another paper by Dalsin et al.[24] that studied bottlebrush block polymers comprising atactic poly(propylene) and poly(styrene) side-chains. They identified a decrease in the scaling exponent (α = 0.26) between N_{BB} = 10−15 and attributed it to "starlike" molecules. These samples lie beyond the N_{BB} boundary (II−III) that we observe as the onset of star-like behavior. By extending the scaling analysis to even smaller N_{BB}, we have uncovered the limiting behavior of α, which further transforms d^* into a minimum and then dips negative. A second key conclusion from their paper is the assertion that bottlebrush backbones are actually significantly more flexible than commonly believed. Our evidence also seems to support this notion. As shown in **Figure 2.10a**, the domain spacing of PLA−P4MCL bottlebrush block copolymers expands by a factor of 1.5−2 when side-chain molar mass increases from 3 to 12 kg mol^{-1}. This result is inconsistent with the traditional interpretation of block bottlebrushes as rigid cylindrical objects always oriented perpendicular to the domain interface. If side-chains only extended parallel to the interface, domain spacing would not (or only weakly) depend on their length. Instead, our data is consistent with the conclusion that a backbone is strongly oriented near the interface, but this order decays with distance, eventually allowing side-chains to influence domain spacing.[24]

2.8 Conclusion

The grafting-through ring-opening metathesis polymerization of two macromonomers with a statistical or blocky sequence generates miktoarm star polymers in the low backbone degree of polymerization limit ($N_{BB} < N_{SC}$). A series of symmetric volume fraction ($f_{PLA} \approx 0.5$) materials with poly(lactide) and poly(4-methyl-ε-caprolactone) side-chains (≈3 or 12 kg mol^{-1}) self-assemble into lamellar structures with a characteristic domain spacing that strongly depends on N_{BB}. Using these trends in conjunction with self-consistent field theoretic simulations, three scaling regimes were identified that are distinguished as: (I) dispersity-dominated, (II) a star-to-bottlebrush transition, and (III) bottlebrush. SCFT calculations have revealed that the miktoarm star-to-bottlebrush transition can be captured by analyzing the redistribution of backbone segments within a lamellar unit cell as a function of N_{BB} for the block sequence. The location of this transition occurs at approximately $N_{BB}^* = 12$ and is largely independent of side-chain length and macromonomer sequence. The synthetic strategy disclosed herein significantly simplifies access to discrete miktoarm star polymers that organize into well-ordered mesostructures when dispersity in composition and the number of arms can be tolerated. These materials have provided insights into the interplay between dispersity, molecular conformations, and self-assembly.

2.9 Experimental

2.9.1 Chemicals

Tin(II) 2-ethylhexanoate ($Sn(Oct)_2$, Aldrich, 92.5−100%) was fractionally distilled 3x under reduced pressure (50 mtorr, 150 □) and stored in a nitrogen filled glovebox before use.

4-Methylcaprolactone (4MCL) was prepared according to literature,[1] purified by fractional distillation 3x from calcium hydride (CaH_2, Fisher Scientific, 93%), 3x from $Sn(Oct)_2$ under reduced pressure (50 mtorr, 50 □), and stored in a nitrogen filled glovebox before use. D,L-Lactide was generously provided by Corbion (PURASORB DL) and recrystallized once from anhydrous ethyl acetate (Fisher Scientific, 99.9%) and twice from anhydrous toluene. N-(hydroxyethyl)-*cis*-5-norbornene-*exo*-2,3-dicarboximide (NbOH) was prepared according to literature[2] and recrystallized from chloroform. Grubbs' second-generation metathesis catalyst [$(H_2IMes)(PCy_3)_2(Cl)_2Ru$=CHPh] was generously provided by Materia. Grubbs' third-generation metathesis catalyst [$(H_2IMes)(pyr)_2(Cl)_2Ru$=CHPh] (G3) was prepared according to literature.[3] 1,8-Diazabicyclo[5.4.0]undec-7-ene (DBU, Alfa Aesar, 99%) was distilled from CaH_2, diluted with anhydrous THF to 1.5 M, and transferred to glass ampoules that were then flame sealed. CH_2Cl_2, toluene, and THF were dried by passing through an activated alumina column (PureSolv, Innovative Technology Inc.). CH_2Cl_2 used for the synthesis of poly(D,L-lactide) was subsequently distilled from CaH_2. Methanol (MeOH, Fisher Scientific, 99%), *n*-hexanes (Fisher Scientific, 99%), ethyl vinyl ether (EVE, Fisher Scientific, 99%), and trifluoroacetic acid (TFA, Fisher Scientific, 97%) were used as received. Deuterated solvents were purchased from Cambridge Isotope Laboratories and used as received.

2.9.2 Characterization

Multi-angle light scattering size-exclusive chromatography (SEC-MALS) was performed using two Agilent PLgel MIXED-B 300 × 7.5 mm columns with 10 μm beads, connected to an Agilent 1260 Series pump, a Wyatt 18-angle DAWN HELEOS light scattering detector, and Optilab rEX differential refractive index detector using THF as the mobile phase. Online determination of d*n*/d*c* assumed 100% mass elution under the peak of interest. Size-

exclusion chromatography was also performed on a Waters instrument using a refractive index detector (dRI) and Agilent PL gel 5 μm MiniMIX-D column. THF at 35 °C was used as the mobile phase with a flow rate of 1.0 mL min^{-1}. Molar mass dispersity ($Đ$) was determined against narrow PS standards (Agilent). ^{1}H NMR spectra were collected on a 600 MHz Varian VNMRS. Spectra of macromonomers and bottlebrushes were collected in $CDCl_3$ and CD_2Cl_2, respectively, at a polymer concentration of 50 – 70 mg mL^{-1} with 128 scans and a pulse delay time of 10 s.

SAXS measurements were performed at beamline 5-ID-D DND-CAT at the Advanced Photon Source (APS) at Argonne National Laboratory (Argonne, Illinois). The beamline was configured with an X-ray wavelength of 0.729 Å. A silver behenate standard was used to calibrate the sample-to-detector distance to 8510 mm. 2D data were reduced by azimuthal averaging to give $I(q)$, where I is intensity in arbitrary units, $q = |\boldsymbol{q}| = 4\pi\lambda^{-1} \sin(\theta/2)$ is the magnitude of the scattering wave vector, λ is the wavelength of incident beam, and θ is the scattering angle.

2.9.3 Macromonomers

Scheme 2.1. Representative Procedure for the Synthesis of Norbornene-poly(D,L-lactide) (PLA-MM-12)

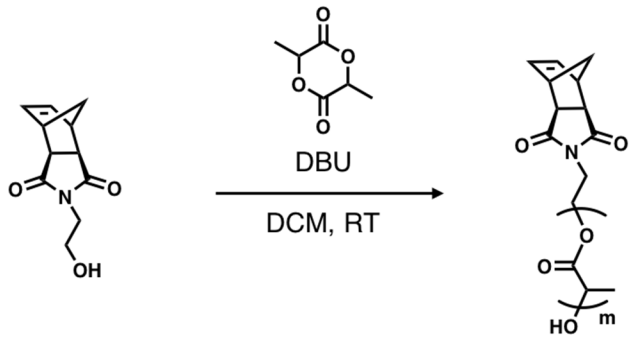

In a nitrogen filled glovebox, 10.00 g D,L-lactide (69.4 mmol, 108 equiv), 133 mg NbOH (0.64 mmol, 1 equiv) were combined in an oven-dried flask with a stir bar, followed by the addition of 110 mL CH_2Cl_2. The mixture was stirred for 10 min to ensure complete dissolution. Then 0.43 mL of DBU (1.5 M in THF, 0.64 mmol, 1 equiv) was added. After 25 minutes, the reaction was quenched with 300 mg benzoic acid (2.45 mmol, 3.8 equiv). An aliquot was pulled to determine the monomer conversion by ^{1}H NMR (83%). The solvent volume was reduced by one half *in vacuo*, 0.1 mL of trifluoroacetic acid (1.28 mmol, 2 equiv) was added with stirring, and the solution then immediately precipitated into 800 mL of cold MeOH. The MeOH was then decanted. The solid product was redissolved in DCM and the precipitation repeated two more times. The resulting PLA was dried *in vacuo*. ^{1}H NMR (600 MHz, $CDCl_3$): δ (ppm) 6.28 (br t, 2H), 5.25–5.02 (m, 175H), 4.40–4.21 (m, 3H), 3.84–3.68 (m, 2H) 3.27 (s, 2H), 2.70 (m, 2H), 1.73–1.39 (m, 533H). M_n (^{1}H NMR) = 13 kg mol^{-1}. SEC (dRI, PS standards): M_n = 19 kg mol^{-1}, M_w/M_n = 1.06.

Scheme 2.2. Representative Procedure for the Synthesis of Norbornene-poly(4-methylcaprolactone) (P4MCL-MM-11)

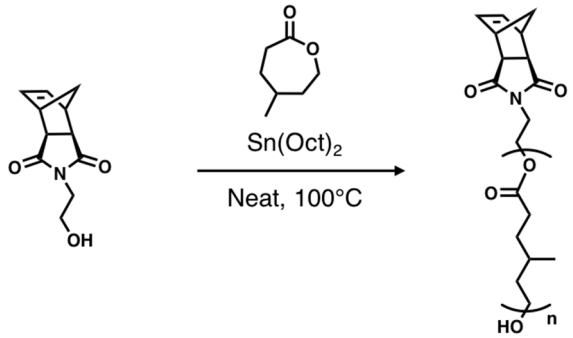

In a nitrogen filled glovebox, 20.00 g 4MCL (156.0 mmol, 218.5 equiv), 148 mg NbOH (0.71 mmol, 1 equiv) and 25 μL of $Sn(Oct)_2$ (0.078 mmol, 0.11 equiv) were combined in an oven-dried heavy wall pressure vessel with a stir bar. The vessel was sealed with a threaded

PTFE bushing using a perfluoro O-ring and removed from the glovebox. The vessel was placed in an oil bath at 100 °C and stirred for 4.5 h. After removal from the oil bath, the vessel was immediately quenched in an ice water bath. An aliquot was pulled to determine the monomer conversion by ^{1}H NMR (42%). The reaction mixture was diluted with CH_2Cl_2 and precipitated into 800 mL of MeOH at −78 °C. The MeOH was decanted. The solid product was redissolved in DCM and the precipitation repeated two more times in MeOH and once more in *n*-hexanes. The resulting P4MCL was dried *in vacuo*. ^{1}H NMR (600 MHz, $CDCl_3$) δ = 6.28 (br t, 2H), 4.17−4.00 (m, 174H), 3.76−3.60 (m, 4H), 3.29−3.22 (s, 2H), 2.70 (s, 2H), 2.47−2.07 (m, 180H), 1.74−1.61 (m, 180H), 1.61−1.37 (m, 271H), 1.06−0.76 (m, 271H), 4.40−4.21 (m, 4H), 3.84−3.68 (m, 2H) 3.27 (s, 2H), 2.70 (m, 2H), 1.73−1.39 (m, 533H). M_n (^{1}H NMR) = 11 kg mol^{-1}. SEC (dRI, polystyrene standards): M_n = 19 kg mol^{-1}, M_w/M_n = 1.09.

2.9.4 Block Bottlebrushes

General Procedure for the ROMP of Block Bottlebrush Copolymers

Scheme 2.3. Synthesis of block bottlebrush copolymers.

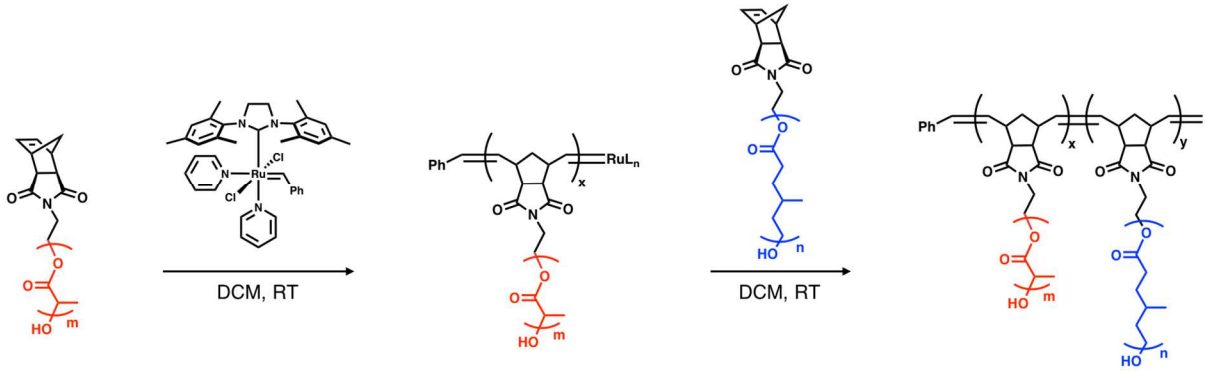

In a nitrogen filled glovebox, stock solutions of the macromonomers were prepared in CH_2Cl_2 (200 mg/mL). In another vial a stock solution of the G3 catalyst was prepared in CH_2Cl_2 (3.5 mg/mL). A 20 mL vial was charged with a stir bar and 0.46 mL of the PLA stock

solution. While stirring vigorously, an appropriate amount of the G3 stock solution was then added. After 30 min, 0.37 mL of the P4MCL stock solution was added. After 30 min, several drops of ethyl vinyl ether were added and the solution was stirred for 30 min. Cold MeOH was added until solid bottlebrush polymer precipitated. The MeOH was decanted and the resulting product dried *in vacuo.*

2.9.5 Statistical Bottlebrushes

General Procedure for the ROMP of Statistical Bottlebrush Copolymers

Scheme 2.4. Synthesis of statistical bottlebrush copolymers.

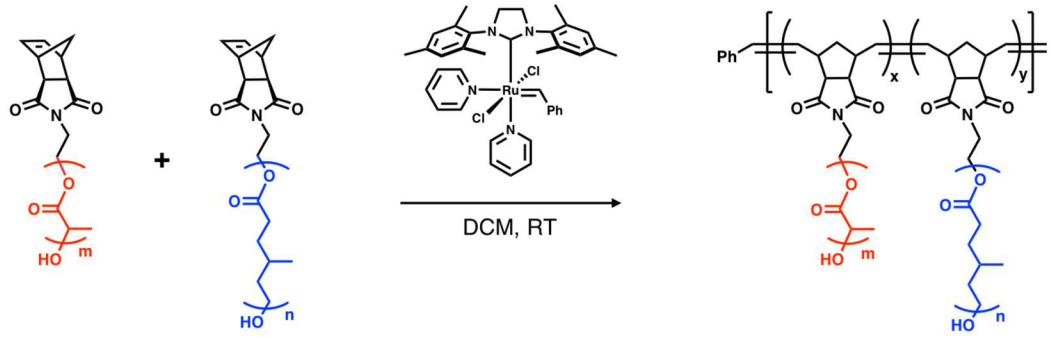

In a nitrogen filled glovebox, stock solutions of the macromonomers were prepared in CH_2Cl_2 (200 mg/mL). In another vial, a stock solution of the G3 catalyst was prepared in CH_2Cl_2 (3.5 mg/mL). A 20 mL vial was charged with a stir bar, 0.46 mL of the PLA stock solution, and 0.37 mL of the P4MCL stock solution. While stirring vigorously, an appropriate amount of the G3 stock solution was then added. After 30 min, several drops of ethyl vinyl ether were added and the solution was stirred for 30 min. Cold MeOH was added until solid bottlebrush polymer precipitated. The MeOH was decanted and the resulting product dried *in vacuo*.

2.10 References

(1) Bates, C. M.; Bates, F. S. 50th Anniversary Perspective: Block Polymers-Pure Potential. *Macromolecules* **2017**, *50* (1), 3–22.

(2) Bates, F. S.; Fredrickson, G. H. Block Copolymers-Designer Soft Materials. *Phys. Today* **1999**, *52* (2), 32–38.

(3) Bates, F. S.; Hillmyer, M. A.; Lodge, T. P.; Bates, C. M.; Delaney, K. T.; Fredrickson, G. H. Multiblock Polymers: Panacea or Pandora's Box? *Science* **2012**, *336* (6080), 434–440.

(4) Ruzette, A. V.; Leibler, L. Block Copolymers in Tomorrow's Plastics. *Nat. Mater.* **2005**, *4* (1), 19–31.

(5) Kim, H.-C.; Park, S.-M.; Hinsberg, W. D. Block Copolymer Based Nanostructures: Materials, Processes, and Applications to Electronics. *Chem. Rev.* **2010**, *110* (1), 146–177.

(6) Kataoka, K.; Harada, A.; Nagasaki, Y. Block Copolymer Micelles for Drug Delivery: Design, Characterization and Biological Significance. *Adv. Drug Deliv. Rev.* **2012**, *64* (1), 37–48.

(7) Lin, T.; Chang, A. B.; Luo, S.; Chen, H.; Lee, B.; Grubbs, R. H. Effects of Grafting Density on Block Polymer Self-Assembly: From Linear to Bottlebrush. *ACS Nano* **2017**, *11* (11), 11632–11641.

(8) Sveinbjornsson, B. R.; Weitekamp, R. A.; Miyake, G. M.; Xia, Y.; Atwater, H. A.; Grubbs, R. H. Rapid Self-Assembly of Brush Block Copolymers to Photonic Crystals. *Proc. Natl. Acad. Sci.* **2012**, *109* (36), 14332–14336.

(9) Vatankhah-Varnosfaderani, M.; Keith, A. N.; Cong, Y.; Liang, H.; Rosenthal, M.;

Sztucki, M.; Clair, C.; Magonov, S.; Ivanov, D. A.; Dobrynin, A. V.; Sheiko, S. S. Chameleon-like Elastomers with Molecularly Encoded Strain-Adaptive Stiffening and Coloration. *Science* **2018**, *359* (6383), 1509–1513.

(10) Bates, C. M.; Chang, A. B.; Schulze, M. W.; Momčilovic, N.; Jones, S. C.; Grubbs, R. H. Brush Polymer Ion Gels. *J. Polym. Sci. Part B Polym. Phys.* **2016**, *54* (2), 292–300.

(11) Vatankhah-Varnoosfaderani, M.; Daniel, W. F. M.; Zhushma, A. P.; Li, Q.; Morgan, B. J.; Matyjaszewski, K.; Armstrong, D. P.; Spontak, R. J.; Dobrynin, A. V.; Sheiko, S. S. Bottlebrush Elastomers: A New Platform for Freestanding Electroactuation. *Adv. Mater.* **2017**, *29*, 1604209.

(12) Sun, G.; Cho, S.; Clark, C.; Verkhoturov, S. V.; Eller, M. J.; Li, A.; Pavía-Jiménez, A.; Schweikert, E. A.; Thackeray, J. W.; Trefonas, P.; Wooley, K. L. Nanoscopic Cylindrical Dual Concentric and Lengthwise Block Brush Terpolymers as Covalent Preassembled High-Resolution and High-Sensitivity Negative-Tone Photoresist Materials. *J. Am. Chem. Soc.* **2013**, *135* (11), 4203–4206.

(13) Cheng, L.; Gadelrab, K. R.; Kawamoto, K.; Yager, K. G.; Johnson, J. A.; Alexander-Katz, A.; Ross, C. A. Templated Self-Assembly of a PS-Branch-PDMS Bottlebrush Copolymer. *Nano Lett.* **2018**, *18* (7), 4360–4369.

(14) Fenyves, R.; Schmutz, M.; Horner, I. J.; Bright, F. V.; Rzayev, J. Aqueous Self-Assembly of Giant Bottlebrush Block Copolymer Surfactants as Shape-Tunable Building Blocks. *J. Am. Chem. Soc.* **2014**, *136* (21), 7762–7770.

(15) Lu, X.; Tran, T. H.; Jia, F.; Tan, X.; Davis, S.; Krishnan, S.; Amiji, M. M.; Zhang, K. Providing Oligonucleotides with Steric Selectivity by Brush-Polymer-Assisted Compaction. *J. Am. Chem. Soc.* **2015**, *137* (39), 12466–12469.

(16) Johnson, J. A.; Lu, Y. Y.; Burts, A. O.; Xia, Y.; Durrell, A. C.; Tirrell, D. A.; Grubbs, R. H. Drug-Loaded, Bivalent-Bottle-Brush Polymers by Graft-through ROMP. *Macromolecules* **2010**, *43* (24), 10326–10335.

(17) Iatrou, H.; Hadjichristidis, N. Synthesis of a Model 3-Miktoarm Star Terpolymer. *Macromolecules* **1992**, *25* (18), 4649–4651.

(18) Xie, N.; Li, W.; Qiu, F.; Shi, A. C. σ Phase Formed in Conformationally Asymmetric AB-Type Block Copolymers. *ACS Macro Lett.* **2014**, *3* (9), 909–910.

(19) Shi, W.; Lynd, N. A.; Montarnal, D.; Luo, Y.; Fredrickson, G. H.; Kramer, E. J.; Ntaras, C.; Avgeropoulos, A.; Hexemer, A. Toward Strong Thermoplastic Elastomers with Asymmetric Miktoarm Block Copolymer Architectures. *Macromolecules* **2014**, *47* (6), 2037–2043.

(20) *Miktoarm Star Polymers: From Basics of Branched Architecture to Synthesis, Self-Assembly and Applications*; Kakkar, A., Ed.; The Royal Society of Chemistry, 2017.

(21) Love, J. A.; Morgan, J. P.; Trnka, T. M.; Grubbs, R. H. A Practical and Highly Active Ruthenium-Based Catalyst That Effects the Cross Metathesis of Acrylonitrile. *Angew. Chem. Int. Ed.* **2002**, *41* (21), 4035–4037.

(22) Roe, R.-J. *Methods of X-Ray and Neutron Scattering in Polymer Science*; Oxford University Press: New York, 2000.

(23) Watts, A.; Kurokawa, N.; Hillmyer, M. A. Strong, Resilient, and Sustainable Aliphatic Polyester Thermoplastic Elastomers. *Biomacromolecules* **2017**, *18* (6), 1845–1854.

(24) Dalsin, S. J.; Rions-Maehren, T. G.; Beam, M. D.; Bates, F. S.; Hillmyer, M. A.; Matsen, M. W. Bottlebrush Block Polymers: Quantitative Theory and Experiments. *ACS Nano* **2015**, *9* (12), 12233–12245.

(25) Anderson, K. S.; Hillmyer, M. A. Melt Chain Dimensions of Polylactide. *Macromolecules* **2004**, *37* (5), 1857–1862.

(26) Düchs, D.; Delaney, K. T.; Fredrickson, G. H. A Multi-Species Exchange Model for Fully Fluctuating Polymer Field Theory Simulations. *J. Chem. Phys.* **2014**, *141* (17), 174103.

(27) Drolet, F.; Fredrickson, G. H. Optimizing Chain Bridging in Complex Block Copolymers. *Macromolecules* **2001**, *34* (15), 5317–5324.

(28) Matsen, M. W.; Thompson, R. B. Equilibrium Behavior of Symmetric ABA Triblock Copolymer Melts. *J. Chem. Phys.* **1999**, *111* (15), 7139–7146.

(29) Kawamoto, K.; Zhong, M.; Gadelrab, K. R.; Cheng, L. C.; Ross, C. A.; Alexander-Katz, A.; Johnson, J. A. Graft-through Synthesis and Assembly of Janus Bottlebrush Polymers from A-Branch-B Diblock Macromonomers. *J. Am. Chem. Soc.* **2016**, *138* (36), 11501–11504.

(30) Xia, Y.; Olsen, B. D.; Kornfield, J. A.; Grubbs, R. H. Efficient Synthesis of Narrowly Dispersed Brush Copolymers and Study of Their Assemblies: The Importance of Side Chain Arrangement. *J. Am. Chem. Soc.* **2009**, *131* (51), 18525–18532.

(31) Gu, W.; Huh, J.; Hong, S. W.; Sveinbjornsson, B. R.; Park, C.; Grubbs, R. H.; Russell, T. P. Self-Assembly of Symmetric Brush Diblock Copolymers. *ACS Nano* **2013**, *7* (3), 2551–2558.

(32) Jha, S.; Dutta, S.; Bowden, N. B. Synthesis of Ultralarge Molecular Weight Bottlebrush Polymers Using Grubbs' Catalysts. *Macromolecules* **2004**, *37* (12), 4365–4374.

(33) Runge, M. B.; Bowden, N. B. Synthesis of High Molecular Weight Comb Block Copolymers and Their Assembly into Ordered Morphologies in the Solid State. *J. Am.*

Chem. Soc. **2007**, *129* (34), 10551–10560.

(34) Li, Z.; Ma, J.; Lee, N. S.; Wooley, K. L. Dynamic Cylindrical Assembly of Triblock Copolymers by a Hierarchical Process of Covalent and Supramolecular Interactions. *J. Am. Chem. Soc.* **2011**, *133* (5), 1228–1231.

(35) Su, L.; Heo, G. S.; Lin, Y.; Dong, M.; Zhang, S.; Chen, Y.; Sun, G.; Wooley, K. L. Syntheses of Triblock Bottlebrush Polymers Through Sequential ROMPs : Expanding the Functionalities of Molecular Brushes. *J. Polym. Sci. Part A Polym. Chem.* **2017**, *55*, 2966–2970.

(36) Xia, Y.; Grubbs, R. H. Efficient Syntheses of Brush Polymers via Living Ring Opening Metathesis Polymerization of Macromonomers. *Macromolecules* **2009**, *50* (2), 197–198.

(37) Lin, T.-P.; Chang, A. B.; Luo, S.-X.; Chen, H.-Y.; Lee, B.; Grubbs, R. H. Effects of Grafting Density on Block Polymer Self-Assembly: From Linear to Bottlebrush. *ACS Nano* **2017**, *11* (11), 11632–11641.

(38) Lin, T. P.; Chang, A. B.; Chen, H. Y.; Liberman-Martin, A. L.; Bates, C. M.; Voegtle, M. J.; Bauer, C. A.; Grubbs, R. H. Control of Grafting Density and Distribution in Graft Polymers by Living Ring-Opening Metathesis Copolymerization. *J. Am. Chem. Soc.* **2017**, *139* (10), 3896–3903.

(39) Widin, J. M.; Schmitt, A. K.; Schmitt, A. L.; Im, K.; Mahanthappa, M. K. Unexpected Consequences of Block Polydispersity on the Self-Assembly of ABA Triblock Copolymers. *J. Am. Chem. Soc.* **2012**, *134* (8), 3834–3844.

(40) Lutz, J.-F.; Ouchi, M.; Liu, D. R.; Sawamoto, M. Sequence-Controlled Polymers. *Science* **2013**, *341*, 1238149.

(41) Milner, S. T. Chain Architecture and Asymmetry in Copolymer Microphases. *Macromolecules* **1994**, *27* (8), 2333–2335.

(42) Grason, G. M.; Kamien, R. D. Interfaces in Diblocks: A Study of Miktoarm Star Copolymers. *Macromolecules* **2004**, *37* (19), 7371–7380.

(43) Tselikas, Y.; Iatrou, H.; Hadjichristidis, N.; Liang, K. S.; Mohanty, K.; Lohse, D. J. Morphology of Miktoarm Star Block Copolymers of Styrene and Isoprene. *J. Chem. Phys.* **1996**, *105* (6), 2456–2462.

(44) Shibuya, Y.; Nguyen, H. V. T.; Johnson, J. A. Mikto-Brush-Arm Star Polymers via Cross-Linking of Dissimilar Bottlebrushes: Synthesis and Solution Morphologies. *ACS Macro Lett.* **2017**, *6* (9), 963–968.

(45) Burts, A. O.; Gao, A. X.; Johnson, J. A. Brush-First Synthesis of Core-Photodegradable Miktoarm Star Polymers via ROMP: Towards Photoresponsive Self-Assemblies. *Macromol. Rapid Commun.* **2014**, *35* (2), 168–173.

(46) Golder, M. R.; Nguyen, H. V; Oldenhuis, N. J.; Grundler, J.; Park, E. J.; Johnson, J. A. Brush-First and ROMP-Out with Functional (Macro)Monomers: Method Development, Structural Investigations, and Applications of an Expanded Brush-Arm Star Polymer Platform. *Macromolecules* **2018**, *51* (23), 9861–9870.

(47) Liu, J.; Burts, A. O.; Li, Y.; Zhukhovitskiy, A. V.; Ottaviani, M. F.; Turro, N. J.; Johnson, J. A. "Brush-First" Method for the Parallel Synthesis of Photocleavable, Nitroxide-Labeled Poly(Ethylene Glycol) Star Polymers. *J. Am. Chem. Soc.* **2012**, *134* (39), 16337–16344.

(48) Liao, L.; Liu, J.; Dreaden, E. C.; Morton, S. W.; Shopsowitz, K. E.; Hammond, P. T.; Johnson, J. A. A Convergent Synthetic Platform for Single-Nanoparticle Combination

Cancer Therapy: Ratiometric Loading and Controlled Release of Cisplatin, Doxorubicin, and Camptothecin. *J. Am. Chem. Soc.* **2014**, *136* (16), 5896–5899.

(49) Barnes, J. C.; Bruno, P. M.; Nguyen, H. V. T.; Liao, L.; Liu, J.; Hemann, M. T.; Johnson, J. A. Using an RNAi Signature Assay to Guide the Design of Three-Drug-Conjugated Nanoparticles with Validated Mechanisms, in Vivo Efficacy, and Low Toxicity. *J. Am. Chem. Soc.* **2016**, *138* (38), 12494–12501.

(50) Nguyen, H. V; Chen, Q.; Paletta, J. T.; Harvey, P.; Jiang, Y.; Zhang, H.; Boska, M. D.; Ottaviani, M. F.; Jasano, A.; Rajca, A.; Johnson, J. A. Nitroxide-Based Macromolecular Contrast Agents with Unprecedented Transverse Relaxivity and Stability for Magnetic Resonance Imaging of Tumors. *ACS Cent. Sci.* **2017**, *3* (7), 800–811.

(51) Nguyen, H. V; Detappe, A.; Gallagher, N. M.; Zhang, H.; Harvey, P.; Yan, C.; Mathieu, C.; Golder, M. R.; Jiang, Y.; Ottaviani, M. F.; Jasano, A.; Rajca, A.; Ghobrial, I.; Ghoroghchian, P. P.; Johnson, J. A. Triply Loaded Nitroxide Brush-Arm Star. *ACS Nano* **2018**, *12* (11), 11343–11354.

(52) Nguyen, H. V; Ehrlich, D. C.; Huh, S. J.; Vangamudi, B.; Economides, K. D.; Neenan, A. M.; Ackley, J. C.; Baddour, J.; Paramasivan, S.; Brady, S. W.; Held, E. J.; Reiter, L. A.; Saucier-sawyer, J. K.; Kopesky, P. W.; Chickering, D. E.; Blume-jensen, P.; Johnson, J. A. Reduction of Liver Fibrosis by Rationally Designed Macromolecular Telmisartan Prodrugs. *Nat. Biomed. Eng.* **2018**, *2*, 822–830.

(53) Sowers, M. A.; Mccombs, J. R.; Wang, Y.; Paletta, J. T.; Morton, S. W.; Dreaden, E. C.; Boska, M. D.; Ottaviani, M. F.; Hammond, P. T.; Rajca, A.; Johnson, J. A. Redox-Responsive Branched-Bottlebrush Polymers for in Vivo MRI and Fluorescence Imaging. *Nat. Commun.* **2014**, *5*, 5460.

(54) Dalsin, S. J.; Hillmyer, M. A.; Bates, F. S. Molecular Weight Dependence of Zero-Shear Viscosity in Atactic Polypropylene Bottlebrush Polymers. *ACS Macro Lett.* **2014**, *3* (5), 423–427.

(55) Pesek, S. L.; Li, X.; Hammouda, B.; Hong, K.; Verduzco, R. Small-Angle Neutron Scattering Analysis of Bottlebrush Polymers Prepared via Grafting-through Polymerization. *Macromolecules* **2013**, *46* (17), 6998–7005.

(56) Guo, Z.; Le, A. N.; Feng, X.; Choo, Y.; Liu, B.; Wang, D.; Wan, Z.; Gu, Y.; Zhao, J.; Li, V.; Osuji, C. O.; Johnson, J. A.; Zhong, M. Janus Graft Block Copolymers: Design of Polymer Architecture for Independently Tuned Nanostructures and Polymer Properties. *Angew. Chem. Int. Ed.* **2018**, *57*, 8493–8497.

Chapter 3. Efficient Synthesis of Asymmetric Miktoarm Star Polymers[1]

3.1 Background

Block copolymers (BCPs) are important in a variety of emerging and established applications due to their self-assembly into well-ordered structures on the nanometer length scale.[1] The phase behavior of linear BCPs with two chemically-distinct blocks arrayed in simple sequences (AB, ABA, …) is now well-understood from both experiments[2–4] and theory[5–8] to depend on the Flory–Huggins interaction parameter (χ), volumetric degree of polymerization (N), block volume fractions (f_i, i = A, B), and conformational asymmetry (ε). These molecular design parameters dictate the self-assembly of two-component BCPs into a handful of classical phases[4] (body-centered cubic spheres, hexagonally close-packed cylinders, a gyroid network, lamellae) and more exotic sphere packings[9–11] (e.g., σ, C14, C15, and A15). While the utility of many such mesophases is indisputable, linear chain connectivity imposes structure–property constraints that are not always desirable. For example, the number of known morphologies remains small,[12] domain periodicities are fairly restricted (typically within a range circa 5–100 nm),[13,14] and the coupling between volume fraction (f) and morphology favors the majority block on the convex side of curved block–block interfaces.[5,15] These (and other) limitations have motivated the search for new molecular design tools that broaden the utility of BCP self-assembly in contemporary applications.

[1] This chapter was originally published in *Macromolecules*. Reproduced with permission from *Macromolecules* 2020, 53, 702-710. Copyright 2020, American Chemical Society.

An exciting opportunity that expands the confines of traditional polymer phase behavior[16] lies in the controlled synthesis of BCPs with branched architectures.[17,18] The introduction of branching imparts useful thermodynamic,[19] photonic,[20,21] and mechanical[22] properties that are otherwise inaccessible with linear analogues. One archetypal example is miktoarm star polymers,[23–32] which are defined[33] as two or more chemically-distinct blocks connected to a common junction (e.g., A_mB_n, $m + n > 2$). The miktoarm star architecture is known or predicted to stabilize new phases,[9,15,34] reduce domain spacing,[35] and manipulate melt[25,26,36,37] or solution[38–40] properties, making them attractive for applications such as lithography and drug delivery. A further subset of miktoarm star polymers that accentuates the role of architecture in self-assembly involves asymmetry in arm number ($m \neq n$); here, we focus on the limit $m = 1$, e.g., AB_n. As result of arm asymmetry, bulk phase boundaries are significantly deflected towards larger values of the A-block volume fraction (f_A).[5,15] This effect has been beautifully exploited by Lynd[41] and Shi[42] to design new thermoplastic elastomers ($A(BA')_n$) that are stronger, stiffer, and tougher than commercial ABA linear triblock copolymers.

Despite the importance of miktoarm star polymers in contemporary polymer science, their synthesis still remains a major challenge. The standard approach to generate precise connectivity at a common junction uses some combination of "grafting-from" and "grafting-to" multi-step reaction schemes.[43] The need for orthogonal reactivity, high yields, and designer core molecules requires tedious synthetic routes that often include time-consuming coupling, polymerization, (de)protection, and purification steps such as fractional precipitation and high performance liquid chromatography.[36,44,45] For example, the materials studied by Shi and coworkers[42] necessitated reaction times in excess of 30 days to push coupling to high

conversion and still required purification via fractionation.[45–47] Moreover, changing the number of arms is non-trivial since a new core starting material must be selected each time.

Motivated by the difficulty of traditional miktoarm star polymer syntheses, we recently exploited the versatility, speed, and efficiency of Grubbs-type ring-opening metathesis polymerization (ROMP)[48–57] to synthesize miktoarm star polymers via the grafting-through copolymerization of two different macromonomers at low backbone degrees of polymerization (N_{BB}).[58] This type of statistical copolymerization is remarkably well controlled and the short backbone behaves physically like the core of a star polymer at $N_{BB} \lesssim 12$ as evidenced by experiments and theory. However, simple copolymerization trades molecular precision for synthetic versatility since the reaction stoichiometry can only control the *average* number of arms and molecular composition. As a result, bulk phase behavior is dominated by dispersity effects that counteract phase boundary deflection, even in the case of nominally asymmetric architectures. Copolymerization therefore cannot generate the unique phase behavior that distinguishes asymmetric miktoarm stars from traditional block copolymers.

Here, we introduce a new synthetic method termed μSTAR (**Table 3.1**, top) — Miktoarm Synthesis by Termination After Ring-opening metathesis polymerization — that efficiently generates asymmetric miktoarm star polymers using ruthenium-catalyzed macromonomer polymerization ($B \rightarrow B_n$) followed by *in-situ* enyne-mediated termination[59] to install the single A arm ($B_n \rightarrow AB_n$). μSTAR sits at an optimal synthetic intersection, combining the versatility and speed of a macromonomer approach using ROMP with the precision of a highly efficient coupling step. Using a handful of macromonomers and macroterminators as building blocks, a diverse library of miktoarm stars can be easily prepared with different numbers of arms and block chemistries. We highlight this modularity by

synthesizing AB_n and $A(BA')_n$ miktoarm star polymers comprising six different permutations of A and B block chemistry selected from poly(siloxane), poly(acrylate), poly(methacrylate), poly(ether), poly(ester), and poly(styrene). The average number of B arms (n) is easily controlled by the equivalents of Grubbs catalyst to macromonomer in the initial polymerization step. Importantly, the phase behavior of these polymers with disperse n exhibits significant phase boundary deflection, in agreement with self-consistent field theory (SCFT) simulations performed on precise (monodisperse n) analogues. A major implication of this finding is that the dispersity in n produced by μSTAR is advantageous from the perspective of significantly simplifying the synthesis of miktoarm star polymers while retaining the characteristic phase behavior that produces interesting bulk properties. The speed, efficiency, and broad scope of μSTAR establishes a compelling new synthetic platform for asymmetric miktoarm star polymers and supports the notion that low dispersity is not always better in block copolymer self-assembly.[60,61]

3.2 Synthesis of Macromonomers, Macroterminators, and Star Polymers

Two types of simple linear precursors are needed in the μSTAR process to create miktoarm polymers: a macromonomer with a single polymerizable end-group and a macroterminator that will irreversibly couple exactly once to the active chain ends. We focus on using Grubbs-type ring-opening metathesis polymerization (ROMP) to construct the junction due to its well-established functional group tolerance, fast reaction rates, and high yields.[65] Norbornene was therefore selected as the polymerizable group on the macromonomer because it undergoes efficient ROMP;[66] both homopolymer (B) and diblocks (BA′) will be discussed with norbornene installed on the B terminus. For the macroterminator, we exploit

enyne-mediated termination chemistry recently developed by Gutekunst and coworkers[59] to perform macromolecular coupling of living metathesis polymers.[67,68] While enyne macroterminators were previously shown to efficiently prepare diblocks, the sterics involved in coupling to the core of a star polymer present a unique challenge.[69] Nevertheless, the high reactivity of enynes makes them suitable for macromolecular couplings that would otherwise not be possible with traditional ROMP termination methods employing substituted vinyl ethers or symmetrical *cis*-olefins.[70–74] The generic end-groups used in μSTAR are illustrated in **Table 3.1** (top).

Table 3.1. (top) Generic μSTAR synthesis of miktoarm star polymers using norbornene-functionalized macromonomers and enyne macroterminators. (bottom) Macromonomers, macroterminators, and miktoarm star polymers synthesized in this work.

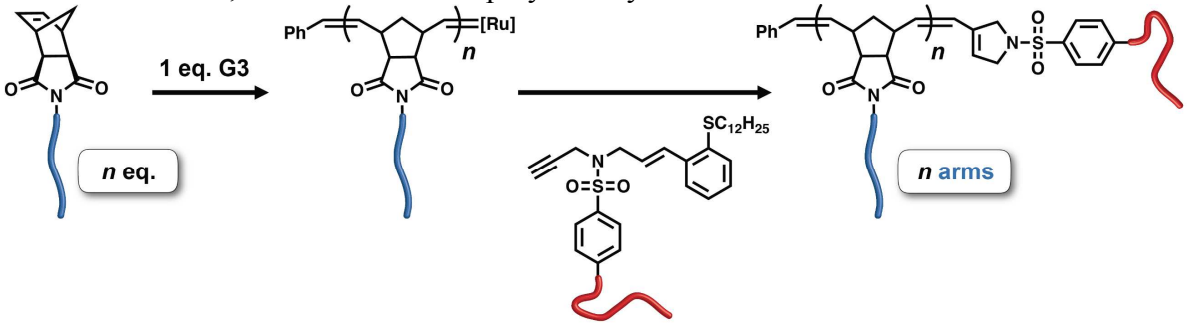

Macromonomer	Macroterminator	Miktoarm Star
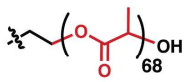	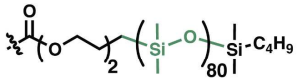	PLA_4-PDMS
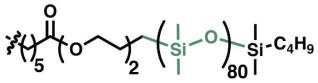	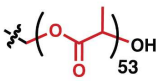	$PDMS_4$-PLA
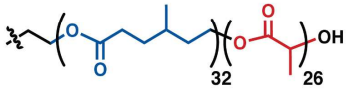	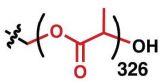	$(PLA\text{-}PMCL)_3$-PLA
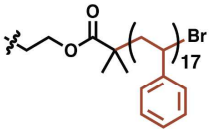	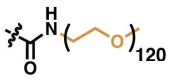	PS_4-PEO
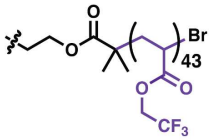	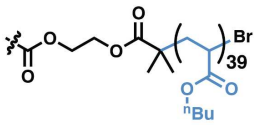	$PTFEA_4$-PnBA
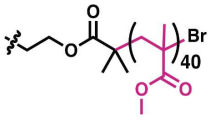	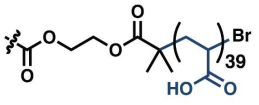	$PMMA_4$-PAA

Macromonomers with different B chemistry were synthesized by polymerization from functional norbornene initiators or coupling reactions between a norbornene acid and commercially available monotelechelic polymers. In summary, six different macromonomers were synthesized that span various classes of polymer chemistry: poly(lactide) (PLA),

poly(dimethylsiloxane) (PDMS), poly(4-methylcaprolactone–*block*–lactide) (PMCL-PLA), poly(styrene) (PS), poly(2-trifluoroethyl acrylate) (PTFEA), and poly(methyl methacrylate) (PMMA) (**Table 3.2)**. Similarly, six macroterminators (A) were prepared by coupling to or directly growing from the enyne terminator molecule (**Table 3.3**). PDMS, PLA, poly(ethylene oxide) (PEO), poly(*n*-butyl acrylate) (PnBA), and poly(*tert*-butyl acrylate) (PtBA) were chosen as the A block. The methyl ester enyne small molecule can be prepared in four high yielding steps and is further derivatized into the terminator of choice by one or two additional reactions.[59] **Table 3.1** (bottom) summarizes these materials; full synthetic details are provided in the experimental section (**Schemes 3.1–3.13**).

Table 3.2. Summary of macromonomer characterization data.

Macromonomer	$M_{n,NMR}$[a]	$M_{n,SEC\text{-}MALS}$[a,b]	$Đ$[b]
PLA-MM-5	5.2	4.3	1.01
PDMS-MM-6	5.6	6.3	1.01
PS-MM-2	2.1	2.1	1.03
P4MCL-MM-4	4.0	4.3	1.07
P4MCL-PLA-MM-4-3	6.6	6.2	1.02
PMMA-MM-4	3.7	4.3	1.05
PTFEA-MM-6	6.9	4.9*	1.16*

[a]In units of kg mol^{-1}. [b]Measured using size-exclusion chromatography with light scattering and differential refractive index detectors. *Determined using dRI detection in $CHCl_3$ relative to polystyrene standards.

Table 3.3. Summary of macroterminator characterization data.

Macroterminator	$M_{n,NMR}$[a]	$M_{n,SEC\text{-}MALS}$[a,b]	$Đ$[b]
PLA-MT-4	5.7	5.1	1.01
PLA-MT-24	23	24	1.02
PDMS-MT-6	5.9	6.3	1.02
PEO-MT-5	6.5	5.8	1.13
PnBA-MT-6	7.3	6.7	1.01
PtBA-MT-5	6.3	5.7	1.07

[a]In units of kg mol^{-1}. [b]Measured using size-exclusion chromatography with light scattering and differential refractive index detectors.

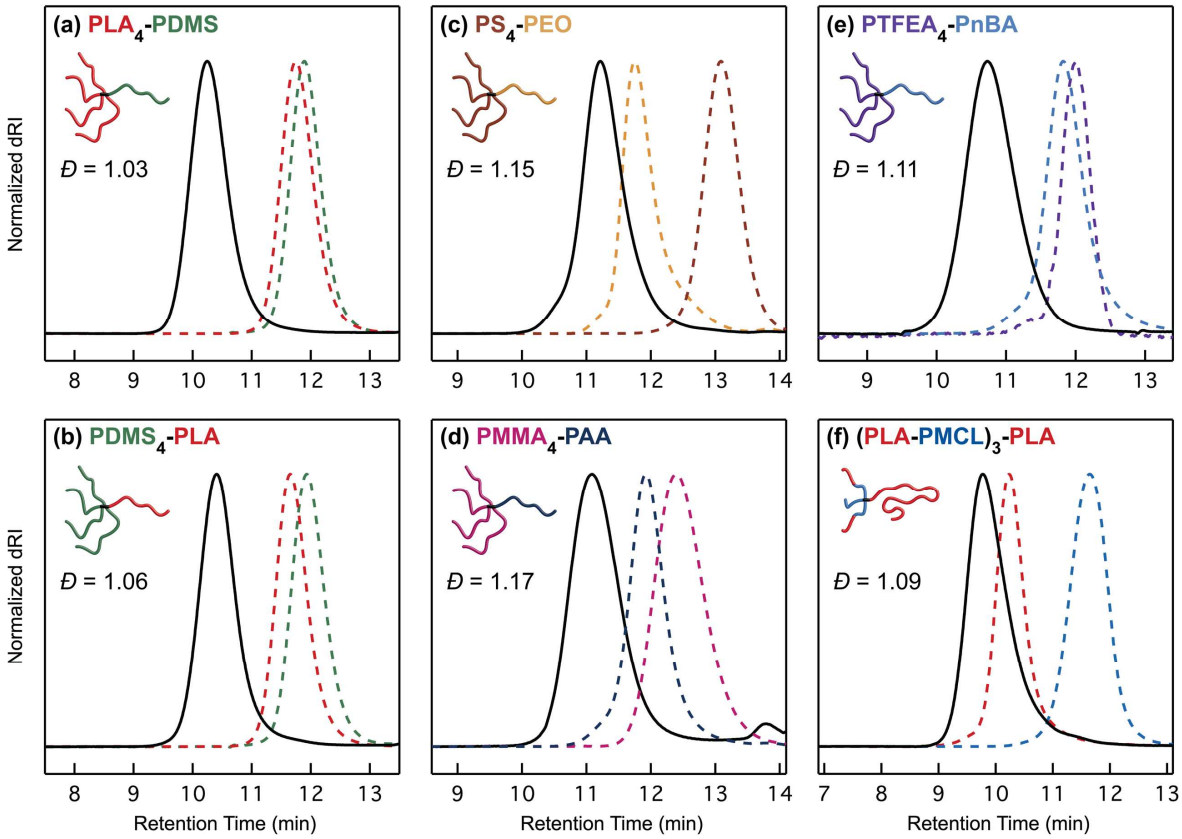

Figure 3.1. Size-exclusion chromatograms (normalized differential refractive index signal, dRI) of the miktoarm star polymers (solid black lines) listed in Table 1: **(a)** PLA_4-PDMS, **(b)** $PDMS_4$-PLA, **(c)** PS_4-PEO, **(d)** $PMMA_4$-PAA, **(e)** $PTFEA_4$-PnBA, and **(f)** $(PLA\text{-}PMCL)_3$-PLA. Macromonomers and macroterminators are depicted with dashed lines. See the experimental section (**Figures 3.11–3.19**) for traces of the poly(macromonomers), which were omitted here for clarity. In (d), the macroterminator trace represents poly(*tert*-butyl acrylate) before deprotection, while the final miktoarm star curve comprises poly(acrylic acid) after deprotection. Also note that the small bump near 14 min is small molecule elution. In (e), the

PTFEA macromonomer and PTFEA$_4$-PnBA samples have negative dn/dc values in THF; the dRI data were multiplied by –1 for the purpose of consistent presentation.

The efficacy of μSTAR at synthesizing asymmetric miktoarm star polymers is evident in **Figure 3.1**, which summarizes size-exclusion chromatograms (SECs) of the macromonomers (dashed lines), macroterminators (dashed lines), and resultant miktoarm star polymers (solid lines) for the combinations described in **Table 3.1**. The general process involves two steps that occur in one pot. (1) Polymerization of the macromonomer creates a short bottlebrush (N_{BB} < 12) with star-like physical properties[58] (*vide infra*); after complete conversion, an aliquot of the poly(macromonomer) is extracted. (2) *In situ* termination by the addition of macroterminator efficiently couples a single A arm to the living star polymer, resulting in AB$_n$ or A(BA′)$_n$ chain connectivity. SEC traces of the poly(macromonomers) are omitted from **Figure 3.1** for clarity but can be found in the experimental section (**Figures 3.11–3.19**). Note that with the exception of **Figure 3.1f**, n = 4 was targeted in this initial set of examples. Kinetic experiments performed with a model 5 kDa PLA macroterminator indicate the coupling process is finished in about 2 hours at room temperature (**Figure 3.2**).

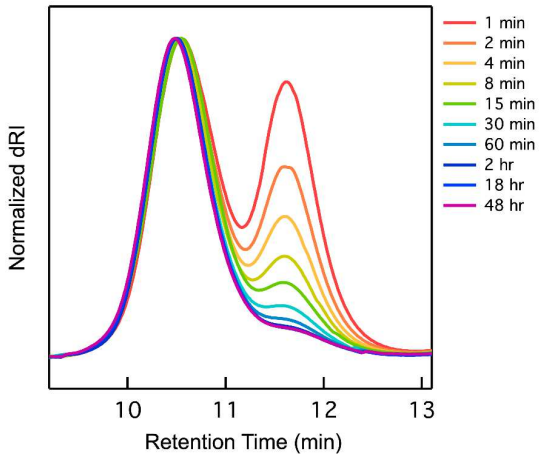

Figure 3.2. SECs (normalized differential refractive index signal) of (PDMS-MM-5)$_4$-PLA-MT-5 coupling kinetics. Time of 0 minutes corresponds to when the PLA-MT-5 was added. No change is observed after 2 hours.

After termination, the increase in poly(macromonomer) absolute molecular weight as measured with multi-angle light scattering (MALS) is consistent with the macroterminator size (**Table 3.4–3.5**). A single precipitation into methanol, diethyl ether, or hexanes is sufficient to isolate the final miktoarm star polymers, which have low molar mass dispersities ($Đ$ < 1.2, **Table 3.5**) and monomodal SEC traces (**Figure 3.1**). ^{1}H nuclear magnetic resonance (NMR) measurements further confirmed the stoichiometric coupling of macroterminator and poly(macromonomer) (**Figure 3.20–3.30**) and were also used to calculate compositions as tabulated in **Table 3.5**. Diffusion-ordered spectroscopy (DOSY) analysis as described in the experimental section revealed that these miktoarm star polymers lack homopolymer contamination within measurement error (**Tables 3.6–3.7, Figure 3.31–3.32**)[75] as attempts to determine the percent of homopolymer contamination with multi-component fits yielded inconsistent results and non-physical diffusion coefficients, which is evidence of data overfitting.[76]

Table 3.4. Summary of poly(macromonomer) characterization data.

Poly(macromonomers)	$M_{n,SEC\text{-}MALS}$[a,b]	$Đ$[b]	n[c]
$(PLA\text{-}MM\text{-}4)_4$	21	1.14	4.1
$(PDMS\text{-}MM\text{-}5)_4$	24	1.16	3.8
$(PMMA\text{-}MM\text{-}4)_4$	18	1.21	4.2
$(PTFEA\text{-}MM\text{-}6)_4$	14*	1.18	-
$(PS\text{-}MM\text{-}2)_4$	8.4	1.16	3.9
$(P4MCL\text{-}PLA\text{-}MM\text{-}4\text{-}3)_3$	17	1.32	2.9
$(P4MCL\text{-}PLA\text{-}MM\text{-}4\text{-}3)_5$	27	1.19	4.5
$(P4MCL\text{-}PLA\text{-}MM\text{-}4\text{-}3)_7$	42	1.16	7.1
$(P4MCL\text{-}PLA\text{-}MM\text{-}4\text{-}3)_9$	54	1.18	9.1

[a]In units of kg mol^{-1}. [b]Measured using size-exclusion chromatography with light scattering and differential refractive index detectors. [c]Determined from $M_{n,SEC\text{-}MALS}$ of the corresponding macromonomer. *Determined using dRI detection in $CHCl_3$ relative to polystyrene standards.

Table 3.5. Summary of miktoarm star polymer characterization data.

Miktoarm Star Polymer	$M_{n,NMR}$[a]	$M_{n,SEC\text{-}MALS}$[a,b]	$Đ$[b]	f_A[c]
(PLA-MM-5)$_4$-PDMS-MT-5	33	24	1.03	0.20
(PDMS-MM-5)$_4$-PLA-MT-4	30	28	1.06	0.14
(PMMA-MM-4)$_4$-PtBA-MT-5	29	22	1.13	0.25
(PMMA-MM-4)$_4$-PAA-MT-5	27	N/A**	1.17	0.13
(PTFEA-MM-6)$_4$-PnBA-MT-6	45	19*	1.11*	0.18
(PS-MM-2)$_4$-PEO-MT-5	14	15	1.15	0.33
(P4MCL-PLA-MM-4-3)$_3$-PLA-MT-24	50	39	1.09	0.71
(P4MCL-PLA-MM-4-3)$_5$-PLA-MT-24	55	46	1.05	0.68
(P4MCL-PLA-MM-4-3)$_7$-PLA-MT-24	66	54	1.09	0.62
(P4MCL-PLA-MM-4-3)$_9$-PLA-MT-24	75	64	1.14	0.58

[a]In units of kg mol^{-1}. [b]Measured using size-exclusion chromatography with light scattering and differential refractive index detectors. [c]Volume fraction of the macroterminator (A block) determined by NMR. [*]Determined using dRI detection in $CHCl_3$ relative to polystyrene standards. [**]Accurate molecular weight could not be determined from MALS.

Another advantage of μSTAR is the ability to easily vary the average number of B or BA′ arms by changing the equivalents of macromonomer to Grubbs initiator. A series of four A(BA′)$_n$ asymmetric miktoarm star polymers (A = PLA, BA′ = PMCL–*block*–PLA) with n = 3, 5, 7, or 9 arms was prepared simultaneously in separate reaction vessels using the same macromonomer and macroterminator precursors (**Figure 3.3**). SEC traces smoothly decrease in elution time as n increases, and absolute molecular weight measurements are consistent with increasing the average number of poly(macromonomer) arms across the range n = 3 – 9 (**Table 3.4**). This ability to easily vary the number of arms stands in stark contrast to all previous synthetic strategies where a different initiator or core must be synthesized whenever the number of arms is varied.[29,45,77] These materials also highlight the tolerance of μSTAR chemistry to high molecular weights; for n = 9, a 54 kDa poly(macromonomer) cleanly couples to a 24 kDa PLA macroterminator using only 1.1 equivalents of the latter.

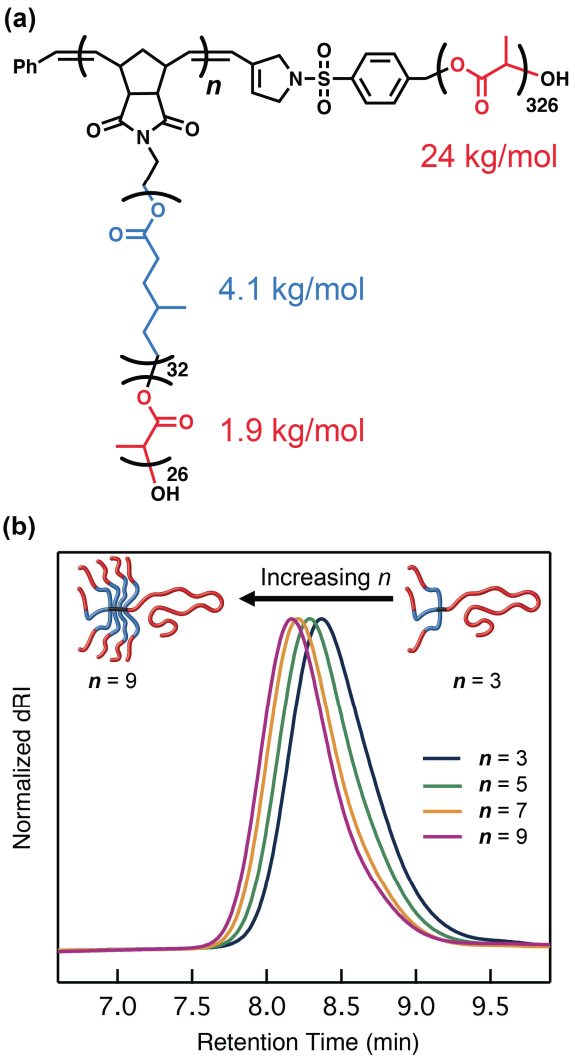

Figure 3.3. μSTAR can easily vary the average number of arms *n* in an asymmetric miktoarm star polymer. **(a)** Chemical structure of $(PLA\text{-}PMCL)_n$-PLA with $n = 3 - 9$. **(b)** Normalized differential refractive index signal from SEC analysis of the isolated miktoarm star polymers. See **Table 3.5** for a summary of molecular weights and dispersities.

3.3 Self-Assembly

A key question that remains is whether asymmetric miktoarm star polymers synthesized via μSTAR (with dispersity in *n*) self-assemble as predicted by theory for precise analogues. We have opted to study in detail the phase behavior of the $(PLA\text{-}PMCL)_n$-PLA samples described in **Figures 3.1** and **3.3** since the addition of a short A′ block flanking B is

predicted to further accentuate the phase boundary deflections that are characteristic of asymmetric AB_n miktoarm star polymers.[41]

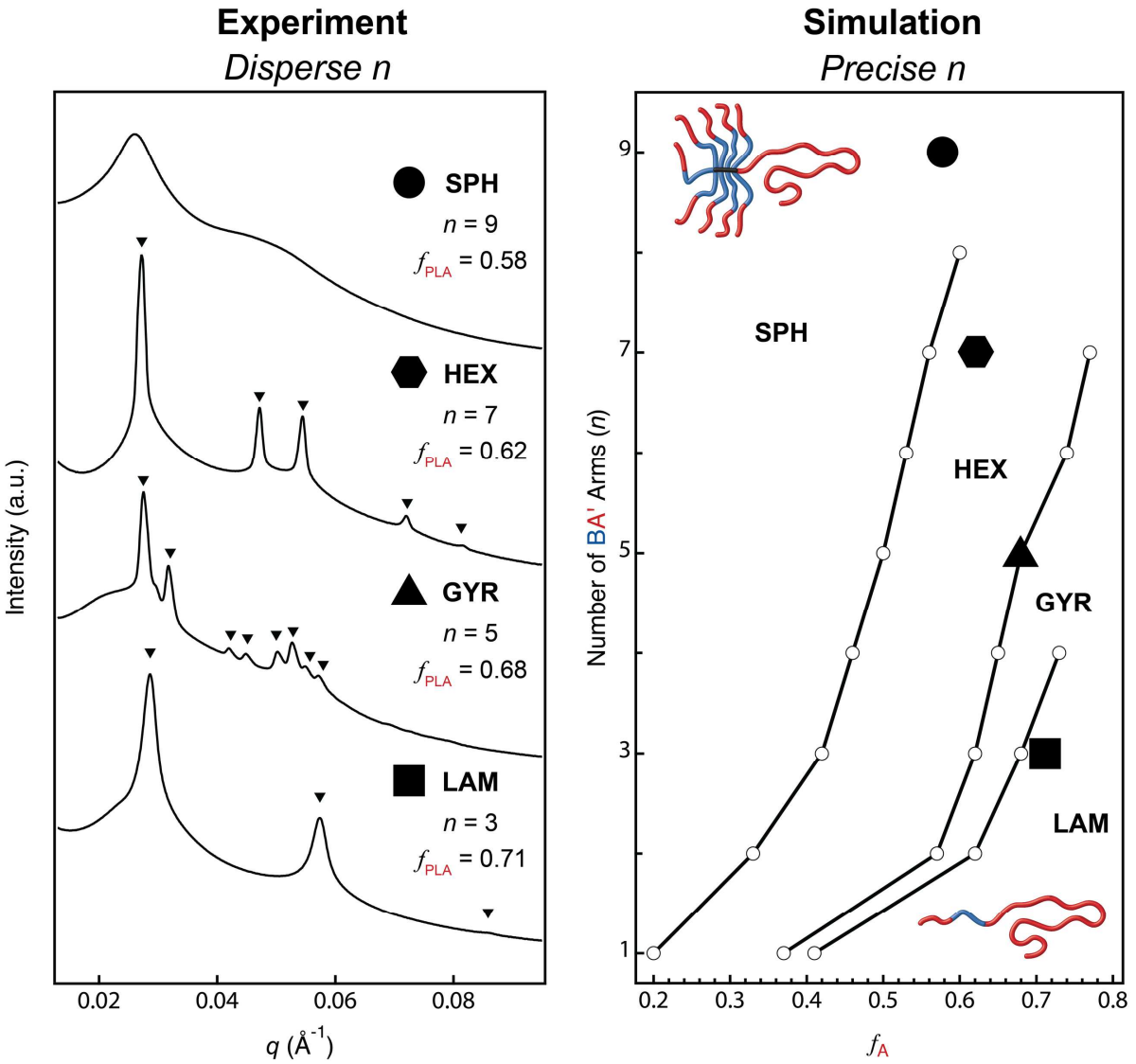

Figure 3.4. The phase behavior of $(PLA\text{-}PMCL)_n$-PLA miktoarm star polymers containing dispersity in n is consistent with simulations of precise analogues. *Left*: Small-angle X-ray scattering data with triangles demarcating the expected location of Bragg reflections for lamellar (LAM, $n = 3$), gyroid (GYR, $n = 5$), and hexagonally close-packed cylinder (HEX, $n = 7$) morphologies. *Right*: SCFT simulations at $\tau \equiv N_A/(N_A + N_{A'}) = 0.91$ relating morphology, PLA volume fraction (f_{PLA}), and the number of PMCL-PLA (BA′) diblock arms (n) at $\chi N = 36$, which corresponds to the segregation strength at 298 K.[79] Superposed symbols represent the four experimental samples from part (a).

The left half of **Figure 3.4** reports synchrotron small angle X-ray scattering (SAXS) patterns collected at room temperature after annealing (PLA-PMCL)$_n$-PLA with a varying number of PLA-PMCL diblock arms (n = 3 – 9) at 140 °C for 18 hours. Note that the volume fraction of PLA (f_{PLA}) changes with n such that these samples span f_{PLA} = 0.58 – 0.71. The SAXS traces for n = 3 (f_{PLA} = 0.71), n = 5 (f_{PLA} = 0.68), and n = 7 (f_{PLA} = 0.62) can be cleanly indexed as indicated by triangles that demarcate the expected location of scattering reflections for lamellar (LAM), gyroid (GYR), and hexagonally close-packed cylinders (HEX), respectively. The n = 9 material shows broader peaks that are less well-defined, but their intensity maxima roughly coincide with those expected for a spherical form factor and Percus–Yevick structure factor[78] (**Figure 3.5**); we tentatively ascribe this morphology as disordered spheres that possibly fail to order on a well-defined lattice due to kinetic limitations.

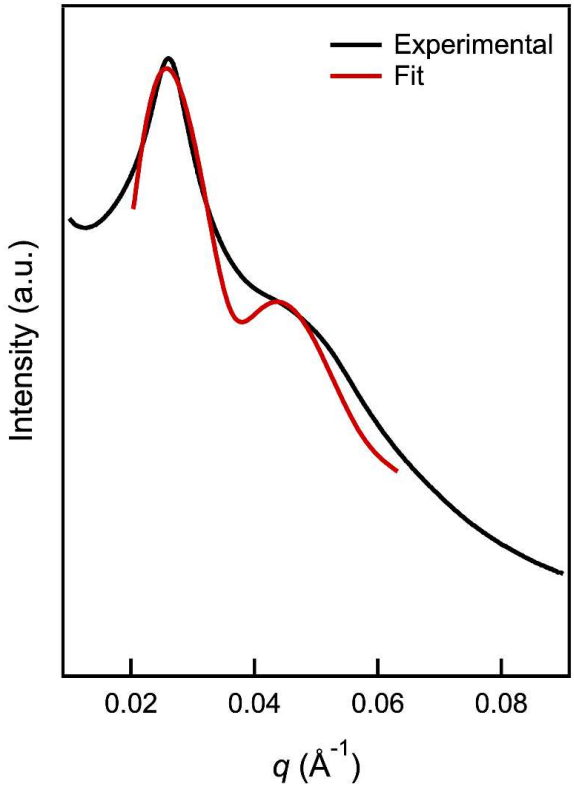

Figure 3.5. SAXS data of (P4MCL-PLA-MM-4-3)$_9$-PLA-MT-24 (black line) is roughly consistent with a disordered spherical micelle model (red line).[9]

Collectively, these data are consistent with a remarkable deflection of order–order phase boundaries towards larger f_A relative to linear AB diblock or ABA triblock copolymers. For example, the HEX–GYR transition occurs near $f_A = 0.3$ with linear diblocks versus in the vicinity of $f_A = 0.62 – 0.68$ that we measure for (PLA-PMCL)$_n$-PLA mikto polymers. We are confident that the PLA block resides in the interior of the cylinders since GYR ($f_{PLA} = 0.68$) and LAM ($f_{PLA} = 0.71$) occur at even larger volume fractions. Perhaps stronger direct proof is the HEX sample exhibits recoverable elasticity in cyclic tensile tests, the details of which will be described in a forthcoming report. These experimental data relating morphology and volume fraction are in agreement with SCFT simulations performed on A(BA′)$_n$ asymmetric miktoarm star polymers using the literature-reported[79] value of $\chi_{PLA–PMCL}$ and the degrees of

polymerization measured experimentally for A = PLA and BA′ = PMCL-PLA (**Figure 3.4**: *right*). We conclude that asymmetric miktoarm star polymers synthesized via μSTAR — which necessarily have dispersity in n — can self-assemble into structures that mimic precise molecular analogues.

3.4 Discussion

Historically, anionic polymerization has been the workhorse synthetic technique used to construct miktoarm star polymers, including AB_n[32,69,77,80,81] and $A(BA')_n$[42,45] asymmetric variants. While effective, rigorous purification requirements, a limited monomer scope, sequence constraints, sluggish coupling kinetics[47] (that can take months to reach full conversion), and the need for additional purification by fractional precipitation[32,45,77] are inconvenient from both practical and design perspectives. μSTAR overcomes all of these challenges, assuming that dispersity in n can be tolerated, by exploiting the well-established functional group compatibility and speed of ROMP. We note that a conceptually similar approach has been attempted with anionic polymerization in the past, namely the grafting-through polymerization of a polystyrene (polyisoprene) macromonomer to construct the B_n core, either preceded or followed by the polymerization of polyisoprene (polystyrene) to grow a single A block.[82] The result was rather broad and multimodal SEC traces, particularly for the poly(macromonomers). Despite improvement after repeated fractional precipitation, even a further optimized anionic methodology would lack the versatility of a ROMP-based approach.

The examples in **Figures 3.1** and **3.3** were selected to accentuate different types of chemistry that are of contemporary importance and challenging to link together using traditional miktoarm star syntheses. For example, PLA_n-PDMS (**Figure 3.1a**) and $PDMS_n$-

PLA (**Figure 3.1b**) may be useful as lithographic materials with higher resolution than linear analogues due to architecture effects while maintaining good etch contrast.[13,19,35,37,83,84] In the field of electrochemical energy storage, miktoarm star polymers containing PEO blocks are of interest as safe battery electrolytes, yet their reported synthesis is involved.[36] We have demonstrated that PS_n-PEO miktoarm stars are straightforward to synthesize with μSTAR (**Figure 3.1c**). μSTAR also provides access to amphiphilic miktoarm star polymers, e.g., by combining a PMMA macromonomer and PtBA terminator (**Figure 3.1d**) followed by acid-catalyzed deprotection of the *tert*-butyl ester to poly(acrylic acid) (PAA). The sulfonamide–pyrroline linkage created during termination is robust enough withstand a concentrated solution of trifluoroacetic acid and yield the partially charged $PMMA_n$-PAA star polymer (**Scheme 3.14, Figure 3.33–3.36**). **Figure 3.1e** further showcases a combination of acrylates ($PTFEA_4$-PnBA) that would be especially difficult to access via a core-first approach since both monomers undergo polymerization with the same type of radical initiator; the incorporation of semi-fluorinated acrylates may also create opportunities in surface coatings and other advanced materials.[85–88]

As introduced earlier, the $A(BA')_n$ architecture presents exciting opportunities for next-generation thermoplastic elastomers.[42] To date, this concept has only been explored using A, A′ = poly(styrene) (PS) and B = poly(isoprene) (PI) blocks synthesized by anionic polymerization and silyl chloride coupling.[45] Inspired by the work of Hillmyer,[79] here we have shown that renewable types of glassy (PLA) and rubbery (PMCL) polyesters can form $A(BA')_n$ miktoarm stars with $n = 3 – 9$ using μSTAR (**Figure 3.1f and 3.3**), which are inaccessible via the established anionic route. The phase behavior of $(PLA\text{-}PMCL)_n$-PLA asymmetric miktoarm star polymers synthesized with μSTAR is consistent with past experimental reports

on precise $(PS\text{-}PI)_3\text{-}PS$[42] and theory that anticipate significant deflection of order–order transitions towards larger volume fractions due to molecular architecture. We have not observed this effect in any simple ROMP copolymerizations involving A and B macromonomers,[58] even at unequal feed compositions, which suggests that efficient termination chemistry (or some other method of installing a single A arm) is key to unlocking the unique self-assembly of asymmetric miktoarm star polymers. This result bolsters our previous finding that short bottlebrushes actually behave like miktoarm star polymers despite the inherent dispersity in n.[58] Note that SCFT simulations reveal a large sensitivity to the relative lengths of A and A′ blocks as parameterized by $\tau = N_A/(N_A+N_{A'})$ (**Figure 3.6**). Although our experimental calculation of τ is based on molar masses measured by NMR (τ = 0.896) and MALS (τ = 0.925) that are within reasonable experimental uncertainty, SCFT simulations match the data in **Figure 3.4** (*left*) best with an intermediate τ = 0.91 shown in **Figure 3.4** (*right*). SCFT also accurately captures the temperature-dependent phase behavior of these materials. By measuring the order–disorder transition temperature (T_{ODT}) with variable temperature SAXS (**Figure 3.7**) and calculating $\chi(T_{ODT})$ from the relationship reported by Watts,[79] $(\chi N)_{ODT}$ was compared to SCFT predictions.

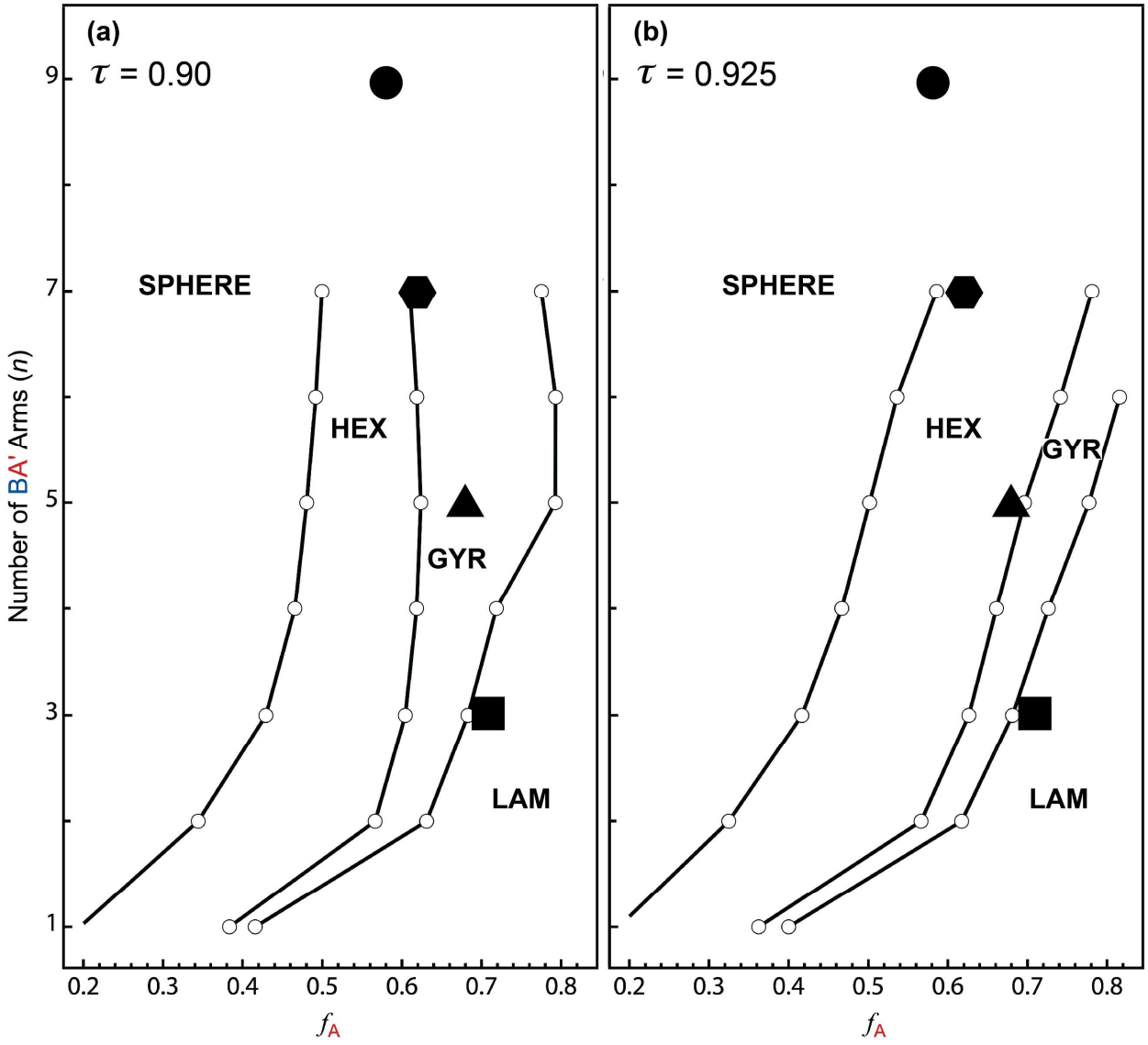

Figure 3.6. SCFT phase diagrams of A(BA′)$_n$ miktoarm star polymers plotted as the number of BA′ arms (n) vs. A-block volume fraction (f_A) at $\chi N_{ABA'}$ = 36, corresponding to the segregation strength of miktoarm star polymers at 298 K.[1] Symbols indicate experimental phases measured by SAXS for (P4MCL-PLA-MM-4-3)$_n$-PLA-MT-24 with (a) τ = 0.90 and (b) τ = 0.925. Neither value of τ perfectly captures the phase behavior observed in (P4MCL-PLA-MM-4-3)$_n$-PLA-MT-24 samples unlike when τ = 0.91 (see Figure 4 in the main text). This analysis highlights the sensitivity of A(BA′)$_n$ miktoarm star phase behavior to τ.

Incredibly, for n = 3, the theoretical and experimental values differ by less than 1% (**Figure 3.8**). As n increases, the deviation grows, but it never exceeds 12%. We hasten to note that not all miktoarm star samples produced with μSTAR show scattering reflections that are as well-resolved as those in **Figure 3.4**.

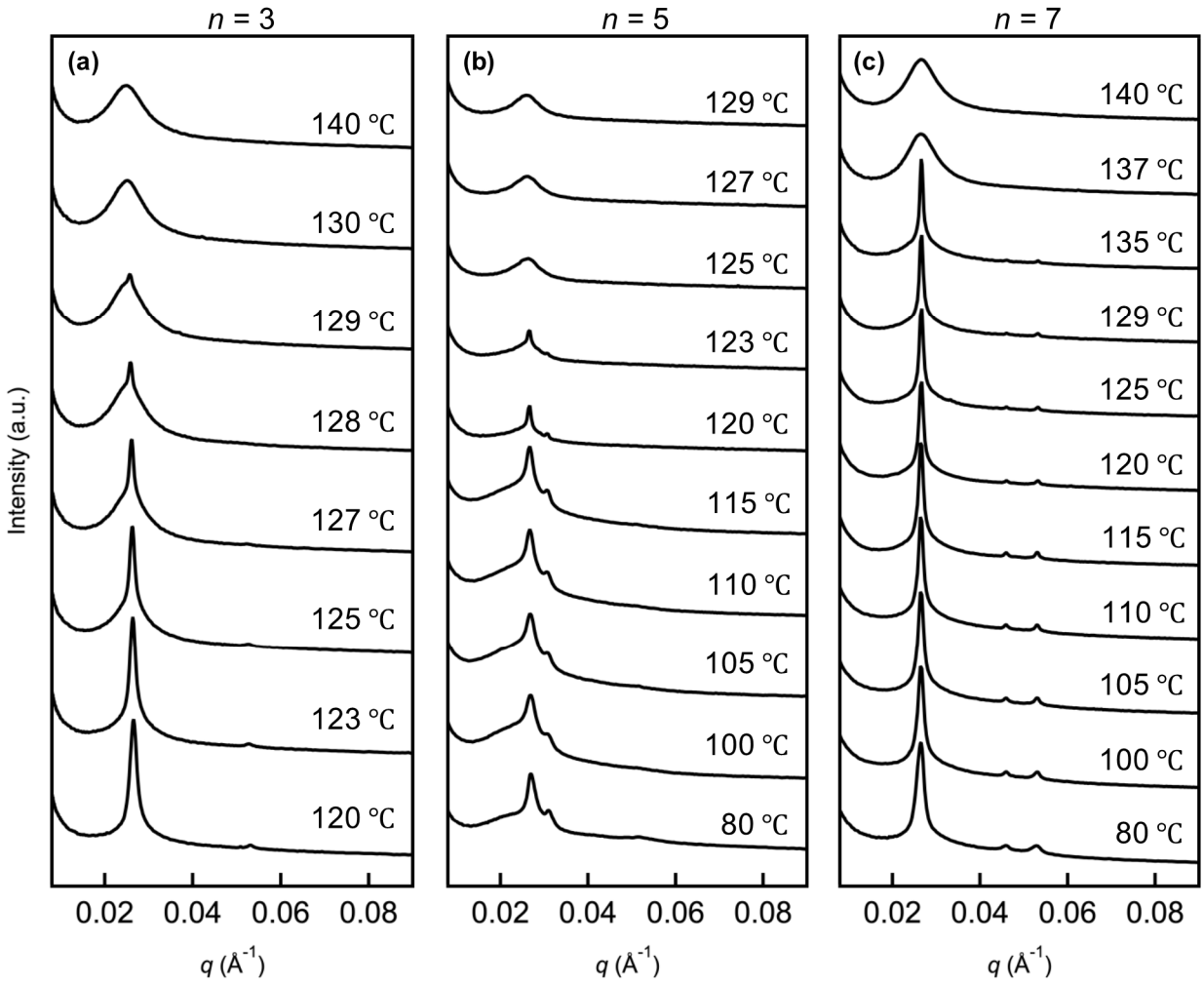

Figure 3.7. Variable temperature SAXS experiments on (P4MCL-PLA-MM-4-3)$_n$-PLA-MT-24 for n = 3, 5, and 7. (a) n = 3: $T_{ODT,Exp}$ = 130 □. (b) n = 5: $T_{ODT,Exp}$ = 125 □. (c) n = 7: $T_{ODT,Exp}$ = 137 □.

This may be the result of thermodynamic or kinetic factors that are influenced by architecture, dispersity, high molecular weight, or a combination thereof. For example, with n = 9 and f_A = 0.58 (**Figure 3.4**, *left*), the thermodynamically stable phase might be A15,[15,89] which is likely kinetically inaccessible above a certain threshold molecular weight.[90] Another possibility is a complex free energy landscape; Grason and coworkers have previously argued that kinetic trapping could cause a similar glassy intermediate phase in AB_2 miktoarm stars due to the near degeneracy of BCC and A15.[15] Thus, it is not surprising that complex sphere phase formation

is suppressed.[10,90] Nevertheless, we find it remarkable that μSTAR can produce clean self-assembly given the dispersity in n.

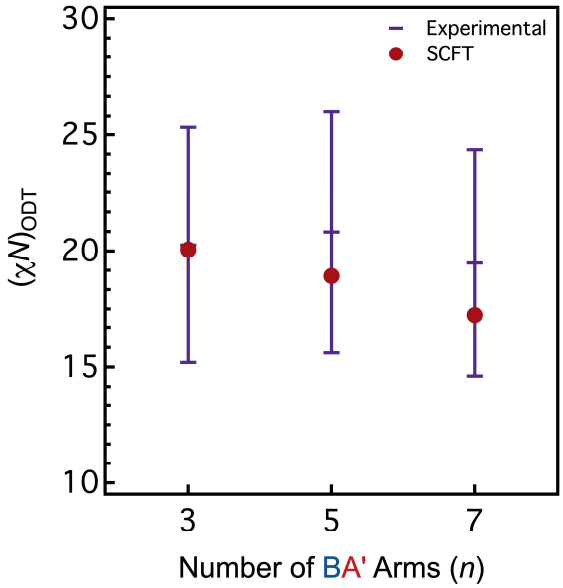

Figure 3.8. Comparison of simulated (red circles) and experimental (purple dashes) values of χN at the order–disorder transition $(\chi N)_{ODT}$ for A(BA′)$_n$ miktoarm star polymers. The experimental value of $\chi(T_{ODT})$ was calculated using the measured T_{ODT} (Figure S30) and the temperature-dependent equation for χ reported by Hillmyer: $\chi = 51.6/T - 0.07$.[1] Error bars are derived from their reported error in χ,[1] which spans a +/– 25% range in χN.

Figure 3.9 illustrates the key differences in molecular composition and self-assembly that result from various miktoarm star synthesis techniques. Simple ROMP copolymerization with either a blocky or statistical sequence at low N_{BB} generates composition and arm-number dispersity that together tend to favor a flat block–block interface (**Figure 3.9a**).[58] At the same overall composition (i.e., $f_A = 0.5$), asymmetric miktoarm star polymers with a precise number of arms (for example, AB_3) bias interfacial curvature toward the A block (**Figure 3.9b**).[15,26] Samples synthesized using μSTAR sit somewhere in between — exactly one A arm and a distribution of B arms still results in self-assembly that favors interfacial curvature, the magnitude of which is evidently similar to precise analogues with the average μSTAR

composition (**Figure 3.9c**). One benefit of incorporating such dispersity lies in relaxing the synthetic burden without drastically impacting self-assembly.

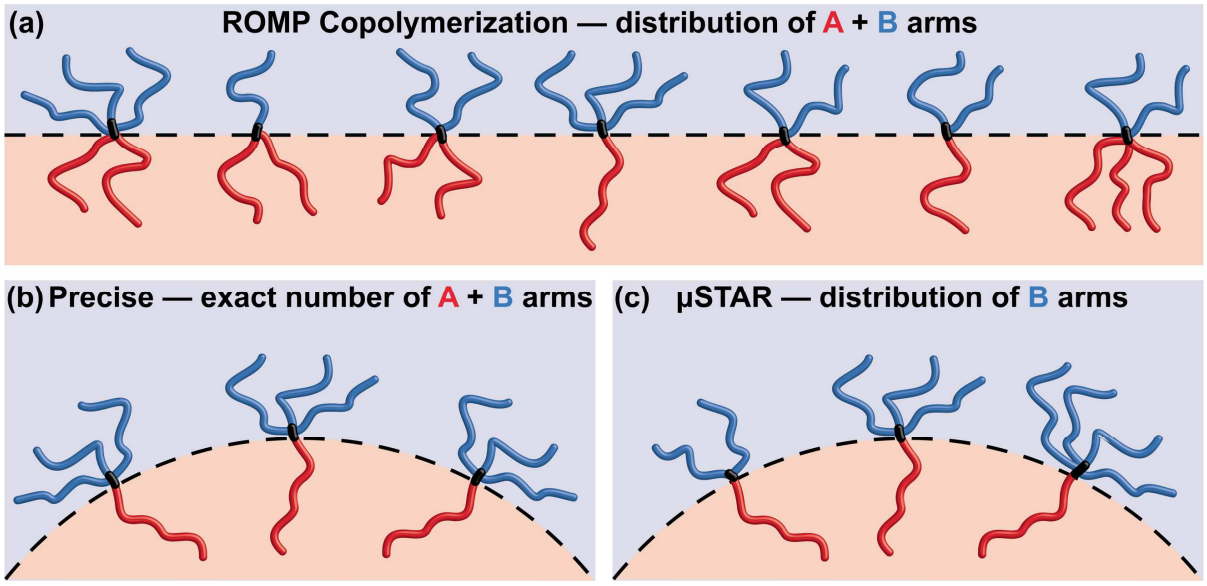

Figure 3.9. Illustration of molecular composition and self-assembly resulting from different miktoarm star synthesis techniques. **(a)** Simple ROMP copolymerization of two macromonomers generates dispersity in composition and the number of A and B arms, which promotes flat block–block interfaces.[58] **(b)** Asymmetric miktoarm stars (e.g., AB_3) created by a precise synthesis favor interfacial curvature toward the A block.[15] **(c)** μSTAR produces miktoarm stars with a distribution of B arms and exactly one A arm, resulting in interfacial curvature that is equivalent to precise analogues comprising the average molecular composition.

3.5 Conclusions

In summary, we have introduced a new synthetic technique termed μSTAR that generates AB_n and $A(BA')_n$ asymmetric miktoarm star polymers using grafting-through polymerization and efficient enyne-mediated polymer–polymer coupling chemistry. This modular approach is compatible with a wide variety of polymer chemistries and can accommodate high molecular weight arms. The average number of B or BA′ arms (n) is easily varied by the ratio of Grubbs catalyst to macromonomer in the initial polymerization step. Miktoarm star polymers made via μSTAR exhibit large deflections in the block copolymer

phase diagram (relative to linear analogues) unlike stars produced by statistical grafting-through copolymerization. Despite the dispersity in *n*, experimental phase behavior matches SCFT calculations performed with precise molecular connectivity. μSTAR significantly simplifies the synthesis of asymmetric miktoarm star polymers when dispersity in arm number can be tolerated.

3.6 Experimental

3.6.1 Chemicals

Unless otherwise stated, all chemicals were purchased at the highest available purity and used as received. All reactions were carried out under a nitrogen atmosphere with dry solvents using anhydrous conditions unless otherwise stated. Dry, degassed dichloromethane (DCM), tetrahydrofuran (THF), and toluene were obtained from a JC Meyer solvent purification system. CH_2Cl_2 used for the synthesis of poly(d,l-lactide) was subsequently distilled from CaH_2. Tin(II) 2-ethylhexanoate ($Sn(Oct)_2$, Aldrich, 92.5–100%) was fractionally distilled 3× under reduced pressure (50 mtorr, 150 □) and stored in a nitrogen filled glovebox before use. 4-Methylcaprolactone (4MCL) was prepared according to literature,[1] purified by fractional distillation 3× from calcium hydride (CaH_2, Fisher Scientific, 93%), 3× from $Sn(Oct)_2$ under reduced pressure (50 mtorr, 50 □), and stored in a nitrogen filled glovebox before use. d,l-Lactide was generously provided by Corbion (PURASORB DL) and recrystallized once from anhydrous ethyl acetate (Fisher Scientific, 99.9%) and twice from anhydrous toluene. 1,8-Diazabicyclo[5.4.0]undec-7-ene (DBU, Alfa Aesar, 99%) was distilled from CaH_2, diluted with anhydrous THF to 1.5 M, and transferred to glass ampoules that were then flame sealed. Grubbs' second-generation metathesis catalyst

[(H_2IMes)(PCy_3)$_2$(Cl)$_2$Ru=CHPh] was generously provided by Materia. Grubbs' third-generation metathesis catalyst [(H_2IMes)(pyr)$_2$(Cl)$_2$Ru=CHPh] (G3) was prepared according to literature.[2] When reported, yields refer to chromatographically and spectroscopically (^{1}H-NMR) homogeneous materials, unless otherwise stated. Reactions were monitored by thin layer chromatography (TLC) carried out on 0.25 mm E. Merck silica gel plates (60F-254) using UV light as the visualizing agent and basic aqueous potassium permanganate ($KMnO_4$), and heat as developing agents. E. Merck silica gel (60, particle size 0.043–0.063 mm) was used for flash column chromatography.

3.6.2 Characterization

^{1}H and ^{13}C NMR spectra of small molecules were recorded on Bruker Avance 400 or 500 MHz instruments and calibrated using residual undeuterated solvent as an internal reference ($CHCl_3$ @ 7.26 ppm ^{1}H NMR, 77.16 ppm ^{13}C NMR). ^{1}H, ^{13}C, and ^{19}F NMR spectra of polymers were collected on a 600 MHz Varian VNMRS. The following abbreviations (or combinations thereof) were used to explain the multiplicities: s = singlet, d = doublet, t = triplet, q = quartet, m = multiplet, br = broad. Mass spectra (MS) were recorded on a LC/MS (Agilent Technologies 1260 Infinity II/6120 Quadrupole) by ESI. Melting points were measured on Bibby Scientific's MEL-TEMP Digital Melting Point Apparatus. Infrared (IR) spectra were recorded on a Thermo Nicolet iS10 Fourier-transform infrared (FTIR) spectrometer with a Smart Diamond attenuated total reflectance (ATR) sampling accessory. Size-exclusion chromatography with multi-angle light scattering detection (SEC-MALS) was performed using two Agilent columns (PLgel, 5 μm MiniMIX-D, 250 × 4.6 mm) connected to a Waters Alliance HPLC System, 2690 Separation Module pump, a Wyatt 18-angle DAWN HELEOS-II light scattering detector, and Wyatt REX differential refractive index detector using THF as

the mobile phase. Absolute molar mass was determined by light scattering using online determination of d*n*/d*c* by assuming 100% mass elution under the peak of interest. Size-exclusion chromatography was also performed on a Waters instrument using a differential refractive index (dRI) detector and two Tosoh columns (TSKgel SuperHZM-N, 3 μm polymer, 150 × 4.6mm) with chloroform at 35 °C as the mobile phase. In this case, molar masses and molar mass dispersity ($Đ$) were determined against narrow PS standards (Agilent). ^{1}H and ^{19}F diffusion-ordered spectroscopy (DOSY) experiments were performed on a Bruker Avance III 300 MHz SWB Diffusion NMR Spectrometer equipped with a Diff50 z-Diffusion Probe using a stimulated echo sequence using bipolar gradients (SteBp) pulse sequence[62] using 16 gradient steps and acquiring 16 scans at each step. All DOSY experiments were run in either chloroform-*d* or acetone-d_6 at polymer concentrations of ≈25 mg/mL without spinning to avoid convection. DOSY data analysis was performed in Mathematica wherein the data were normalized and fit to a single exponential function. Room temperature SAXS measurements were performed at beamline 7.3.3 of the Advanced Light Source (ALS) at Lawrence Berkeley National Laboratory in Berkeley, CA. A sample-to-detector distance of 3815 mm was used with an X-ray wavelength of 1.24 □. Variable temperature SAXS measurements were performed at beamline 1-5 of Stanford Synchrotron Radiation Lightsource (SSRL) to determine order–disorder transition temperatures (T_{ODT}) using a sample-to-detector distance of 2870 mm and a 1.03 □ X-ray wavelength. Heating was performed on a custom stage with temperatures measured at the sample position to ensure accuracy. Samples were equilibrated for 5 minutes at each temperature before collecting scattering images. For all SAXS experiments, a silver behenate standard was used to calibrate the scattering angles. 2D data were reduced by azimuthal averaging to give $I(q)$, where I is intensity in arbitrary units, $q = |\mathbf{q}|$

$= 4\pi\lambda^{-1} \sin(\theta/2)$ is the magnitude of the scattering wave vector, λ is the wavelength of the incident beam, and θ is the scattering angle.

3.6.3 Self-Consistent Field Theory

Self-consistent field theory (SCFT) simulations were performed using the standard model of an incompressible diblock copolymer melt (Model E in Ref. 63) using chain propagators suitably adjusted to account for the star architecture with all polymer arms extending from a single point.[63] The modified diffusion equation was solved pseudo-spectrally in the field variables using the second-order operator splitting (SOS) algorithm for the contour variable with contour resolution of $\Delta s = 0.001$. Note that this relatively small value of Δs was necessary to sufficiently resolve the block bi-dispersity parameter τ. Field updates were performed using the semi-implicit Siedel (SIS) scheme. Phase diagrams were constructed in the standard manner by computing the free energy of different candidate phases and then determining where the free energies of two phases are equal. Candidate phases considered (and corresponding spatial resolution) were BCC spheres (32×32×32), cylinders (32×32), double gyroid (32×32×32), lamellae (128), and the disordered phase. The ODT was determined using the experimentally relevant f_A and adjusting χ until the free energy of the disordered and closest ordered phase were equal. The statistical segment length of the two blocks were assumed to be equal ($b_A/b_B = 1$). A more detailed computational study of the miktoarm architecture will be the topic of a forthcoming publication.[64]

Scheme 3.1. Synthesis of enyne-functionalized ATRP initiator

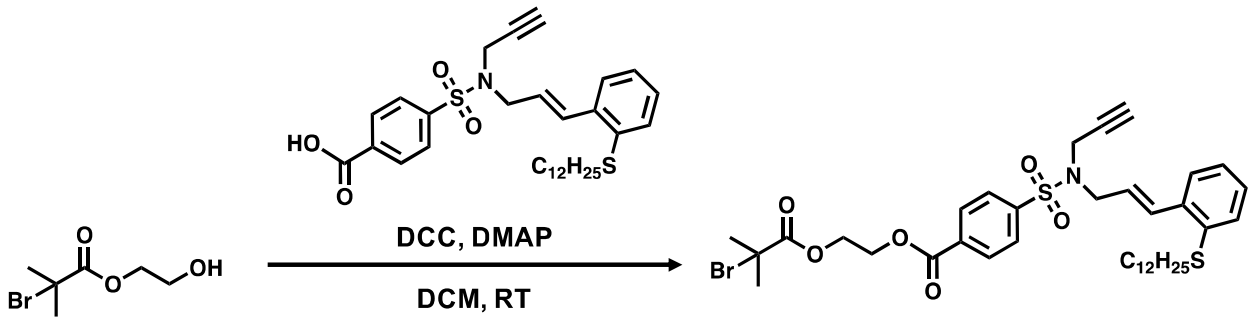

To a stirred suspension of the carboxylic acid[3] (4.17 g, 7.50 mmol, 1.0 eq) in dry DCM (80 mL) was added 2-hydroxyethyl 2-bromoisobutyrate[4] (1.58 g, 7.50 mmol, 1.0 eq), 4-Dimethylaminopyridine (DMAP) (92 mg, 0.75 mmol, 0.1 eq), and N,N'-Dicyclohexylcarbodiimide (DCC) (1.86 g, 9.0 mmol, 1.2 eq) at room temperature. The reaction mixture was stirred for 24 hours at room temperature, during which time white solids precipitated. The white solids were filtered off and washed with 10 mL DCM. The filtrates were concentrated *in vacuo* and purified by column chromatography (hexanes: EtOAc = 5:1) to give the product as a colorless powder (5.35 g, 95%). m. p.: 62 – 64 □;

MS (ESI) $[M+Na]^+$ calcd. for $C_{37}H_{50}BrNNaO_6S_2$, 770.216, found, 770.214.

^{1}H NMR (500 MHz, $CDCl_3$): δ. 8.21 (d, *J* = 8.6 Hz, 2H), 7.99 (d, *J* = 8.6 Hz, 2H), 7.42 (dd, *J* = 7.6, 1.4 Hz, 1H), 7.36 (dd, *J* = 7.8, 1.2 Hz, 1H), 7.24 (td, *J* = 7.6, 1.5 Hz, 1H), 7.19 (td, *J* = 7.6, 1.2 Hz, 1H), 7.15 (d, *J* = 15.7 Hz, 1H), 6.02 (dt, *J* = 15.6, 6.9 Hz, 1H), 4.67 – 4.63 (m, 2H), 4.59 – 4.55 (m, 2H), 4.20 (d, *J* = 2.4 Hz, 2H), 4.07 (dd, *J* = 6.9, 0.8 Hz,2H), 2.87 – 2.81 (m, 2H), 2.06 (t, *J* = 2.5 Hz, 1H), 1.96 (s, 6H), 1.61 (dt, *J* = 15.0, 7.4 Hz, 2H), 1.39 (dd, *J* = 14.4, 7.0 Hz, 2H), 1.28 (m, 16H), 0.90 (t, *J* = 7.0 Hz, 3H).

^{13}C NMR (126 MHz, $CDCl_3$): δ. 171.41, 164.83, 143.13, 136.59, 135.47, 133.41, 133.25, 130.19, 129.87, 128.34, 127.80, 126.44, 126.27, 124.18, 75.90, 74.28, 63.23, 62.81, 55.27,

48.86, 35.91, 34.09, 31.84, 30.59, 29.57, 29.56, 29.52, 29.43, 29.28, 29.10, 29.01, 28.80, 22.63, 14.08.

Scheme 3.2. Synthesis of PDMS-MM-6

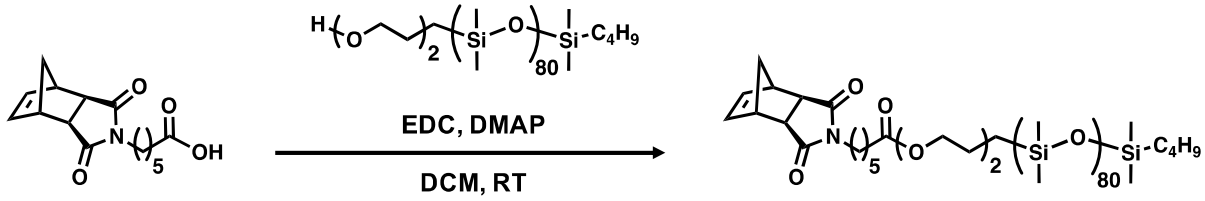

To a solution of monocarbinol terminated polydimethylsiloxane (PDMS) (5 kDa, 18.00 g, 3.6 mmol, Gelest) in dry DCM (250 mL) was added *N*-(hexanoic acid)-cis-5-norbornene-exo-dicarboximide[5] (2.58 g, 9.0 mmol, 2.5 eq), 1-ethyl-3-(3-dimethylaminopropyl)carbodiimide (EDC) (2.41 g, 12.5 mmol, 3.5 eq), and 4-dimethylaminopyridine (DMAP) (540 mg, 3.6 mmol, 1.0 eq) at room temperature. After 48 hours, the reaction was washed with 3× 75 ml 1 M HCl, brine, dried over $MgSO_4$, and then filtered through a plug of basic alumina.

^{1}H NMR (600 MHz, $CDCl_3$) δ 6.28 (t, *J* = 1.9 Hz, 2H), 4.24 – 4.16 (m, 2H), 3.64 – 3.57 (m, 2H), 3.44 (dt, *J* = 20.9, 7.2 Hz, 4H), 3.27 (p, *J* = 1.7 Hz, 2H), 2.66 (d, *J* = 1.4 Hz, 2H), 2.33 (t, *J* = 7.5 Hz, 2H), 1.69 – 1.46 (m, 11H), 1.36 – 1.27 (m, 6H), 1.23 – 1.19 (m, 1H), 0.88 (t, *J* = 6.9 Hz, 3H), 0.58 – 0.47 (m, 4H), 0.07 (s, 436H).

Scheme 3.3. Synthesis of PTFEA-MM-7

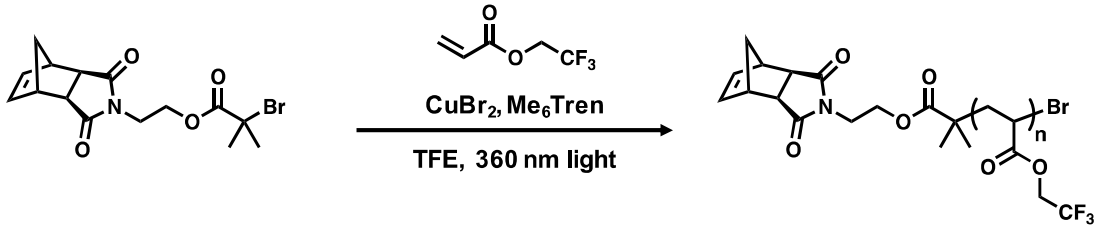

In a 20 mL vial, 17.4 mg of $CuBr_2$ (0.08 mmol, 0.05 eq) and 108 mg of Me_6Tren (0.47 mmol, 0.18 eq) were combined with 3.9 mL of trifluoroethanol (TFE) and sonicated for 15 minutes. In another 20 mL vial charged with a stir bar, 277 mg of *N*-(ethyl 2-bromo-2-methylpropanoate)-*cis*-5-norbornene-*exo*-dicarboximide[6] (0.78 mmol, 1 eq) was added. Then 5.6 mL of TFE and 7.8 g of trifluoroethyl acrylate (6.4 mL, 50.6 mmol, 64.9 eq) were added. Next, 0.78 mL of the $CuBr_2$/Me_6Tren stock solution was added. The vial was sparged with N_2 for 15 min. The reaction mixture was then placed into a commercial UV nail lamp system and irradiated with 360 nm light. After 1.5 hours the reaction mixture was precipitated into 0.1 M HCl in methanol. The polymer was dissolved in DCM, passed through a plug of basic alumina, and precipitated 3 more times in methanol.

^{1}H NMR (600 MHz, CD_2Cl_2) δ 6.35 – 6.24 (m, 2H), 4.73 – 4.31 (m, 88H), 4.15 (t, *J* = 5.0 Hz, 2H), 3.73 (q, *J* = 4.8, 4.2 Hz, 2H), 3.24 (s, 2H), 2.69 (s, 2H), 2.66 – 2.25 (m, 44H), 2.25 – 1.94 (m, 21H), 1.80 (p, *J* = 6.6 Hz, 44H), 1.63 (ddd, *J* = 31.3, 22.4, 14.7 Hz, 22H), 1.28 (d, *J* = 9.6 Hz, 1H), 1.16 – 1.02 (m, 7H).

^{19}F NMR (564 MHz, CD_2Cl_2) δ –73.70 – –74.57 (m)

Scheme 3.4. Synthesis of PMMA-MM-4

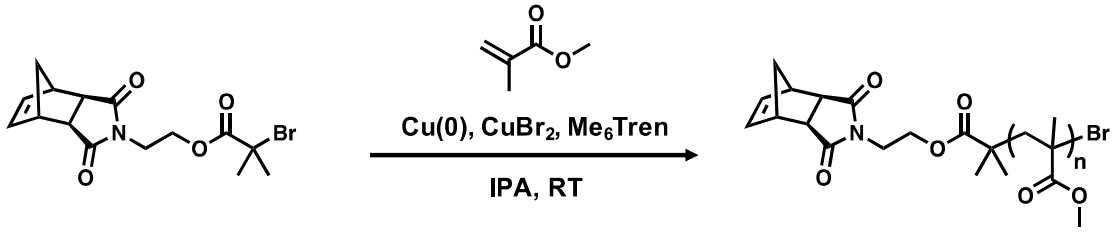

In a 100 mL flask, 31.5 mg of $CuBr_2$ (0.14 mmol, 0.05 eq) and 117 mg of Me_6Tren (0.51 mmol, 0.18 eq) were combined with 15 mL of isopropanol (IPA) and sonicated for 15 minutes. Then, 1.00 g (2.82 mmol, 1 eq) of *N*-(ethyl 2-bromo-2-methylpropanoate)-*cis*-5-

norbornene-*exo*-dicarboximide[6] was added followed by 42 g (45 mL, 422.5 mmol, 150 eq) of methyl methacrylate. The flask was sealed with a septum and sparged with N_2 for 10 minutes, after which a stir bar with copper wire wrapped around it was added, followed by sparging for 5 more minutes. After 7 hours the reaction was quenched by precipitating the polymer into 0.1M HCl in methanol. The reaction mixture was dissolved in DCM, passed through a plug of basic alumina and precipitated 3 more times in methanol.

^{1}H NMR (600 MHz, $CDCl_3$) δ 6.28 (q, *J* = 2.2 Hz, 2H), 4.22 – 4.05 (m, 2H), 3.73 (q, *J* = 5.2 Hz, 6H), 3.57 (q, *J* = 3.1, 2.6 Hz, 105H), 3.28 – 3.22 (m, 2H), 2.75 – 2.67 (m, 3H), 2.15 (s, 4H), 1.97 – 1.71 (m, 68H), 1.53 – 1.34 (m, 7H), 1.27 – 1.16 (m, 3H), 1.08 (s, 3H), 1.06 – 0.89 (m, 33H), 0.81 (t, *J* = 8.6 Hz, 74H).

Scheme 3.5. Synthesis of PS-MM-2

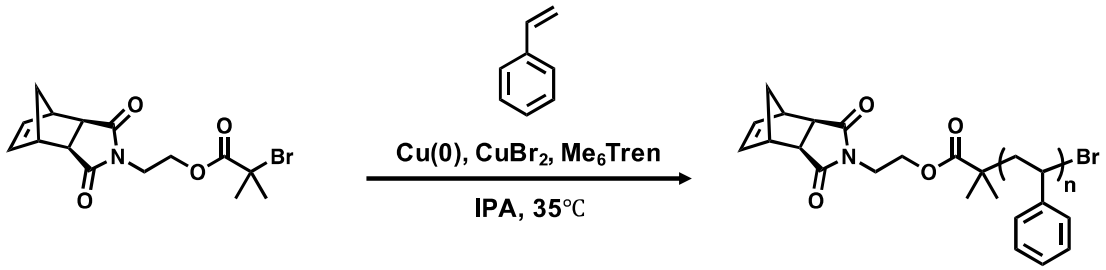

In a 100 mL flask, 23 mg of $CuBr_2$ (0.10 mmol, 0.05 eq) and 86 mg of Me_6Tren (0.38 mmol, 0.18 eq) were combined with 10 mL of isopropanol (IPA) and sonicated for 15 minutes. Then, 742 mg (2.08 mmol, 1 eq) of *N*-(ethyl 2-bromo-2-methylpropanoate)-*cis*-5-norbornene-*exo*-dicarboximide[6] was added followed by 45.3 g (50 mL, 435 mmol, 209 eq) of styrene. The flask was sealed with a septum and then sparged for 10 minutes, after which a stir bar with copper wire wrapped around it was added, followed by sparging with N_2 for 5 more minutes. The reaction was placed in an oil bath and heated to 35 □. After 7 hours the reaction was

quenched by precipitating the polymer into acidic methanol. The reaction mixture was dissolved in DCM, passed through a plug of basic alumina, and precipitated 5 more times.

^{1}H NMR (600 MHz, $CDCl_3$) δ 7.25 – 6.32 (m, 91H), 6.27 (s, 2H), 4.62 – 4.37 (m, 1H), 3.69 – 3.31 (m, 4H), 3.24 (s, 2H), 2.66 – 2.58 (m, 2H), 2.21 – 1.31 (m, 55H), 1.20 (d, *J* = 8.9 Hz, 1H), 1.02 – 0.77 (m, 6H).

Scheme 3.6. Synthesis of P4MCL-MM-4

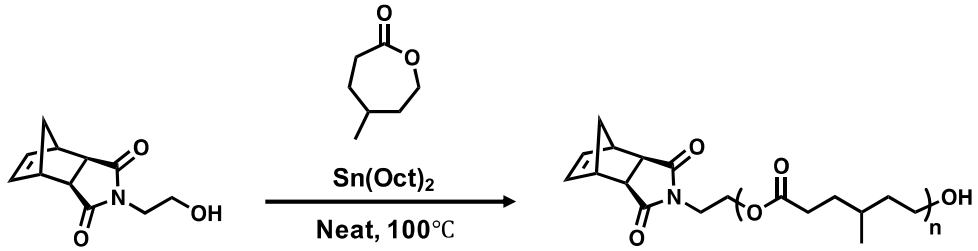

In a nitrogen filled glovebox, 11.00 g of 4MCL (85.8 mmol, 218.5 eq), 532 mg of norbornene alcohol[7] (2.57 mmol, 1 eq) and 17 mg of $Sn(Oct)_2$ (0.043 mmol, 0.017 eq) were combined in an oven-dried heavy wall pressure vessel with a stir bar. The vessel was sealed with a threaded PTFE bushing using a perfluoro O-ring and removed from the glovebox. The vessel was placed in an oil bath at 115 □ and stirred for 70 minutes. After removal from the oil bath, the vessel was immediately quenched in an ice water bath. An aliquot was pulled to determine the monomer conversion by ^{1}H NMR (80%). The reaction mixture was diluted with CH_2Cl_2 and precipitated into 800 mL of MeOH at –78 □. The MeOH was decanted. The solid product was redissolved in DCM and the precipitation repeated two more times in MeOH. The resulting P4MCL was dried *in vacuo*.

^{1}H NMR (600 MHz, $CDCl_3$) δ 6.27 (t, *J* = 1.9 Hz, 2H), 4.23 – 4.20 (m, 2H), 4.14 – 4.01 (m, 60H), 3.73 (t, *J* = 5.3 Hz, 2H), 3.71 – 3.59 (m, 2H), 3.26 (p, *J* = 1.7 Hz, 2H), 2.68 (d, *J* = 1.3

Hz, 2H), 2.37 – 2.18 (m, 62H), 1.71 – 1.60 (m, 62H), 1.60 – 1.50 (m, 33H), 1.50 – 1.36 (m, 62H), 1.28 (dt, *J* = 9.9, 1.6 Hz, 1H), 0.90 (d, *J* = 6.6 Hz, 94H).

Scheme 3.7. Synthesis of PLA-MM-5

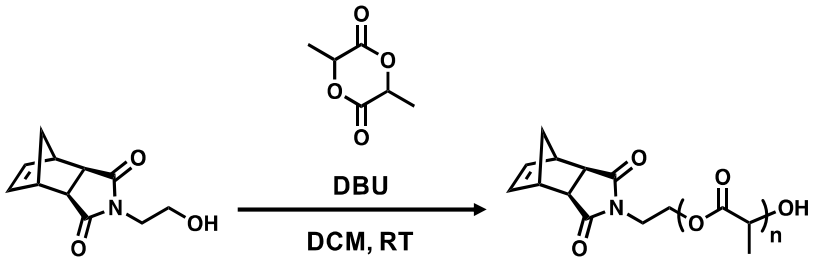

In a nitrogen filled glovebox, 6.00 g d,l-lactide (41.7 mmol, 38.6 eq), 224 mg alcohol[7] (1.08 mmol, 1 eq) were combined in an oven-dried flask with a stir bar, followed by the addition of 70 mL CH_2Cl_2. The mixture was stirred for 10 min to ensure complete dissolution. Then 0.72 mL of DBU solution (1.5 M in THF, 1.08 mmol, 1 eq) was added. After 6 minutes, the reaction was quenched with 525 mg benzoic acid (4.3 mmol, 4.0 eq). An aliquot was pulled to determine the monomer conversion by ^{1}H NMR (87%). The solvent volume was reduced by one half *in vacuo*, 0.1 mL of trifluoroacetic acid (1.28 mmol, 2 equiv) was added with stirring, and the solution was immediately precipitated into 500 mL of cold MeOH. The MeOH was then decanted. The solid product was redissolved in DCM and the precipitation repeated two more times. The resulting PLA was dried *in vacuo*.

^{1}H NMR (600 MHz, $CDCl_3$) δ 6.27 (d, *J* = 1.9 Hz, 2H), 5.31 – 5.10 (m, 69H), 4.39 – 4.29 (m, 2H), 4.29 – 4.20 (m, 1H), 3.79 (ddd, *J* = 14.2, 7.6, 4.0 Hz, 1H), 3.70 (ddd, *J* = 14.3, 5.8, 3.9 Hz, 1H), 3.25 (t, *J* = 1.8 Hz, 2H), 2.74 – 2.62 (m, 2H), 1.69 – 1.62 (m, 2H), 1.62 – 1.48 (m, 210H), 1.23 (dd, *J* = 9.8, 1.7 Hz, 1H).

Scheme 3.8. Synthesis of P4MCL-PLA-MM

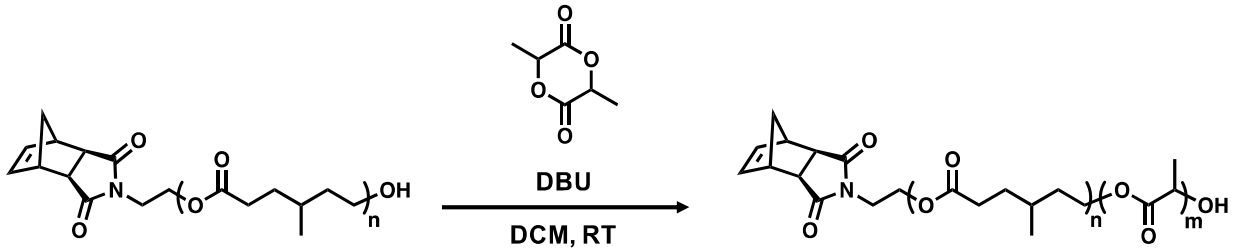

In a vial charged with a stir bar, 1.00 g P4MCL-MM-4 (0.24 mmol, 1 eq) was dried *in vacuo* for 3 days. In a nitrogen filled glovebox, 740 mg of d,l-lactide (5.1 mmol, 21.7 eq) was added, followed by the addition of 7.2 mL of CH_2Cl_2. The mixture was stirred for 10 min to ensure complete dissolution. Then 0.16 mL of DBU solution (1.5 M in THF, 0.24 mmol, 1 eq) was added. After 6 minutes, the reaction was quenched with 120 mg benzoic acid (1.0 mmol, 4.0 eq). An aliquot was pulled to determine the monomer conversion by ^{1}H NMR (98%). The solvent volume was reduced by one half *in vacuo*, 0.1 mL of trifluoroacetic acid (1.28 mmol, 2 eq) was added with stirring, and the solution was immediately precipitated into 500 mL of cold MeOH. The MeOH was then decanted. The solid product was redissolved in DCM and the precipitation repeated two more times. The resulting diblock was dried *in vacuo*.

^{1}H NMR (600 MHz, $CDCl_3$) δ 6.28 (t, J = 1.9 Hz, 2H), 5.17 (dq, J = 27.3, 7.2 Hz, 40H), 4.36 (dq, J = 21.0, 7.0 Hz, 1H), 4.22 (t, J = 5.3 Hz, 2H), 4.14 – 4.01 (m, 62H), 3.74 (t, J = 5.3 Hz, 2H), 3.27 (d, J = 2.1 Hz, 2H), 2.69 (s, 2H), 2.37 – 2.20 (m, 65H), 1.73 – 1.39 (m, 302H), 1.29 (d, J = 10.1 Hz, 1H), 0.91 (d, J = 6.8 Hz, 97H).

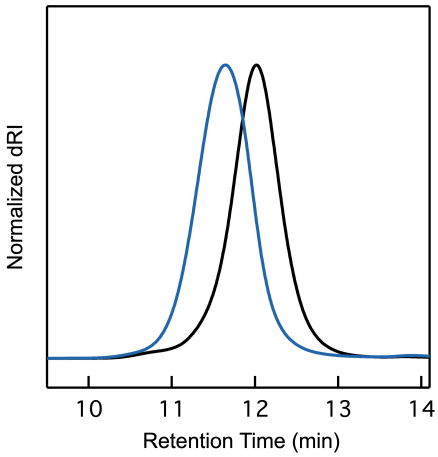

Figure 3.10. SECs (normalized differential refractive index signal) of P4MCL-MM-4 (black) and the PLA-*b*-P4MCL diblock macromonomer (blue) denoted (P4MCL-PLA-MM-4-3).

Scheme 3.9. Synthesis of PLA-MT

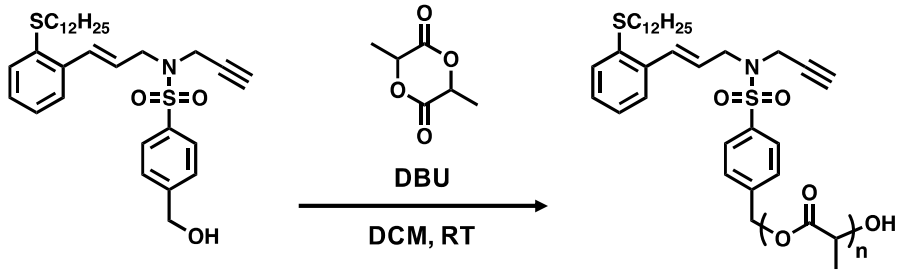

In a nitrogen filled glovebox, 3.00 g of d,l-lactide (20.8 mmol, 204 eq) and 55 mg of alcohol[3] (0.1 mmol, 1 eq) were combined in an oven-dried flask with a stir bar, followed by the addition of 35 mL of CH_2Cl_2. The mixture was stirred for 10 min to ensure complete dissolution. Then 0.07 mL of DBU solution (1.5 M in THF, 0.1 mmol, 1 eq) was added. After 90 minutes, the reaction was quenched with 50 mg benzoic acid (0.4 mmol, 4.0 eq). An aliquot was pulled to determine the monomer conversion by ^{1}H NMR (85%). The solvent volume was reduced by one half *in vacuo*, 0.1 mL of trifluoroacetic acid (1.28 mmol, 2 eq) was added with stirring, and the solution was immediately precipitated into 300 mL of cold MeOH. The MeOH was then decanted. The solid product was redissolved in DCM and the precipitation repeated two more times. The resulting PLA was dried *in vacuo*. ^{1}H NMR (600 MHz, $CDCl_3$): δ (ppm) 6.28

(br t, 2H), 5.25–5.02 (m, 175H), 4.40–4.21 (m, 3H), 3.84–3.68 (m, 2H) 3.27 (s, 2H), 2.70 (m, 2H), 1.73–1.39 (m, 533H). M_n (^{1}H NMR) = 13 kg mol^{-1}.

^{1}H NMR (600 MHz, $CDCl_3$) δ 7.88 (dd, *J* = 8.3, 1.8 Hz, 2H), 7.46 (d, *J* = 8.2 Hz, 2H), 7.38 (dd, *J* = 7.6, 1.6 Hz, 1H), 7.33 (dd, *J* = 7.8, 1.3 Hz, 1H), 7.20 (td, *J* = 7.6, 1.7 Hz, 1H), 7.16 (td, *J* = 7.6, 1.3 Hz, 1H), 7.10 (d, *J* = 15.4 Hz, 1H), 5.99 (dt, *J* = 15.7, 6.9 Hz, 1H), 5.17 (dq, *J* = 20.9, 7.1 Hz, 432H), 4.35 (dq, *J* = 13.9, 7.1 Hz, 1H), 4.15 (d, *J* = 2.4 Hz, 2H), 2.84 (dt, *J* = 28.3, 7.5 Hz, 2H), 1.70 – 1.42 (m, 1329H), 1.24 (d, *J* = 5.5 Hz, 22H), 0.87 (t, *J* = 7.0 Hz, 4H).

Scheme 3.10. Synthesis of PDMS-MT-6

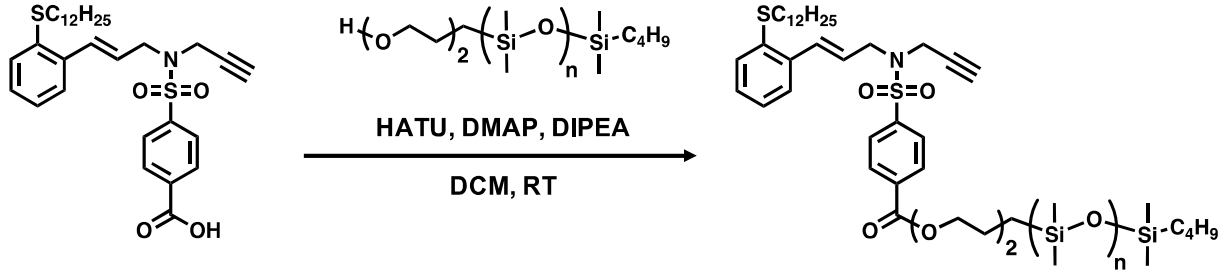

To a solution of monocarbinol terminated polydimethylsiloxane (PDMS) (5 kDa, 5.00 g, 1.0 mmol, Gelest) in dry DCM (20 mL) was added the carboxylic acid (1.11 g, 2.0 mmol, 2.0 eq), 1-[Bis(dimethylamino)methylene]-1H-1,2,3-triazolo[4,5-b]pyridinium-3-oxide-hexafluorophosphate (HATU) (1.15 g, 3.0 mmol) and 4-dimethylaminopyridine (DMAP) (134 mg, 1.1 mmol, 1.1 eq) at room temperature. After 30 minutes, *N,N*-diisopropylethylamine (DIPEA) (647 mg, 0.87 mL, 5.0 mmol, 5.0 eq) was added. The reaction was stirred at room temperature for 48 hours, after which ^{1}H NMR analysis showed full conversion of the starting PDMS. Then the reaction mixture was treated with excess MeOH and centrifuged. The supernatant was carefully decanted. This process was performed twice. The thick oil on the bottom was collected, combined and dried *in vacuo*.

^{1}H NMR (600 MHz, $CDCl_3$) δ 8.24 – 8.14 (m, 2H), 7.99 – 7.90 (m, 2H), 7.40 (dd, *J* = 7.7, 1.6 Hz, 1H), 7.34 (dd, *J* = 7.8, 1.3 Hz, 1H), 7.22 (td, *J* = 7.5, 1.6 Hz, 1H), 7.17 (td, *J* = 7.5, 1.4 Hz, 1H), 7.13 (d, *J* = 15.7 Hz, 1H), 6.00 (dt, *J* = 15.7, 6.9 Hz, 1H), 4.54 – 4.46 (m, 2H), 4.19 (d, *J* = 2.4 Hz, 2H), 4.05 (dd, *J* = 7.0, 1.4 Hz, 2H), 3.82 – 3.73 (m, 2H), 3.48 (t, *J* = 7.0 Hz, 2H), 2.85 – 2.79 (m, 2H), 2.03 (t, *J* = 2.4 Hz, 1H), 1.68 – 1.55 (m, 4H), 1.37 (q, *J* = 6.8 Hz, 2H), 1.35 – 1.19 (m, 21H), 0.88 (td, *J* = 7.1, 2.6 Hz, 6H), 0.57 – 0.51 (m, 4H), 0.07 (s, 432H).

Scheme 3.11. Synthesis of PEO-MT-5

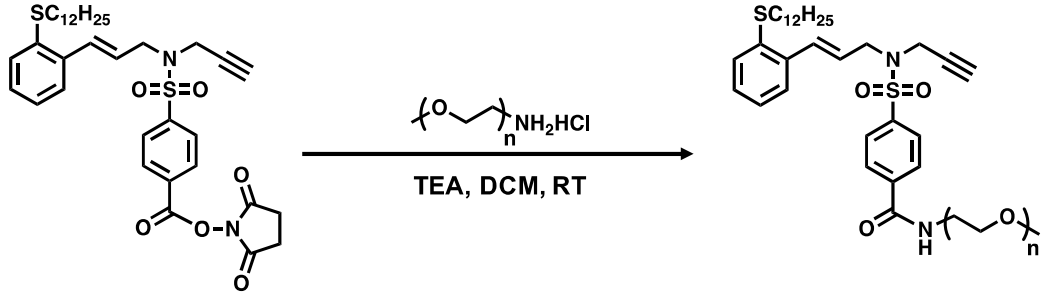

This compound was prepared according to a previously published procedure:[3] To a stirred solution of the sulfonamide NHS ester (1.44 g, 2.2 mmol, 2.2 eq) and polyethylene oxide (PEO) amine hydrochloride (5 kDa, 5.00 g, 1.0 mmol, 1.0 eq, JenKem) in dry DCM (20 mL) was added triethylamine (TEA) (222 mg, 2.2 mmol, 2.2 eq). The reaction was stirred at room temperature for 48 hours before it was precipitated into a mixture of hexanes/diethyl ether (1/1). The supernatant was decanted and the polymer was dried *in vacuo* to afford the product as a white solid.

^{1}H NMR (600 MHz, $CDCl_3$) δ 7.99 – 7.83 (m, 4H), 7.35 (dd, *J* = 7.7, 1.6 Hz, 1H), 7.29 (dd, *J* = 7.8, 1.4 Hz, 1H), 7.19 – 7.03 (m, 4H), 5.95 (dt, *J* = 15.6, 6.9 Hz, 1H), 4.17 – 4.07 (m, 2H), 3.99 (dd, *J* = 6.9, 1.3 Hz, 2H), 3.59 (s, 524H), 3.33 (s, 3H), 3.06 (q, *J* = 7.4 Hz, 7H), 2.78 (t, *J*

= 7.4 Hz, 2H), 2.63 (s, 2H), 2.05 (t, *J* = 2.4 Hz, 1H), 1.54 (p, *J* = 7.5 Hz, 2H), 1.37 (t, *J* = 7.3 Hz, 12H), 1.20 (d, *J* = 5.1 Hz, 18H), 0.83 (t, *J* = 7.0 Hz, 3H).

The characterization data matched literature.[3]

Scheme 3.12. Synthesis of PtBA-MT-5

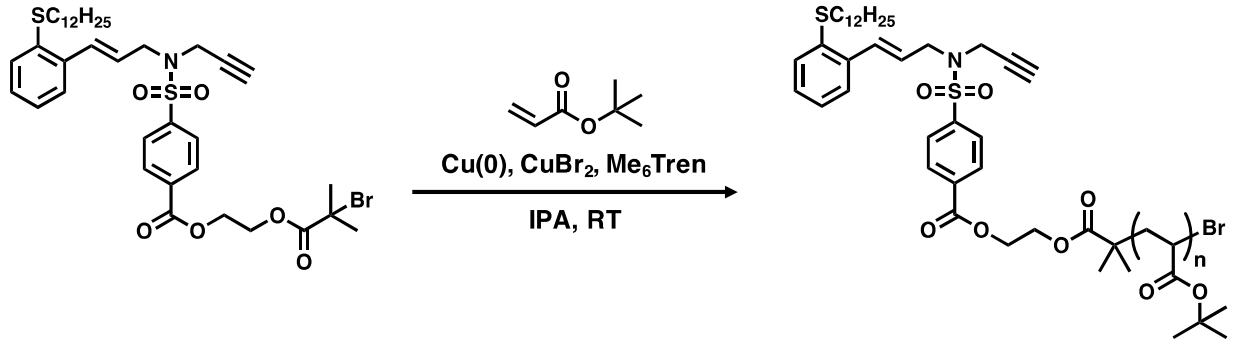

A stir bar with a copper wire was immersed in concentrated HCl. At the same time, a solution of $CuBr_2$ (14.52 mg, 0.065 mmol, 0.05 eq) and Me_6Tren (53.89 mg, 0.234 mmol, 0.18 eq) in isopropanol (IPA) (8.9 mL) was prepared and was sonicated until all material was dissolved. 1 eq of the acrylate monomer was filtered through basic alumina prior to use. The enyne based ATRP initiator (973 mg, 1.30 mmol, 1 eq), 100 equivalents of the acrylate monomer (16.5 mL, 130.0 mmoL, 100 eq), the stock solution prepared above, and 10 mL of IPA (to reach equal total volume compared to monomer) were combined in a 100 mL RBF to ensure minimal headspace. The mixture was purged with nitrogen for 10 minutes. The stir bar with copper wire was thoroughly rinsed with deionized water, acetone, then dried with nitrogen. The stir bar was then suspended above the reaction mixture with a magnet. The flask was further purged with nitrogen for 5 minutes. Then the stir bar/Cu wire was dropped in to start the reaction. The reaction was stirred at 50 □ for c.a. 3 hours and reached ca. 35% conversion. The stir bar was removed from the flask and the reaction mixture was concentrated.

Purification was performed using column chromatography (hexanes:EtOAc = 3:1 to 1:2) to give the product as a colorless oil.

^{1}H NMR (600 MHz, $CDCl_3$) δ 8.16 (dd, *J* = 8.5, 2.1 Hz, 2H), 7.96 (d, *J* = 8.4 Hz, 2H), 7.39 (dd, *J* = 7.7, 1.5 Hz, 1H), 7.33 (d, *J* = 7.9 Hz, 1H), 7.21 (td, *J* = 7.6, 1.4 Hz, 1H), 7.16 (t, *J* = 7.5 Hz, 1H), 7.12 (d, *J* = 15.7 Hz, 1H), 6.00 (dt, *J* = 15.7, 6.9 Hz, 1H), 4.57 (t, *J* = 4.8 Hz, 2H), 4.40 (dq, *J* = 9.6, 5.1, 4.6 Hz, 2H), 4.18 (d, *J* = 2.5 Hz, 2H), 4.13 – 4.09 (m, 1H), 4.04 (d, *J* = 6.9 Hz, 2H), 2.85 – 2.78 (m, 2H), 2.39 – 2.09 (m, 46H), 1.91 – 1.72 (m, 16H), 1.61 – 1.48 (m, 59H), 1.44 (td, *J* = 6.1, 5.4, 2.5 Hz, 416H), 1.35 – 1.28 (m, 11H), 1.28 – 1.17 (m, 20H), 1.14 (d, *J* = 5.4 Hz, 7H), 0.87 (t, *J* = 7.0 Hz, 3H).

Scheme 3.13. Synthesis of PnBA-MT-6

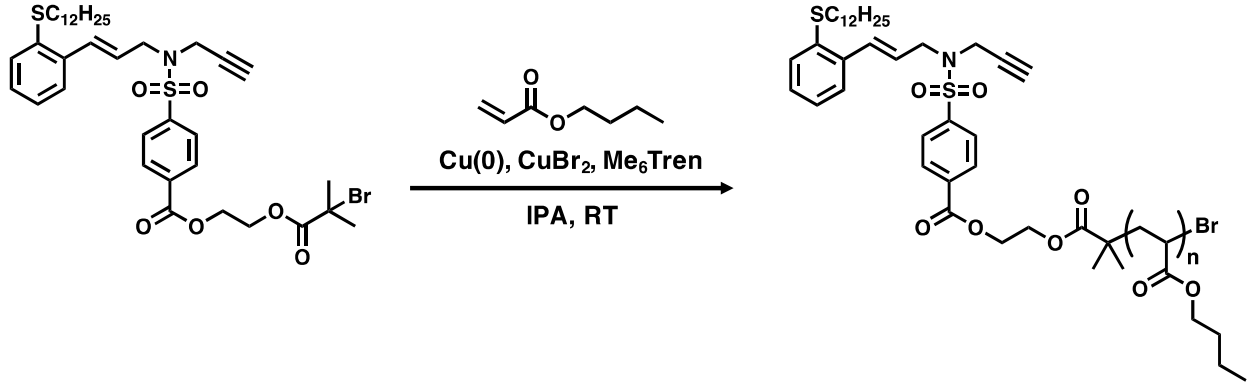

A stir bar with a copper wire was immersed in concentrated HCl. At the same time, a solution of $CuBr_2$ (14.52 mg, 0.065 mmol, 0.05 eq) and Me_6Tren (53.89 mg, 0.234 mmol, 0.18 eq) in isopropanol (IPA) (8.5 mL) was prepared and was sonicated until all material dissolved. 1 eq of the acrylate monomer was filtered through basic alumina prior to use. The enyne functionalized ATRP initiator (973 mg, 1.30 mmol, 1 eq), 100 equivalent of the acrylate monomer (18.7 mL, 130.0 mmol, 100 eq), the stock solution prepared above, and 8 mL of IPA were combined in a 100 mL RBF to ensure minimal headspace. The mixture was purged with

nitrogen for 10 minutes. The stir bar with copper wire was thoroughly rinsed with deionized water, acetone, then dried with nitrogen. The stir bar was then suspended above the reaction mixture with a magnet. The flask was further purged with nitrogen for 5 minutes. Then the stir bar/Cu wire was dropped in to start the reaction. The reaction was stirred at room temperature for ca. 4 hours and reached ca. 50% conversion. The stir bar was removed from the flask and the reaction mixture was concentrated. Purification was performed using column chromatography (hexanes:EtOAc = 3:1 to 1:1) to give the product as a colorless oil.

^{1}H NMR (600 MHz, $CDCl_3$) δ 8.14 (d, *J* = 8.0 Hz, 2H), 7.94 (d, *J* = 8.4 Hz, 2H), 7.37 (dd, *J* = 7.7, 1.5 Hz, 1H), 7.31 (d, *J* = 7.5 Hz, 1H), 7.19 (td, *J* = 7.6, 1.6 Hz, 1H), 7.13 (t, *J* = 7.5 Hz, 1H), 7.10 (d, *J* = 15.7 Hz, 1H), 5.98 (dt, *J* = 15.8, 6.9 Hz, 1H), 4.59 – 4.49 (m, 2H), 4.36 (tdd, *J* = 12.1, 7.5, 4.7 Hz, 2H), 4.23 – 4.11 (m, 5H), 4.01 (ttd, *J* = 18.9, 10.2, 9.3, 6.7 Hz, 104H), 2.87 – 2.75 (m, 2H), 2.63 (dtt, *J* = 19.1, 9.5, 4.1 Hz, 1H), 2.47 – 2.10 (m, 52H), 2.10 – 1.96 (m, 4H), 1.87 (td, *J* = 21.7, 18.0, 10.7 Hz, 24H), 1.77 – 1.28 (m, 290H), 1.28 – 1.16 (m, 18H), 1.16 – 1.06 (m, 7H), 0.91 (t, *J* = 7.5 Hz, 153H).

3.6.4 Miktoarm Star Polymer Synthesis and Characterization

μSTAR: General Synthetic Technique for AB_n Miktoarm Stars

A 20 mL vial was charged with a stir bar and then the macromonomer was massed into the vial. The macroterminator was massed into a separate vial and then both vials were brought into a nitrogen filled glovebox. The macroterminator and macromonomer were dissolved in DCM at 100 mg/mL (20 mg/mL for PS and PDMS macromonomer). Then a stock solution of G3 was prepared in DCM. All stock solutions were prepared by mass. A given volume of G3 catalyst stock solution (1.0 eq) was added quickly to a vigorously stirring solution of the

macromonomer (*n* eq). The vial was massed before and after G3 addition to accurately determine the amount of G3 catalyst that was added. The reaction was left to react for 30 minutes after which an aliquot was extracted into a tared vial, brought outside the glovebox, and quenched with excess ethyl vinyl ether. The reaction vial was massed before and after taking the aliquot to determine the amount removed. Then 1.0 equivalent of the macroterminator was added (accounting for the amount of reaction volume that was removed for the aliquot). The reaction was left to stir overnight in the glovebox. The vial was then removed from the glovebox and ethyl vinyl ether was added to ensure the catalyst was completely quenched. 2,4,6-Trimercaptotriazine-functionalized silica gel was added (20 equiv) and stirred for 30 minutes. The solution was then passed through a syringe filter, concentrated *in vacuo*, and precipitated into methanol, diethyl ether, or hexanes and then dried.

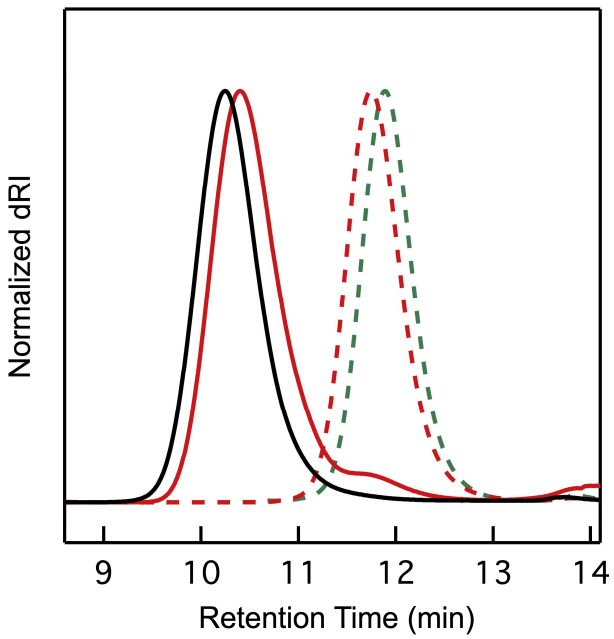

Figure 3.11. SECs (normalized differential refractive index signal) of $(PLA\text{-}MM\text{-}5)_4$-PDMS-MT-6 (solid black line) and constituent materials: PLA-MM-5 (orange dashed lined), PDMS-MT-6 (green dashed line), and $(PLA\text{-}MM\text{-}5)_4$ (solid orange line).

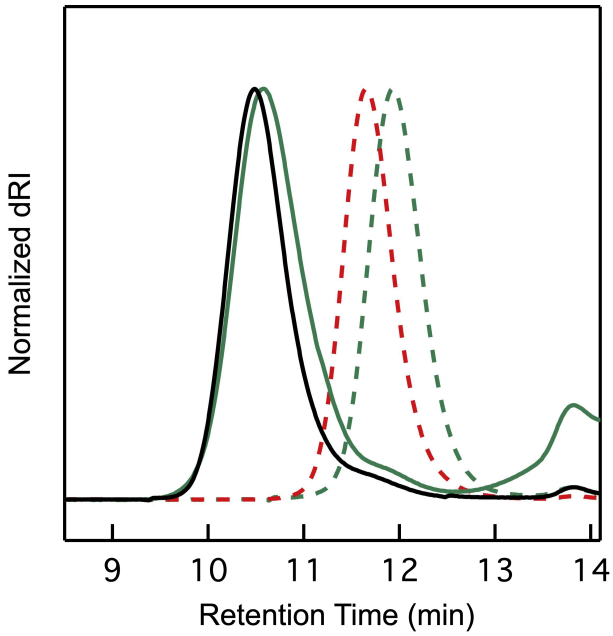

Figure 3.12. SECs (normalized differential refractive index signal) of $(PDMS\text{-}MM\text{-}6)_4$-PLA-MT-4 (solid black line) and constituent materials: PDMS-MM-6 (green dashed line), PLA-MT-4 (orange dashed line), and $(PDMS\text{-}MM\text{-}6)_4$ (green solid line).

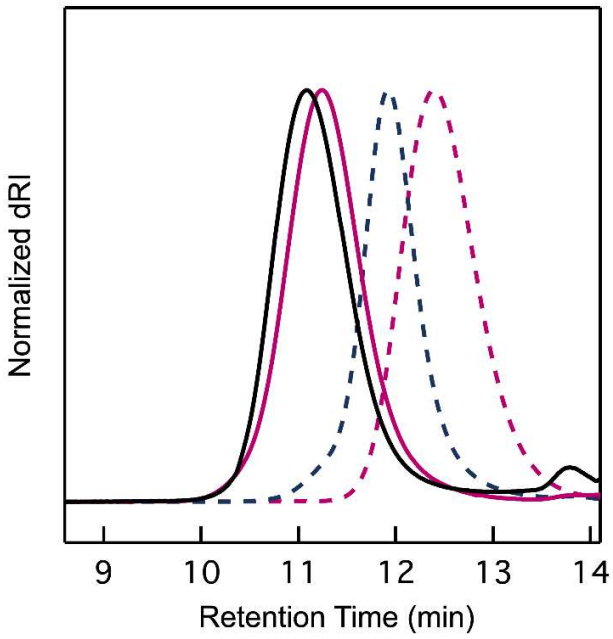

Figure 3.13. SECs (normalized differential refractive index signal) of $(PMMA\text{-}MM\text{-}4)_4$-PAA-MT-5 (solid black line) and constituent materials: PMMA-MM-4 (pink dashed line), PtBA-MT-5 (dark dashed line), and $(PMMA\text{-}MM\text{-}4)_4$ (solid pink line).

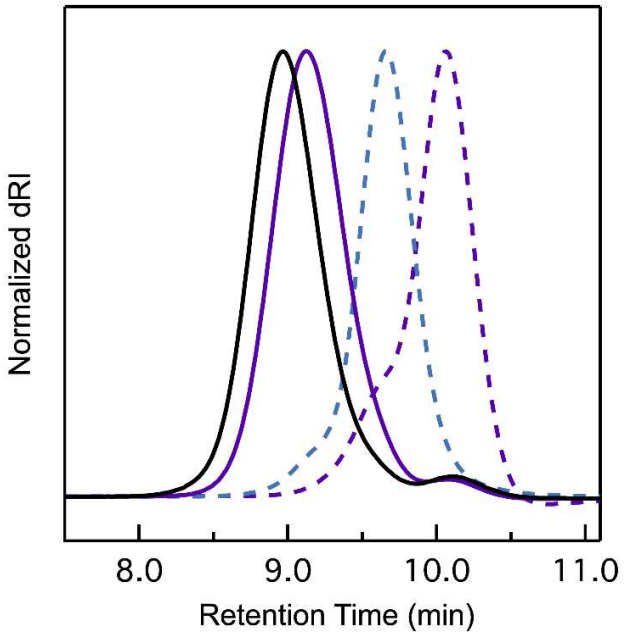

Figure 3.14. SECs (normalized differential refractive index signal) of $(PTFEA\text{-}MM\text{-}6)_4$-PnBA-MT-6 (solid black line) and constituent materials: PTFEA-MM-6 (purple dashed line), PnBA-MT-6 (blue dashed line), and $(PTFEA\text{-}MM\text{-}6)_4$ (purple solid line).

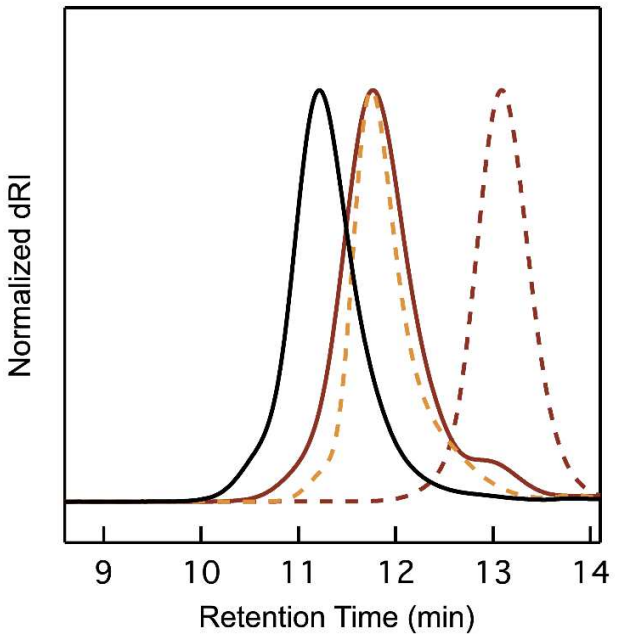

Figure 3.15. SECs (normalized differential refractive index signal) of $(PS\text{-}MM\text{-}2)_4$-PEO-MT-5 (solid black line) and constituent materials: PS-MM-2 (brown dashed line), PEO-MT-5 (yellow dashed line), and $(PS\text{-}MM\text{-}2)_4$ (brown solid line).

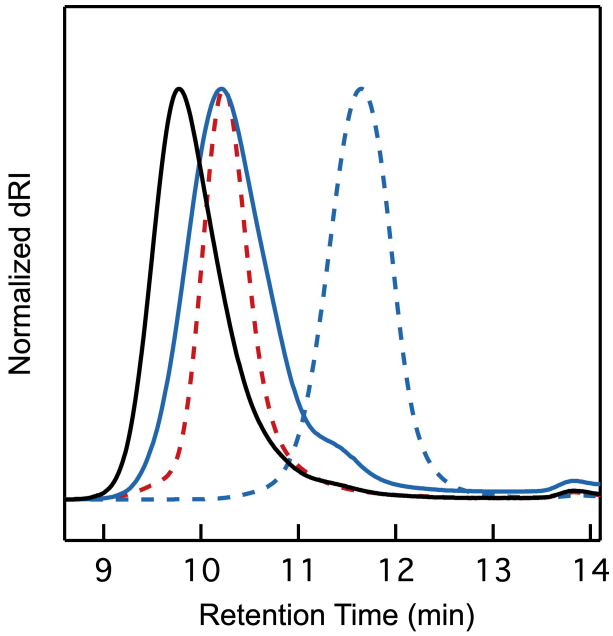

Figure 3.16. SECs (normalized differential refractive index signal) of (P4MCL-PLA-MM-4-3)$_3$-PLA-MT-24 (solid black line) and constituent materials: P4MCL-PLA-MM-4-3 (blue dashed line), PLA-MT-24 (orange dashed line), and (P4MCL-PLA-MM-4-3)$_3$ (blue solid line).

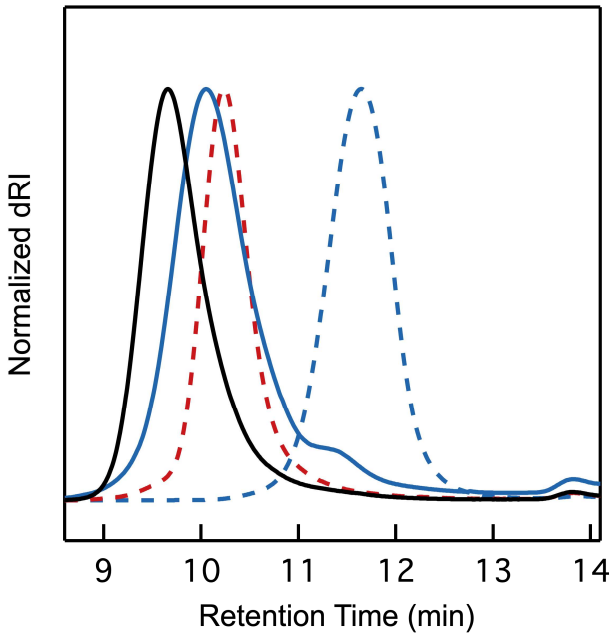

Figure 3.17. SECs (normalized differential refractive index signal) of (P4MCL-PLA-MM-4-3)$_5$-PLA-MT-24 (solid black line) and constituent materials: P4MCL-PLA-MM-4-3 (blue dashed line), PLA-MT-24 (orange dashed line), and (P4MCL-PLA-MM-4-3)$_5$ (blue solid line).

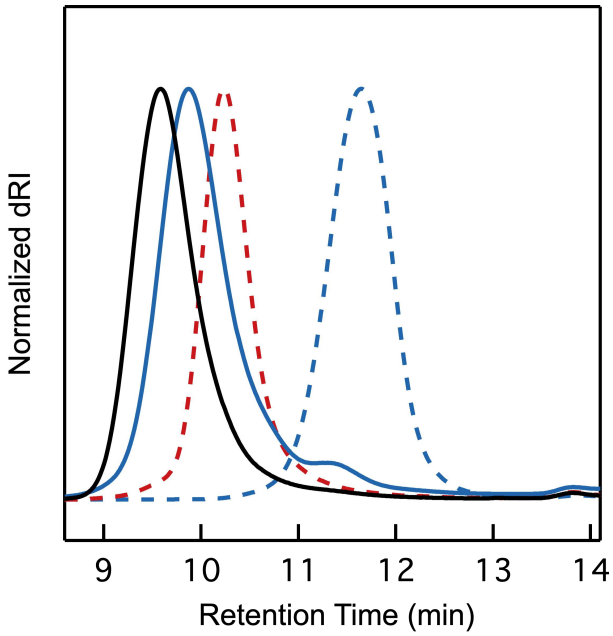

Figure 3.18. SECs (normalized differential refractive index signal) of (P4MCL-PLA-MM-4-3)$_7$-PLA-MT-24 (solid black line) and constituent materials: P4MCL-PLA-MM-4-3 (blue dashed line), PLA-MT-24 (orange dashed line), and (P4MCL-PLA-MM-4-3)$_7$ (blue solid line).

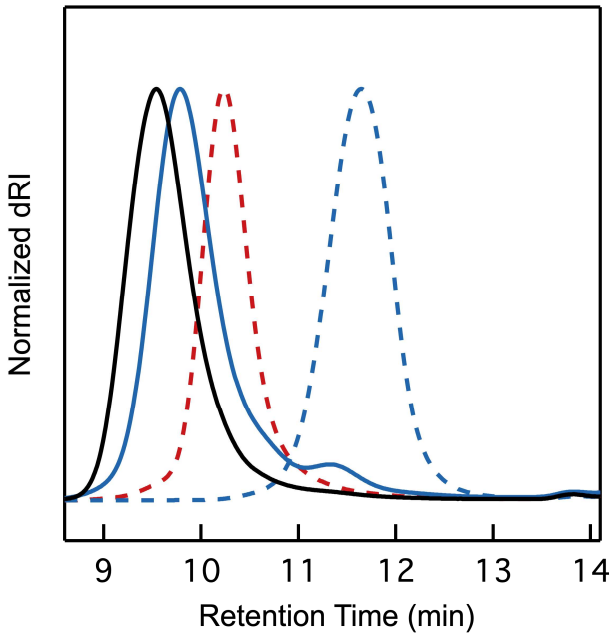

Figure 3.19. SECs (normalized differential refractive index signal) of (P4MCL-PLA-MM-4-3)$_9$-PLA-MT-24 (solid black line) and constituent materials: P4MCL-PLA-MM-4-3 (blue dashed line), PLA-MT-24 (orange dashed line), and (P4MCL-PLA-MM-4-3)$_9$ (blue solid line).

3.6.5 Miktoarm Star NMR Data

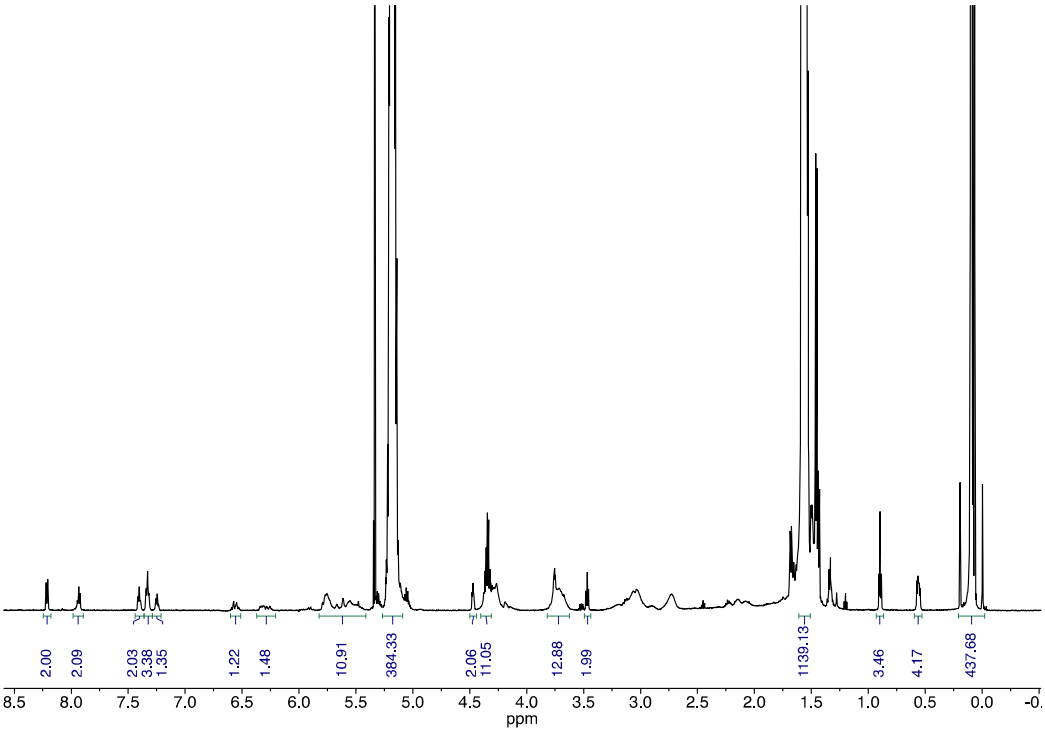

Figure 3.20. ^{1}H NMR spectrum of (PLA-MM-5)$_4$-PDMS-MT-5 (CD_2Cl_2, 600 MHz).

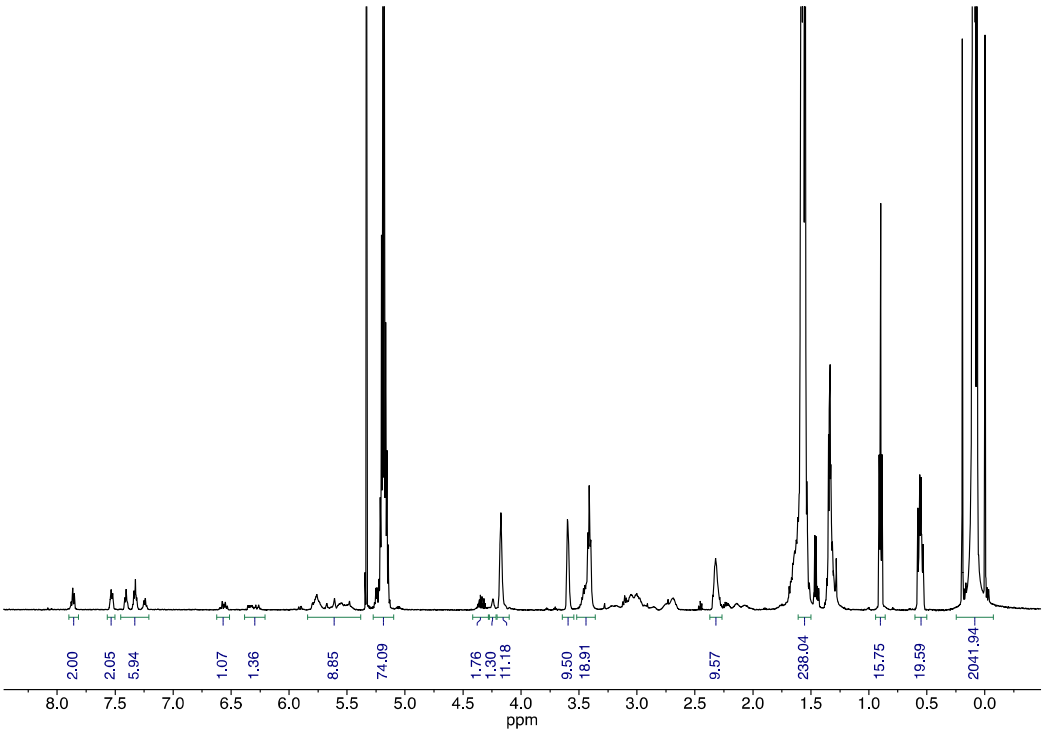

Figure 3.21. ^{1}H NMR spectrum of (PDMS-MM-5)$_4$-PLA-MT-4 (CD_2Cl_2, 600 MHz).

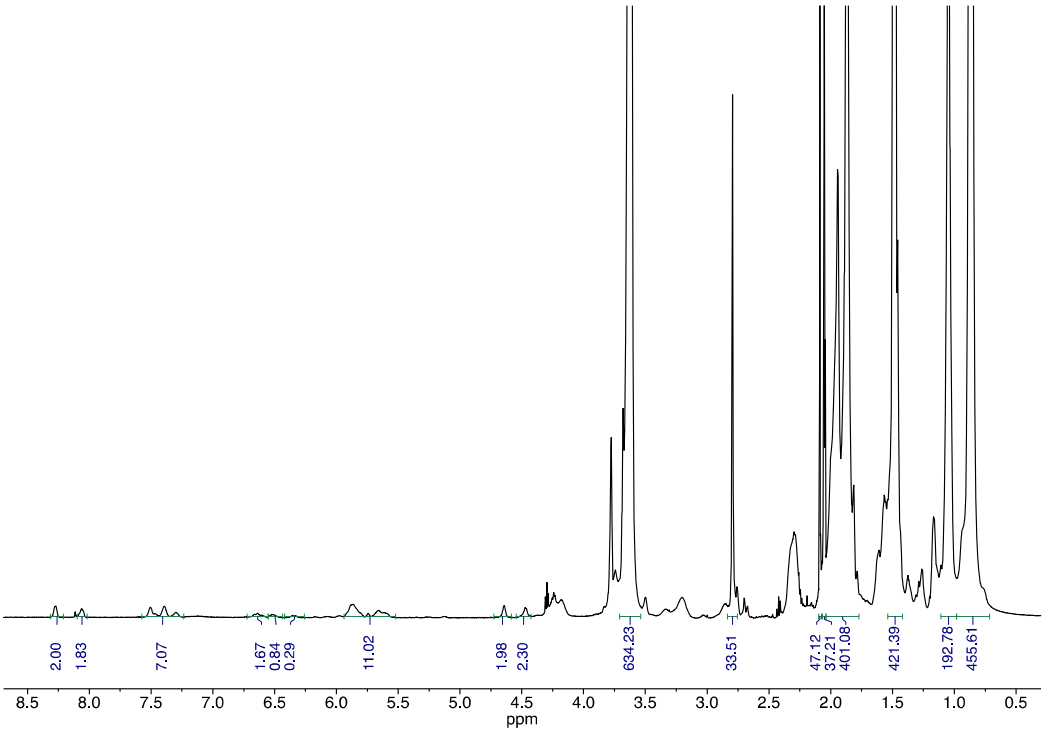

Figure 3.22. ^{1}H NMR spectrum of $(PMMA\text{-}MM\text{-}4)_4$-PtBA-MT-5 ($(CD_3)_2CO$, 600 MHz).

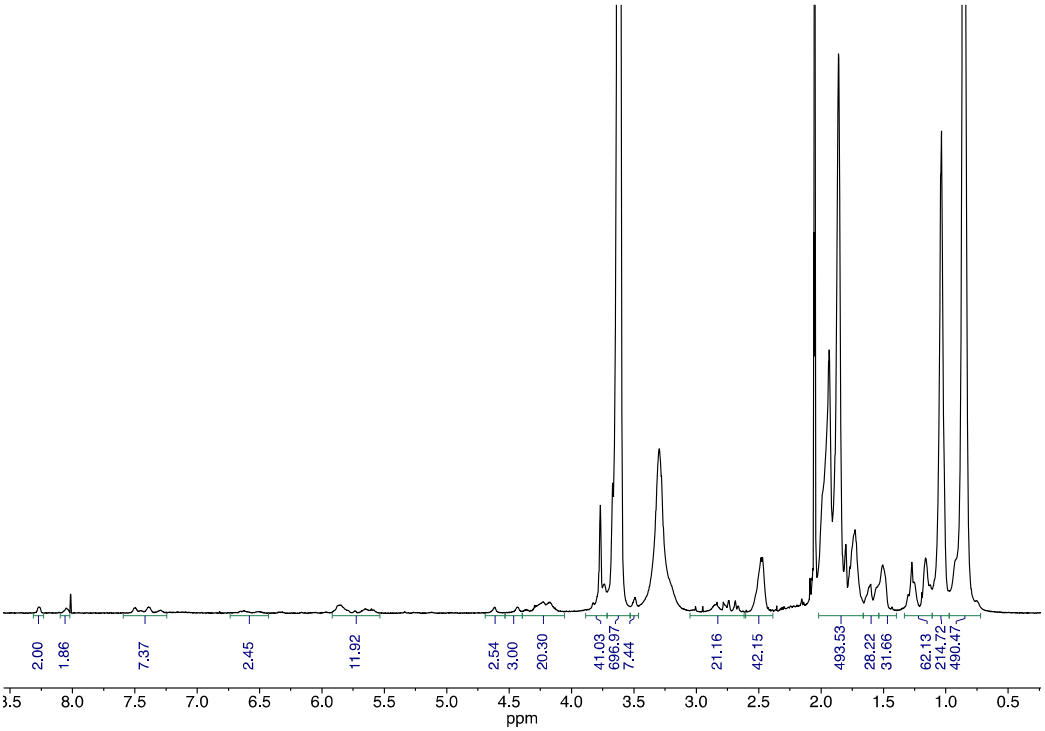

Figure 3.23. ^{1}H NMR spectrum of $(PMMA\text{-}MM\text{-}4)_4$-PAA-MT-5 with added D_2O ($(CD_3)_2CO$, 600 MHz).

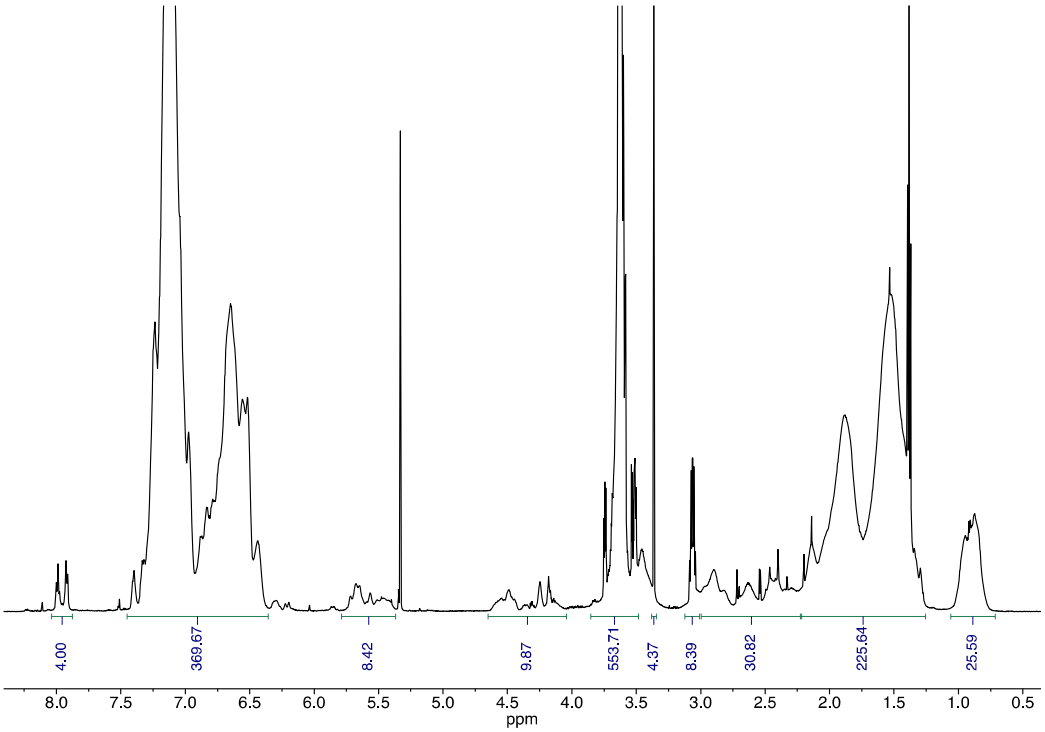

Figure 3.24. ^{1}H NMR spectrum of $(PS\text{-}MM\text{-}2)_4$-PEO-MT-5 ($CD_2Cl_2$, 600 MHz).

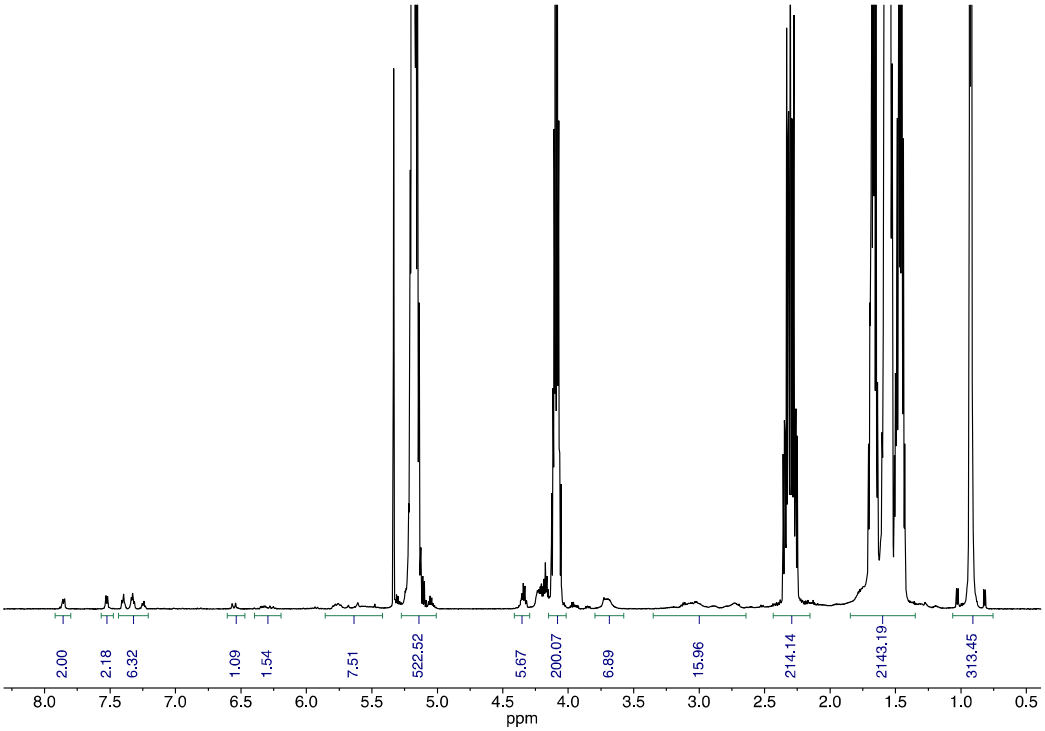

Figure 3.25. ^{1}H NMR spectrum of $(P4MCL\text{-}PLA\text{-}MM\text{-}4\text{-}3)_3$-PLA-MT-24 ($CD_2Cl_2$, 600 MHz).

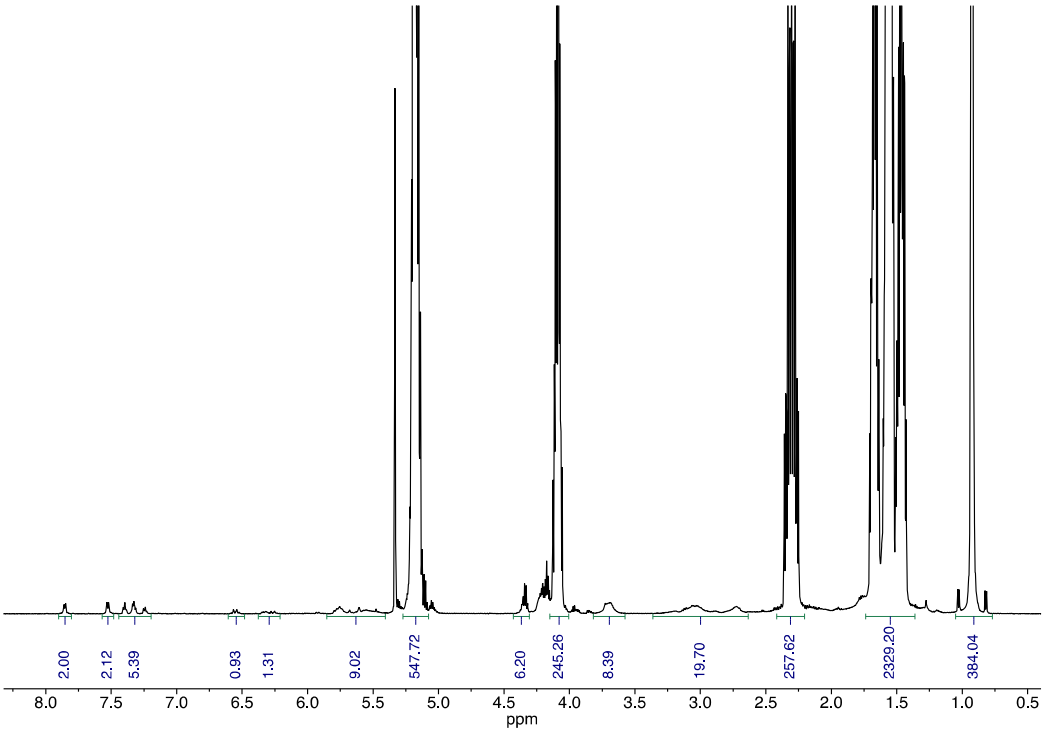

Figure 3.26. ^{1}H NMR spectrum of (P4MCL-PLA-MM-4-3)$_5$-PLA-MT-24 (CD_2Cl_2, 600 MHz).

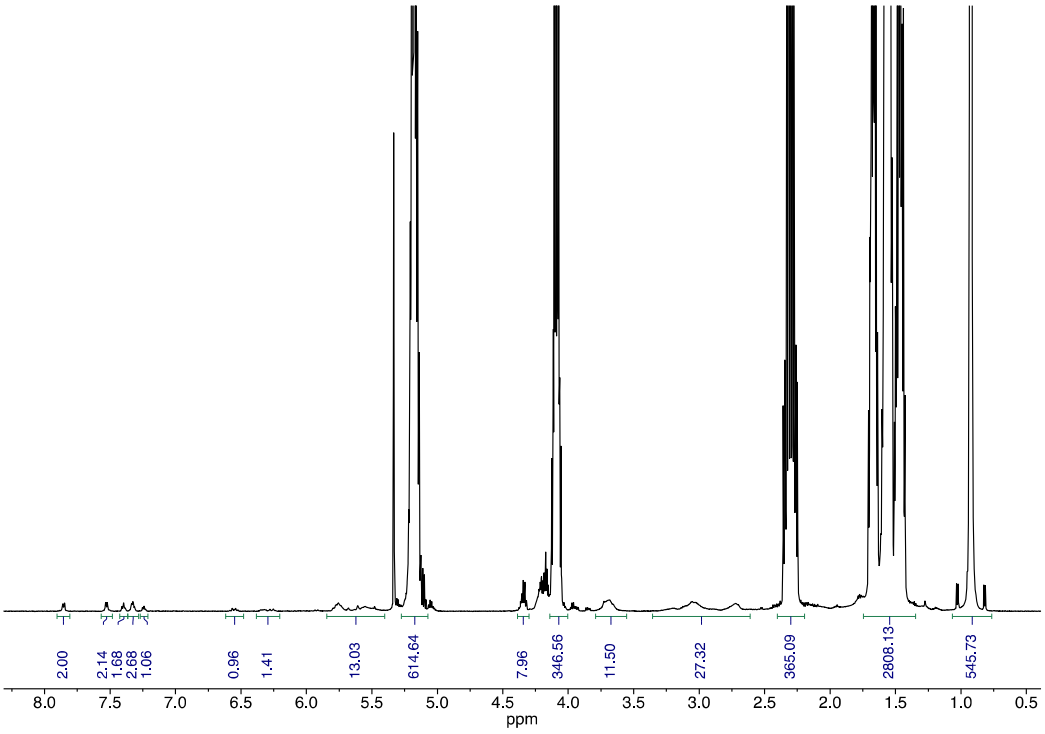

Figure 3.27. ^{1}H NMR spectrum of (P4MCL-PLA-MM-4-3)$_7$-PLA-MT-24 (CD_2Cl_2, 600 MHz).

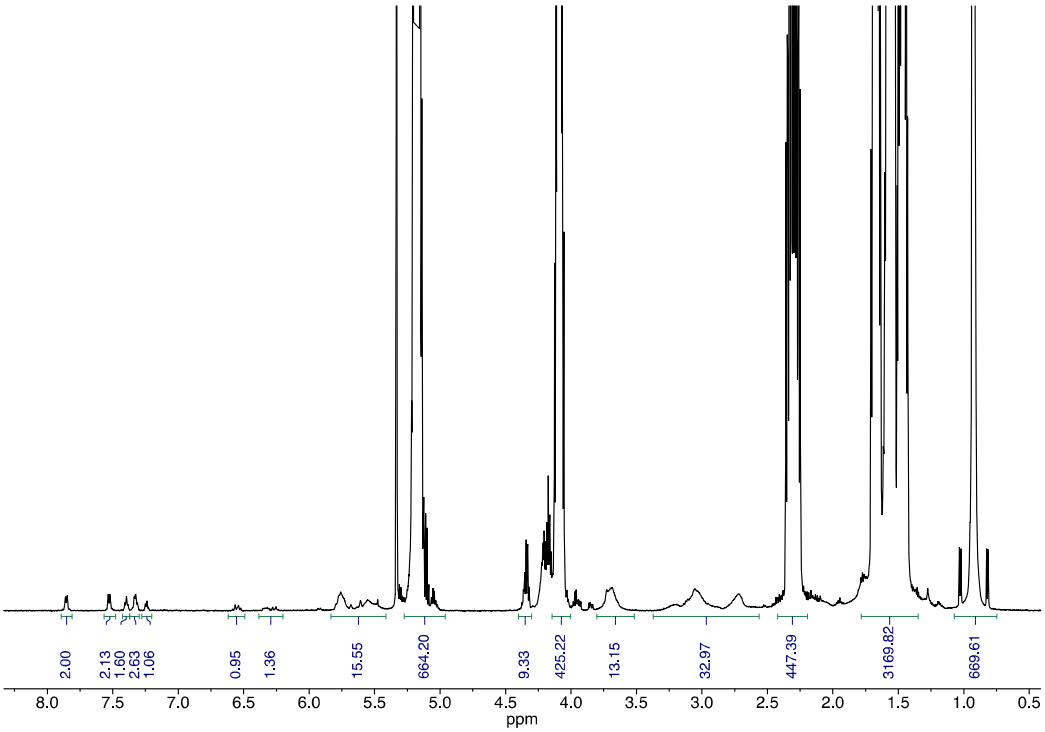

Figure 3.28. ^{1}H NMR spectrum of (P4MCL-PLA-MM-4-3)$_9$-PLA-MT-24 (CD_2Cl_2, 600 MHz).

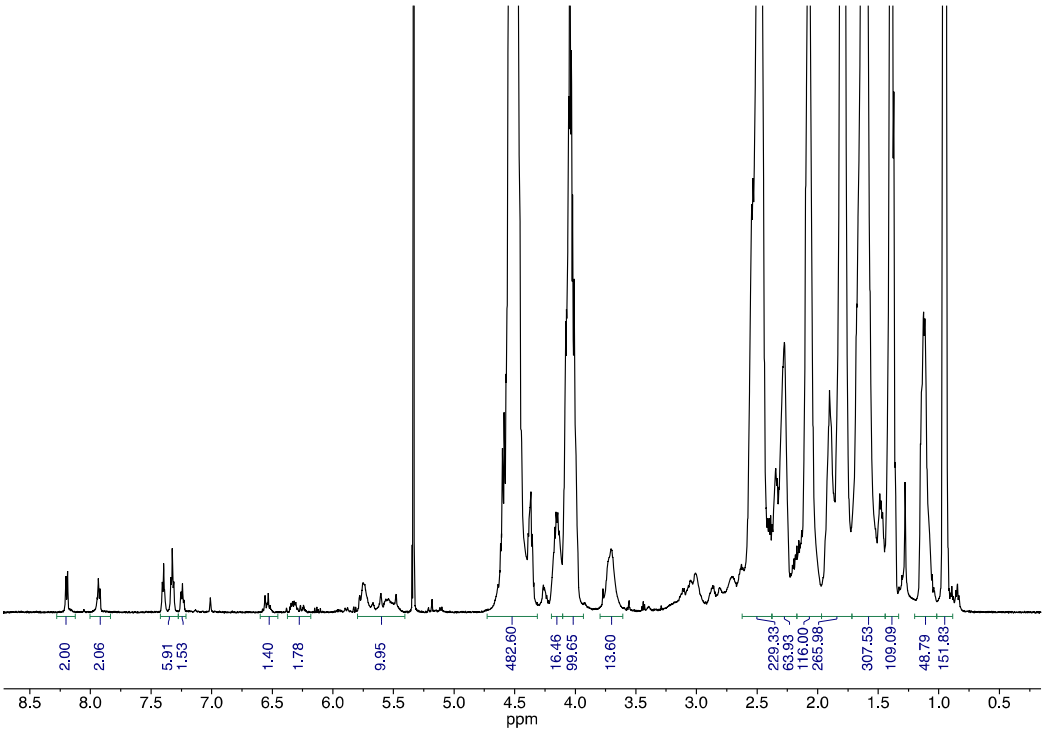

Figure 3.29. ^{1}H NMR spectrum of (PTFEA-MM-6)$_4$-PnBA-MT-6 (CD_2Cl_2, 600 MHz).

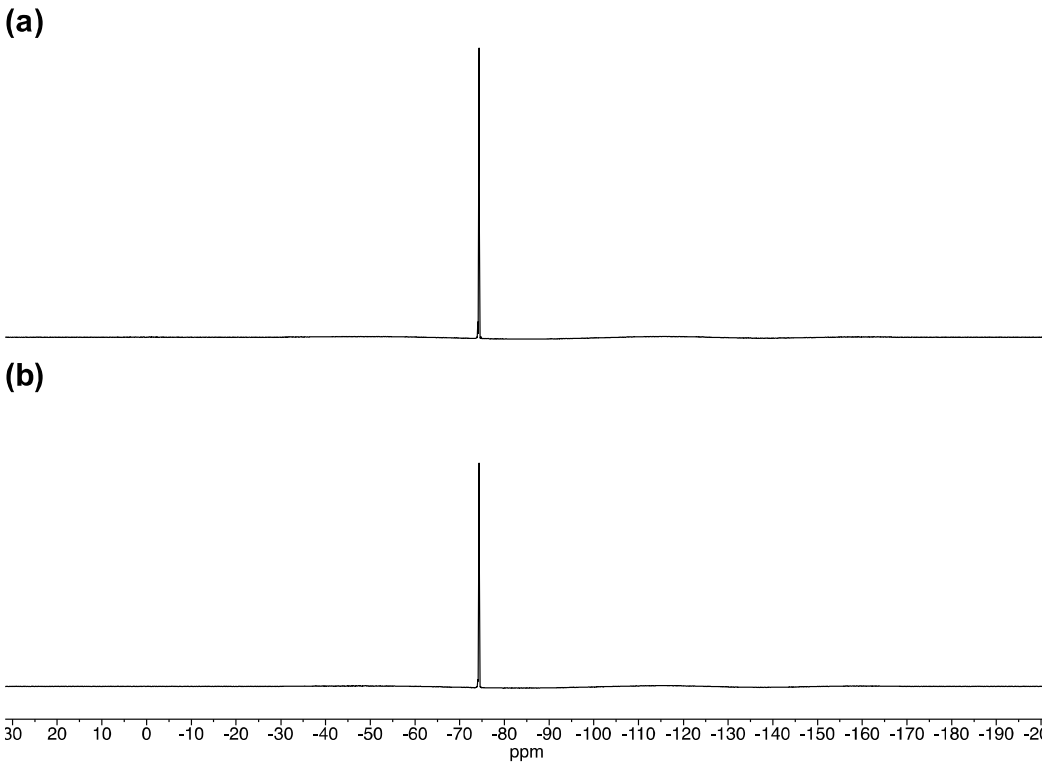

Figure 3.30. ^{19}F NMR spectrum of (a) PTFEA-MM-6 and (b) (PTFEA-MM-6)$_4$-PnBA-MT-6.

3.6.6 DOSY Data Analysis

DOSY data analysis was performed in Mathematica. The data were normalized and, to determine the self-diffusion coefficient, fit to a single exponential function. $I = I_0 \exp[-(\gamma g \delta)^2(\Delta - g/3)D]$,[8] where γ is the magnetogyric ratio, δ is the effective gradient duration, g is the magnitude of the gradient pulse, Δ is the diffusion time, and D is the self-diffusion coefficient. In the same star polymer sample, diffusion coefficients where found to be consistent across all the peaks analyzed, indicating there is only one species diffusing. Additionally, R^2 values > 0.999 were obtained for all fits. The data were also fit with a multiple-exponential form $\frac{I}{I_0} = \sum f_i \exp[-(\gamma g \delta)^2(\Delta - g/3)D_i]$ in an attempt to analyze the purity of star polymers from the ratio of $\frac{f_i}{\sum f_i} = X_i$. However, the presence of multiple components

failed to significantly improve the fit compared to a single exponential on the basis of R^2 values. More importantly, multi-component fits gave inconsistent results for the same sample at different chemical shifts and non-physical diffusion coefficient values for the assumed macromonomer and macroterminator components, which were often too large (on the order of small molecules). Thus, within measurement error, we conclude that these stars are diffusing as a single component without macromonomer or macroterminators impurities. A representative comparison between the single and multiple exponential fitting results is provided for the highest molecular weight species synthesized by μSTAR (P4MCL-PLA-MM-4-3)$_9$-PLA-MT-24 (**Tables 3.6, 3.7**).

Table 3.6. Comparison of single and multi-component fits derived from ^{1}H DOSY data for (P4MCL-PLA-MM-4-3)$_3$-PLA-MT-24 at two different chemical shifts. The diffusion constant of solvent ($CHCl_3$) is included for reference. The multi-component fits give physically unrealistic values of the macromonomer and macroterminator diffusion constants. We conclude that, within error, the (P4MCL-PLA-MM-4-3)$_3$-PLA-MT-24 miktoarm star contains no homopolymer contaminants.

	7.26 ppm	5.2 ppm		1.5 ppm	
		Single	Multi	Single	Multi
D_{Star}[a]	-	30	29	30	29
D_{MT}[a]	-	-	3150[c]	-	3010[c]
D_{MM}[a]	-	-	3150[c]	-	3010[c]
$D_{Solvent}$	2000	-	-	-	-
X_{Star}[b]	-	1	0.98	1	0.96
R^2	-	0.99993	0.99994	0.99980	0.99991

[a]μm^2/s. [b]Mole fraction of miktoarm star polymer. [c]Physically unrealistic ($D > D_{Solvent}$).

Table 3.7. Comparison of single and multi-component fits derived from ^{1}H DOSY data for (P4MCL-PLA-MM-4-3)$_9$-PLA-MT-24 at two different chemical shifts. The diffusion constant of solvent ($CHCl_3$) is included for reference. The multi-component fits give physically unrealistic values of the macromonomer and macroterminator diffusion constants. We conclude that, within error, the (P4MCL-PLA-MM-4-3)$_9$-PLA-MT-24 miktoarm star contains no homopolymer contaminants.

	7.26 ppm	5.2 ppm		1.5 ppm	
		Single	Multi	Single	Multi
D_{Star}[a]	-	24	23	23	23
D_{MT}[a]	-	-	3000[c]	-	3000[c]
D_{MM}[a]	-	-	3000[c]	-	3000[c]
$D_{Solvent}$	2000	-	-	-	-
X_{Star}[b]	-	1	0.97	1	0.96
R^2	-	0.99982	0.99989	0.99978	0.99991

[a]μm^2/s. [b]Mole fraction of miktoarm star polymer. [c]Physically unrealistic ($D > D_{Solvent}$).

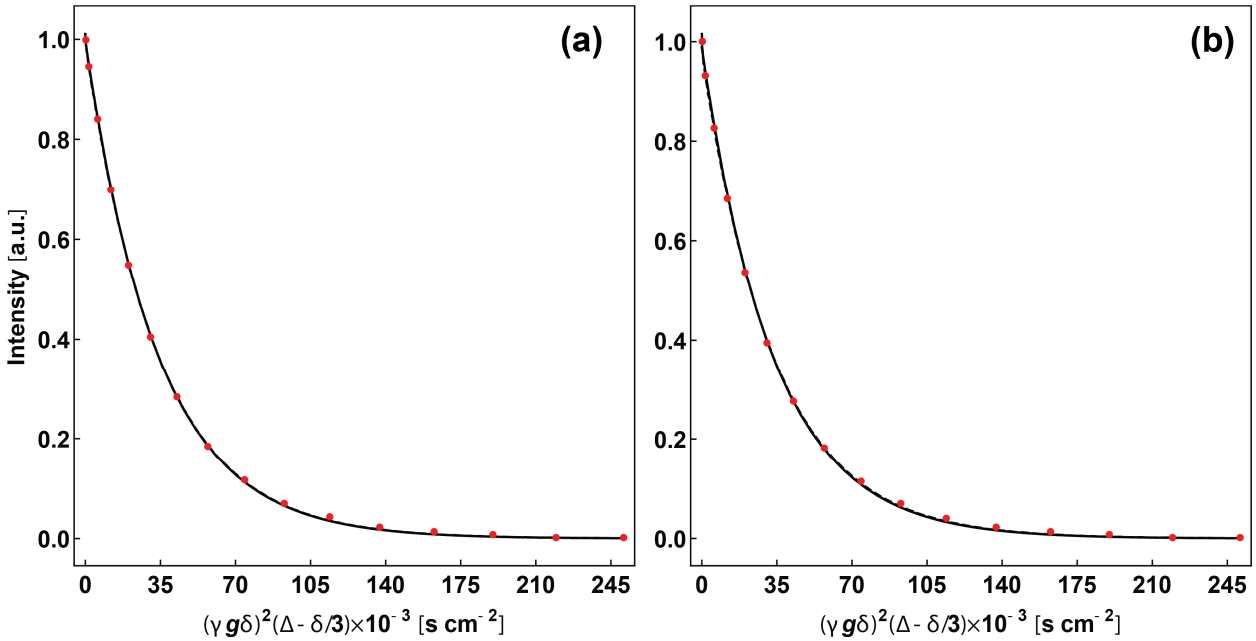

Figure 3.31. Stimulated echo intensity attenuation intensities of the NMR signal at **(a)** 5.2 ppm and **(b)** 1.5 ppm for (P4MCL-PLA-MM-4-3)$_3$-PLA-MT-24. Raw data is displayed as red dots, single exponential fits as solid black lines, and multi-exponential fits are dashed black lines.

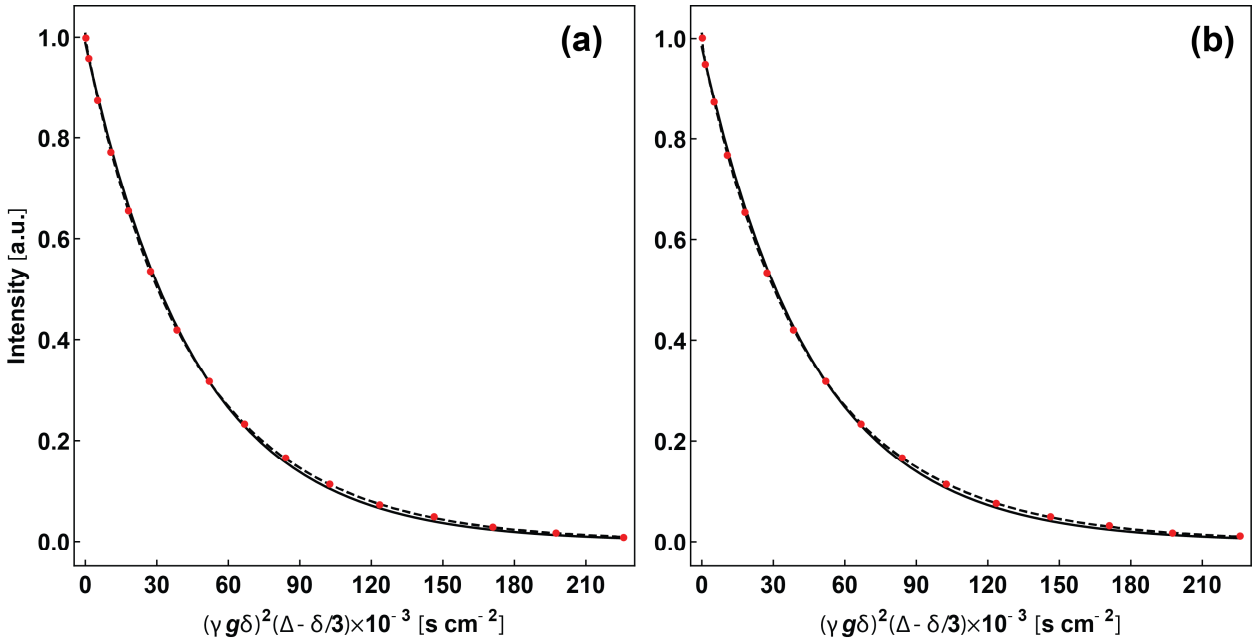

Figure 3.32. Stimulated echo intensity attenuation intensities of the NMR signal at **(a)** 5.2 ppm and **(b)** 1.5 ppm for $(P4MCL\text{-}PLA\text{-}MM\text{-}4\text{-}3)_9$-PLA-MT-24. Raw data is displayed as red dots, single exponential fits as solid black lines, and multi-exponential fits as dashed black lines.

Scheme 3.14. $(PMMA\text{-}MM\text{-}4)_4$-PtBA-MT-5 Deprotection

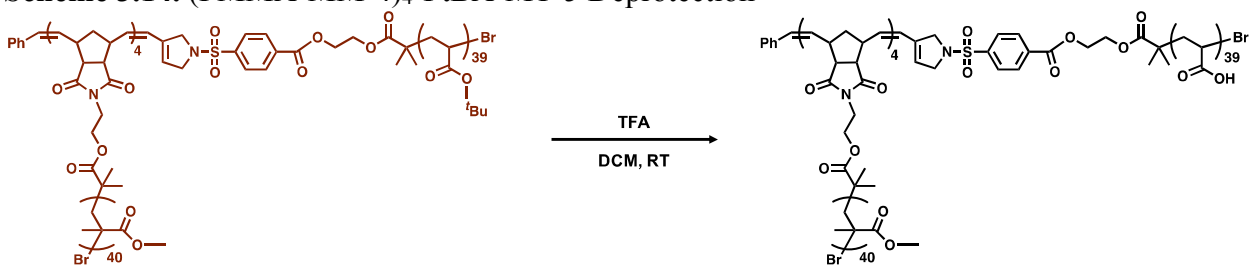

A vial was charged with a stir bar and 100 mg of $(PMMA\text{-}MM\text{-}4)_4$-PtBA-MT-5. It was dissolved in 1 mL of $CHCl_3$ and then 1 mL of trifluoroacetic acid (TFA) was added. After stirring for 24 hours, the reaction was precipitated into hexanes and centrifuged. The hexanes was decanted and the polymer was dried *in vacuo*.

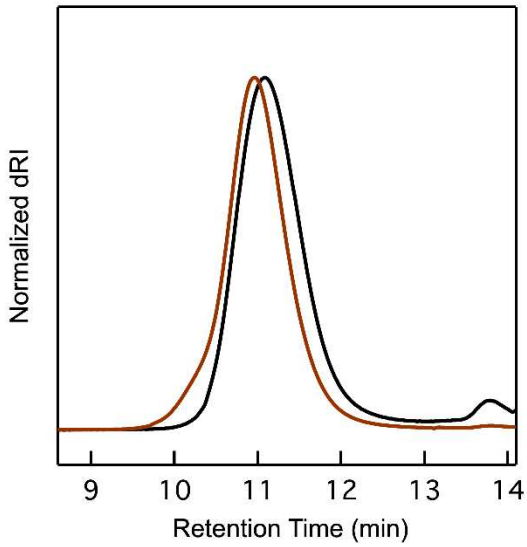

Figure 3.33. SECs (normalized differential refractive index signal) of (PMMA-MM-4)$_4$-PtBA-MT-5 (brown trace) and (PMMA-MM-4)$_4$-PAA-MT-5 (black trace) before and after *tert*-butyl deprotection, respectively.

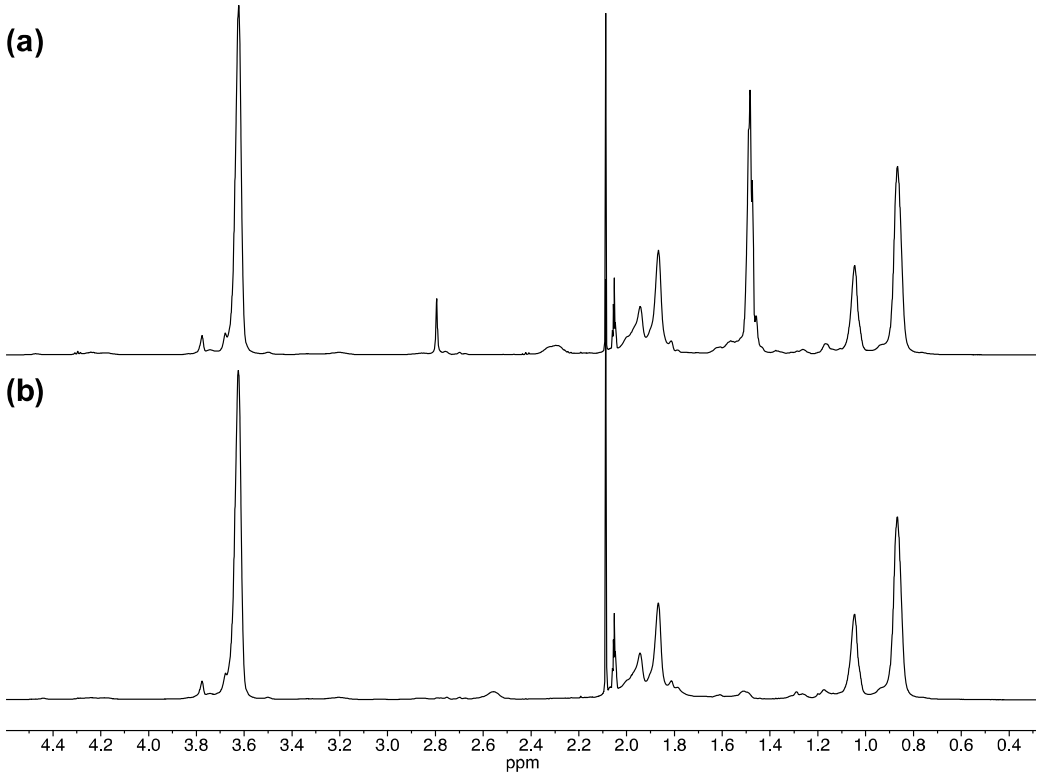

Figure 3.34. ^{1}H-NMR of (a) (PMMA-MM-4)$_4$-PtBA-MT-5 and (b) (PMMA-MM-4)$_4$-PAA-MT-5 (before and after *t*-butyl deprotection). Absence of the *t*-butyl group is apparent at 1.5 ppm after treatment with TFA.

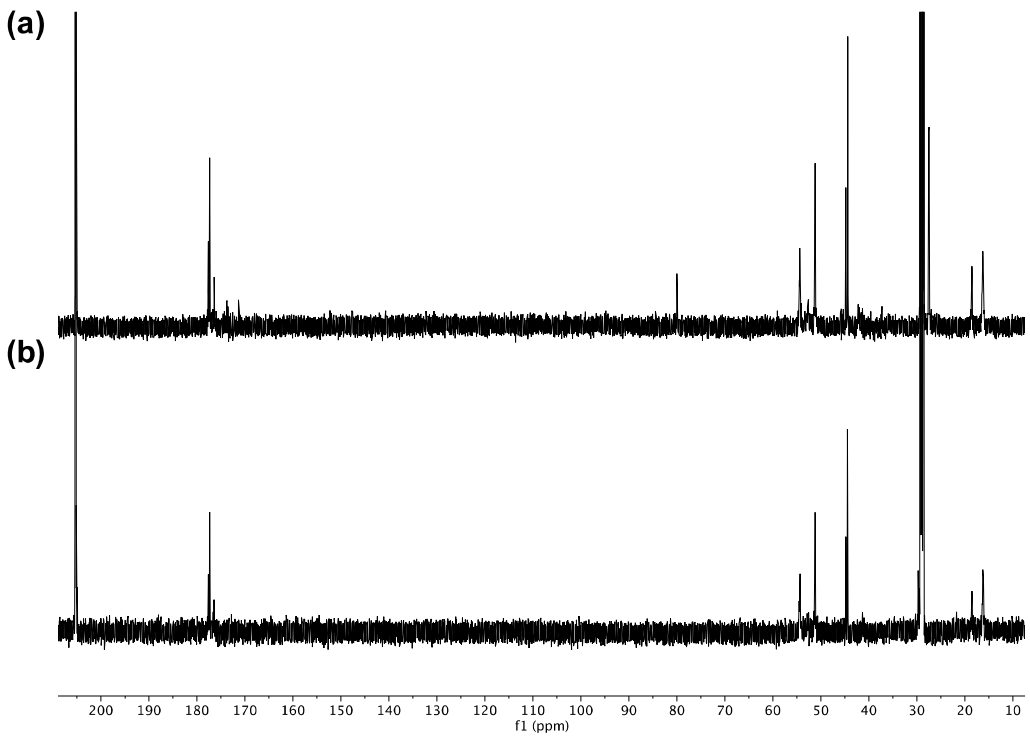

Figure 3.35. ^{13}C-NMR of (a) (PMMA-MM-4)$_4$-PtBA-MT-5 and (b) (PMMA-MM-4)$_4$-PAA-MT-5 (before and after t-butyl deprotection). Absence of the *t*-butyl group is apparent at 28 and 80 ppm after treatment with TFA.

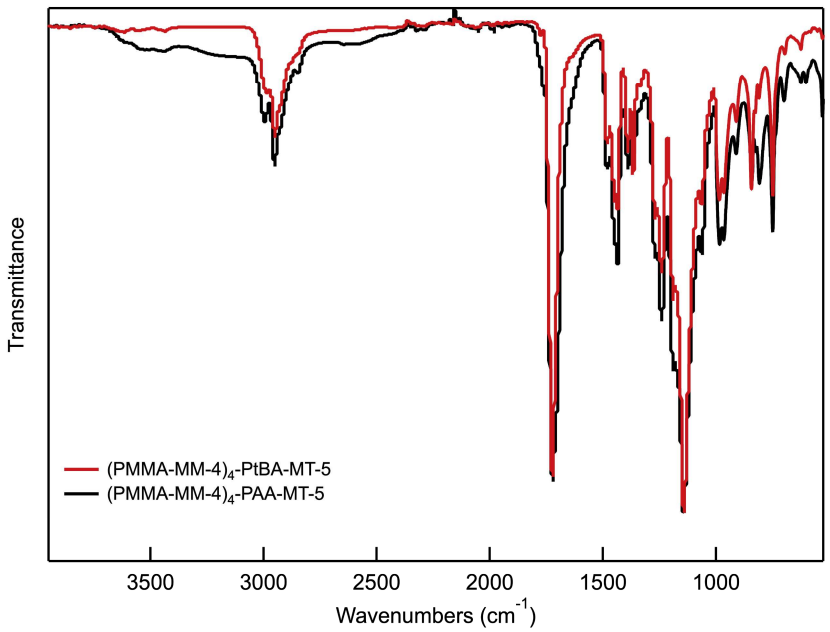

Figure 3.36. FTIR spectra of (PMMA-MM-4)$_4$-PtBA-MT-5 (red trace) and (PMMA-MM-4)$_4$-PAA-MT-5 (black trace) (before and after *t*-butyl deprotection) normalized to the peak at 1140 cm^{-1}.

3.6.7 Additional NMR Spectra

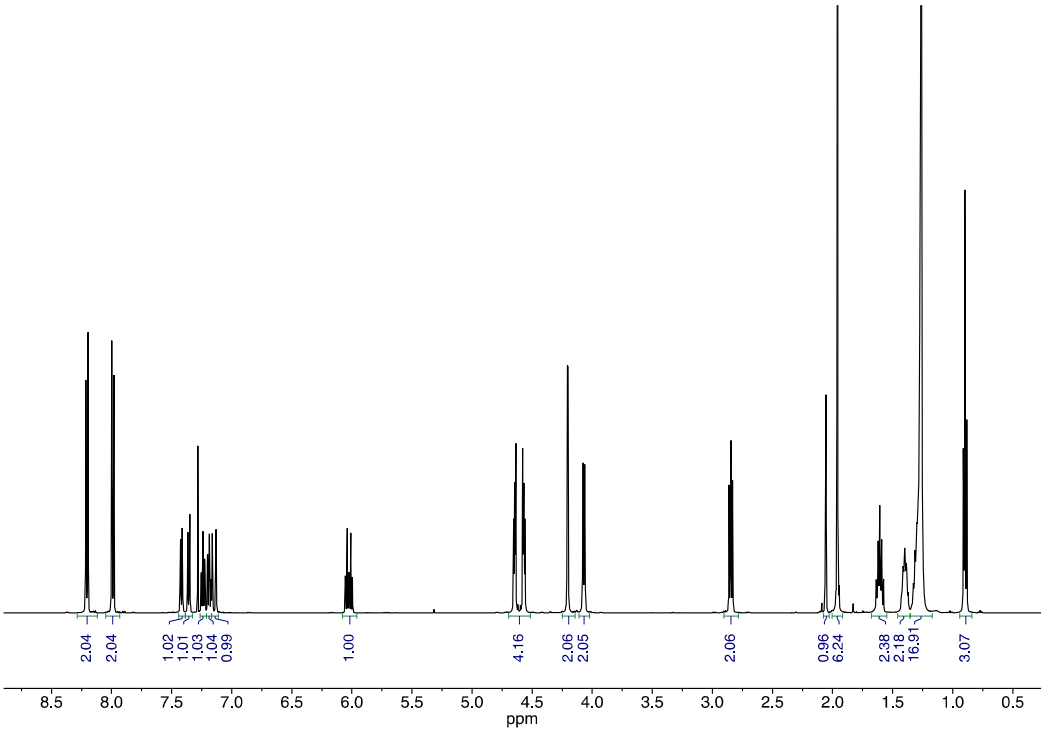

Figure 3.37. ^{1}H NMR spectrum of enyne ATRP initiator ($CDCl_3$, 500 MHz).

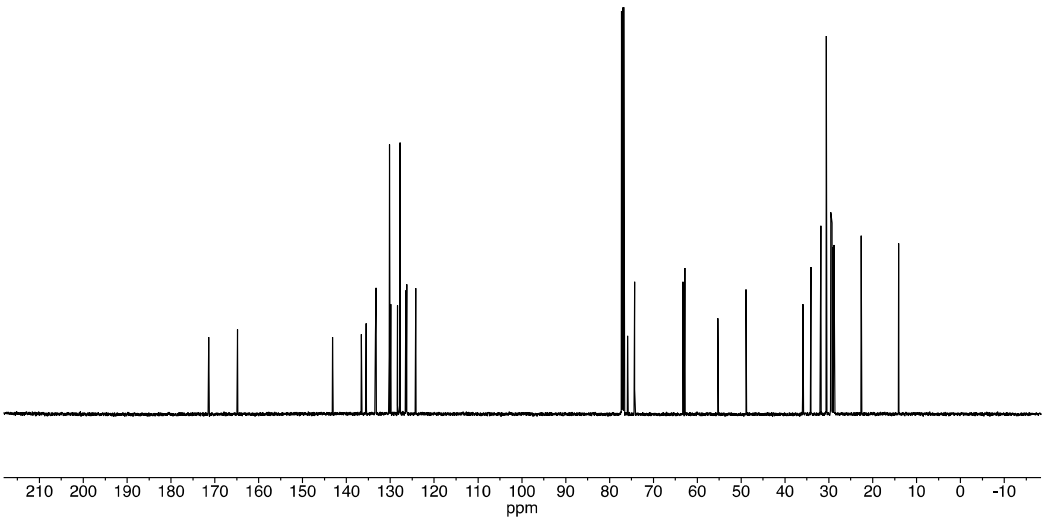

Figure 3.38. ^{13}C NMR spectrum of enyne ATRP initiator ($CDCl_3$, 126 MHz).

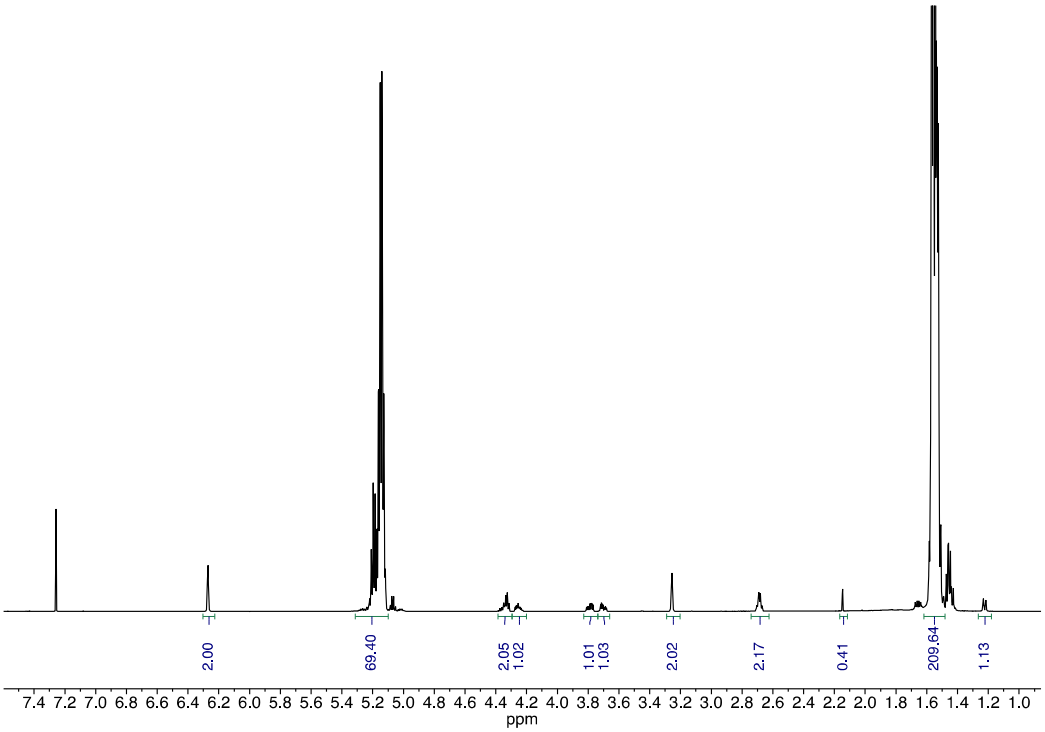

Figure 3.39. ^{1}H NMR spectrum of PLA-MM-5 ($CDCl_3$, 600 MHz).

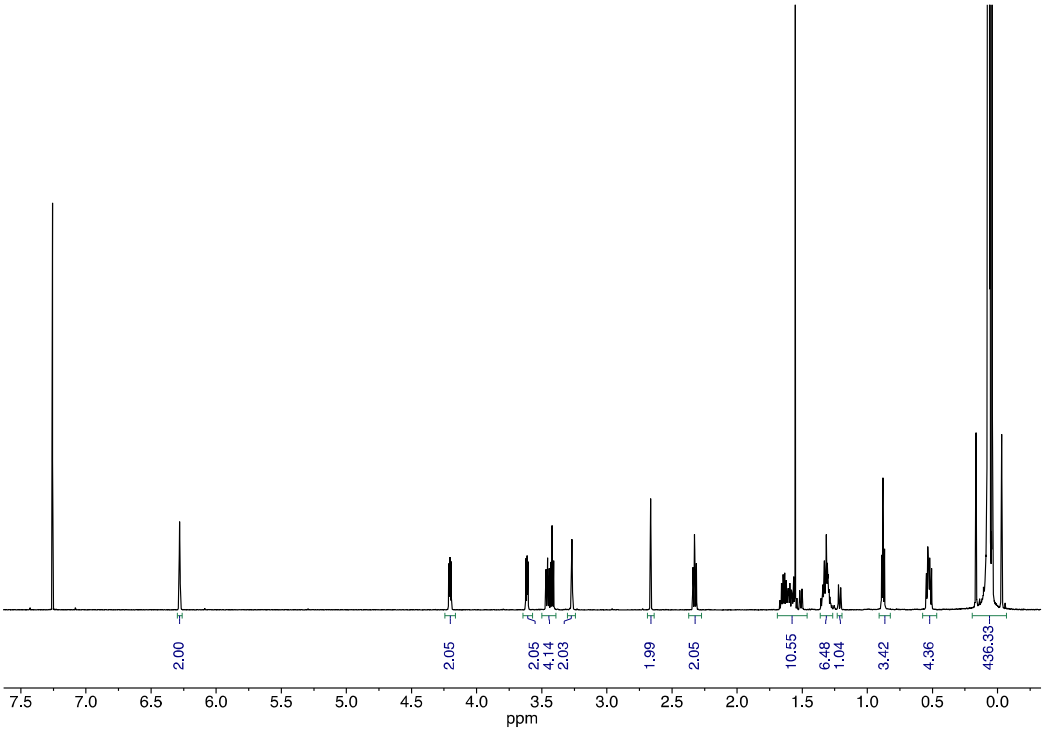

Figure 3.40. ^{1}H NMR spectrum of PDMS-MM-5 ($CDCl_3$, 600 MHz).

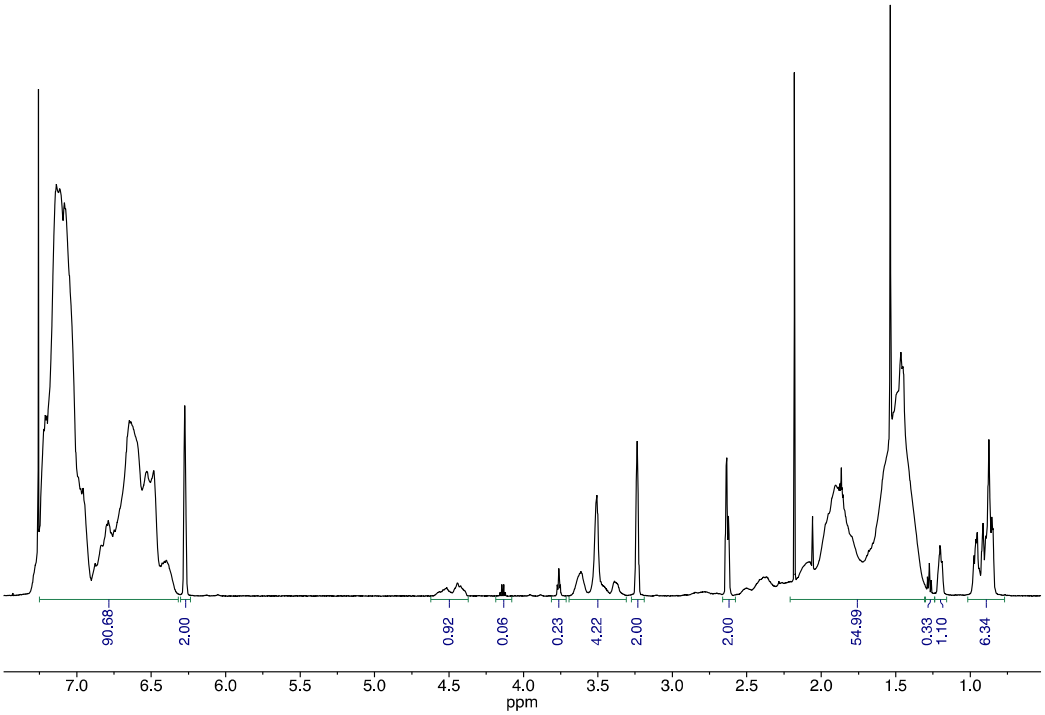

Figure 3.41. ^{1}H NMR spectrum of PS-MM-2 ($CDCl_3$, 600 MHz).

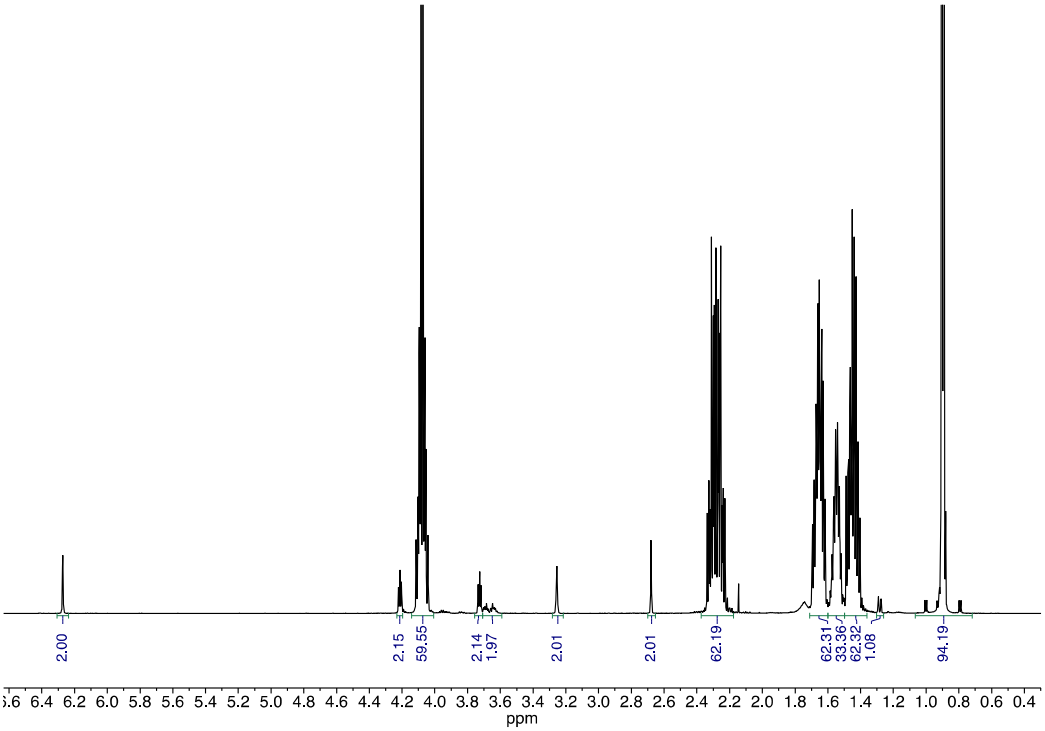

Figure 3.42. ^{1}H NMR spectrum of P4MCL-MM-4 ($CDCl_3$, 600 MHz).

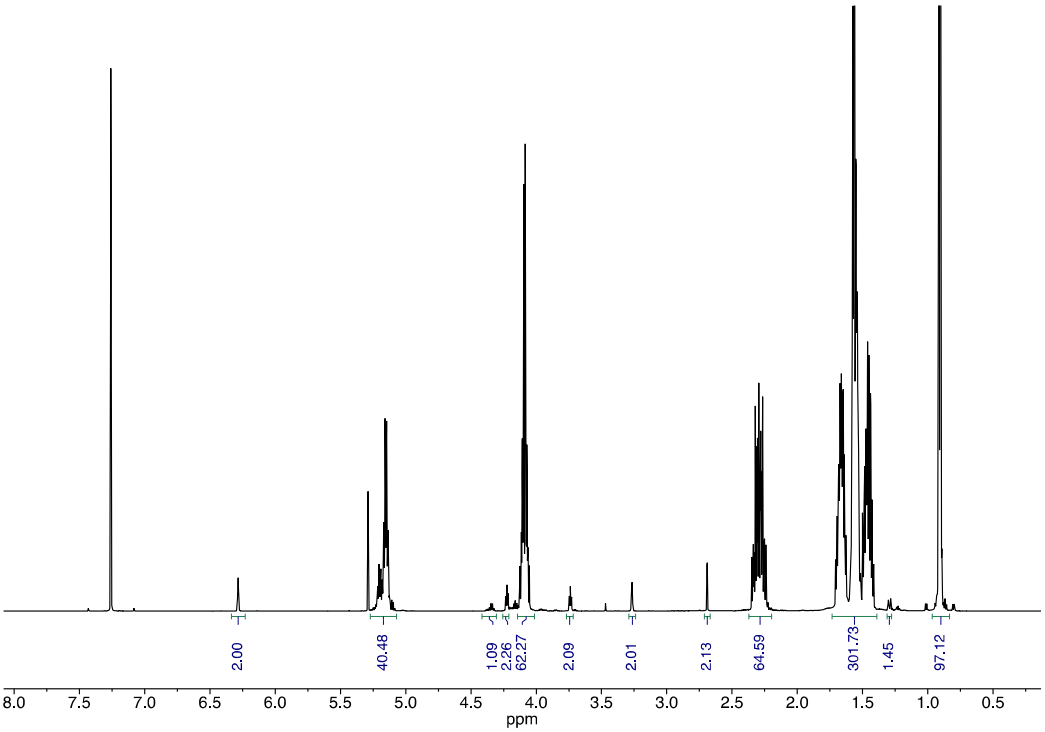

Figure 3.43. ^{1}H NMR spectrum of P4MCL-PLA-MM-4-3 ($CDCl_3$, 600 MHz).

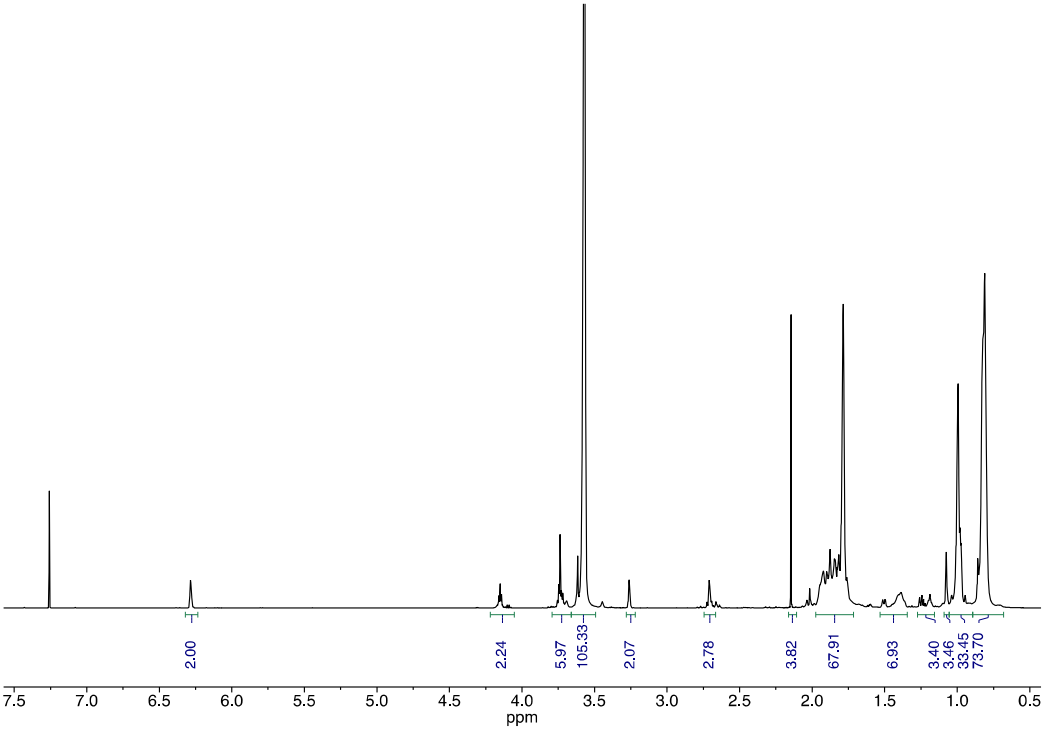

Figure 3.44. ^{1}H NMR spectrum of PMMA-MM-4 ($CDCl_3$, 600 MHz).

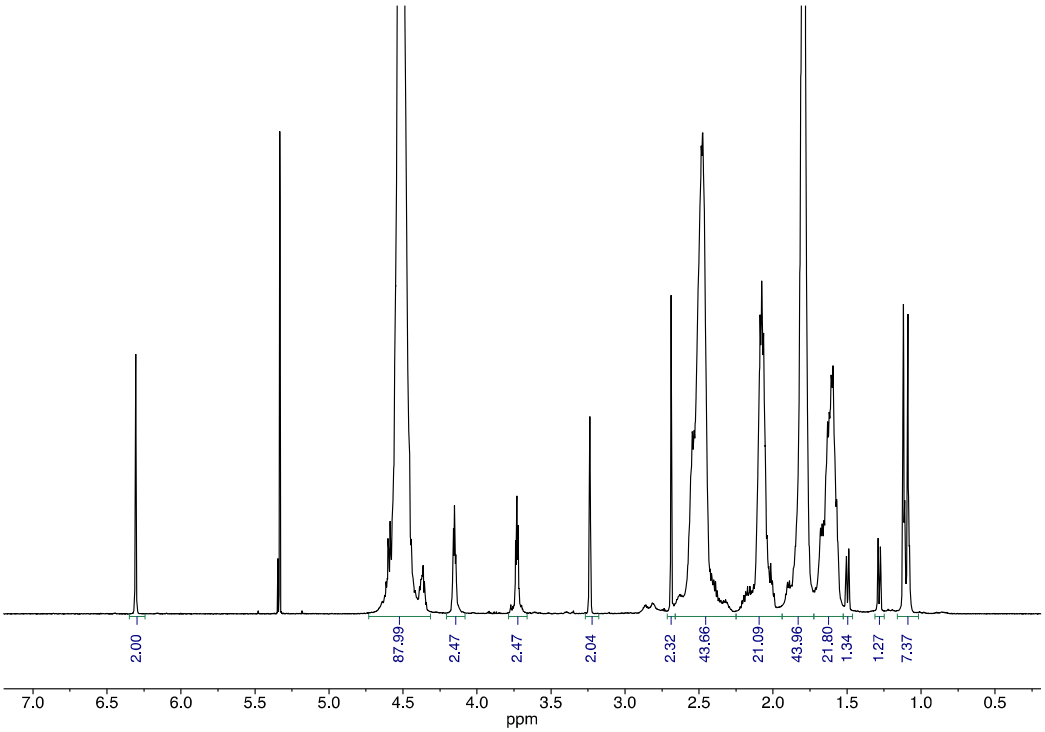

Figure 3.45. ^{1}H NMR spectrum of PTFEA-MM-6 (CD_2Cl_2, 600 MHz).

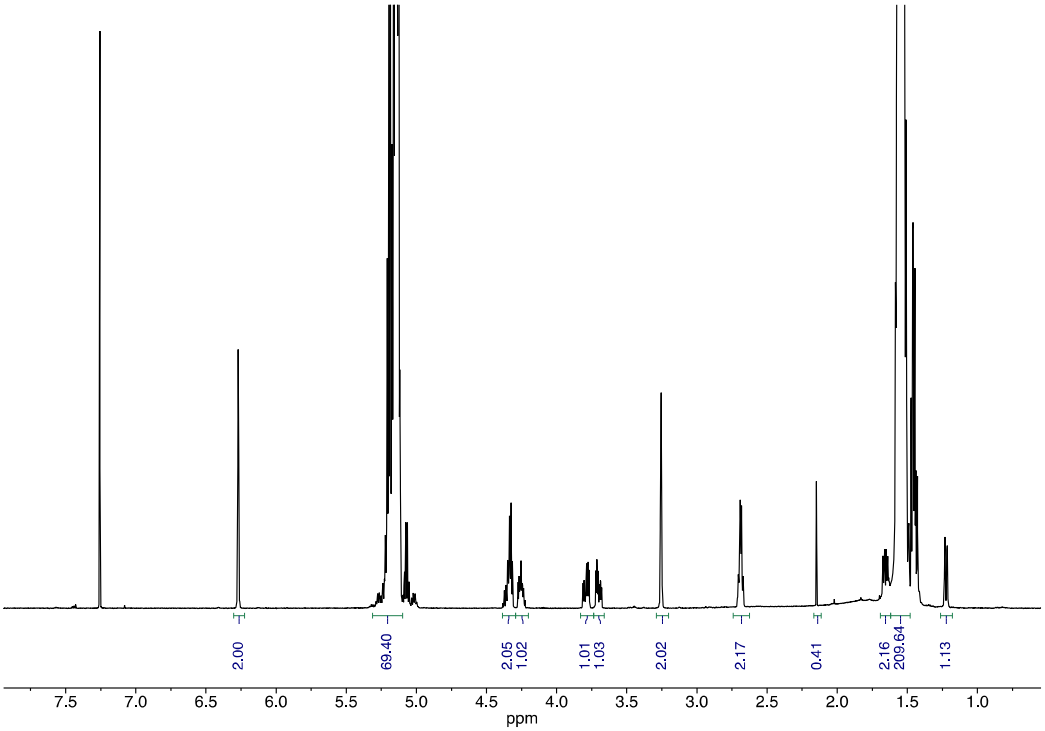

Figure 3.46. ^{1}H NMR spectrum of PLA-MT-4 ($CDCl_3$, 600 MHz).

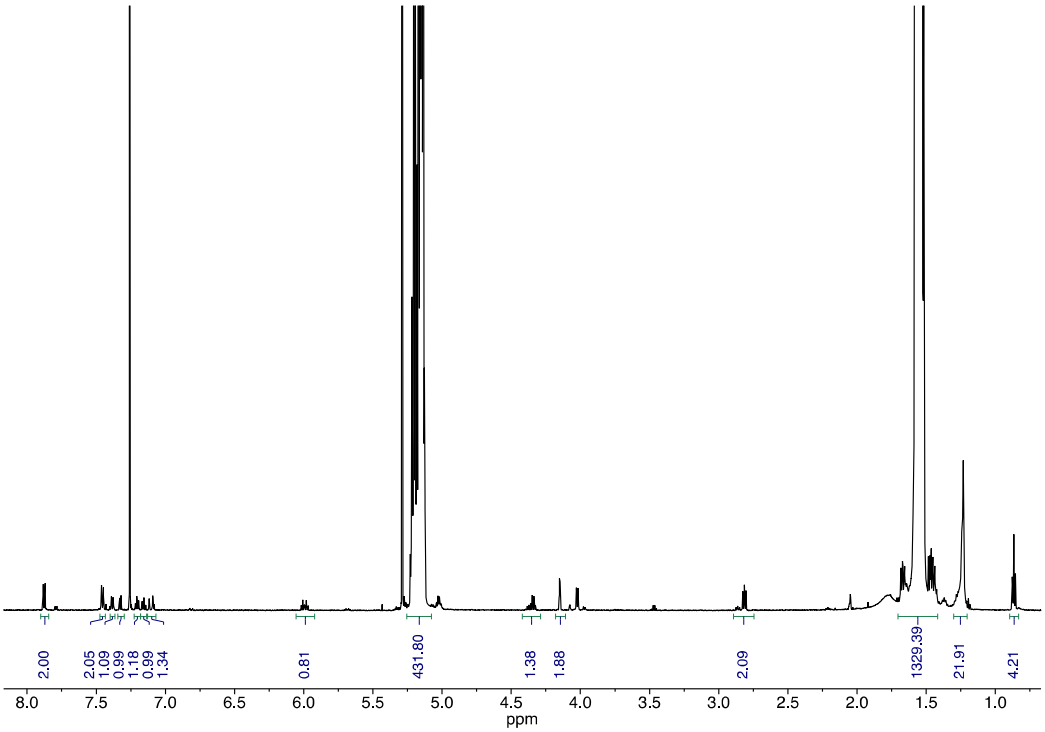

Figure 3.47. NMR spectrum of PLA-MT-24 ($CDCl_3$, 600 MHz).

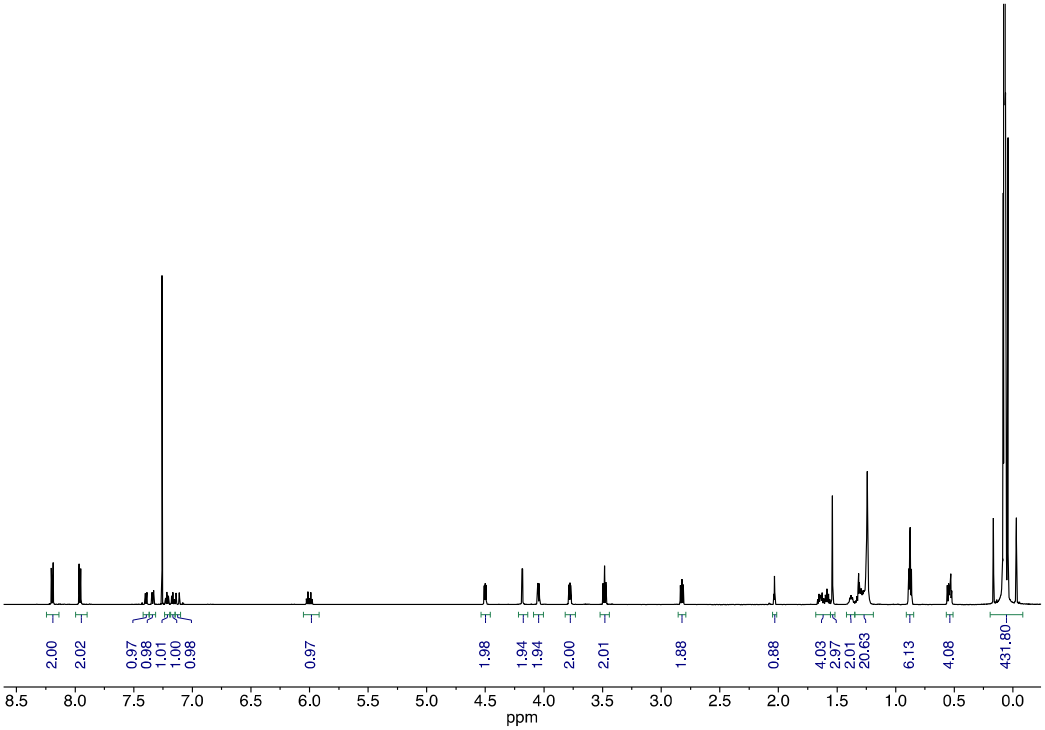

Figure 3.48. ^1H NMR spectrum of PDMS-MT-5 ($CDCl_3$, 600 MHz).

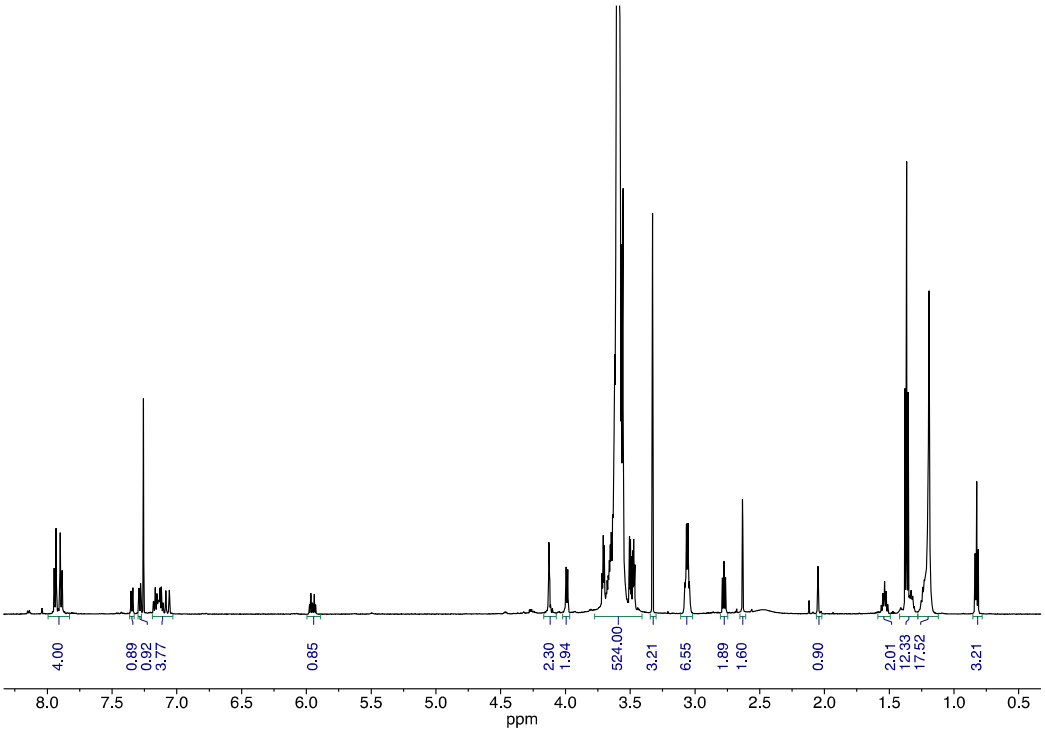

Figure 3.49. ^{1}H NMR spectrum of PEO-MT-5 ($CDCl_3$, 600 MHz).

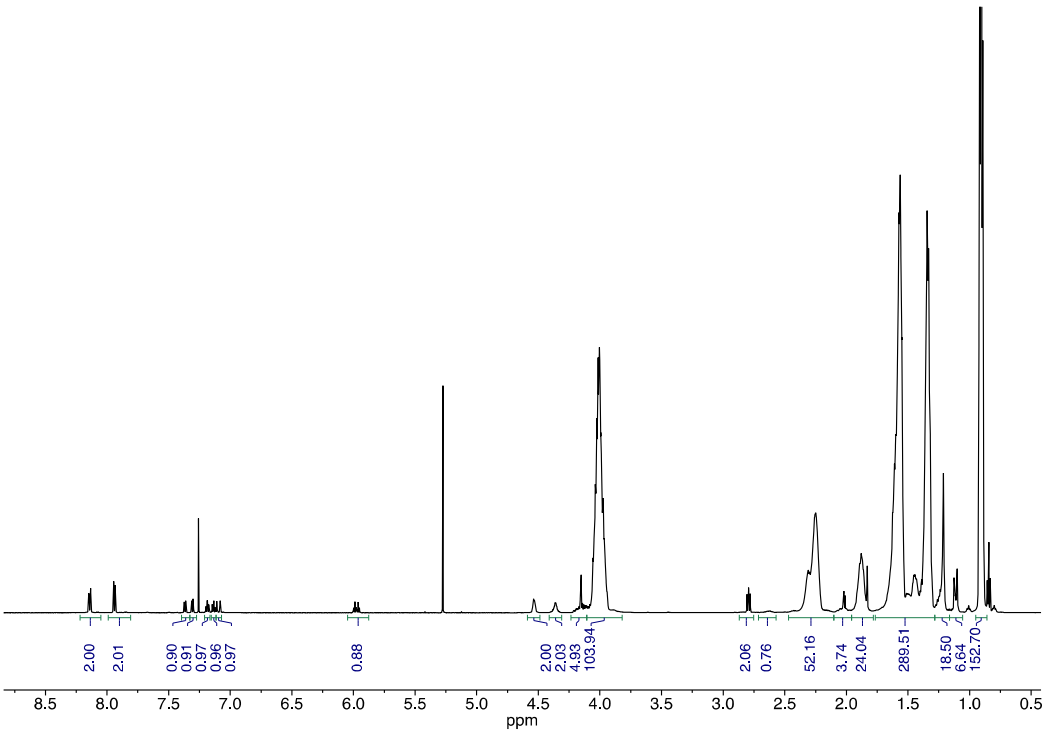

Figure 3.50. ^{1}H NMR spectrum of PnBA-MT-6 ($CDCl_3$, 600 MHz).

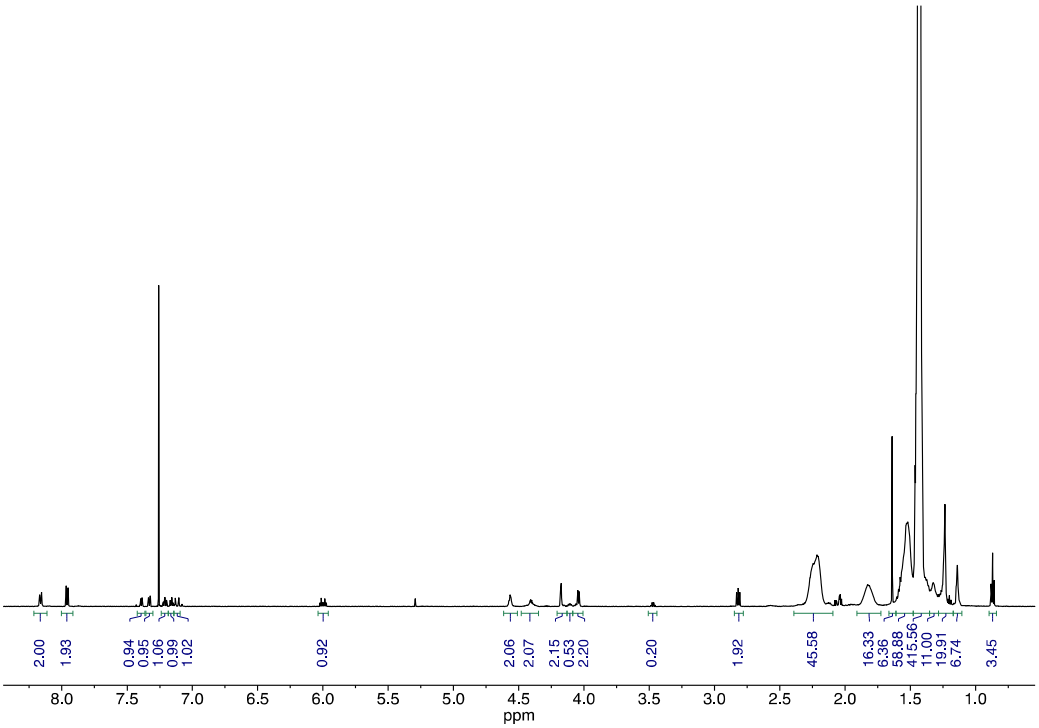

Figure 3.51. ^{1}H NMR spectrum of PtBA-MT-5 ($CDCl_3$, 600 MHz).

3.7 References

(1) Bates, F. S.; Hillmyer, M. A.; Lodge, T. P.; Bates, C. M.; Delaney, K. T.; Fredrickson, G. H. Multiblock Polymers: Panacea or Pandora's Box? *Science* **2012**, *336*, 434–440.

(2) Hajduk, D. A.; Harper, P. E.; Gruner, S. M.; Honeker, C. C.; Kim, G.; Fetters, L. J.; Kim, G. The Gyroid: A New Equilibrium Morphology in Weakly Segregated Diblock Copolymers. *Macromolecules* **1994**, *27*, 4063–4075.

(3) Bates, F. S.; Schulz, M. F.; Khandpur, A. K.; Förster, S.; Rosedale, J. H.; Almdal, K.; Mortensen, K. Fluctuations, Conformational Asymmetry and Block Copolymer Phase Behaviour. *Faraday Discuss.* **1994**, *98*, 7–18.

(4) Bates, F. S.; Fredrickson, G. H. Block Copolymer Thermodynamics: Theory And Experiment. *Annu. Rev. Phys. Chem.* **1990**, *41*, 525–557.

(5) Milner, S. T. Chain Architecture and Asymmetry in Copolymer Microphases. *Macromolecules* **1994**, *27*, 2333–2335.

(6) Leibler, L. Theory of Microphase Separation in Block Copolymers. *Macromolecules* **1980**, *13*, 1602–1617.

(7) Matsen, M. W.; Schick, M. Stable and Unstable Phases of a Diblock Copolymer Melt. *Phys. Rev. Lett.* **1994**, *72*, 2660–2663.

(8) Matsen, M. W.; Bates, F. S. Unifying Weak- and Strong-Segregation Block Copolymer Theories. *Macromolecules* **1996**, *29*, 1091–1098.

(9) Li, W.; Duan, C.; Shi, A. C. Nonclassical Spherical Packing Phases Self-Assembled from AB-Type Block Copolymers. *ACS Macro Lett.* **2017**, *6*, 1257–1262.

(10) Bates, M. W.; Lequieu, J.; Barbon, S. M.; Lewis, R. M.; Delaney, K. T.; Anastasaki, A.; Hawker, C. J.; Fredrickson, G. H.; Bates, C. M. Stability of the A15 Phase in Diblock Copolymer Melts. *Proc. Natl. Acad. Sci.* **2019**, *116*, 13194–13199.

(11) Kim, K.; Schulze, M. W.; Arora, A.; Lewis, R. M.; Marc, A.; Dorfman, K. D.; Bates, F. S. Thermal Processing of Diblock Copolymer Melts Mimics Metallurgy. *Science* **2017**, *356*, 520–523.

(12) Bates, C. M.; Bates, F. S. 50th Anniversary Perspective: Block Polymers-Pure Potential. *Macromolecules* **2017**, *50*, 3–22.

(13) Sinturel, C.; Bates, F. S.; Hillmyer, M. A. High χ-Low N Block Polymers: How Far Can We Go? *ACS Macro Lett.* **2015**, *4*, 1044–1050.

(14) Jeong, S. J.; Kim, J. Y.; Kim, B. H.; Moon, H. S.; Kim, S. O. Directed Self-Assembly of Block Copolymers for next Generation Nanolithography. *Mater. Today* **2013**, *16*, 468–476.

(15) Grason, G. M.; Kamien, R. D. Interfaces in Diblocks: A Study of Miktoarm Star Copolymers. *Macromolecules* **2004**, *37*, 7371–7380.

(16) Bates, F. S. Polymer-Polymer Phase Behavior. *Science* **1991**, *251*, 898.

(17) Le, A. N.; Liang, R.; Zhong, M. Synthesis and Self-Assembly of Mixed-Graft Block Copolymers. *Chem. - A Eur. J.* **2019**, *25*, 8177–8189.

(18) Polymeropoulos, G.; Zapsas, G.; Ntetsikas, K.; Bilalis, P.; Gnanou, Y.; Hadjichristidis, N. 50th Anniversary Perspective: Polymers with Complex Architectures. *Macromolecules* **2017**, *50*, 1253–1290.

(19) Guo, Z.; Le, A. N.; Feng, X.; Choo, Y.; Liu, B.; Wang, D.; Wan, Z.; Gu, Y.; Zhao, J.; Li, V.; Osuji, C. O.; Johnson, J. A.; Zhong, M. Janus Graft Block Copolymers: Design of Polymer Architecture for Independently Tuned Nanostructures and Polymer Properties. *Angew. Chem. Int. Ed.* **2018**, *57*, 8493–8497.

(20) Sveinbjornsson, B. R.; Weitekamp, R. A.; Miyake, G. M.; Xia, Y.; Atwater, H. A.; Grubbs, R. H. Rapid Self-Assembly of Brush Block Copolymers to Photonic Crystals. *Proc. Natl. Acad. Sci.* **2012**, *109*, 14332–14336.

(21) Vatankhah-Varnosfaderani, M.; Keith, A. N.; Cong, Y.; Liang, H.; Rosenthal, M.; Sztucki, M.; Clair, C.; Magonov, S.; Ivanov, D. A.; Dobrynin, A. V.; Sheiko, S. S. Chameleon-like Elastomers with Molecularly Encoded Strain-Adaptive Stiffening and Coloration. *Science* **2018**, *359*, 1509–1513.

(22) Wang, H.; Lu, W.; Wang, W.; Shah, P. N.; Misichronis, K.; Kang, N. G.; Mays, J. W. Design and Synthesis of Multigraft Copolymer Thermoplastic Elastomers: Superelastomers. *Macromol. Chem. Phys.* **2018**, *219*, 1–11.

(23) Li, Z.; Kesselman, E.; Talmon, Y.; Hillmyer, M. A.; Lodge, T. P. Multicompartment

Micelles from ABC Miktoarm Stars in Water. *Science* **2004**, *306*, 98–101.

(24) *Miktoarm Star Polymers: From Basics of Branched Architecture to Synthesis, Self-Assembly and Applications*; Kakkar, A., Ed.; The Royal Society of Chemistry, 2017.

(25) Yang, L.; Hong, S.; Gido, S. P.; Velis, G.; Hadjichristidis, N. I5S Miktoarm Star Block Copolymers: Packing Constraints on Morphology and Discontinuous Chevron Tilt Grain Boundaries. *Macromolecules* **2001**, *34*, 9069–9073.

(26) Beyer, F. L.; Gido, S. P.; Velis, G.; Hadjichristidis, N.; Tan, N. B. Morphological Behavior of A5B Miktoarm Star Block Copolymers. *Macromolecules* **1999**, *32*, 6604–6607.

(27) Pochan, D. J.; Gido, S. P.; Pispas, S.; Mays, J. W. Morphological Transitions in an I2S Simple Graft Block Copolymer: From Folded Sheets to Folded Lace to Randomly Oriented Worms at Equilibrium. *Macromolecules* **1996**, *29*, 5099–5105.

(28) Pochan, D. J.; Gido, S. P.; Zhou, J.; Mays, J. W.; Whitmore, M.; Ryan, A. J. Morphologies of Microphase□separated Conformationally Asymmetric Diblock Copolymers. *J. Polym. Sci. Part B Polym. Phys.* **1997**, *35*, 2629–2643.

(29) Beyer, F. L.; Gido, S. P.; Poulos, Y.; Avgeropoulos, A.; Hadjichristidis, N. Morphology of Vergina Star 16-Arm Block Copolymers and Scaling Behavior of Interfacial Area with Graft Point Functionality. *Macromolecules* **1997**, *30*, 2373–2376.

(30) Gido, S. P.; Lee, C.; Pochan, D. J.; Pispas, S.; Mays, J. W.; Hadjichristidis, N. Synthesis, Characterization, and Morphology of Model Graft Copolymers with Trifunctional Branch Points. *Macromolecules* **1996**, *29*, 7022–7028.

(31) Hadjichristidis, N.; Iatrou, H.; Behal, S. K.; Chludzinski, J. J.; Disko, M. M.; Garner, R. T.; Liang, K. S.; Lohse, D. J.; Milner, S. T. Morphology and Miscibility of Miktoarm

Styrene-Diene Copolymers and Terpolymers. *Macromolecules* **1993**, *26*, 5812–5815.

(32) Tselikas, Y.; Iatrou, H.; Hadjichristidis, N.; Liang, K. S.; Mohanty, K.; Lohse, D. J. Morphology of Miktoarm Star Block Copolymers of Styrene and Isoprene. *J. Chem. Phys.* **1996**, *105*, 2456–2462.

(33) Iatrou, H.; Hadjichristidis, N. Synthesis and Characterization of Model 4-Miktoarm Star Co- and Quaterpolymers. *Macromolecules* **1993**, *26*, 2479–2484.

(34) Aissou, K.; Choi, H. K.; Nunns, A.; Manners, I.; Ross, C. A. Ordered Nanoscale Archimedean Tilings of a Templated 3-Miktoarm Star Terpolymer. *Nano Lett.* **2013**, *13*, 835–839.

(35) Shi, W.; Tateishi, Y.; Li, W.; Hawker, C. J.; Fredrickson, G. H.; Kramer, E. J. Producing Small Domain Features Using Miktoarm Block Copolymers with Large Interaction Parameters. *ACS Macro Lett.* **2015**, *4*, 1287–1292.

(36) Lee, D.; Jung, H. Y.; Park, M. J. Solid-State Polymer Electrolytes Based on AB3-Type Miktoarm Star Copolymers. *ACS Macro Lett.* **2018**, *7*, 1046–1050.

(37) Minehara, H.; Pitet, L. M.; Kim, S.; Zha, R. H.; Meijer, E. W.; Hawker, C. J. Branched Block Copolymers for Tuning of Morphology and Feature Size in Thin Film Nanolithography. *Macromolecules* **2016**, *49*, 2318–2326.

(38) Kakkar, A.; Traverso, G.; Farokhzad, O. C.; Weissleder, R.; Langer, R. Evolution of Macromolecular Complexity in Drug Delivery Systems. *Nat. Rev. Chem.* **2017**, *1*, 1–17.

(39) Lin, W.; Nie, S.; Zhong, Q.; Yang, Y.; Cai, C.; Wang, J.; Zhang, L. Amphiphilic Miktoarm Star Copolymer (PCL)3-(PDEAEMA-b-PPEGMA)3 as PH-Sensitive Micelles in the Delivery of Anticancer Drug. *J. Mater. Chem. B* **2014**, *2*, 4008–4020.

(40) Gelissen, A. P. H.; Pergushov, D. V.; Plamper, F. A. Janus-like Interpolyelectrolyte Complexes Based on Miktoarm Stars. *Polymer (Guildf).* **2013**, *54*, 6877–6881.

(41) Lynd, N. A.; Oyerokun, F. T.; O'Donoghue, D. L.; Handlin, D. L.; Fredrickson, G. H. Design of Soft and Strong Thermoplastic Elastomers Based on Nonlinear Block Copolymer Architectures Using Self-Consistent-Field Theory. *Macromolecules* **2010**, *43*, 3479–3486.

(42) Shi, W.; Lynd, N. A.; Montarnal, D.; Luo, Y.; Fredrickson, G. H.; Kramer, E. J.; Ntaras, C.; Avgeropoulos, A.; Hexemer, A. Toward Strong Thermoplastic Elastomers with Asymmetric Miktoarm Block Copolymer Architectures. *Macromolecules* **2014**, *47*, 2037–2043.

(43) Ren, J. M.; McKenzie, T. G.; Fu, Q.; Wong, E. H. H.; Xu, J.; An, Z.; Shanmugam, S.; Davis, T. P.; Boyer, C.; Qiao, G. G. Star Polymers. *Chem. Rev.* **2016**, *116*, 6743–6836.

(44) Liu, H.; Pan, W.; Tong, M.; Zhao, Y. Synthesis and Properties of Couplable ABCDE Star Copolymers by Orthogonal CuAAC and Diels-Alder Click Reactions. *Polym. Chem.* **2016**, *7*, 1603–1611.

(45) Avgeropoulos, A.; Hadjichristidis, N.; Copolymer, S. B. Synthesis of Model Nonlinear Block Copolymers of A(BA)2, A(BA)3, and (AB)3A(BA)3 Type. *J. Polym. Sci. Part A Polym. Chem.* **1997**, *35*, 813–816.

(46) Avgeropoulos, A.; Dair, B. J.; Hadjichristidis, N.; Thomas, E. L. Tricontinuous Double Gyroid Cubic Phase in Triblock Copolymers of the ABA Type. **1997**, *9297*, 5634–5642.

(47) Zhu, Y.; Gido, S. P.; Moshakou, M.; Iatrou, H.; Hadjichristidis, N.; Park, S.; Chang, T. Effect of Junction Point Functionality on the Lamellar Spacing of Symmetric (PS)n(PI)n Miktoarm Star Block Copolymers. *Macromolecules* **2003**, *36*, 5719–5724.

(48) Shibuya, Y.; Nguyen, H. V. T.; Johnson, J. A. Mikto-Brush-Arm Star Polymers via Cross-Linking of Dissimilar Bottlebrushes: Synthesis and Solution Morphologies. *ACS Macro Lett.* **2017**, *6*, 963–968.

(49) Burts, A. O.; Gao, A. X.; Johnson, J. A. Brush-First Synthesis of Core-Photodegradable Miktoarm Star Polymers via ROMP: Towards Photoresponsive Self-Assemblies. *Macromol. Rapid Commun.* **2014**, *35*, 168–173.

(50) Gorodetskaya, I. A.; Choi, T. L.; Grubbs, R. H. Hyperbranched Macromolecules via Olefin Metathesis. *J. Am. Chem. Soc.* **2007**, *129*, 12672–12673.

(51) Liu, J.; Burts, A. O.; Li, Y.; Zhukhovitskiy, A. V.; Ottaviani, M. F.; Turro, N. J.; Johnson, J. A. "Brush-First" Method for the Parallel Synthesis of Photocleavable, Nitroxide-Labeled Poly(Ethylene Glycol) Star Polymers. *J. Am. Chem. Soc.* **2012**, *134*, 16337–16344.

(52) Dutertre, F.; Bang, K. T.; Vereroudakis, E.; Loppinet, B.; Yang, S.; Kang, S. Y.; Fytas, G.; Choi, T. L. Conformation of Tunable Nanocylinders: Up to Sixth-Generation Dendronized Polymers via Graft-Through Approach by ROMP. *Macromolecules* **2019**, *52*, 3342–3350.

(53) Xia, Y.; Olsen, B. D.; Kornfield, J. A.; Grubbs, R. H. Efficient Synthesis of Narrowly Dispersed Brush Copolymers and Study of Their Assemblies: The Importance of Side Chain Arrangement. *J. Am. Chem. Soc.* **2009**, *131*, 18525–18532.

(54) Xia, Y.; Grubbs, R. H. Efficient Syntheses of Brush Polymers via Living Ring Opening Metathesis Polymerization of Macromonomers. *Macromolecules* **2009**, *50*, 197–198.

(55) Teo, Y. C.; Xia, Y. Facile Synthesis of Macromonomers via ATRP-Nitroxide Radical Coupling and Well-Controlled Brush Block Copolymers. *Macromolecules* **2019**, *52*,

81–87.

(56) Walsh, D. J.; Guironnet, D. Macromolecules with Programmable Shape, Size, and Chemistry. *Proc. Natl. Acad. Sci. U. S. A.* **2019**, *116*, 1538–1542.

(57) Kawamoto, K.; Zhong, M.; Gadelrab, K. R.; Cheng, L. C.; Ross, C. A.; Alexander-Katz, A.; Johnson, J. A. Graft-through Synthesis and Assembly of Janus Bottlebrush Polymers from A-Branch-B Diblock Macromonomers. *J. Am. Chem. Soc.* **2016**, *138*, 11501–11504.

(58) Levi, A. E.; Lequieu, J.; Horne, J. D.; Bates, M. W.; Ren, J. M.; Delaney, K. T.; Fredrickson, G. H.; Bates, C. M. Miktoarm Stars via Grafting-Through Copolymerization: Self-Assembly and the Star-to-Bottlebrush Transition. *Macromolecules* **2019**, *52*, 1794–1802.

(59) Fu, L.; Zhang, T.; Fu, G.; Gutekunst, W. R. Relay Conjugation of Living Metathesis Polymers. *J. Am. Chem. Soc.* **2018**, *140*, 12181–12188.

(60) Lutz, J.-F.; Ouchi, M.; Liu, D. R.; Sawamoto, M. Sequence-Controlled Polymers. *Science* **2013**, *341*, 1238149.

(61) Widin, J. M.; Schmitt, A. K.; Schmitt, A. L.; Im, K.; Mahanthappa, M. K. Unexpected Consequences of Block Polydispersity on the Self-Assembly of ABA Triblock Copolymers. *J. Am. Chem. Soc.* **2012**, *134*, 3834–3844.

(62) Donghui Wu, Aidi Chen, C. S. J. J. An Improved Diffusion-Ordered Spectroscopy Experiment Incorporating Bipolar-Gradient Pulses. *J. Magn. Reson. Ser. A* **1995**, *115*, 260–264.

(63) Fredrickson, G. H. *The Equilibrium Theory of Inhomogeneous Polymers*; Oxford University Press: Oxford, New York, 2005.

(64) Lequieu, J.; Trenton, K.; Delaney, K. T.; Fredrickson, G. H. Extreme Deflection of Phase Boundaries with A(BA')n Miktoarm Star Polymers. *Submitted*.

(65) Ogba, O. M.; Warner, N. C.; O'Leary, D. J.; Grubbs, R. H. Recent Advances in Ruthenium-Based Olefin Metathesis. *Chem. Soc. Rev.* **2018**, *47*, 4510–4544.

(66) Jha, S.; Dutta, S.; Bowden, N. B. Synthesis of Ultralarge Molecular Weight Bottlebrush Polymers Using Grubbs' Catalysts. *Macromolecules* **2004**, *37*, 4365–4374.

(67) Elling, B. R.; Xia, Y. Efficient and Facile End Group Control of Living Ring-Opening Metathesis Polymers via Single Addition of Functional Cyclopropenes. *ACS Macro Lett.* **2018**, *7*, 656–661.

(68) Elling, B. R.; Su, J. K.; Feist, J. D.; Xia, Y. Precise Placement of Single Monomer Units in Living Ring-Opening Metathesis Polymerization. *Chem* **2019**, 1–11.

(69) Mavroudis, A.; Avgeropoulos, A.; Hadjichristidis, N.; Thomas, E. L.; Lohse, D. J. Synthesis and Morphological Behavior of Model Linear and Miktoarm Star Copolymers of 2-Methyl-1,3-Pentadiene and Styrene. *Chem. Mater.* **2003**, *15*, 1976–1983.

(70) Matson, J. B.; Grubbs, R. H. Monotelechelic Poly(Oxa)Norbornenes by Ring-Opening Metathesis Polymerization Using Direct End-Capping and Cross-Metathesis. *Macromolecules* **2010**, *43*, 213–221.

(71) Hilf, S.; Kilbinger, A. F. M. Thiol-Functionalized ROMP Polymers via Sacrificial Synthesis. *Macromolecules* **2009**, *42*, 4127–4133.

(72) Hilf, S.; Grubbs, R. H.; Kilbinger, A. F. M. End Capping Ring-Opening Olefin Metathesis Polymerization Polymers with Vinyl Lactones. *J. Am. Chem. Soc.* **2008**, *130*, 11040–11048.

(73) Gordon, E. J.; Gestwicki, J. E.; Strong, L. E.; Kiessling, L. L. Synthesis of End-Labeled

Multivalent Ligands for Exploring Cell-Surface-Receptor-Ligand Interactions. *Chem. Biol.* **2000**, *7*, 9–16.

(74) Hilf, S.; Kilbinger, A. F. M. Functional End Groups for Polymers Prepared Using Ring-Opening Metathesis Polymerization. *Nat. Chem.* **2009**, *1*, 537–546.

(75) Yu, Q.; Pichugin, D.; Cruz, M.; Guerin, G.; Manners, I.; Winnik, M. A. NMR Study of the Dissolution of Core-Crystalline Micelles. *Macromolecules* **2018**, *51*, 3279–3289.

(76) Hugh G. Gauch. Prediction, Parsimony and Noise. *Am. Sci.* **1993**, *81*, 468–478.

(77) Velis, G.; Hadjichristidis, N. Synthesis of Model PS(PI)5 and (PI)5PS(PI)5 Nonlinear Block Copolymers of Styrene (S) and Isoprene (I). *Macromolecules* **1999**, *32*, 534–536.

(78) Bates, C. M.; Chang, A. B.; Schulze, M. W.; Momčilovic, N.; Jones, S. C.; Grubbs, R. H. Brush Polymer Ion Gels. *J. Polym. Sci. Part B Polym. Phys.* **2016**, *54*, 292–300.

(79) Watts, A.; Kurokawa, N.; Hillmyer, M. A. Strong, Resilient, and Sustainable Aliphatic Polyester Thermoplastic Elastomers. *Biomacromolecules* **2017**, *18*, 1845–1854.

(80) Lee, C.; Gido, S. P.; Pitsikalis, M.; Mays, J. W.; Tan, N. B.; Trevino, S. F.; Hadjichristidis, N. Asymmetric Single Graft Block Copolymers: Effect of Molecular Architecture on Morphology. *Macromolecules* **1997**, *30*, 3732–3738.

(81) Iatrou, H.; Siakali□Kioulafa, E.; Hadjichristidis, N.; Roovers, J.; Mays, J. Hydrodynamic Properties of Model 3□miktoarm Star Copolymers. *J. Polym. Sci. Part B Polym. Phys.* **1995**, *33*, 1925–1932.

(82) Se, K.; Hayashino, Y. Anionic Living Polymerization of Macromonomers : Preparation of (A)n-Star-(B)1 Star Block Copolymers and Some Properties of the Products Obtained. *Macromolecules* **2007**, *40*, 429–437.

(83) Rodwogin, M. D.; Spanjers, C. S.; Leighton, C.; Hillmyer, M. A. Polylactide-

Poly(Dimethylsiloxane)- Polylactide Triblock Copolymers as Multifunctional Materials for Nanolithographic Applications. *ACS Nano* **2010**, *4*, 725–732.

(84) Pitet, L. M.; Wuister, S. F.; Peeters, E.; Kramer, E. J.; Hawker, C. J.; Meijer, E. W. Well-Organized Dense Arrays of Nanodomains in Thin Films of Poly(Dimethylsiloxane)-b-Poly(Lactide) Diblock Copolymers. *Macromolecules* **2013**, *46*, 8289–8295.

(85) Kassis, C. M.; Steehler, J. K.; Betts, D. E.; Guan, Z.; Romack, T. J.; DeSimone, J. M.; Linton, R. W. XPS Studies of Fluorinated Acrylate Polymers and Block Copolymers with Polystyrene. *Macromolecules* **1996**, *29*, 3247–3254.

(86) Zhang, J.; Clark, M. B.; Wu, C.; Li, M.; Trefonas, P.; Hustad, P. D. Orientation Control in Thin Films of a High-χ Block Copolymer with a Surface Active Embedded Neutral Layer. *Nano Lett.* **2016**, *16*, 728–735.

(87) Morita, M.; Ogisu, H.; Kubo, M. Surface Properties of Perfluoroalkylethyl Acrylate / n-Alkyl. *J. Appl. Polym. Sci.* **1998**, No. 2, 1741–1749.

(88) Fu, C.; Zhang, C.; Peng, H.; Han, F.; Baker, C.; Wu, Y.; Ta, H.; Whittaker, A. K. Enhanced Performance of Polymeric 19F MRI Contrast Agents through Incorporation of Highly Water-Soluble Monomer MSEA. *Macromolecules* **2018**, *51*, 5875–5882.

(89) Xie, N.; Li, W.; Qiu, F.; Shi, A. C. σ Phase Formed in Conformationally Asymmetric AB-Type Block Copolymers. *ACS Macro Lett.* **2014**, *3*, 909–910.

(90) Lewis, R. M.; Arora, A.; Beech, H. K.; Lee, B.; Lindsay, A. P.; Lodge, T. P.; Dorfman, K. D.; Bates, F. S. Role of Chain Length in the Formation of Frank-Kasper Phases in Diblock Copolymers. *Phys. Rev. Lett.* **2018**, *121*, 208002.

Chapter 4. Design, Synthesis, and Characterization of Asymmetric Miktoarm Star Polymers Thermoplastic Elastomers

4.1 Background

Block polymer thermoplastic elastomers (TPEs) are industrially important materials due to their high Young's modulus, elasticity, and processability, which make them suitable for a variety of applications in transportation, footwear, medical devices, and pressure sensitive adhesives.[1] These TPEs typically comprise ABA triblock copolymers where the A blocks are high T_g and glassy while B is low T_g and amorphous. Due to their chemical incompatibility, these blocks microphase separate on the nanometer length scale. To ensure elasticity, there is a morphological requirement that the block polymer self-assembles into discrete domains of the A block embedded in a continuous matrix of the B block; spherical or cylindrical morphologies of the A blocks meet this requirement. Discrete domains of the hard A block serve as physical cross-links for the elastomeric matrix. However, the morphological requirement imposes an upper limit of $f_A \approx 0.3$ to retain elasticity — past this point a cylinder-to-gyroid phase transition occurs, producing a morphology that is non-elastomeric.[2] The mechanical performance improves with an increasing volume fraction of the A component up to this limit.[1,3] Stabilizing cylindrical morphologies past this point should produce even tougher and stiffer elastomers.

Asymmetric miktoarm star polymers ($A(BA')_n$) can significantly deflect the cylinder-to-gyroid phase boundary towards higher f_A and lift this upper limit (**Figure 4.1**).[4–7] The combination of block bidispersity and steric frustration at the domain interface induces domain

curvature with the A block on the concave side. Key to this approach is optimizing the block bidispersity defined as $\tau \equiv \frac{N_A}{N_A+N_{A'}}$. Self-consistent field theory (SCFT) simulations predict that at an optimal value of $\tau = 0.925$, cylinders can be stabilized up to $f_A = 0.78$.[5] The cooperative effect of block bidispersity combined with multiple arms is evidenced by the substantially elevated phase boundary deflection at the optimal value of τ compared to when $\tau = 0$, $\tau = 0.5$ (AB_n), or when $n = 1$ (ABA).

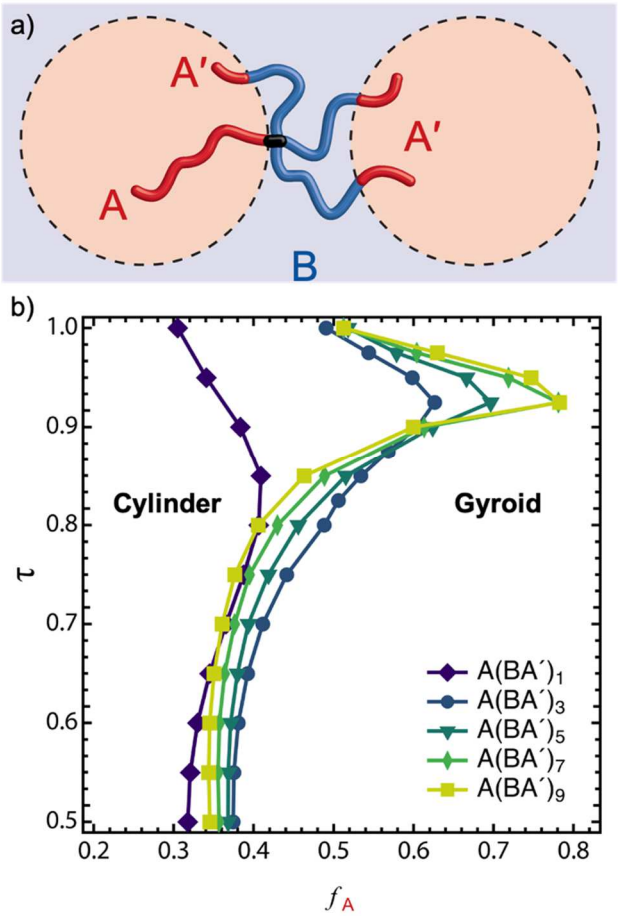

Figure 4.1. a) Illustration of an $A(BA')_3$ miktoarm star polymer forming phases with curved interfaces. b) SCFT-generated cylinder–gyroid phase boundary of $A(BA')_3$ miktoarm star polymers at $\chi N = 40$ as a function of τ and volume fraction for stars with 1, 3, 5, 7, and 9 arms. Adapted with permission from *Macromolecules*. Copyright 2020 American Chemical Society.[5]

The high value of this optimal τ value means that a high degree of block asymmetry is required for these large phase boundary deflections: the A block should be approximately 10 times longer than the A′ block.

The most prevalent examples of these TPEs are linear, petroleum-derived, styrenic-based, non-biodegradable polymers. Almost 2 million metric tons of these materials are produced annually to supply a multi-billion dollar market.[8] The development of biodegradable TPEs that can be produced from renewable feedstocks is a key to the development of next-generation sustainable plastics. Recent efforts have been made to include biodegradable polymers in TPEs, such as polyester-containing polymers that can undergo enzymatic degradation in the natural environment.[9] Poly(L-lactide) (PLLA) is an excellent sustainable polymer to replace polystyrene as the hard block as its semicrystalline nature makes it more thermally and solvent resistant than petroleum-derived alternatives.[10] While a variety of poly(lactones) have been investigated for their performance in TPEs as the elastomeric midblock, recently Watts and coworkers reported impressive performance by pairing PLLA with poly(4-methylcaprolactone) (PMCL) in an ABA linear triblock polymer.[9,11] Just like the PLLA hard block, PMCL is enzymatically degradable and can be produced from renewable feedstocks.[12,13] Developing sustainable TPEs that outperform petroleum-derived analogues would facilitate their widespread adoption. Moving past the traditional linear ABA architecture to A(BA′)$_n$ asymmetric miktoarm star polymer architectures could unlock these higher levels of performance.

Traditional approaches to synthesizing A(BA′)$_n$ asymmetric miktoarm star polymers employ anionic synthesis and thus are not compatible with the use of polyesters like PMCL and PLLA.[14,15] Moreover, these traditional techniques are experimentally cumbersome,

making it challenging to produce many materials. While Shi and coworkers demonstrated they could make PS(PI-PS′)$_3$ star polymers that were elastic at f_{PS} = 0.5, the difficultly involved with the synthesis limited their study to just three miktoarm stars.[7] The large number of parameters that define these complex stars necessitate efficient synthetic techniques to explore molecular design effects on mechanical performance.

In light of these obstacles, we recently developed a technique known as μSTAR to efficiently generate asymmetric miktoarm star polymers by taking advantage of the high reactivity of the Grubbs third generation metathesis catalyst (G3). This one-pot synthesis is amenable to a wide range of chemistries including the PMCL and PLA.[4] μSTAR utilizes grafting-through polymerization of macromonomers to couple multiple BA′ arms together followed by the additional of enyne-functionalized macroterminator[16] to introduce a single A arm (**Scheme 4.1**). So long as there are less than 12 arms on average these materials will behave like stars.[17] Despite dispersity in the number of BA′ arms, these asymmetric miktoarm star polymers retain similar phase behavior as their discrete counterparts.

Scheme 4.1. Synthesis of A(BA′)$_n$ miktoarm stars via μSTAR employing macromonomers and macroterminators.

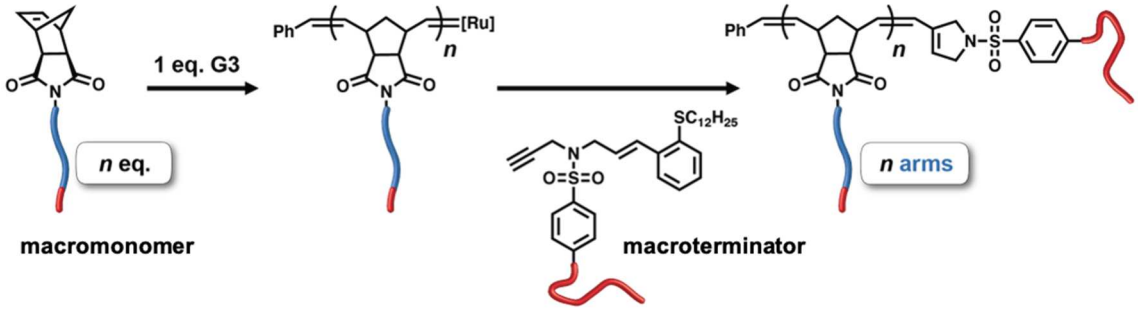

This chapter discusses the synthesis and characterization of PLLA(PMCL-*b*-PLLA′)$_n$ asymmetric miktoarm star polymers that are stiff, tough, and elastic at unusually high volume fractions of PLLA (f_{PLLA}). The high throughput nature of μSTAR generated a library of

A(BA′)$_n$ with a variety of molecular weights of each component, number of arms, f_{PLLA}, and τ. With this library of star polymers, structure–property relationships that govern mechanical performance were evaluated.

4.2 Synthesis of High Molecular Weight Miktoarm Stars via μSTAR

The synthetic challenge of accessing miktoarm stars for thermoplastic elastomers with μSTAR is two-fold. First, macromonomers and macroterminators need to be synthesized at high molecular weights (>50 kDa) with good chain-end fidelity to minimize linear polymer contamination. Second, μSTAR had previously only been shown to couple macroterminators and poly(macromonomers) up to 25 kDa and 50 kDa, respectively. Great care was taken in the purification of all starting materials in order to afford materials with high degree of chain-end functionalization. Importantly, stereopure L-lactide was employed as semi-crystalline PLLA thermoplastic elastomers are higher performing than their amorphous counterparts.[9,18]

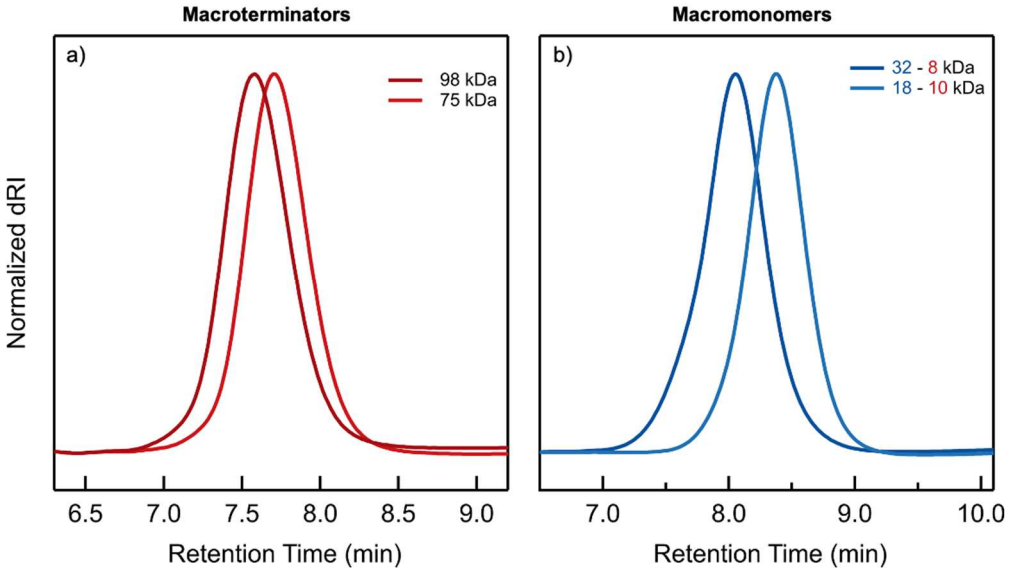

Figure 4.2. SECs (normalized refractive index signal) of a) PLLA macroterminators and b) PMCL-PLLA macromonomers.

Table 4.1. Summary of Physical Characterization of PLLA-PMCL Macromonomers and Macroterminators

Star	$M_{n,B}$[a]	$M_{n,A}$[a]	$Đ$[b]
MM-18-10	18	9.5	1.11
MM-32-8	32	7.5	1.20
MT-75	-	75	1.13
MT-98	-	98	1.17

[a]Determined from ^{1}H NMR chain-end analysis. [b]Calculated from SEC with PS standards.

Two semicrystalline macromonomers and four semicrystalline macroterminators were synthesized via ring-opening transesterification polymerization from hydroxyl functionalized norbornene or an enyne (**Figure 4.2**). High molecular weights, up to 98 kDa, and low dispersity, $Đ < 1.2$, materials were synthesized (**Table 4.1**). With these four materials, six star polymers were synthesized (**Table 4.2)**. Four structural parameters define each star: the molecular weight of each block (M_A, M_B, $M_{A'}$) and the average number of arms (n); thus the stars are referred to as $M_A(M_B\text{-}M_{A'})_n$ and correspondingly the macromonomers are referred to as $M_B\text{-}M_{A'}$. The shift towards lower retention times from macromonomer (MM) to poly(macromonomer) (p(MM)) and terminated star in the SEC traces are indicative that the ROMP and termination chemistries work even at high molecular weights (**Figure 4.3**). Despite its high molecular weight, the macromonomer clearly polymerizes well given there is just a small bump from residual unreacted macromonomer at lower retention times. The high molecular weight of these materials makes it difficult to precisely determine important structural parameters such as n. Hindering these efforts is the limited solubility of PLLA, due to its crystallinity, in common SEC solvents such as THF. To circumvent these challenges, we have calculated n from a combination of molecular weights of the macromonomer and the

macroterminators determined by ^{1}H NMR and f_{PLLA}. The values of n determined this way were within 10% of what was synthetically targeted.

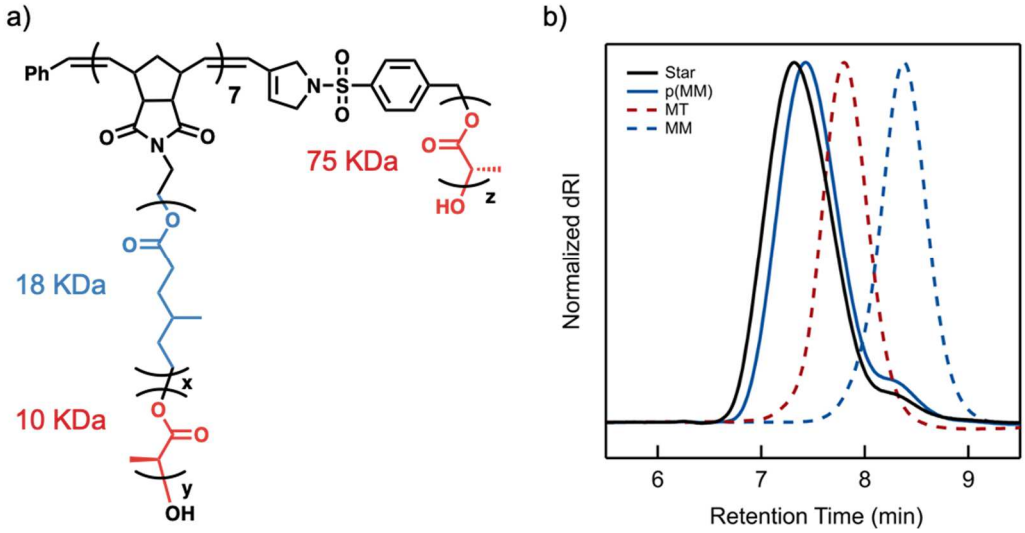

Figure 4.3. Chemical structure of 75(18-10)$_7$ star polymer (a) and corresponding SEC traces of the star and reactants (b).

Table 4.2. Summary of Physical Characterization of PLLA-PMCL A(BA′)$_n$ Miktoarm Star Polymers

Star	f_{PLLA}[a]	$M_{n,A}$[b]	$M_{n,B}$[b]	$M_{n,A'}$[b]	n[c]	$Đ$	τ[d]
75(18-10)$_7$	0.50	75	18	9.5	6.5	1.38	0.89
75(18-10)$_9$	0.46	75	18	9.5	9.4	1.40	0.89
98(18-10)$_7$	0.53	98	18	9.5	7.2	1.40	0.91
98(32-8)$_9$	0.33	98	32	7.5	8.5	1.53	0.93
98(32-8)$_6$	0.40	98	32	7.5	5.6	1.46	0.93
98(32-8)$_3$	0.52	98	32	7.5	2.9	1.44	0.93

[a]Calculated from ^{1}H NMR using ρ_{PLLA}= 1.25 g cm^{-3} and ρ_{PMCL}= 1.03 g cm^{-3}. [b]Determined from ^{1}H NMR chain-end analysis. [c]Determined from the volume fraction and M_n. [d]Calculated from $M_{n,A}/(M_{n,A} + M_{n,A'})$.

To further prove that the termination works at such high molecular weights, the poly(macromonomer) used in the synthesis of 75(18-10)$_7$ was quenched with excess ethyl vinyl ether and then one equivalent of the macroterminator was added. The SEC trace of the blend overlaps the poly(MM) at high retention times and is a bit broader a lower retention

times (**Figure 4.4**). Importantly, the blend is shifted significantly toward higher retention time from the terminated star. The difference in these dRI traces indicate the termination chemistry works well even at such high molecular weights.

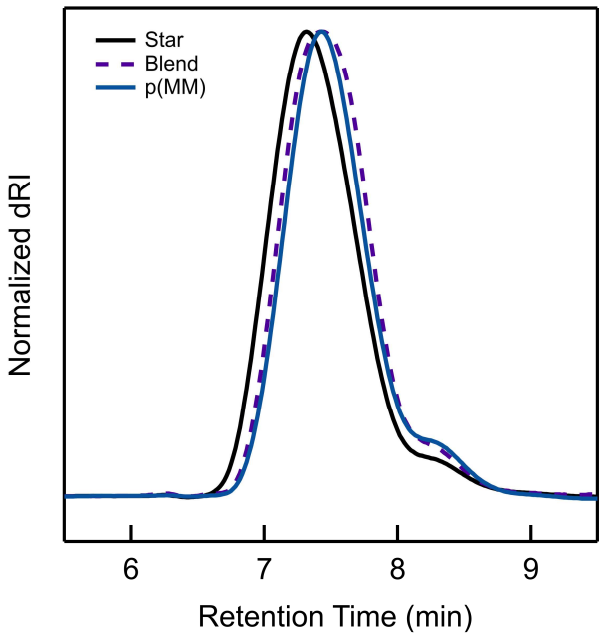

Figure 4.4. Comparison of 75(18-10)$_7$ terminated star to a stoichiometric blend of the poly(macromonomer) and macroterminator.

Of particular importance is the self-assembly of these materials. While small-angle X-ray scattering experiments yielded inconclusive results, transmission electron microscopy (TEM) was more fruitful. Micrographs of 98(32-8)$_3$ indicate this star forms discrete particles of PLLA in a continuous matrix of PMCL at f_{PLLA} = 53% (**Figure 4.5**). Therefore, this star satisfies the morphological requirement for elasticity even at such high f_{PLLA}. Additionally, we confirmed these star polymers are semi-crystalline with a melting transition at approximately 180 □ as determined by differential scanning calorimetry (**Figure 4.6**).

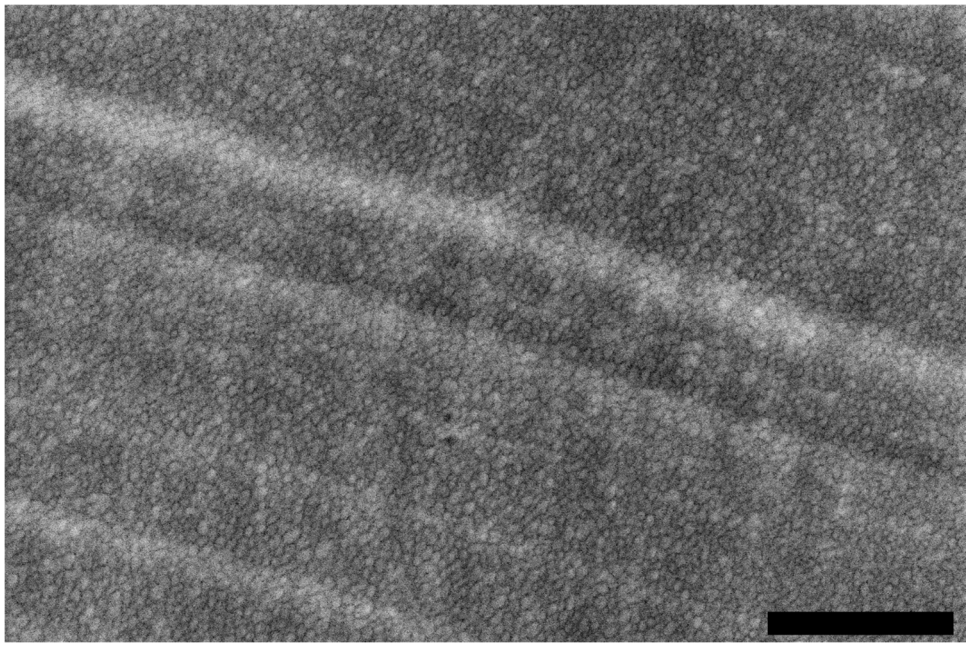

Figure 4.5. Representative TEM micrograph of $98(32\text{-}8)_3$ revealing microphase separated particles of PLLA (light) and PMCL (dark). Scale bar corresponds to 2 μm.

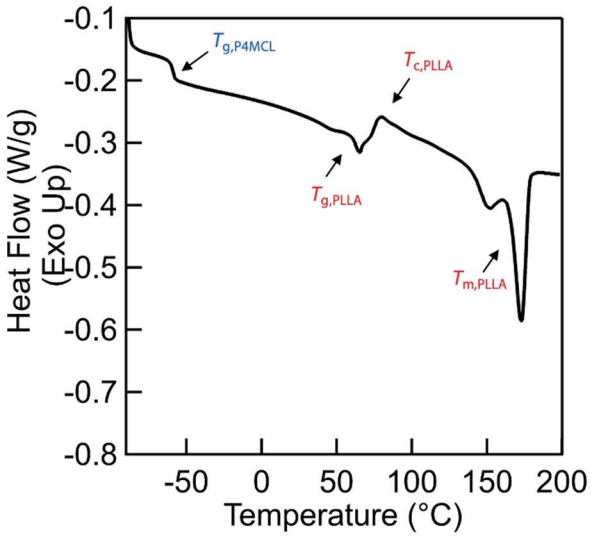

Figure 4.6. Differential scanning calorimetry of a $75(18\text{-}10)_7$ miktoarm star labeled with the glass transition temperatures for each block (T_g), crystallization temperature (T_c), and melting temperature (T_m).

4.3 Mechanical Properties

4.3.1 Effect of A′ Block

The main mode of block copolymer TPE failure is via chain pull out of the A block from the hard domain.[19] Therefore, the length of the A block can have a large impact on TPE performance. Given the extreme block asymmetry that is required to achieve large phase boundary deflections, small A′ blocks could lead to failure at low stresses and strains. To investigate this, we chose to use amorphous PLA as the hard block rather than semi-crystalline PLLA to avoid the conflating effects of molecular weight and crystallinity, especially at the low molecular weights investigated.[20] The same 12 kDa PMCL macromonomer was chain extended with PLA to 4 kDa and 5 kDa to form the A′ block. While there is only a one kDa difference, prior reports have suggested large changes in TPE performance with small increases in the hard block length.[21,22] Both macromonomers were polymerized to form an 8-arm poly(macromonomer) which was then terminated with a 33 kDa PLA macroterminator. The materials were then tensile tested, both monotonic extension to failure as well as in step-cycle manner where the strain was incremented by 50% and brought back to zero load with each cycle (**Figure 4.7**).

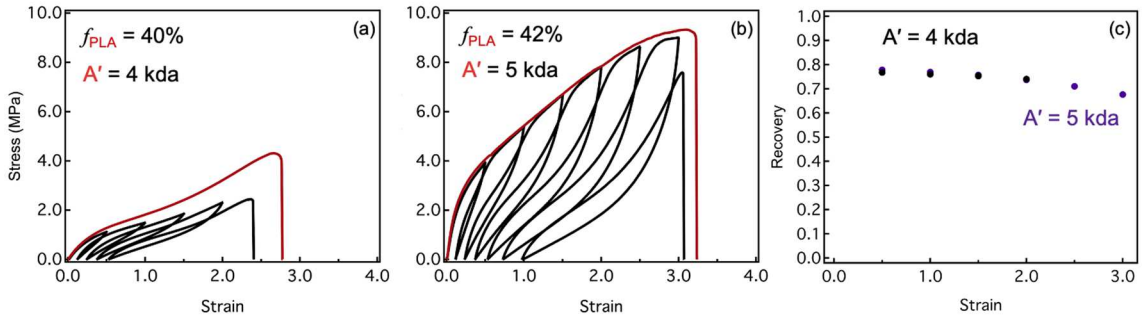

Figure 4.7. Stress-strain curves including step-cyclic tests of $33(12\text{-}4)_8$ (a), $33(12\text{-}5)_8$ (b), and step-cycle recovery (c).

By using μSTAR to make these two materials we can be sure that they are close to identical with the exception of the A′ block, so any performance enhancements can be attributed to this one key difference. The effects of A′ molecular weight are apparent: the 1 kDa increase leads to higher stress and strain at break culminating in a more than 3 times higher fracture toughness. Given the large differences in mechanical properties, it is surprising that the recovery in step-cycle testing is so similar. This similarity may indicate other structural parameters dictate the recovery of the material much more so than the length of A′. Note that the significantly higher initial Young's modulus of the larger A′ block material could indicate yielding due to an undesirable morphology. Indeed, this is one tradeoff of a larger A′ block: the material may be tougher, but it will also have a lower τ and thus cannot remain elastic at nearly as high f_A due to morphological constraints. This is an important consideration in the design of miktoarm star thermoplastic elastomers. In order to have both large A′ blocks and an optimally high τ, a correspondingly longer A block must be employed with a higher molecular weight macroterminator. Going forward in our study of semi-crystalline TPEs, we focused on A blocks 75 kDa and higher and A′ blocks 7.5 kDa and higher.

4.3.2 Effect of B Length

Thermoplastic elastomers derive a significant amount of strength from trapped entanglements in the soft B block.[23] With traditional styrenic thermoplastic elastomers, the requirements that the block copolymer must be microphase separated at $f_A < 30\%$ means the B block is sufficiently long that, assuming constant f_A, the properties of thermoplastic elastomer are considered to be independent of molecular weight.[21,22] In the case of miktoarm stars, the B block will be smaller than a linear TPE at the same f_A as the same number of total B monomers must be distributed over more chains per molecule. In the case of semi-crystalline

thermoplastic elastomers, where ideally $T_{ODT} > T_C > T_{g,B}$, there is one more phenomenon to consider. In this case the crystalline A block is under "soft" confinement as at the crystallization temperature of the A block, the B block is above its T_g and thus it can be deformed by crystal breakout as the A block crystallizes.[24] This can lead to the formation of a continuous crystalline domains of A block even if it is not the thermodynamic equilibrium morphology. However, the crystal breakout phenomenon can be suppressed at sufficiently high segregation strengths (χN) and with a sufficiently entangled soft B block.

To investigate the effect of a PMCL B block on the performance of semi-crystalline miktoarm star TPEs, two materials were synthesized using the same macroterminators and a similar number of arms: $98(32\text{-}8)_6$ and $98(18\text{-}10)_7$. Tensile testing results revealed large differences in the performance of these materials (**Figure 4.8**). While $98(18\text{-}10)_7$ with the shorter B block breaks at significantly higher stress and is overall tougher, it is not very elastic as indicated by the recovery plot; instead, it yields at low strains. To be sure, the slightly longer A′ block coupled with the shorter B block implies a higher f_{PLLA} material, so the higher toughness is not surprising. However, the inelasticity is surprising as at a $\tau = 0.91$ and f_{PLLA} = 53% the material should be well within the cylinder forming envelope predicted by SCFT. Instead, this behavior might be explained by crystal breakout occurring in the case of the 18 kDa B block; the higher segregation strength and degree of entanglement of the longer B block may suppress crystal breakout. This is further evidenced by $98(32\text{-}8)_3$ and $75(18\text{-}10)_9$, which will be discussed in depth in the next section. $98(32\text{-}8)_3$ is elastic while $75(18\text{-}10)_9$ has an even lower f_{PLLA} and yet still exhibits yielding and poor recovery. Further, $98(32\text{-}8)_3$ has nearly the same f_{PLLA} as the inelastic $98(18\text{-}10)_7$. While these materials have different values of τ, they are all within the cylinder forming area predicted by SCFT. To examine if crystal breakout is

occurring, real space images will be acquired and discussed in future work. Crystallization issues aside, both materials have very respectable toughness, especially compared to the lower molecular weight materials made for the A′ comparison.

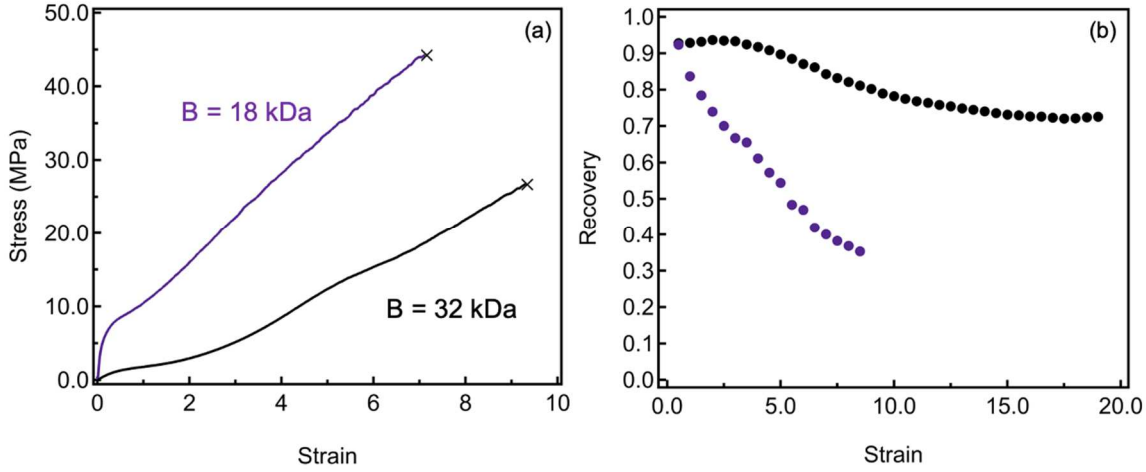

Figure 4.8. Mechanical testing data of 98(32-8)$_6$ (black) and 98(18-10)$_7$ (purple): monotonic extension to failure stress–strain curve (a) and recovery plot from step-cycle tensile testing (b).

4.3.3 Effect of the Number of BA′ Diblock Arms

μSTAR offers an excellent platform for examining the effect of arm number on mechanical properties of miktoarm star thermoplastic elastomers as the average number of arms can be tuned by adjusting the molar ratio of macromonomer to G3 catalyst. Thus, the molecular weight of A, B, and A′ can be held perfectly constant while *n* is varied, which reciprocally affects f_{PLLA}. Two series of stars were synthesized, 98(32-8)$_n$ and 75(18-10)$_n$. First, the 98(32-8)$_n$ materials were examined with three stars having *n* = 3, 6, and 9. Step cyclic testing shows all three samples are elastic, including 98(32-8)$_3$ at f_{PLLA} = 52% (**Figure 4.9**).

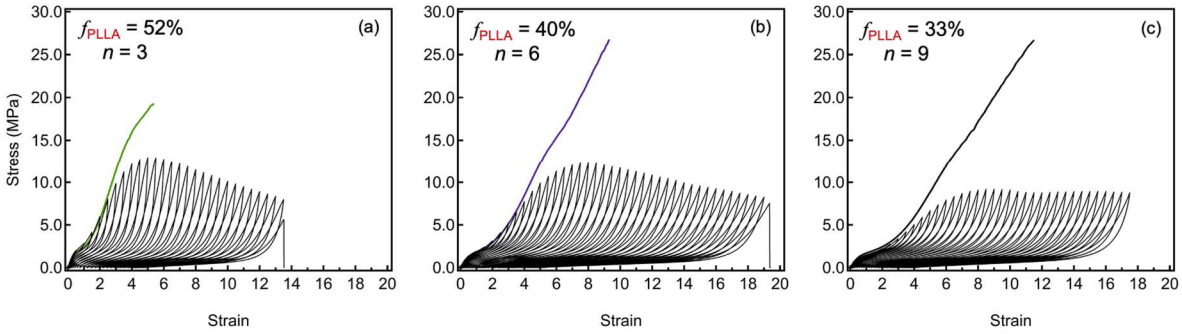

Figure 4.9. Stress–strain curves including step-cycle tests of 98(32-8)$_3$ (a), 98(32-8)$_6$ (b), and 98(32-8)$_9$ (c).

Comparing the monotonic extension stress–strain curves and recovery plots of the three materials it is apparent that the strain at break and recovery increases with the *n* while the Young's modulus across the range of strains decreases with *n* (**Figure 4.10)**. This trend is expected for thermoplastic elastomers with decreasing f_{PLLA} and may not be purely due to architectural effects.[7,9] However, the trend of toughness deviates entirely from the typical paradigm wherein a larger f_{PLLA} should increase toughness. Despite having the lowest f_{PLLA}, 98(32-8)$_9$ was the toughest material while 98(32-8)$_3$, with the highest f_{PLLA}, was the least. In fact, 98(32-8)$_9$ is more than 160% tougher than 98(32-8)$_3$ and more than 25% tougher than 98(32-8)$_6$. Further, while *n* = 3 breaks at noticeably less stress than the large *n* materials, the stress at break of *n* = 6 and 9 are nearly identical (26.7 v.s. 26.8 MPa). This invariance suggests an increase and then saturation of the ultimate stress for stars with increasing *n*, which has previously been observed in (AB)$_n$ thermoplastic elastomers.[25] Simulations of A(BA′)$_n$ stars have shown that *n* = 3 stars have almost a 20% probability of not bridging any domains and any stars that are not bridging domains do not structurally contribute to the strength of the material.[26] The probability of higher *n* materials not structurally contributing decreases rapidly with increasing *n*. Likewise, the fraction of arms that bridge domains also increases markedly with increasing *n*. These findings raise interesting questions, suggesting that the ultimate stress

at break may be related to the percent of structurally enforcing molecules while the toughness may be related to the fraction of bridging arms.

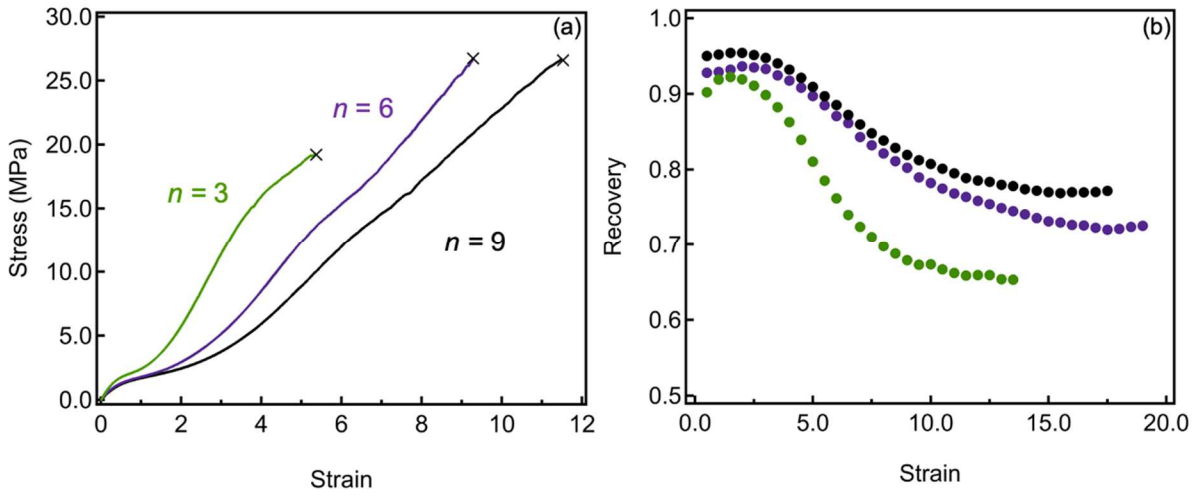

Figure 4.10. Mechanical testing data of 98(32-8)$_3$ (green), 98(32-8)$_6$ (purple) 98(32-8)$_9$ (black): stress–strain curves showing monotonic extension to failure (a) and recovery plot from step-cycle tensile testing (b).

Next we examined the lower molecular weight 75(18-10)$_n$ materials for n = 7 and 9 (**Figure 4.11**). Similar to 98(18-10)$_7$, these materials are not very elastic as evidenced by recovery step cyclic testing even though they are well within the cylinder forming envelope predicted by SCFT. However, similar trends to the 98(32-8)$_n$ series are observed. Increasing n from 7 to 9 increases the toughness and strain at break and decreases Young's modulus, although the stress at break is nearly the same. This supports the idea that more arms increase toughness despite decreasing f_{PLLA}, which is perhaps due to more domain bridging. The invariance of the stress at break observed here may be because there is a similar percent of stars that are not structurally contributing to the network. The effect of n on the melt rheology

will be studied in future work, which is important for processability. Prior investigations into stars with multiple diblock arms indicate that melt viscosity is independent of n.[27]

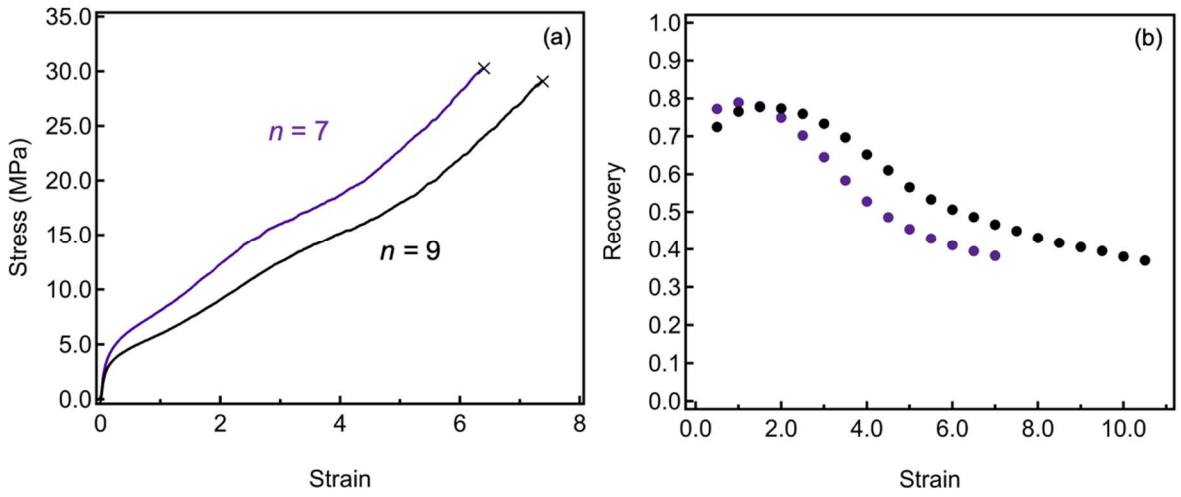

Figure 4.11. Mechanical testing data of 75(18-10)$_9$ (black) and 75(18-10)$_7$ (purple): stress–strain curve showing monotonic extension to failure (a) and recovery plot from step-cycle tensile testing (b).

4.3.4 Comparison to Prior Work

μSTAR offers an excellent platform to explore structure–property relationships with A(BA′)$_n$ miktoarm star polymers. However, it is important to consider how these materials perform relative to linear thermoplastic elastomers as well as other miktoarm star polymer thermoplastic elastomers synthesized via anionic polymerization. Watts and coworkers reported the stress–strain curves for several linear PLLA-*b*-PMCL-*b*-PLLA triblocks at various volume fractions of PLLA. Here, the stress–strain curves of our elastic PLLA-PMMCL miktoarm star polymers are compared to the triblocks from Watts et al. with demonstrated elasticity (**Figure 4.12**). While the highest performing linear triblock, 16-135-16, has a slightly higher stress at break with f_{PLLA} = 17%, in all other ways the star polymers exhibit either comparable or superior performance.

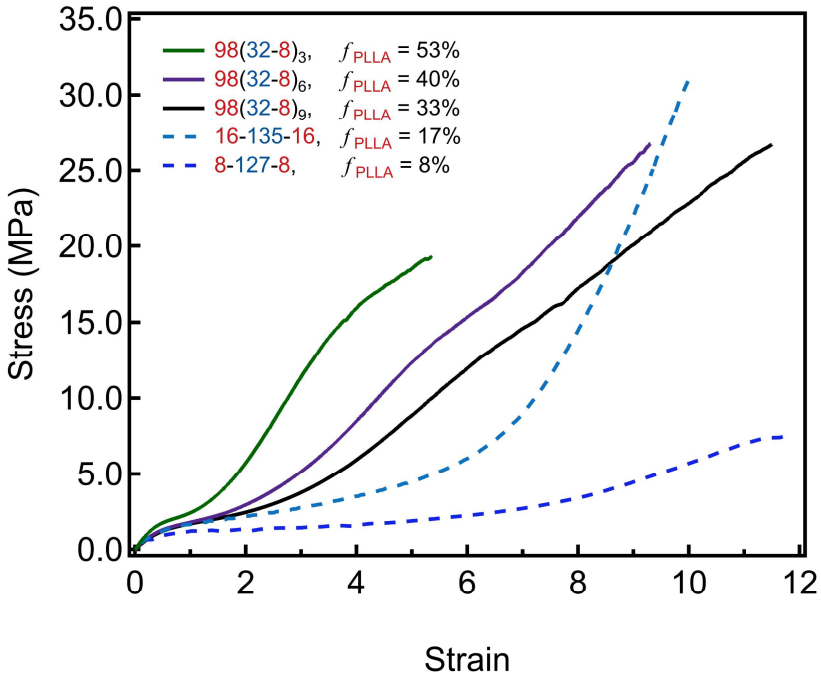

Figure 4.12. Comparison of elastic miktoarm star polymers (solid traces) to elastic linear triblock polymers (dashed traces), both using PLLA as the hard block and PMCL as the soft block. Adapted with permission from *Biomacromolecules*. Copyright 2017 American Chemical Society.[9]

The star polymers begin to strain harden at lower strains and thus the Young's modulus across the range of strains is higher in the stars. Ultimately, they absorb more energy before failure and therefore are tougher than the linear materials. The higher stress at failure of the 16-135-16 linear triblock may be related to the larger 16 kDa end blocks, more than twice as large as the A′ block of the star polymers, which we showed plays a key role in influencing mechanical properties.

Shi and coworkers reported tensile testing results of two anionically synthesized elastic $A(BA')_3$ miktoarm star polymers comprised of poly(styrene) (PS) instead of PLLA and poly(isoprene) (PI) instead of PMCL. PS and PI blocks are one of the most popular choices in mass produced TPEs and are widely used in commercial applications. The molecular weights of each component are comparable to those of our polyester stars, making this a reasonable

comparison (**Figure 4.13**). The mechanical performance of our sustainable star polymers synthesized via μSTAR are superior in most respects. The stress and strain at break and importantly, fracture toughness, are much higher in the polyester stars. Given the improvement in mechanical properties that we observe with increasing *n*, μSTAR offers a clear advantage over anionic synthesis as increasing *n* past *n* = 3 is simple compared to the anionic route.

Recovery and initial Young's modulus are the two properties where the PS-PI stars perform comparably to the PLA-PMCL stars. While the recovery is slightly worse, the initial Young's modulus of the f_{PLLA} = 40% 98(32-8)$_6$ PLLA-PMCL star is higher than that of the f_{PS} = 41% of the 81(32-11)$_3$ PS-PI star. It should be noted that this PLLA-PMCL star can be cycled to much higher strains than the PS-PI star (see **Figure 4.9**). In the case of the 98(32-8)$_9$ f_{PLLA} = 52% star, the recovery is noticeably better but the initial Young's modulus is lower compared to the 81(56-11)$_3$ PS-PI f_{PS} = 52% star. Although select PS-PI stars have slightly better performance by some metrics, overall the PMCL-PLA stars presented here offer superior mechanical performance (see **Tables 4.3** and **4.4**).

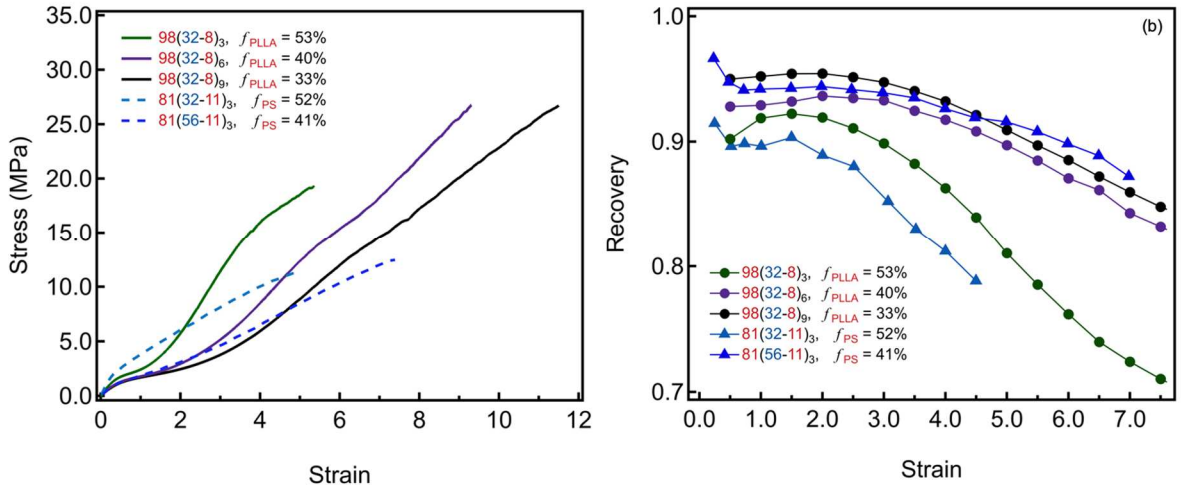

Figure 4.13. Comparison of mechanical properties to Shi et al. (a) Stress–strain curves of elastic PLA-PMCL miktoarm star polymers (solid traces) and elastic PS-PI miktoarm star polymers (dashed traces). (b) Comparison of the recovery during step-cycle tensile testing of elastic PLA-PMCL miktoarm star polymers (circles) and elastic PS-PI miktoarm star polymers (triangles). The strain range is truncated to the point of failure of the PS-PI stars for clarity. Adapted with permission from *Macromolecules*. Copyright 2014 American Chemical Society.[7]

Table 4.3. Summary of Mechanical Properties of PLLA-PMCL A(BA′)$_n$ Miktoarm Star Polymers

Star	f_{PLLA}[a]	σ (MPa)[b]	ε_B[b]	U_T[c] (MJ m^{-3})	E[d] (MPa)	E @ 300%[e] (MPa)
75(18-10)$_7$	0.50	29.2 ± 1.7	6.3 ± 0.5	102.8 ± 10.1	67.1 ± 11.7	2.3 ± 0.5
75(18-10)$_9$	0.46	30.6 ± 5.4	7.6 ± 1.1	117.1 ± 32.1	44.3 ± 3.4	2.9 ± 0.4
98(18-10)$_7$	0.53	42.3 ± 1.8	6.8 ± 0.4	164.6 ± 16.8	77.2 ± 5.8	6.0 ± 0.1
98(32-8)$_9$	0.33	26.8	11.5	135.4	3.3	1.7
98(32-8)$_6$	0.40	26.7	9.3	107.2	4.4	2.8
98(32-8)$_3$	0.52	19.3	5.3	51.6	5.5	5.7

[a]Calculated from ^{1}H NMR using ρ_{PLLA}= 1.25 g cm^{-3} and ρ_{PMCL}= 1.03 g cm^{-3}. [b]Determined from tensile testing to the break point. [c]Fracture toughness determined by integrating stress over strain from monotonic tensile tests. [d]Determined from a linear fit of monotonic tensile test data at low strains (ε < 0.1). [e]Determined from a linear fit of monotonic tensile test at ε = 3. Averages ± standard deviations are included for samples with at least three specimens tested.

Table 4.4. Summary of Mechanical Properties of Other Thermoplastic Elastomers

TPE	f_A[a]	σ[b] (MPa)	ε_B[b]	U_T[c] (MJ m^{-3})	E[d] (MPa)	E @ 300%[e] (MPa)
8-127-8[f]	0.08	7.8 ± 0.5	11.9 ± 0.6	35.6	2.2 ± 0.1	0.2
16-135-16[f]	0.17	31 ± 4	12.0 ± 0.3	81.8	4.0 ± 0.3	0.7
81(32-11)$_3$[g]	0.41	12.6	7.4	45.9	3.5 ± 0.5	4.6 ± 0.1
81(56-11)$_3$[g]	0.52	11.3	5.0	33.1	12.3 ± 0.3	8.1 ± 0.2

[a]Calculated from ^{1}H NMR using ρ_{PLLA}= 1.25 g cm^{-3} and ρ_{PMCL}= 1.03 g cm^{-3}. [b]Determined from tensile testing to the break point. [c]Fracture toughness determined by integrating stress over strain from monotonic tensile tests. [d]Determined from a linear fit of monotonic tensile test data at low strains ($\varepsilon < 0.1$). [e]Determined from a linear fit of monotonic tensile test at $\varepsilon = 3$. [f]Data taken from ref. 9. [g]Data taken from ref. 7. Averages ± standard deviations are included for samples with at least three specimens tested.

4.4 Conclusions

We have used a synthetic platform known as μSTAR to synthesize sustainable and high performing thermoplastic elastomers. These materials not only have more favorable mechanical properties compared to linear triblocks of the same chemistry but also compared to petroleum derived TPEs of the same miktoarm star architecture. Employing the modularity and versatility of μSTAR allowed us to determine preliminary insights into how the mechanical properties of A(BA′)$_n$ miktoarm star polymers depend on structural parameters such as n, $M_{A'}$, and M_B. These findings demonstrate that μSTAR is capable of producing materials with unique properties. Investigations continue into using μSTAR in other applications where miktoarm stars could provide improved properties, such as ion conduction[28] and ultrafiltration membranes.[29]

4.5 Experimental

4.5.1 Chemicals

Unless otherwise stated, all chemicals were purchased at the highest available purity and used as received. All reactions were carried out under a nitrogen atmosphere with dry solvents using anhydrous conditions unless otherwise stated. Dry, degassed dichloromethane (DCM), tetrahydrofuran (THF), and toluene were obtained from a JC Meyer solvent purification system. Toluene used for the synthesis of poly(D,L-lactide) and poly(L-lactide) was distilled from Na/benzophenone. Chlorobenzene was distilled from P_2O_5. Tin(II) 2-ethylhexanoate ($Sn(Oct)_2$, Aldrich, 92.5–100%) was fractionally distilled 3× under reduced pressure (50 mtorr, 150 □) and stored in a nitrogen filled glovebox before use. 4-Methylcaprolactone (MCL) was prepared according to literature,[9] purified by fractional distillation 3× from calcium hydride (CaH_2, Fisher Scientific, 93%), 3× from $Sn(Oct)_2$ under reduced pressure (50 mtorr, 50 □), and stored in a nitrogen filled glovebox before use. D,L-Lactide and L-lactide were generously provided by Corbion (PURASORB DL) and recrystallized six times from anhydrous toluene. Grubbs' third-generation metathesis catalyst [$(H_2IMes)(pyr)_2(Cl)_2Ru$=CHPh] (G3) was prepared according to literature.[30]

4.5.2 Characterization

NMR spectra were collected on a 600 MHz Varian VNMRS. Size-exclusion chromatography was performed on a Waters instrument using a differential refractive index detector and two Tosoh columns (TSKgel SuperHZM-N, 3 μm polymer, 150 × 4.6 mm) with chloroform at 35 °C as the mobile phase. In this case, molar masses and molar mass dispersity ($Đ$) were determined against narrow PS standards (Agilent). Differential scanning calorimetry

(DSC) data were collected on a liquid-nitrogen-cooled TA Instruments Q2000 Differential Scanning Calorimeter with an indium standard calibration. The samples were measured under a nitrogen environment and in a temperature range from −75 to 210 °C at a ramp rate of 10 °C per minute. Samples for mechanical testing and transmission electron microscopy (TEM) were compression molded using a Carver press (Wabash, IN). Samples were press in a 0.5 mm thick steel rectangular mold with 3000 lbf at 200 □ for 15 minutes and then quenched to room temperature. For TEM, polymers were cut to into ultrathin (~100 nm) sections by cryo-ultramicrotomed at -100℃ and imaged without staining. For mechanical testing, a dog bone cutting die was used to punch out samples of the correct geometry. Monotonic and step-cyclic tensile mechanical tests were performed on these dog bone-shaped specimens (gauge width = 1.5 mm, gauge length = 10 mm, 2.5 mm transition zone radius) using a custom-built setup with a vertical TwinRail positioning table (Lintech, CA) and a 10 N load cell (LSB2000 Miniature S-Beam, FUTEK, CA). A deformation rate of 10 mm/min was used for all test (strain rate = 1 min^{-1}). Step-cyclic tensile tests were brought to zero force between cycles by increasing the minimum applied strain as the specimens deformed.

Scheme 4.2. Representative synthesis of PMCL-*b*-PLLA macromonomer (MM-32-8)

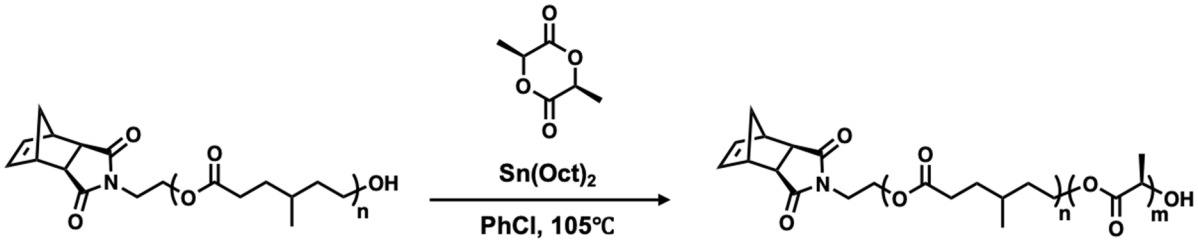

In a Schlenk flask charged with a stir bar, 7.71 g PMCL macromonomer[17] (32 kDa, 0.240 mmol, 1 eq) was dried for 3 days at 50 □ *in vacuo*. The flask was brought into a nitrogen filled glovebox where 3.15 g L-lactide (21.8 mmol, 79.3 eq) was added, followed by 21 mL

chlorobenzene and 0.111 g $Sn(Oct)_2$ (0.275 mmol, 1.0 eq). The reaction mixture was heated to 105 □ for 36 minutes in an oil bath under nitrogen and then quenched in cold water. The mixture was diluted with DCM and an aliquot was extracted to determine the monomer conversion by ^{1}H NMR (63%). The sample was precipitated 5 times into cold methanol, filtered, and dried *in vacuo*.

Scheme 4.3. Representative synthesis of PLLA macroterminator (MT-98)

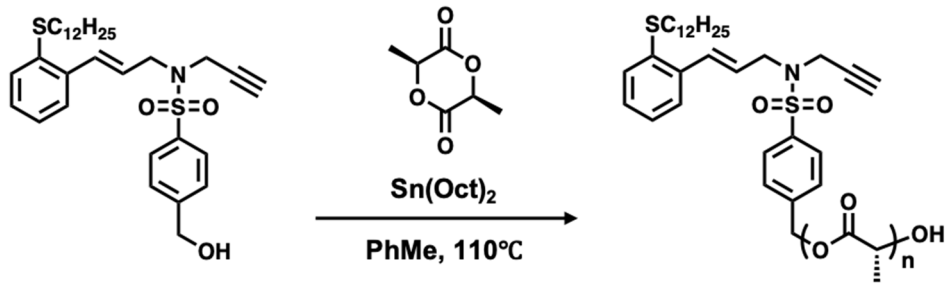

In a nitrogen filled glovebox, 10.18 g L-lactide (70.6 mmol, 992 eq), 39.1 mg terminator alcohol[16] (0.071 mmol, 1 eq), 28.6 mg $Sn(Oct)_2$ (1.0 eq, 0.071 mmol), and 5.90 mL toluene were combined in an oven-dried heavy-wall pressure vessel with a stir bar. The vessel was sealed with a threaded PTFE bushing using a perfluoro O-ring and removed from the glovebox. The reaction mixture was heated to 110 □ in an oil bath for 28 minutes and then quenched in cold water. The mixture was diluted with DCM and an aliquot was extracted to determine the monomer conversion by ^{1}H NMR (88%). The sample was precipitated 6 times into cold methanol, filtered, and dried *in vacuo*.

4.6 References

(1) Holden, G. Thermoplastic Elastomers. In *Rubber Technology*; Morton, M., Ed.; Springer US, 1987; pp 465–481.

(2) Matsen, M. W. Effect of Architecture on the Phase Behavior of AB-Type Block Copolymer Melts. *Macromolecules* **2012**, *45*, 2161–2165.

(3) Holden, C.; Bishop, E. T.; Legge, N. R. Thermoplastic Elastomers. **1969**, *57*, 37–57.

(4) Levi, A. E.; Fu, L.; Lequieu, J.; Horne, J. D.; Blankenship, J.; Mukherjee, S.; Zhang, T.; Fredrickson, G. H.; Gutekunst, W. R.; Bates, C. M. Efficient Synthesis of Asymmetric Miktoarm Star Polymers. *Macromolecules* **2020**, *53*, 702–710.

(5) Lequieu, J.; Koeper, T.; Delaney, K. T.; Fredrickson, G. H. Extreme Deflection of Phase Boundaries and Chain Bridging in A(BA′)n Miktoarm Star Polymers. *Macromolecules* **2020**, *53*, 513–522.

(6) Lynd, N. A.; Oyerokun, F. T.; O'Donoghue, D. L.; Handlin, D. L.; Fredrickson, G. H. Design of Soft and Strong Thermoplastic Elastomers Based on Nonlinear Block Copolymer Architectures Using Self-Consistent-Field Theory. *Macromolecules* **2010**, *43*, 3479–3486.

(7) Shi, W.; Lynd, N. A.; Montarnal, D.; Luo, Y.; Fredrickson, G. H.; Kramer, E. J.; Ntaras, C.; Avgeropoulos, A.; Hexemer, A. Toward Strong Thermoplastic Elastomers with Asymmetric Miktoarm Block Copolymer Architectures. *Macromolecules* **2014**, *47*, 2037–2043.

(8) Drobny, J. G. *Handbook of Thermoplastic Elastomers*; 2014.

(9) Watts, A.; Kurokawa, N.; Hillmyer, M. A. Strong, Resilient, and Sustainable Aliphatic Polyester Thermoplastic Elastomers. *Biomacromolecules* **2017**, *18*, 1845–1854.

(10) Farah, S.; Anderson, D. G.; Langer, R. Physical and Mechanical Properties of PLA, and Their Functions in Widespread Applications — A Comprehensive Review. *Adv. Drug Deliv. Rev.* **2016**, *107*, 367–392.

(11) Watts, A.; Hillmyer, M. A. Aliphatic Polyester Thermoplastic Elastomers Containing Hydrogen-Bonding Ureidopyrimidinone Endgroups. *Biomacromolecules* **2019**, *20*, 2598–2609.

(12) De Hoe, G. X.; Zumstein, M. T.; Tiegs, B. J.; Brutman, J. P.; McNeill, K.; Sander, M.; Coates, G. W.; Hillmyer, M. A. Sustainable Polyester Elastomers from Lactones: Synthesis, Properties, and Enzymatic Hydrolyzability. *J. Am. Chem. Soc.* **2018**, *140*, 963–973.

(13) Lundberg, D. J.; Lundberg, D. J.; Hillmyer, M. A.; Dauenhauer, P. J. Techno-Economic Analysis of a Chemical Process to Manufacture Methyl-ε-Caprolactone from Cresols. *ACS Sustain. Chem. Eng.* **2018**, *6*, 15316–15324.

(14) R. Kricheldorf, H.; Kreiser-Saunders, I. Anionic Polymerization of L-Lactide in Solution. *Makromol. Chem.* **1990**, *1066*, 1057–1066.

(15) Avgeropoulos, A.; Hadjichristidis, N.; Copolymer, S. B. Synthesis of Model Nonlinear Block Copolymers of A(BA)2, A(BA)3, and (AB)3A(BA)3 Type. *J. Polym. Sci. Part A Polym. Chem.* **1997**, *35*, 813–816.

(16) Fu, L.; Zhang, T.; Fu, G.; Gutekunst, W. R. Relay Conjugation of Living Metathesis Polymers. *J. Am. Chem. Soc.* **2018**, *140*, 12181–12188.

(17) Levi, A. E.; Lequieu, J.; Horne, J. D.; Bates, M. W.; Ren, J. M.; Delaney, K. T.; Fredrickson, G. H.; Bates, C. M. Miktoarm Stars via Grafting-Through Copolymerization: Self-Assembly and the Star-to-Bottlebrush Transition. *Macromolecules* **2019**, *52*, 1794–1802.

(18) Xiong, M.; Schneiderman, D. K.; Bates, F. S.; Hillmyer, M. A.; Zhang, K. Scalable Production of Mechanically Tunable Block Polymers from Sugar. *Proc. Natl. Acad. Sci.*

2014, *111*, 8357–8362.

(19) Bishop, E. T.; Davison, S. Network Characteristics of the Thermoplastic Elastomers. **1969**, *79*, 59–79.

(20) Sveinbjörnsson, B. R.; Miyake, G. M.; El-Batta, A.; Grubbs, R. H. Stereocomplex Formation of Densely Grafted Brush Polymers. *ACS Macro Lett.* **2014**, *3*, 26–29.

(21) Morton, M. Mechanisms of Reinforcement of Elastomers by Polymeric Fillers. In *Journal of Elastomers and Plastics*; 1971; Vol. 3, pp 112–125.

(22) Meier, D. J. Theory of Block Copolymers. I. Domain Formation in A-B Block Copolymers. *J. Polym. Sci. Part B Polym. Phys.* **1996**, *34*, 1821–1838.

(23) Holden, G.; Legge, N. R.; Quirk, R.; Schroeder, H. E. *Thermoplastic Elastomers*, 2nd ed.; 2004.

(24) Schmalz, H.; Müller, A. J.; Abetz, V. Crystallization in ABC Triblock Copolymers with Two Different Crystalline End Blocks: Influence of Confinement on Self-Nucleation Behavior. *Macromol. Chem. Phys.* **2003**, *204*, 111–124.

(25) Shim, J. S.; Kennedy, J. P. Novel Thermoplastic Elastomers. II. Properties of Star-Block Copolymers of PSt-b-PIB Arms Emanating from Cyclosiloxane Cores. *J. Polym. Sci. Part A Polym. Chem.* **1999**, *37*, 815–824.

(26) Lequieu, J.; Trenton, K.; Delaney, K. T.; Fredrickson, G. H. Extreme Deflection of Phase Boundaries with A(BA')n Miktoarm Star Polymers. *Submitted*.

(27) Bi, L. K.; Fetters, L. J. Synthesis and Properties of Block Copolymers. 3. Polystyrene-Polydiene Star Block Copolymers. *Macromolecules* **1976**, *9*, 732–742.

(28) Lee, D.; Jung, H. Y.; Park, M. J. Solid-State Polymer Electrolytes Based on AB3-Type Miktoarm Star Copolymers. *ACS Macro Lett.* **2018**, *7*, 1046–1050.

(29) Hampu, N.; Werber, J. R.; Chan, W. Y.; Feinberg, E. C.; Hillmyer, M. A. Next-Generation Ultrafiltration Membranes Enabled by Block Polymers. *ACS Nano* **2020**, *14*, 16446–16471.

(30) Love, J. A.; Morgan, J. P.; Trnka, T. M.; Grubbs, R. H. A Practical and Highly Active Ruthenium-Based Catalyst That Effects the Cross Metathesis of Acrylonitrile. *Angew. Chem. Int. Ed.* **2002**, *41*, 4035–4037